Scientific report ; WR 2009-06

Bird detection by operational weather radar

Adriaan M. Dokter, Felix Liechti and Iwan Holleman

De Bilt, 2009

KNMI scientific report = wetenschappelijk rapport; WR 2009-06

De Bilt, 2009

PO Box 201
3730 AE De Bilt
Wilhelminalaan 10
De Bilt
The Netherlands
http://www.knmi.nl
Telephone +31(0)30-220 69 11
Telefax +31(0)30-221 04 07

Authors: Dokter, A.M.
Liechti, F.
Holleman, I.

Bird detection by operational weather radar

Adriaan M. Dokter[1], Felix Liechti[2], and Iwan Holleman[1]

[1]Royal Netherlands Meteorological Institute, De Bilt, The Netherlands
[2]Swiss Ornithological Institute, Sempach, Switzerland

November 20, 2009

Executive summary

Within the Avian Alert System of Systems (SoS) initiative of the European Space Agency (ESA), we have explored the potential of operational C-band Doppler weather radar as a bird migration sensor. A bird migration recognition algorithm has been developed, extracting bird density, speed and direction as a function of altitude. The weather radar data have been validated against simultaneous and co-located bird density measurements by a high precision bird radar, provided by the Swiss Ornithological Institute (SOI). This mobile tracking radar has been stationed next to weather radar sites in the Netherlands, Belgium and France during the peak bird migration season in autumn 2007 and spring 2008. The mobile tracking radar is capable of detecting and discriminating bird echoes with a high accuracy, providing additional bird species information by analyzing wing beat frequencies observed in bird echoes, making it an ideal reference for validating the weather radar observations.

We find that Doppler weather radar is highly successful in determining quantitative bird densities as a function of altitude. The detection probability is very high (up to 99%) and the fraction of false alarms is low (down to 2%). We find that weather radar reflectivity can be quantitatively correlated to the bird-densities determined by bird radar. We converted weather radar reflectivity to bird densities using a fixed radar cross section of 10 cm^2. For nocturnal migration under the assumption of broad front migration, 74% of the weather radar height specific bird densities are correct within a factor of 2 and 87% within a factor of 3. As the weather radar and bird radar are not surveying exactly the same area and have different time resolutions, the quantitative correspondence in bird density may even higher than these figures suggest.

The current bird detection algorithm meets the requirements for operational implementation. At the Royal Dutch Airforce (RNLAF), the subsequent levels of Bird Strike Warnings (so-called BIRDTAMs) differ in bird density by factors of 2, which is on the order of accuracy obtained by weather radar.

The current study shows that weather radar has a high potential for providing information on the spatial distribution of birds during migration. This is especially important in areas with prominent topographical features, like the Netherlands where large water bodies and coastal areas structure the spatial distribution of birds. Obtaining spatial information from weather radar would therefore be a useful future development.

Further research on the use dual polarization radar (which is rapidly becoming the new operational standard) for bird detection is highly recommended. This study suggests that the combined use of dual-polarization techniques for precipitation filtering and high quality Doppler data for insect filtering is most adequate for high quality bird migration quantification. A field study using a weather radar that combines these characteristics would be valuable to explore the full potential of operational weather radar for bird detection.

For upscaling of the operational bird detection by weather to a European scale, the Operational Program on Exchange of Radar data (OPERA) running within EUMETNET, which is the network grouping of 26 European National Meteorological Services, offers an excellent opportunity. OPERA's operational network consists of more than 180 weather radars. An OPERA Data Center is currently being developed and the start of operation is planned for January 2011. This data center will provide the kind of infrastructure needed to build a system for the detection of bird migration.

Contents

Chapter 1

Introduction

Within the Avian Alert System of Systems (SoS) initiative of the European Space Agency (ESA), the FlySafe precursor will show the potentials of a European system to enhance (military) flight safety. The goal of the KNMI contribution to the FlySafe precursor is to understand, validate, and improve the extraction of quantitative bird migration information (density, speed, direction) as a function of altitude from operational weather radars and to demonstrate the real-time distribution of these data. In this scientific report we present a bird migration recognition algorithm which extracts bird density, speed and direction as a function of altitude. The weather radar data have been validated against simultaneous and co-located bird density measurements by a high precision bird radar, designed for research purposes, which was provided by the Swiss Ornithological Institute (SOI). This mobile tracking radar has been stationed next to weather radar sites in the Netherlands, Belgium and France during the peak bird migration season in autumn 2007 and spring 2008. The mobile tracking radar is capable of detecting and discriminating bird echoes with a high accuracy, providing additional bird species information by analyzing wing beat frequencies observed in bird echoes, making it an ideal reference for validating the weather radar observations. We report on an extensive comparison of the processed results from De Bilt and Wideumont radar with bird densities, direction, speed, and altitude distributions from the bird radar.

Real time bird strike warning systems used for prevention of en-route bird strikes only exist in the Netherlands, Germany and recently Belgium militaries. One drawback of these systems is that they rely on radar measurements of only a limited number of Air Defense Radars. Bird migration is essentially a cross border phenomenon, which intimately responds to the

Responsible Institute: KNMI

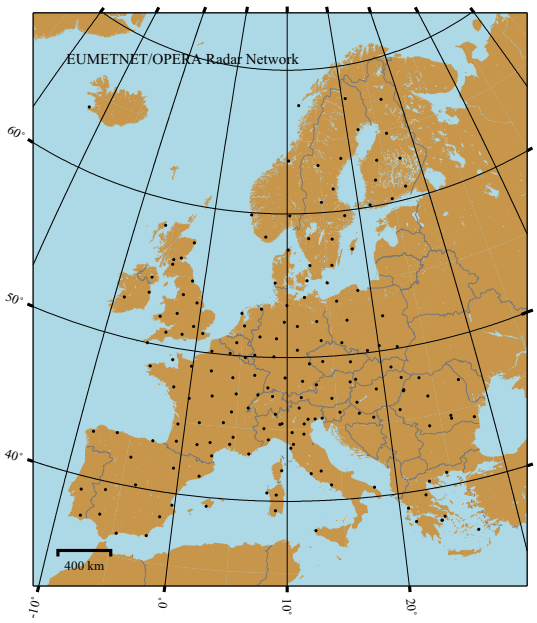

Figure 1.1: Map of operational European weather radars contained by the EUMETNET/OPERA network.

larger scale (synoptic) weather conditions. The dense network of weather radars in Europe coordinated by the Operational Program on Exchange of Radar data (OPERA, part of EUMETNET which is the network grouping of 26 European National Meteorological Services) is a potential source of sensors that covers large areas of Europe (see Fig. 1.1). Quantitative bird migration information from a weather radar network can provide essential information for bird migration forecast models, analogous to the meteorological data assimilated by numerical weather prediction models. A reliable forecast is a badly needed operational extension of the present bird warning systems.

Even more promising than Doppler radars for detection of bird migration using operational radar networks are the so-called dual-polarization weather radars which are slowly becoming the new operational standard. These radars measure the scattering from atmospheric targets in horizontal and vertical polarization. This enables a classification of the scatterers into different types of (non)hydrometeors. Detection of bird migration by dual-polarization radar has already been reported in literature, but further optimization and validation of the algorithms are needed. Météo France operates a dual-polarization radar in Trappes, and we report on the development and validation of a bird migration detection algorithm using the dual polarization capabilities of this radar.

Chapter 2

Radiowave scattering on birds

2.1 Bird scattering versus hydrometeor scattering: signal magnitudes

It is instructive to compare the magnitude of radar signals in cases of precipitation and bird migration. In meteorology so-called Z-$\tilde{R}$ relationships express reflectivity factors Z in terms of the rain rate $\tilde{R}$ in mm/hour. A commonly used Z-$\tilde{R}$ relation under assumption of a Marshall Palmer Droplet Size Distribution (Marshall and Palmer, 1948) equals

$$Z = 200 \cdot \tilde{R}^{1.6} \tag{2.1}$$

The reflectivity factor during a moderate rain rate of $\tilde{R}$=1 mm/hour thus equals 23 dBZ (reflectivity in $\mathrm{mm^6 m^{-3}}$ is converted to a reflectivity factor in dBZ according to $Z_{\mathrm{dB}} = 10 \log_{10} Z$).

The relation between reflectivity and liquid water content of the air is expressed by empirical Z-M relationships. A commonly used Z-M relationship is

$$M = 3.44 \times 10^3 Z^{4/7} \tag{2.2}$$

with M in $\mathrm{kg/km^3}$ and Z in $\mathrm{mm^6 m^{-3}}$ (Green and Clark, 1972). The liquid water content during moderate precipitation (1mm/hour, 23 dBZ) thus equals $M = 7 \times 10^4$ $\mathrm{kg/km^3}$. The reflectivity factor and liquid water content of precipitation can be compared to cases of bird migration. During strong migration the bird density is on the order of 100 $\mathrm{birds/km^3}$, amounting to a water content of only 5 $\mathrm{kg/km^3}$ (assuming the average passerine can be approximated by a water sphere of 50 ml). The "water content" during intense

Responsible Institute: KNMI

bird migration is therefore much lower (4 orders of magnitude) than during light precipitation.

Radar backscattering not only depends on the mass density of the scatterers, but also intimately on their shape. The corresponding reflectivity factor for a density of 5 kg/km^3 of Rayleigh scattered precipitation would be very low (-27 dBZ). Since birds are of the size of the radar wavelength their scattering is not Rayleigh-like but resonant (see Section 2.3), and as a result we find higher reflectivity factors: in Chapter 8 we will show that at C-band 100 birds/km^3 gives rise to a reflectivity factor of about 3 dBZ, still much lower than the typical reflectivity factors observed during light precipitation.

The following sections will summarize the theoretical framework that relates scatterer geometry to the backscattering signal detected by radar. For details we refer to (Doviak and Zrnić, 1993).

2.2 Reflectivity and bird density

We start out with the radar equation for a single target. A scatterer located at position (R,θ,ϕ) (angles defined with respect to the transmitter orientation) will give a received power P_i (in the absence of attenuation) of

$$P_i = \frac{P_t G^2 \lambda^2 f^4(\theta,\phi)\sigma}{(4\pi)^3 R^4} \tag{2.3}$$

with $f^2(\theta,\phi)$ the normalized power density pattern of the transmitted beam, P_t the transmitted pulse power, λ the transmitted wavelength, G the antenna gain, σ the target radar cross section and R the range (note that . In general space will be occupied by several randomly distributed targets. Let us consider an elemental volume dV at position (R,θ,ϕ). The chance for this volume to be occupied by a scatterer will be ρdV with ρ the scatterer density. The average contribution of the volume element to the received power is therefore

$$dP_r = P_i \rho dV \tag{2.4}$$

We find the full received power by integration over all space. We may write for the elemental volume in polar coordinates

$$dV = R^2 dR sin(\theta) d\theta d\phi \tag{2.5}$$

Summing over all (θ,ϕ) we find

$$d\bar{P}_r = \frac{P_t G^2 \lambda^2 \rho \sigma}{(4\pi)^3 R^2} dR \int_{\theta=0}^{\pi} \int_{\phi=0}^{2\pi} f^4(\theta,\phi) sin(\theta) d\theta d\phi \tag{2.6}$$

If the antenna radiation pattern has a Gaussian profile with standard deviation σ_{beam}

$$f^2(\theta,\phi) = \exp(-(\theta^2+\phi^2)/2\sigma^2_{\text{beam}})/2\pi\sigma^2_{\text{beam}} \tag{2.7}$$

the right-hand double integral can be calculated explicitly

$$\int_{\theta=0}^{\pi}\int_{\phi=0}^{2\pi} f^4(\theta,\phi)sin(\theta)d\theta d\phi = \pi\theta_1^2/8\ln 2 \tag{2.8}$$

with $\theta_1 = \sigma_{\text{beam}}/2\sqrt{2\log 2}$ the 3-dB width (i.e. the Full Width at Half Maximum, FWHM) in radians of the power density pattern. We finally obtain the average received power for a single range gate by integrating R over the range gate length. Since R is nearly constant over a single gate we can replace dR by $c\tau/2$ which is the range gate length in terms of the pulse length τ. The final radar equation equals (Probert-Jones, 1962)

$$\bar{P}_r = \frac{P_t G^2 \lambda^2 c\tau\pi\theta_1^2}{(4\pi)^3 16\ln 2}\frac{\eta}{R^2} \tag{2.9}$$

Note that the received power now decays inversely quadratic with range. We also defined the reflectivity (radar cross section per unit volume) as

$$\eta = \rho\sigma \tag{2.10}$$

Reflectivity is the physical observable of interest and its value depends on the nature of the scatterers only (and not on the radar geometry). Note that in the above derivation we did not make any assumptions on the number of targets present per sampling volume. The equation also holds in the limit of very low target density when not every sample volume is occupied (as can be the case during bird migration). In practice the average return power $\bar{P}_r$ is then determined by an average over a representative number of sample volumes.

In the case of birds we are usually dealing with an ensemble of different species of birds i, each with a different associated radar cross section and density.

$$\bar{\eta}_{\text{bird}} = \sum_i \rho_{\text{bird},i}\sigma_{\text{bird},i} = \overline{\rho_{\text{bird}}\sigma_{\text{bird}}} \tag{2.11}$$

We may define a net bird cross section σ_{bird} by:

$$\sigma_{\text{bird}} \equiv \bar{\eta}_{\text{bird}}/\rho_{\text{bird}}, \tag{2.12}$$

where ρ_{bird} equals the total bird density. Strictly we cannot factor the right hand average of Eq. 2.11 into separate expressions for bird density and bird

radar cross section. Only when the spread in cross sections is not too large or when the bird densities of different species are similar the net bird cross section equals the true average bird radar cross section $\overline{\sigma_{\text{bird}}}$.

In the next section we will discuss the differences in radar cross section σ for meteorological and avian targets.

2.3 Radar cross sections for hydrometeors, birds and insects

The radar cross section of a target strongly depeirectivnds on its size and shape with respect to the dimensions of the scattering wavelength. Meteorological targets are usually much smaller than the radar wavelength, while birds are typically of the same size or larger. This makes the type of scattering of precipitation and birds essentially different.

Scattering by a target much smaller than the wavelength of the electromagnetic wave is called Rayleigh scattering. The backscatter cross section for Rayleigh scattering on spherical water droplets of diameter D ($D \ll \lambda$) equals

$$\sigma_{\text{Rayleigh}} = \frac{\pi^5}{\lambda^4}|K_m|^2 D^6 \tag{2.13}$$

where $K_m = (m^2-1)/(m^2+2)$ and m the complex refractive index of water[1]. In meteorology one deals nearly exclusively with Rayleigh scattered signals, however people use different radar wavelengths to probe hydrometeors. Because of the wavelength dependence of the radar cross section the measured reflectivity η also depends on the radar wavelength. To eliminate this wavelength dependence and make the radar observables comparable for different wavelengths, it is conventional to define a so-called reflectivity factor Z. This quantity already divides out the Rayleigh-type wavelength dependency of the cross section and has the same magnitude when probing precipitation at different radar wavelengths:

$$\eta = \frac{\pi^5}{\lambda^4}|K_m|^2 Z \tag{2.14}$$

where Z has dimensions [m^3]. Conventionally Z is expressed in units of mm^6/m^3 expressed on a dB logarithmic scale (unit [dBZ]). Using the index

[1]The complex refractive index of water can be written as $m = n - jn\kappa$ with n the refractive index and κ the attenuation index. For water at 0° Celsius we have at C-band (5.5 cm) $n = 8.3$ and $\kappa = 0.26$ and at S-band (10 cm) $n = 9.1$ and $\kappa = 0.15$. For the constants $|K_m|^2$ and $|R_m|^2$ we find at C-band 0.93 and 0.64 and at S-band 0.93 and 0.65.

of refraction of water and the radar wavelength at C-band ($\lambda = 5.3$ cm) we find

$$\eta = 360 \times 10^{\tilde{Z}/10}, \tag{2.15}$$

with the reflectivity factor $\tilde{Z}$ in dBZ and the reflectivity η in cm^2/km^3.

For targets larger than the radar wavelength ($D \gg \lambda$) we enter the normal reflection regime. For infinitely large targets the backscatter cross section becomes equal to the power reflection coefficient of a plane surface. In that case the radar cross section is given by

$$\sigma_{\text{normal}} = |R_m|^2 A \tag{2.16}$$

with $R_m = (m-1)/(m+1)$ the electric field reflection coefficient, m the complex refractive index of the scatterer and A the targets surface. The radar cross section now varies with the wavelength only through the refractive index m. The refractive index is usually similar for different radar wavelengths. For radar wavelengths at C or S-band (5-10 cm) the reflection coefficient is approximately 0.65 for water and therefore $\sigma \simeq 0.65A$.

Birds are of similar size as the radar wavelength, and their scattering is therefore neither in the Rayleigh nor in the normal reflection regime, but in the intermediate resonant (Mie) regime. No analytical expressions exist for radar cross sections of bird-shaped objects in the resonant regime. For scattering from spheroids there are well-developed numerical techniques (e.g. T-matrix method) to calculate cross sections (Bringi and Chandrasekar, 2001). Larger passerines have a body length of 10-20 cm and for these birds we may expect the radar cross sections to approach the normal reflection regime.

Considering spherical water scatterers only, we may calculate the scaling factor between Rayleigh scattering and normal reflection at equal air water contents. Assuming $A = \pi D^2_{\text{normal}}/4$ in Eq. 2.16 we find

$$\begin{aligned} f &= \frac{D^3_{\text{normal}}}{D^3_{\text{Rayleigh}}} \frac{\sigma_{\text{Rayleigh}}}{\sigma_{\text{normal}}} \\ &= \frac{4\pi}{\lambda^4} \frac{|K_m|^2}{|R_m|^2} D^3_{\text{Rayleigh}} D_{\text{normal}} = 0.23\ D^3_{\text{Rayleigh}} \end{aligned} \tag{2.17}$$

where the right-hand expression is a numerical example for scattering at C-band when D_{normal}=10 cm (typical songbird size), with D_{Rayleigh} in units of [cm]. We may use the equation to obtain an order of magnitude estimate of the relative contribution of insect echoes (small scatterers) and bird echoes (large scatterers) in weather radar. We find that the total reflectivity of insects on the size of a mm is reduced by a factor 4×10^3 (at equal air

masses of birds and insects), while the signal from insects with a size of a cm is weaker by only a factor 5. It strongly depends on the insect type and densities whether insects contribute significantly to the total measured reflectivity (and whether insect reflectivity can be neglected with respect to bird reflectivity).

By Eq. 2.16 we see that in the normal reflection regime C-band and S-band radars give similar cross sections for equally sized objects. The reflectivities measured during bird migration are thus expected to be similar at C-band and S-band. The *reflectivity factors* however will be very different: a factor 16 stronger at S-band because of the factor 2 larger wavelength in Eq. 2.14. In the context of bird migration detection, this difference implies that at S-band birds show up at much higher reflectivity factors than at C-band, during intense migration easily reaching levels of strong precipitation (40 dBZ).

While the scattered energy in the Rayleigh regime is radiated nearly isotropically, larger objects have a much more directed radiation pattern. The radar cross section of a bird target may strongly depend on the view angle. The cross section of a bird is therefore in principle both azimuth and elevation dependent. In section 7.6 we empirically determine a radar cross section for passerine birds (averaged over all azimuths and elevations). For nocturnal passerine migration we find $\sigma \simeq 10$ cm^2. At a bird density of ρ_{bird}=100 km^{-3} this amounts to a reflectivity (by Eq. 2.15) of Z_{bird}=3 dBZ. Section 9.4 discusses the azimuthal dependence of radiowave scattering by birds in the context of polarimetry.

2.4 radar beam size

To estimate the number of birds occupying a single sample volume (range gate) we list the equation describing the radar beam size. The main lobe of radiation reflected from the paraboloid reflector is mostly well approximated by a Gaussian power density pattern. For Gaussian beam propagation the distance over which a collimated electromagnetic beam keeps its approximate radius is given by the Rayleigh range R_R:

$$R_R(r) = \frac{\pi D_0^2}{4\lambda} \tag{2.18}$$

Here, D_0 is the antenna diameter (4.2 m) and λ the radar wavelength (5.3 cm), which gives us $R_R = 0.26$ km. We are only in the far field ($R \gg R_R$),

in which case the 3dB beam waist expands according to

$$w(R) = D_0\sqrt{1+\frac{R}{R_R}} \approx D_0 R/R_R = \frac{4R\lambda}{\pi D_0} \tag{2.19}$$

The 3-dB beamwidth (the angle within which the microwave radiation is at least one-half its peak intensity) for the power density pattern resulting from reflection from an antenna paraboloid is therefore

$$\theta_1 = \frac{4\lambda}{\pi D_0} \tag{2.20}$$

For D_0=4.2 m and λ=5.3 cm we find θ_1=0.9°.

2.5 Birds per radar cell

For a beam width angle θ_1 the beam cross section $A_{\rm beam}$ at range R equals

$$A_{\rm beam}(R) = \pi r^2\theta_1^2/4 \tag{2.21}$$

The volume $V_{\rm gate}$ of a range gate of length $R_{\rm gate}$ centered at range R equals

$$\begin{aligned} V_{\rm gate}(R) &= \int_{R-R_{\rm gate}/2}^{R+R_{\rm gate}/2} A_{\rm beam}(R) = A_{\rm beam}(R)R_{\rm gate} + \pi R_{\rm gate}^3\theta_1/24 \\ &\approx A_{\rm beam}(r)R_{\rm gate} \end{aligned} \tag{2.22}$$

The mean number of birds per gate at a bird density $\rho_{\rm bird}$ is simply

$$\bar{N}(R,\rho_{\rm bird}) = V_{\rm gate}(R)\rho_{\rm bird} \tag{2.23}$$

The chance P to find k birds in a range gate at range R is given by a Poisson distribution:

$$P(k,\rho_{\rm bird},R) = \frac{\exp^{-\bar{N}}\bar{N}^k}{k!} \tag{2.24}$$

Using this equation we can find the average number of birds within the *non-empty* range gates. Under the assumption that a single bird is above the detection threshold of the radar for ranges of interest, this will be the range gates giving a non-zero signal.

$$\bar{N}_{\rm filled}(R,\rho_{\rm bird}) = \frac{\sum_{k=1}^{\infty} k\ P(k,\rho_{\rm bird},R)}{1-P(0,\rho_{\rm bird},R)} \tag{2.25}$$

Figure 2.2 shows the number of birds per range gate as a function of range at different bird densities (both $\bar{N}$ and $\bar{N}_{\rm filled}$). Figure 2.1 shows the minimum range at which the number of birds per gate is at least 1. At low and moderate bird densities ($\rho_{\rm bird} < 50$ km^{-3}) a large fraction of the range gates occupies only a single bird. Only at very high bird densities ($\rho_{\rm bird} > 100$ km^{-3}) all range gates are occupied.

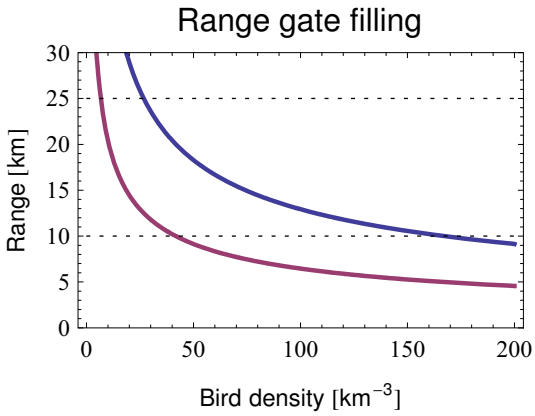

Figure 2.1: Plot of the curve $\bar{N}(r, \rho_{\text{bird}}) = 1$, showing as a function of bird density the range at which the average number of birds per gate equals 1. Above this range radar cells can be assumed to be homogeneously filled with one or more birds. The beam width has been taken 1 degree and the range gate length 0.25 km (blue curve) or 1 km (purple curve). In dotted lines the minimum and maximum range used in the bird density profiling algorithm.

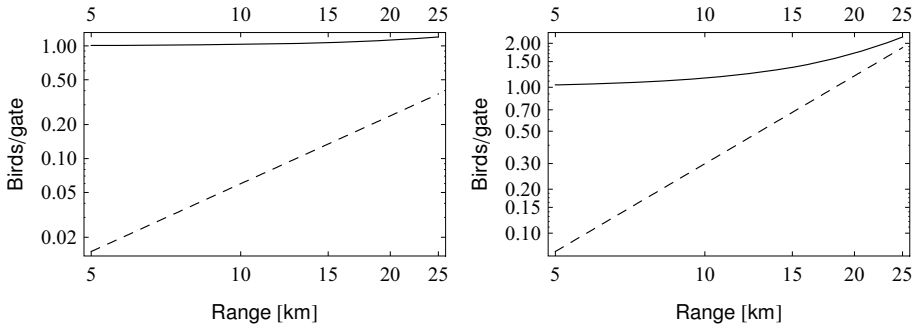

(a) $\rho_{\text{bird}} = 10$ km^{-3} (b) $\rho_{\text{bird}} = 50$ km^{-3}

(c) $\rho_{\text{bird}} = 100$ km^{-3} (d) $\rho_{\text{bird}} = 500$ km^{-3}

Figure 2.2: Number of birds per gate $\bar{N}$ (dashed) and $\bar{N}_{\text{filled}}$ (solid) for various bird densities ρ_{bird}, assuming a beam cone angle of 1 degree and a range gate length of 0.25 km (log-log scale).

Chapter 3

Doppler weather radar characteristics and settings

This chapter contains a description of the technical characteristics of the weather radars involved. The hardware and software currently in use, coverage and beam shapes, data rate, time/space resolution and accuracy will be described. In addition technical characteristics like the TX peak power, frequency, antenna rotation, pre-processing capabilities (clutter filtering), and calibration procedures are given. Clutter filtering methods specific for the bird detection algorithm are described in the separate Section 7.2. The scanning elevations used for bird detection are summarized for all used radars in Section 3.4.

3.1 De Bilt and Den Helder

3.1.1 Technical characteristics of the radar system

KNMI operates two identical C-band Doppler weather radars (Meteo 360 AC) from SELEX (formerly known as Gematronik). One weather radar is located at KNMI in De Bilt (52.103N, 5.179E) and the other radar at a naval air base in Den Helder (52.96N, 4.79E). A picture of the radar tower in de Bilt is shown in Figure 3.1. The radars have an antenna with a 4.2 m diameter and a beam width of about 1 degree. The peak power of the transmitted pulses varies between 250 and 300 kW. In long-pulse mode (for Pulse Repetition Frequencies below 500 Hz) the pulse duration is roughly 2 microsecond and in short pulse mode (PRFs up to 1200 Hz) it is 0.8 microseconds.

Responsible Institute: KNMI in collaboration with the Royal Meteorological Institute of Belgium and Météo France

Figure 3.1: Doppler weather radar of KNMI in De Bilt

The returned signal is transferred to a IF (Intermediate Frequency) receiver and subsequently digested by a GDRX radar signal processor. The radial velocity and spectral width are extracted from the received in-phase and quadrature phase components using pulse-pair processing. Prior to the pulse-pair processing, ground clutter has been removed from the signal by a DFT Doppler filter with spectral reconstruction. The data are averaged to 0.5 km and 1 degree in range and azimuth, respectively. The unambiguous velocity is extended using the dual-PRF technique (Sirmans et al., 1976; Holleman and Beekhuis, 2003). In dual-PRF mode, the primary velocity is obtained by combining data from the actual ray with that from the previous ray. Subsequently, the velocity data from the actual ray are unfolded using the primary velocity estimate. The dual-PRF unfolding is completely handled by the radar signal processor. The data acquisition and generation of products is performed using the Rainbow software package of SELEX (www.gematronik.com). A schematic overview of the radar system and data processing chain is given in Figure 3.2.

The KNMI radar system consists of:

- Radar hardware, i.e. transmitter, antenna, servos, etc
- Radar control unit, in charge of controlling and monitoring the radar,

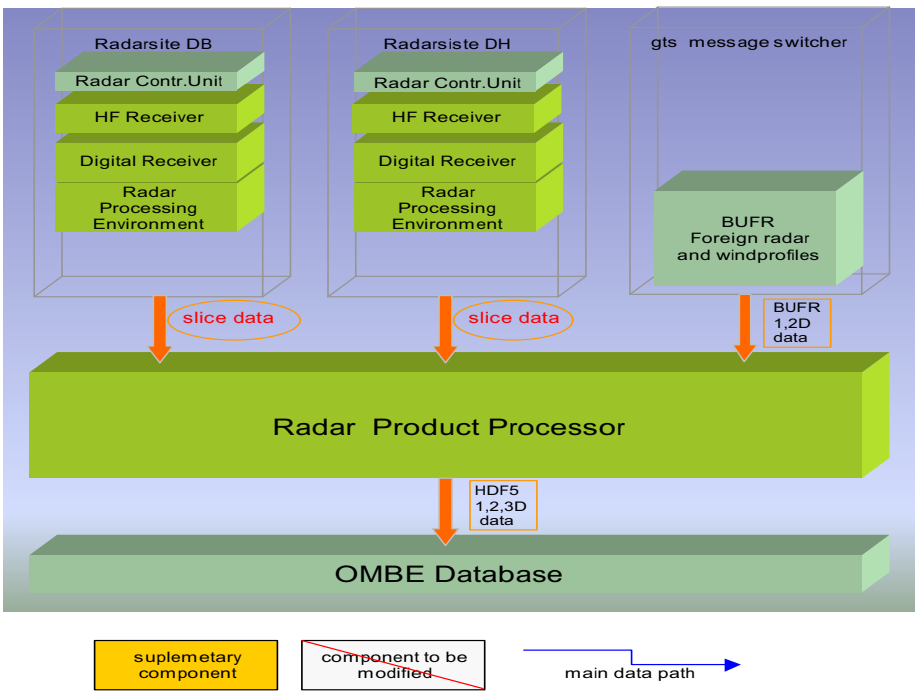

Figure 3.2: Schematic overview of the KNMI radar system and data processing chain

and directing the operational scans

- High-Frequency receiver, receiving the C-band (5.6 GHz) radiation and down-converting it to the intermediate frequency (IF) of 60 MHz

- Digital receiver (GDRX which digitizes the IF data and processes the data into the well-known radar moments: (uncorrected) reflectivity, radial velocity, and spectral width

- Radar Processing Environment (RPE), collecting the volume data of the moments for each scan

- Radar Product Processor (RPP), which ingests the radar volume data and produces all standard single-site products and composite products from several radars

- Finally, radar data are transferred to central image data base at KNMI (OMBE) for further distribution

3.1.2 Scanning strategy, data processing and derived products

The operational scanning of the KNMI weather radars generates a 14-elevation volume and this volume scan is repeated every 5 minutes. Figure 3.3 displays the Volume Coverage Pattern of the KNMI weather radars and Table 3.1 lists the main parameters of the volume scan.

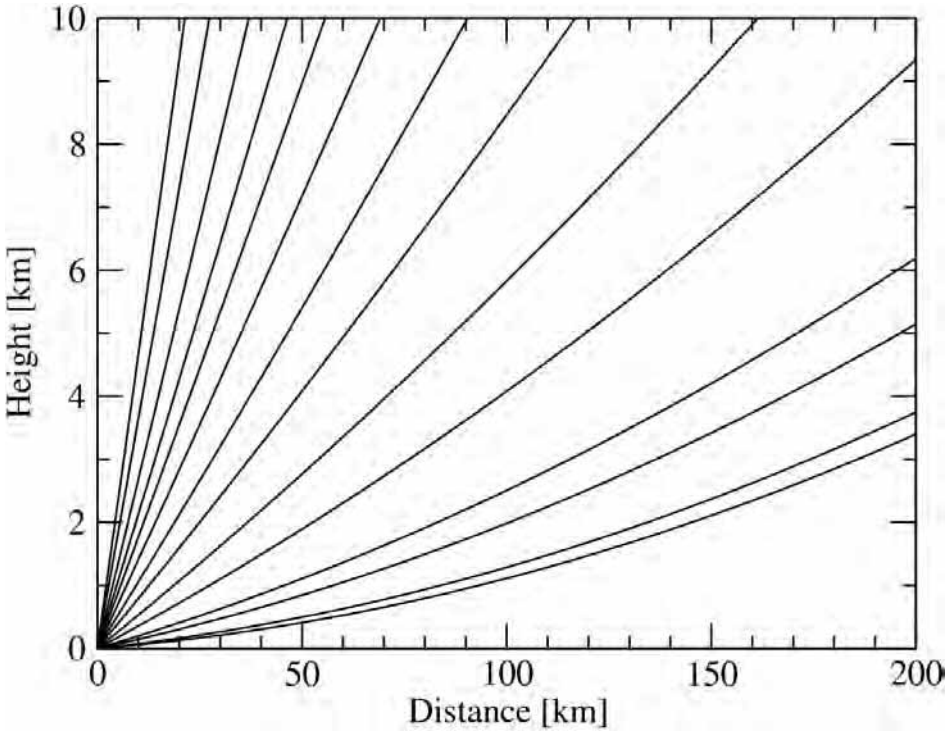

Figure 3.3: Volume Coverage Pattern (VCP) of the KNMI weather radars

Polar volume datasets with reflectivity, uncorrected reflectivity, radial velocity, and spectral width are produced every 5 minutes in HDF5 format (www.hdfgroup.org/products/hdf5/). The azimuth resolution of the polar data is 1 degree. All weather radar products (and other remote sensing imagery) of KNMI are available in the same KNMI HDF5 format (Roozekrans and Holleman 2003). A snapshot of the HDF5 viewer with an example of a KNMI radar volume dataset is shown in Figure 3.4.

The following products are produced operationally from the weather radar scans:

Reflectivity composites at low altitude (1500 meter above msl) for Netherlands and Western Europe. These main radar products are

Number	Elevation [°]	°/sec	PRF [Hz]	Range [km]	Range bin [km]
1	0.3	18	250	320	1.0
2	0.4	18	600/450	240	1.0
3	0.8	18	600/450	240	1.0
4	1.1	18	600/450	240	1.0
5	2	18	600/450	240	1.0
6	3	24	800/600	170	0.5
7	4.5	24	800/600	170	0.5
8	6	30	1000/750	145	0.5
9	8	30	1000/750	145	0.5
10	10	36	1200/900	120	0.5
11	12	36	1200/900	120	0.5
12	15	36	1200/900	120	0.5
13	20	36	1200/900	120	0.5
14	25	36	1200/900	120	0.5

Table 3.1: Operational scanning scheme of KNMI weather radars.

showing the temporal and spatial evolution of precipitation patterns

Accumulated precipitation over 3 hour and 24 hour periods. The accumulations are based on the reflectivity composite and are adjusted with rain gauge observations.

Echotop height composites. This product showing the maximum height of the radar echoes

Hail warning product. Large hail is detected using the height difference between the 45 dBZ echotops and the freezing level from a Numerical Weather Prediction model (Holleman 2001).

Weather radar wind profiles extracted from the Doppler scans. A study focused on the optimization and verification of these wind profiles has been performed at KNMI (Holleman 2005).

3.2 Wideumont

3.2.1 Technical characteristics of the radar system

The Wideumont weather radar (49.915N, 5.505E, 585 m asl) is a Gematronik METEOR 500C. It is a single polarization C-band Doppler radar. The ME-

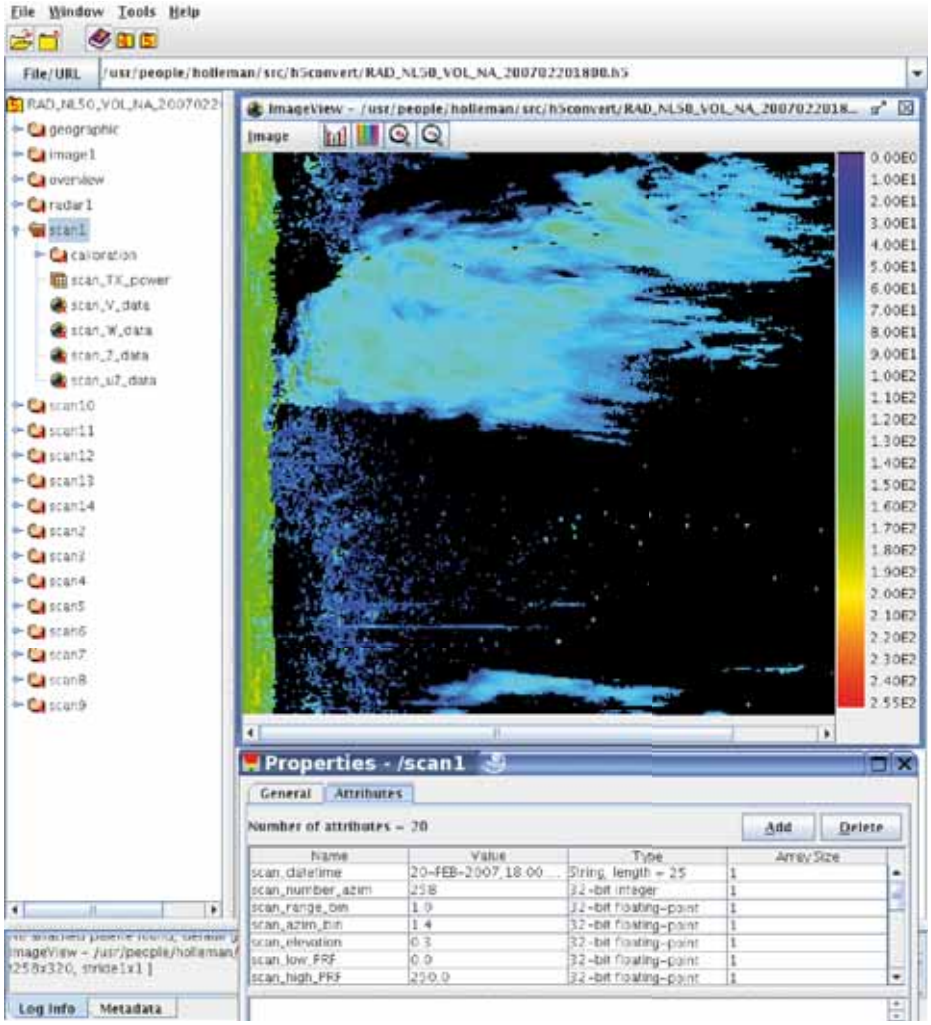

Figure 3.4: Snapshot of the HDF5 viewer with a KNMI radar volume dataset

TEOR 500C Radar System comprises the following major subsystems:

- The antenna system CLP10 which features a one degree C-band reflector, a pedestal with high positioning accuracy and a low loss sandwich panel radome.

- The Transmitter/Digital Receiver Front-end featuring a 250 kW peak power Magnetron transmitter driven by a dual pulse solid state modulator and a dual conversion low-noise receiver. The operating frequency is 5.64 GHz.

- The ASPEN DRX signal processor, which performs fast, high-

resolution digitizing, flexible clutter filtering, time and range averaging and pulse pair processing.

- The radar control processor DIRAC for the control and supervision of the radar system.

- The Unix based RAINBOW 3.4 Application Software featuring the remote control of the radar and the generation of meteorological products.

The antenna system, the transmitter and digital receiver, and the signal processor are installed on top of a steel tower 46 meter high (Figure 3.5), the antenna being positioned at a height of 585 m above mean sea level. Raw data are transferred from the radar site to the meteorological center at RMI Brussels via a 128 kbit/s leased line. At RMI, the Rainbow Main Workstation (HP B1000 with UNIX OS) performs the control and the supervision, receives the volume raw data and generates the meteorological products. In addition, a Rainbow Display Workstation (HP Kayak Xas) is used to display selected products. Pictures of the Wideumont radar and its antenna are shown in Figure 3.5.

The radar system is complemented with two Linux Workstations configured to generate additional home-made products (composite, hail detection...), to route the products to various users in the network and to archive raw volume data and a large set of radar products.

3.2.2 Scanning strategy, data processing and derived products

The radar performs three different scan series, which are detailed in Table 3.2. Figure 3.6 displays the Volume Coverage Pattern for scan series 3.

- Scan series 1 is repeated every 5 minutes and includes 5 elevation angles with reflectivity measurements up to 240 km.

- Scan series 2 is repeated every 15 minutes and includes 10 elevations angles with reflectivity measurements up to 240 km.

- Scan series 3 is repeated every 15 minutes and includes 8 elevation angles with reflectivity, radial velocity and spectral width measurements up to 120 km. Only data from this scan series is used for the bird detection.

(a) (b)

Figure 3.5: Doppler weather radar of RMI in Wideumont (left) and its antenna at the factory (right)

A time-domain Doppler filtering is applied to scan series 1 and 3 for ground clutter removal. Besides, for scan series 1, a static clutter map is used for eliminating the residual permanent clutter caused by some surrounding hills. Reflectivity data contaminated by permanent ground clutter are replaced by data collected at a higher elevation.

Table 3.6. Scans at elevations below 0.5 degrees are not used by the bird detection algorithm to reduce ground clutter contamination.

Derived meteorological products are listed in Table 3.3. Precipitation estimates are produced from scan 1 by extracting a Pseudo-CAPPI at 1500 m and by converting reflectivity values in precipitation rates using the Marshall-Palmer relation $Z = aR^b$ with a=200 and b=1.6.

Reflectivity data from scan series 2 are used to generate the Max Reflectivity, the Echotop-45 dBZ and the hail detection products.

Radial velocity data from scan series 3 are used to generate a Pseudo CAPPI radial velocity at 1500 m and a wind profile using a Volume Ve-

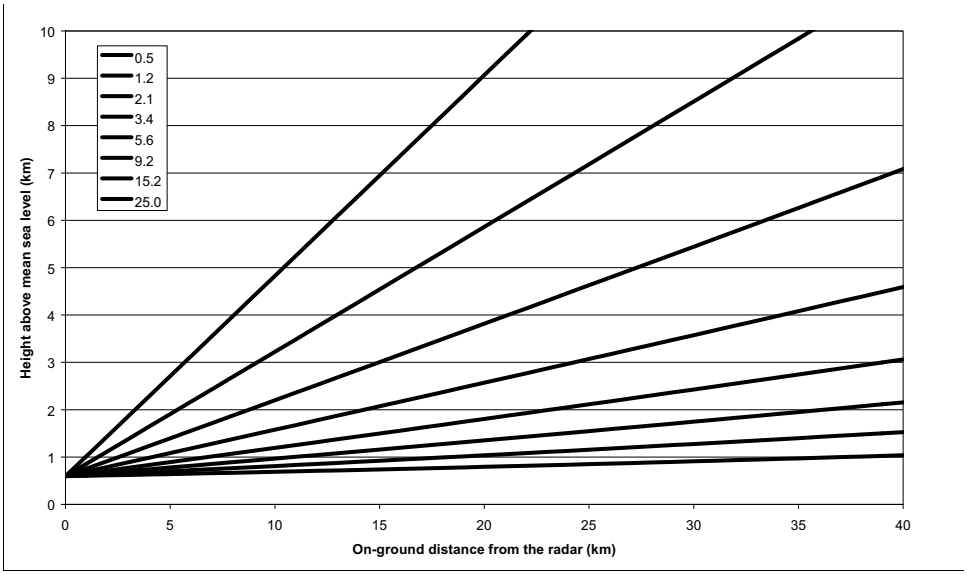

Figure 3.6: Volume Coverage Pattern of Wideumont radar for scan series 3.

locity Processing technique. The radar beam pattern of scan 3 is shown in Figure 3.6.

A monitoring of the electronic calibration is performed using the mean ground clutter reflectivity at short range and the reflectivity produced by three towers in the vicinity of the radar. These point targets also allow controlling range and azimuth assignments. A verification of the radar precipitation estimates is performed on a daily base through comparison with rain gauge observations.

3.3 Trappes

3.3.1 Technical characteristics of the radar system

A C-band Doppler weather radar system (type 510C) has been purchased from SELEX (Formerly known as Gematronik) and operates continuously as part of the French operational radar network. This dual-polarization (polarimetric) radar is located in Trappes (48.775N, 2.009E) (see Fig. 3.7). The radar transmits linearly polarized radiation. The two receiving channels, which have nearly identical waveguide runs, operate in parallel and thus enable the Simultaneous Transmission And Reception (STAR mode) of polarized signals. A diagram of the radar system is provided in Figure 3.8. A staggered PRT scheme was developed for retrieving and dealiasing Doppler

Scanning Definition

	Scan series 1	**Scan series 2**	**Scan series 3**
Quantity	Reflectivity (Z)	Reflectivity (Z)	Velocity (Z,V,W)
Range	240 km	240 km	120 km
Time interval	5 min	15 min	15 min
Azimuthal speed	18°/s	24°/s	24°/s
PRF	600 Hz	483 Hz	1153/864 Hz
Pulse length	0.836 μs	2.095 μs	0.836 μs
Range sampling	2	2	2
Time sampling	33	20	48
Resolution	250 m	500 m	250 m
No Elevations	5	10	8
Elevations	0.3° 0.9° 1.8° 3.3° 6.0°	0.5° 1.2° 1.9° 2.6° 3.3° 4.0° 4.9° 6.5° 9.4° 17.5°	0.5° 1.2° 2.1° 3.4° 5.6° 9.2° 15.2° 25.0°
Clutter Filter	Doppler 7	none	Doppler 7
Filter parameters	CSR=10.0 LOG th=2.0 (SQI=0.5)	(CSR=15.0) LOG th=2.0 (SQI=0.5)	(CSR=15.0) LOG th=2.0 SQI=0.3
Speckle remover	On	On	Off

Table 3.2: Operational scanning scheme of RMI weather radar in Wideumont.

velocities (Tabary et al., 2006). Technical details of the antenna, transmitter, receiver, and processor are provided in Table 3.4.

Products generated

Scan series 1	**Scan series 2**	**Scan series 3**
Pseudo CAPPI Rain rate at 1500 m.	Max Reflectivity product.	Pseudo CAPPI radial velocity at 1500 m.
1h and 24h precipitation accumulation.	Echotop-45 dBZ.	Wind profile.
	Hail detection product.	

Table 3.3: Radar products from Wideumont weather radar.

Antenna	
Type	Center-fed paraboloid
Diameter	3.7 m
Beam width (3 dB) H and V	1.1°
Side lobe level within ±5°(H and V)	-25 dB
Side lobe levels beyond 10°(H and V)	-40 dB
Gain (H and V)	$>$ 43.8 dB
Max cross polar isolation	$<$ -30 dB
Azimuth travel range	0 → 360° (continuous)
Elevation travel range	-3 → 183°
Azimuth / elevation pointing accuracy	±0.1°
Azimuth / elevation velocity	Up to 36°/s
Transmitter	
Peak power	250 kW
Pulse width	2 microseconds
Frequency	5.640 GHz
Wavelength	5.31 cm
PRF	Staggered triple-PRT : 379, 321 and 305 Hz
Receiver	
Minimum detectable signal	$<$ -112 dBm
Total instantaneous dynamic range (H and V)	$>$ 95 dB
Radar processor	
CASTOR2	

Table 3.4: Technical characteristics of the polarimetric radar in Trappes.

H→H+5	**H+5→H+10**	**H+10→H+15**	**H+15→H+20**	**...**
T01 = 90.°	T07 = 9.5°	T13 = 8.5°	T01 = 90.°	...
T02 = 7.5°	T08 = 6.5°	T14 = 5.5°	T02 = 7.5°	...
T03 = 0.8°	T09 = 0.8°	T15 = 0.8°	T03 = 0.8°	...
T04 = 1.5°	T10 = 1.5°	T16 = 1.5°	T04 = 1.5°	...
T05 = 4.5°	T11 = 3.5°	T17 = 2.5°	T05 = 4.5°	...
T06 = 0.4°	T12 = 0.4°	T18 = 0.4°	T06 = 0.4°	...

Table 3.5: Operational scanning scheme of the Météo France radar in Trappes.

Figure 3.7: Dual-polarization weather radar of Météo France in Trappes

3.3.2 Scanning strategy, data processing and derived products

The scan strategy of the dual-polarization Trappes radar (48.775N, 2.009E) is detailed in Table 3.5. Three elevation angles (0.4°,0.8°,1.5°) are revisited every 5 minutes. A complete volume scan cycle is completed in 15 minutes. The 90° elevation scan is only used for calibrating the dual-polarization variables (Z_{DR}). In Figure 3.9 the volume coverage pattern is presented.

The Trappes radar uses a triple-PRT Doppler scheme which consists in transmitting pulses spaced apart by a varying time interval. Three time intervals are currently used: PRT_1 = 1/379 s, PRT_2 = 1/325 s and PRT_3 = 1/303 s. This triplet of PRT allows solving the Doppler dilemma and obtaining Doppler information with no ambiguity (up to 60 m s^{-1}) up to 250 km. The following data are available:

Cartesian (1 km^2, 512x512 km^2) PPIs of reflectivity (coded between –10 and 70 dBZ with 1 dB increment);

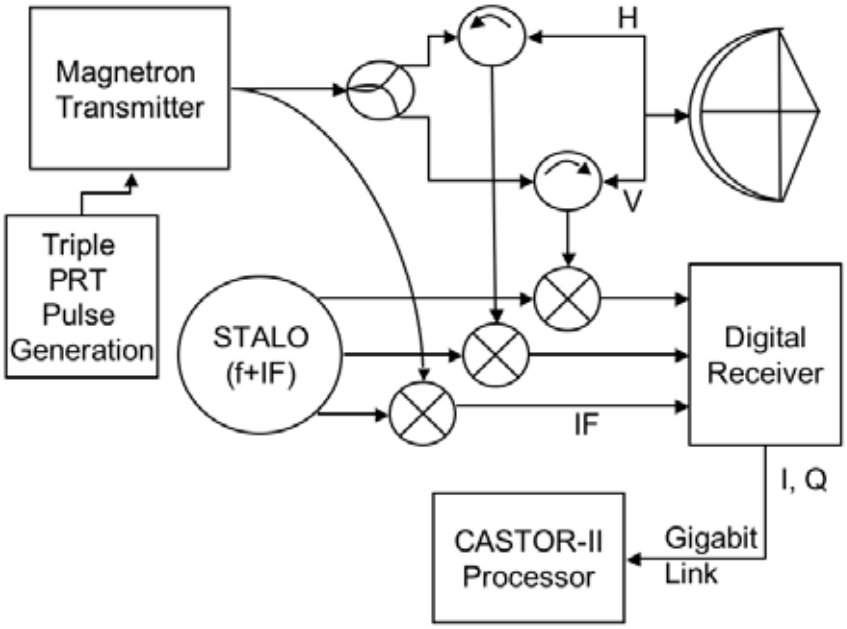

Figure 3.8: Diagram of the Trappes polarimetric radar system in simultaneous transmission and reception mode.

Cartesian (1 km^2, 512x512 km^2) PPIs of unfolded radial velocities;

Cartesian (1km^2, 512x512 km^2) PPIs of Doppler spectrum width

Polar (0.5°x240 m, 720x1066) PPIs of reflectivity;

Polar (0.5°x240 m, 720x1066) PPIs of unfolded radial velocities at the three PRFs;

Polar (0.5°x240 m, 720x1066) PPIs of differential reflectivity;

Polar (0.5°x240 m, 720x1066) PPIs of correlation coefficient;

Polar (0.5°x240 m, 720x1066) PPIs of differential phase;

Velocity Azimuth Display (VAD) wind profile;

Quantitative Precipitation Estimate (QPE) image;

The polar volume datasets were converted at KNMI to HDF5 format for further analysis. Polar radial velocities were found to be of insufficient quality for unfolding into the proper Nyquist interval. It is recommended to increase

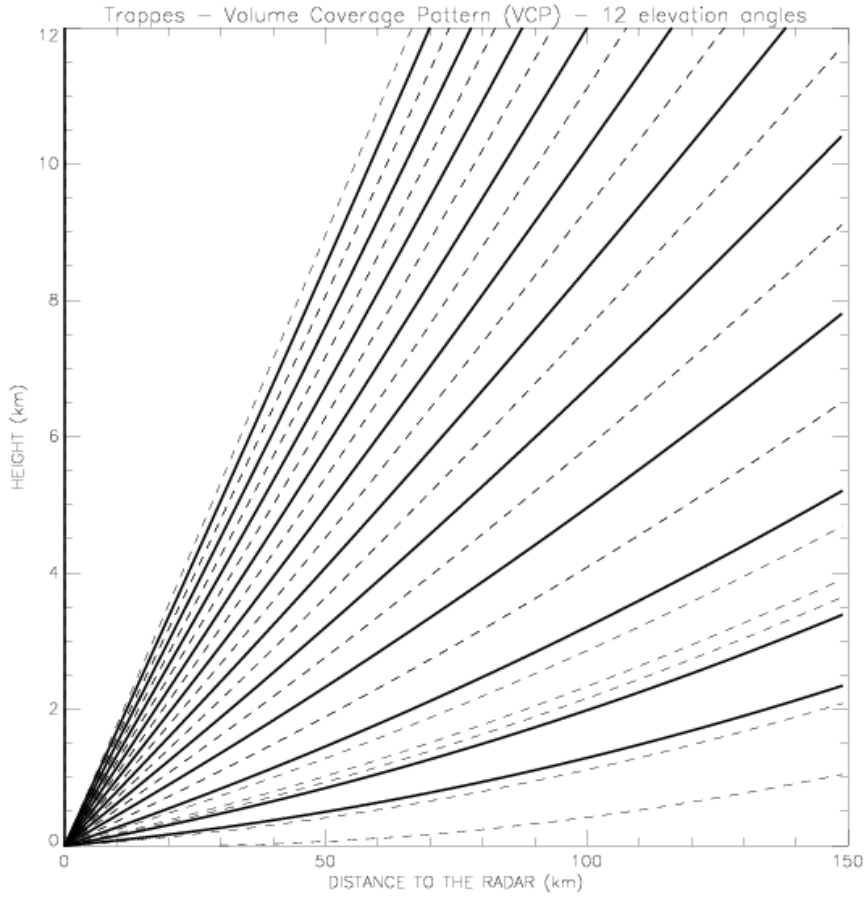

Figure 3.9: Volume Coverage Pattern of Trappes radar

the sampling per gate (i.e. increase the used PRFs, or increase the range and azimuth gate size (now 250 m. and 0.5°)). Cartesian unfolded radial velocities were mapped onto a polar grid and used instead.

3.3.3 Polarimetric variables Trappes radar

The Trappes radar measures reflectivity at horizontal polarization Z_H defined as

$$Z_{\mathrm{H}} = 10 \log_{10} \langle |S_{\mathrm{HH}}|^2 \rangle \tag{3.1}$$

where S_{HH} (S_{VV}) is the copolar, horizontal (vertical) component of the backscatter amplitude. The inner brackets indicate averaging across each i^{th} independent sample in each 240m x 0.5° pulse volume. Given the operational values of the Trappes radars nominal beam width, pulse repetition

frequency, antenna rotation rate, and wavelength (see Table 3.4), the total number of samples at a given bin has been computed to be 23. The degree to which these samples are independent depends on the observed spectrum width. Differential reflectivity is defined as follows:

$$Z_{\mathrm{DR}} = 10 \log_{10} \frac{\langle |S_{\mathrm{HH}}|^2 \rangle}{\langle |S_{\mathrm{VV}}|^2 \rangle} \tag{3.2}$$

The copolar cross-correlation coefficient at zero lag ($\rho_{\mathrm{HV}}(0)$) is the magnitude of the cross-correlation coefficient and is defined as

$$\rho_{\mathrm{HV}}(0) = \left| \frac{\langle S^*_{\mathrm{HH}} S_{\mathrm{VV}} \rangle}{\sqrt{\langle |S_{\mathrm{HH}}|^2 \rangle \langle |S_{\mathrm{VV}}|^2 \rangle}} \right| \tag{3.3}$$

The differential propagation phase shift (Φ_{DP}) is the argument of the cross-correlation coefficient defined as:

$$\Phi_{\mathrm{DP}} = \arg \left(\frac{\langle S^*_{\mathrm{HH}} S_{\mathrm{VV}} \rangle}{\sqrt{\langle |S_{\mathrm{HH}}|^2 \rangle \langle |S_{\mathrm{VV}}|^2 \rangle}} \right) = \arg(\langle S^*_{\mathrm{HH}} S_{\mathrm{VV}} \rangle) \tag{3.4}$$

The Trappes radar also collects radial velocity measurements (V_r) as well as a parameter describing the pulse-to-pulse fluctuations of the instantaneous power (sigma; Nicol et Al. 2003). This latter variable has been shown to be useful in ground clutter recognition and rejection.

3.4 Weather radar scanning schemes used for bird detection

The weather radar scans that are available for the bird detection algorithm are listed in Table 3.6. Scans at elevations below 0.5 degrees are not used by the bird detection algorithm to reduce ground clutter contamination. The De Bilt/Den Helder radar data is available every 5 minutes, the Wideumont and Trappes data every 15 minutes.

Scan strategies

	De Bilt / Den Helder				Wideumont				Trappes				
Scan	Elev	PRF1	PRF2	v_m	Elev	PRF1	PRF2	v_m	Elev	PRF1	PRF2	PRF3	v_m
1	0.3	250	-	3.3	0.5	865	1153	45.9	0.4	379	325	303	60.6
2	0.4	450	600	23.9	1.2	865	1153	45.9	0.8	379	325	303	60.6
3	0.8	450	600	23.9	2.1	865	1153	45.9	1.5	379	325	303	60.6
4	1.1	450	600	23.9	3.4	865	1153	45.9	2.5	379	325	303	60.6
5	2.0	450	600	23.9	5.6	865	1153	45.9	3.5	379	325	303	60.6
6	3.0	600	800	31.8	9.2	865	1153	45.9	4.5	379	325	303	60.6
7	4.5	600	800	31.8	15.2	865	1153	45.9	5.5	379	325	303	60.6
8	6.0	750	1000	39.8	25.0	865	1153	45.9	6.5	379	325	303	60.6
9	8.0	750	1000	39.8	-	-	-	-	7.5	379	325	303	60.6
10	10.0	900	1200	47.7	-	-	-	-	8.5	379	325	303	60.6
11	12.0	900	1200	47.7	-	-	-	-	9.5	379	325	303	60.6
12	15.0	900	1200	47.7	-	-	-	-	90.0	379	325	303	60.6
13	20.0	900	1200	47.7	-	-	-	-	-	-	-	-	-
14	25.0	900	1200	47.7	-	-	-	-	-	-	-	-	-

Table 3.6: Scan elevations [degrees], Pule Repetition Frequencies (PRF) [Hz] and unambiguous velocities v_m [m s^{-1}] used for the different radars. The azimuth/range resolution are 1°/[1 km scan 1-5, 500 m scan 6-14], 1°/250 m and 0.5°/240 m. for the De Bilt/Den Helder, Wideumont and Trappes data, respectively.

Chapter 4

Bird radar characteristics and settings

4.1 The radar system

An ex-military pencil-beam radar of the type "Superfledermaus" (Fig. 4.1) was used for the monitoring of nocturnal and diurnal bird movements. It is an X-band radar (3 cm wavelength) with a peak power output of 150 kW and a pulse repetition frequency of 2082 Hz. The detection range of the radar is 4-5 km for small birds and up to 8 km for large birds or flocks of birds. The tracking accuracy of the radar is ± 0.06 ° in the side and elevation angle and ± 10 m in the distance. To store the radar data, the "Superfledermaus" has been modified and equipped with a digital recording system, developed by the SOI. At the beginning of the observation period, the sensitivity of the whole system was calibrated with a reference signal generator. More detailed information about the technical background of the Birdradar "Superfledermaus" and its operational modes can be found in .

The "Superfledermaus" radar system can be used to measure the intensity of bird migration as well as to obtain three-dimensional flight path data of single birds or flocks of birds. Quantitative samples of the temporal and altitudinal distribution of bird migration were recorded with a fixed beam mode (Fig. 4.2), whereas directions and speeds were collected by tracking a selection of single targets (Fig. 4.3). The amplitude of the echo intensity of a target usually shows rhythmic fluctuations that are, in case of birds, correlated with the wingbeats. These so-called echo signatures are recorded and used to distinguish between echoes of birds and those caused by other objects like insects (Fig. 4.4). To classify the targets collected by the bird

Responsible Institute: SOI

Figure 4.1: The Bird radar "Superfledermaus" equipped with a telescope and a camera mounted parallel to the radar antenna and a satellite connection for data transfer.

radar, an automatic algorithm has been developed to distinguish between the targets. This algorithm, a "vector support machine" was trained based on a large sample of visually classified targets by an expert. Within the echoes classified as birds it is possible to distinguish between three types, specified as passerines, waders/waterfowl and swifts .

In the tracking mode the tailor made software records the position of the tracked target every second and calculates flight direction, vertical and horizontal speed for intervals of 20 seconds (Fig. 4.5). If wind information at the target's altitude is available, also heading and airspeed are computed (post-hoc). In the fixed beam mode all echoes entering the static beam are recorded for a given time interval (Fig. 4.6). With an automatic algorithm single echoes are detected, identified as birds or non-birds, and eventually assign to a type of bird (s. above) . From these data migration traffic rates are calculated for selected time and height intervals (MTR = number of birds per hour crossing a hypothetic line of 1km perpendicular to the mean

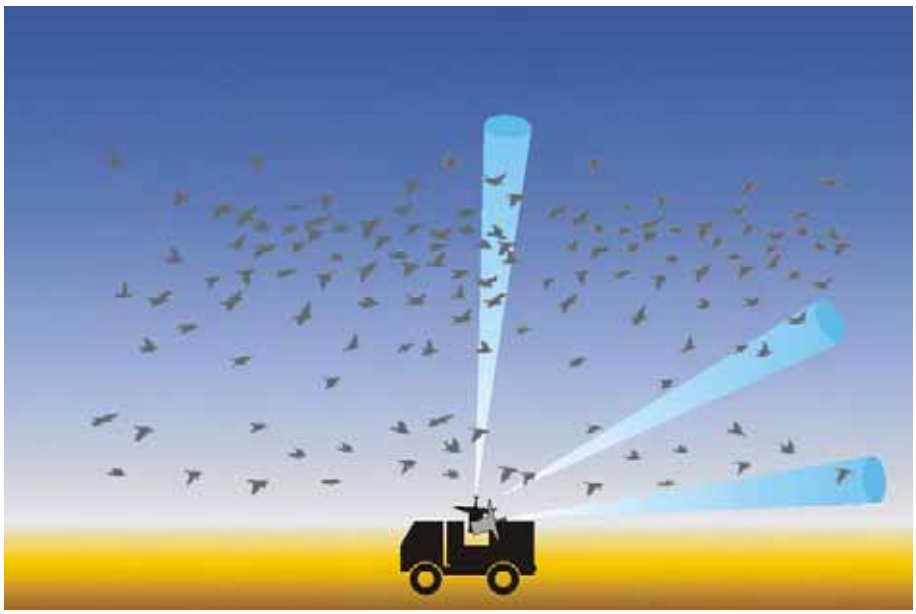

Figure 4.2: In the fix beam mode all objects showing up in the static beam are recorded. To get samples from relevant flight altitudes the measurement is repeated at different elevations (three in the case shown).

migratory direction).

Figure 4.3: In the tracking mode the three dimensional flight path and the echo signature of a single target is recorded. During daytime an observer seeks to identify the target through a telescope mounted parallel to the radar antenna. During the night and with bad visibility (fog) only the echo signature is used to classify the targets.

(a) Wingbeat pattern of a songbird

(b) Wingbeat pattern of an insect

Figure 4.4: The top figure shows a wingbeat pattern of a passerine with regular phases of wingbeats and pauses. The single wingbeats are clearly visible. The increasing and decreasing amplitude (vertical axis) of the signal along the time axis (horizontal axis) reflects the bird's flight entering the radar beam at one edge, flying through the center and leaving at the other edge. The wingbeat pattern of an insect shows no regular pattern of wingbeats and pauses.

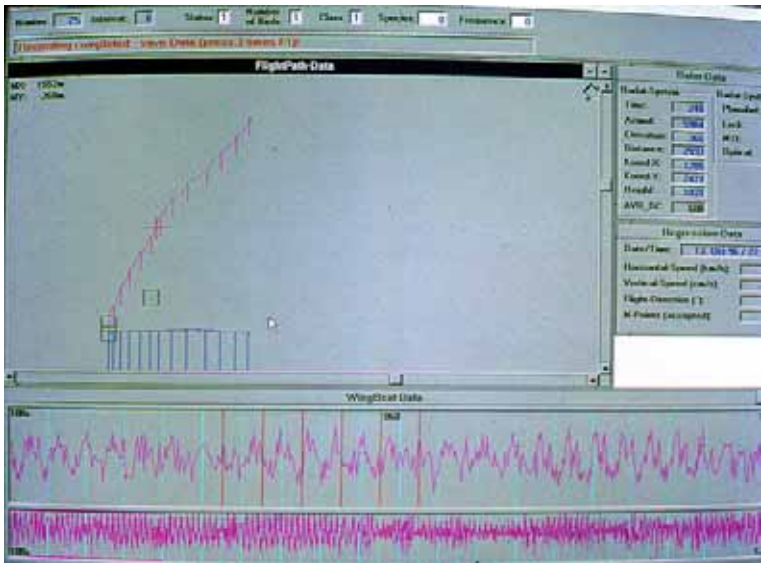

Figure 4.5: Image of a flight path. In the central window a projection of the x-y (pink) and x-z (blue) is shown. Intervals of 20sec are marked with vertical bars. Below is the echo signature (wing beat data) corresponding to the flight sequence marked with a cross.

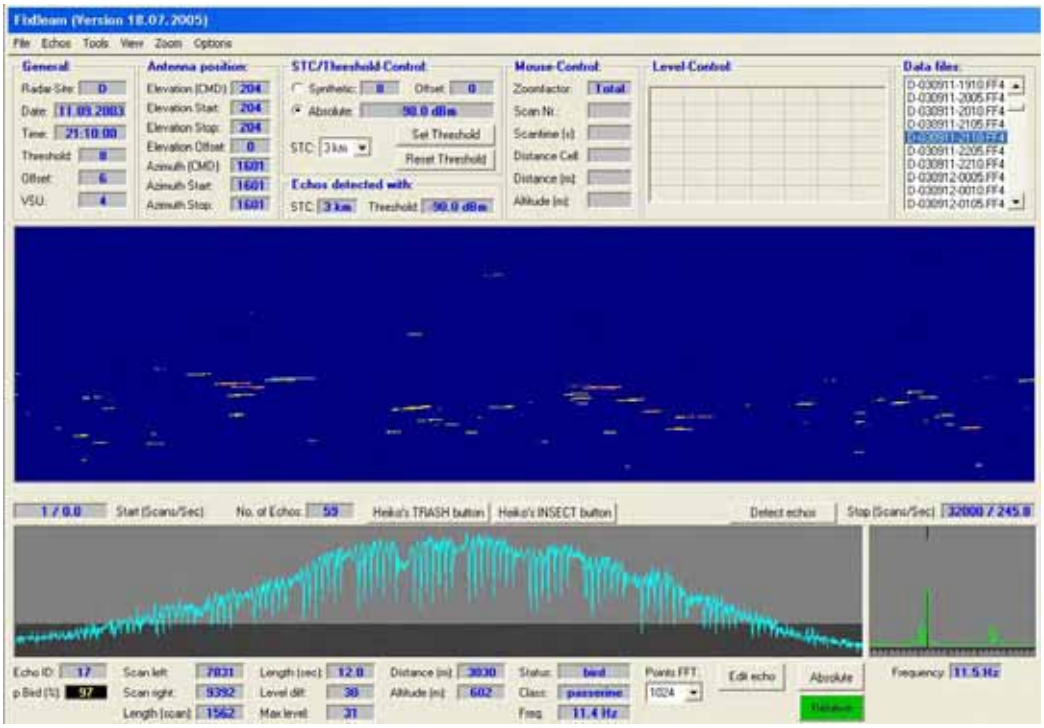

Figure 4.6: Image of a single fix beam measurement. In the upper part various information on the measurement are given - the blue part in the middle represents the detected echoes in time (x-axis) and distance (y-bar), echoes above the noise level show up as short lines in colors from yellow to red. A single echo is marked in light blue and visualized in detail in the lowest part (echo signature→wingbeat pattern), where also information on the selected echo are given.

Chapter 5

Bird radar field campaigns

5.1 superfledermaus as weather radar reference

The bird radar data are based on point targets, whereas the weather radar is recording volume targets. The bird radar can detect and discriminate all sorts of singly flying objects, however within a relatively small range, whereas the weather radar provides an overall picture of the average movement of objects in the given air layer over a wide range. The bird radar allows to verify the targets as birds by analyzing the wing beat pattern or due to visual identification, which is important because insects can make up a significant part of the echoes detected in the air, in the bird radar as well as in the weather radar.

Due to the difference in the surveyed range between the two radar systems compared, the measurements performed by the bird radar provide only a subsample of what is surveyed by the weather radar. Therefore, an important assumption is that migration occurs at a broad front, which is the case for passerine migration in the absence of prominent topographical features such as coast lines and high mountain ranges. Large birds, like cranes or storks are much more aggregated in flocks, and therefore are more likely to pass outside the range of the bird radar. On the other hand due to the volume scan by the weather radar these single large tracks can not yet automatically be extracted. The present study has focused to verify the timing and altitude distribution of the broad front migration as it is recorded by the two radar systems.

Responsible Institute: SOI

5.2 simultaneous collocated field campaigns

5.2.1 De Bilt

The bird radar was situated on the airfield of Soesterberg on a small hill surrounded by forest (N 52° 7.8' / E 5° 16.8' , 10m asl; cf. Fig. 5.1 Soesterberg). The close forest protected the radar image from most ground clutter. Tracking of single birds or flocks was possible down to elevation of 1.5°, whereas the lowest quantitative measurement was provided at 5.6°. The observation period lasted from 19.8. – 16.9.07, which was 2 days more than originally planed (20.8. – 15.9.07). In total 2618 fix beam measurements were recorded.

Figure 5.1: The Birdradar "Superfledermaus" installed on the military airfield of Soesterberg (the Netherlands), about 6 km from the Doppler weather radar in de Bilt.

Fixed beam measurements were carried at three elevation angles (5.6°, 22.5°, 79°), which allowed a good coverage of all flight altitudes up to 6km. The beam was directed towards WNW (293°), thus perpendicular to the main migratory direction. During the night such a series of three measurements took place every half an hour between 18h and 6h (UTC+1), and for the rest of the day every hour. Detection range was restricted to 7.5 km and recording time for a single measurement was 4 min.; for further details about these measurements see . Between fixed beam measurements tracks of single targets were recorded for at least 20 seconds. During the night this was performed by an automatic search algorithm selecting targets from all relevant heights. During daytime tracking was performed manually with an operator selecting targets on the radar screen and an observer watching through a telescope mounted parallel to the radar antenna. Tracked targets were identified by the observer in the best case to species level.

Hourly migration traffic rates were determined at De Bilt (19.8. – 16.9.07) over a height range of 4 km, divided into 200m height intervals. The temporal coverage comprised 83% of the total time. Failure of measurements were due meteorological restrictions (rain) and technical malfunctions.

5.2.2 Wideumont

The bird radar was situated on the military airfield of St. Hubert (Belgium) at the end of the runway, surrounded by forest (N 50° 1.8' / E 5° 26.4' , 577m asl; cf. Fig. 5.2). The close forest protected the radar image from most ground clutter. Tracking of single birds or flocks was possible down to elevation of 1.3°, whereas the lowest quantitative measurement was provided at 7.0°. The observation period lasted from 18.9. – 22.10.07, which was 8 days more than originally planed (24.9. – 20.10.07). In total 3082 fix beam measurements were recorded.

Figure 5.2: The Birdradar "Superfledermaus" installed on the military airfield of St. Hubert (Belgium), about 12 km from the Doppler weather radar in Wideumont.

Fixed beam measurements were carried at three elevation angles (7.0°, 22.5°, 79°), which allowed a good coverage of all flight altitudes up to 6km. The lowest beam was slightly higher than in De Bilt due to ground clutter. The beam was directed in the same direction as in De Bilt, towards WNW (293°), thus perpendicular to the main migratory direction. The daily time schedule (UTC+1) of the measurements, the detection range and the duration of the measurements was the same as in de Bilt (s. above). Between fixed beam measurements tracks of single targets were recorded in the same way as in de Bilt.

Hourly migration traffic rates were determined for Wideumont (18.9. – 22.10.07) over a height range of 4 km, divided into 200m height intervals. The

temporal coverage comprised 88% of the total time. Failure of measurements were due meteorological restrictions (rain) and technical malfunctions.

5.2.3 Trappes

The bird radar was situated near Flins sur Seine (France), on the land of the water treatment company "Lyonnaise des eaux,", within a former seepage reservoir (N 48° 34.8' / E 1° 31.2'; cf. Fig. 5.3). Tracking of single birds or flocks was possible down to elevation of 5°, whereas the lowest quantitative measurement was provided at 5.3°. The observation period lasted from 8.3. – 9.5.08, which was 2 days more than originally planed (10.3. – 9.5.07). In total 5839 fix beam measurements were recorded.

Figure 5.3: The Birdradar "Superfledermaus" installed near Flins sur Seine (France) in a former seepage reservoir, about 24 km from the dual-polarized Doppler weather radar in Trappes.

Fixed beam measurements were carried at three elevation angles (5.3°, 22.5°, 79°), which allowed a good coverage of all flight altitudes up to 6km. The beam was directed in the same direction as in De Bilt, towards SE (138°), thus perpendicular to the main migratory direction. The daily time schedule (UTC+1) of the measurements, the detection range and the duration of the measurements was the same as in de Bilt and Wideumont (s. above). Between fixed beam measurements tracks of single targets were recorded in the same way as in De Bilt and Wideumont.

Hourly migration traffic rates were determined for Trappes (18.9. – 22.10.07) over a height range of 4 km, divided into 200m height intervals. The temporal coverage comprised 96% of the total time. Failure of measurements were due meteorological restrictions (rain) and technical malfunctions.

Chapter 6

Bird radar observations

6.1 Flight directions and species composition

6.1.1 De Bilt

2864 targets were tracked during daytime (6h to 20h) and 3795 during the night (20h to 6h). 2160 of the diurnal tracks were identified as birds, whereas 511 could be identified to species or near species level (see table 6.1). Many birds passed out of range for identification due to their small size or a reduced visibility. The most common species tracked and identified was the common buzzard (Fig. 6.1).

Table 6.1: Number of species tracked by radar and identified visually by the observer at de Bilt during autumn 2007.

Latin	English	tracks	birds
Phalacrocorax carbo	Cormorant	7	23
Ardea cinerea	Grey Heron	5	8
Ciconia ciconia	White Stork	6	61
Platalea leucorodia	Spoonbill	1	10
Anser anser	Grey-lag Goose	2	9
Anser sp.	Anser sp.	1	4
Anas acuta	Pintail	2	4
Aythya sp.	unident. diving duck	2	8
Pernis apivorus	Honey Buzzard	17	14
Accipiter gentilis	Goshawk	1	1
Accipiter nisus	Sparrowhawk	29	21

Responsible Institute: SOI

Buteo buteo buteo	Buzzard	121	137
Circus cyaneus	Hen Harrier	1	0
Circus pygargus	Montagu's Harrier	2	1
Circus aeruginosus	Marsh Harrier	7	6
Falco subbuteo	Hobby	22	15
Falco columbarius	Merlin	2	1
Falco vespertinus	Red-footed Falcon	1	0
Falco tinnunculus	Kestrel	11	8
Falco sp.	unident. Falcon	5	5
Vanellus vanellus	Lapwing	5	78
Pluvialis squatarola	Grey Plover	1	3
Pluvialis apricaria	Golden Plover	1	1
Charadrius hiaticula	Ringed Plover	1	3
Charadrius sp.	unident. Plover	4	41
Numenius phaeopus	Whimbrel	3	5
Numenius arquata	Curlew	1	1
Tringa totanus	Redshank	2	8
Tringa ochropus	Green Sandpiper	2	1
Tringa sp.	Tringa sp.	1	1
Gallinago gallinago	Snipe	22	43
Calidris canutus	Knot	4	265
Stercorarius longicaudus	Long-tailed Skua	1	0
Larus canus	Common Gull	2	3
Larus argentatus	Herring Gull	1	1
Larus fuscus	Lesser Black-backed Gull	34	108
Larus sp.	unident. Gull	5	11
Larus ridibundus	Black-headed Gull	10	49
Chlidonias niger	Black Tern	1	0
Columba livia domestica	Feral Pigeon	1	1
Columba oenas	Stock Dove	2	0
Columba palumbus	Wood Pigeon	2	8
Columba/Streptop.sp.	unident. Dove	10	13
Apus apus	Swift	15	48
Hirundo rustica	Swallow	73	185
Delichon urbica	House Martin	18	80
Hirundinidae sp.	unident. Swallow	17	48
Corvus corax	Raven	5	5
Corvus corone	Carrion Crow	3	2
Corvus corone corone	Carrion Crow	1	1
Turdus philomelos	Song Thrush	1	0
Anthus pratensis	Meadow Pipit	1	2

Anthus sp.	unident. Pipit	2	3
Motacilla alba	Pied Wagtail	1	0
Motacilla alba alba	White Wagtail (M.a.alba)	1	0
Motacilla cinerea	Grey Wagtail	1	2
Motacilla flava	Yellow Wagtail	4	4
Motacilla flava flava	Yellow Wagtail (M.f.flava)	1	2
Sturnus vulgaris	Starling	6	35

Mean flight directions were towards SSW during the day (209°) and SW night (218°). The scatter of directions was much larger in diurnal migration than in nocturnal migration (Fig. 6.2). Mean headings were more to the West (260° and 239°, respectively), due to the common westerly winds. Mean ground speed was slightly higher through the day than the night (12.2 m/s and 11.5 m/s, respectively), and much more scattered than air speed (Fig. 6.3). Mean airspeed was also slightly higher during the day than the night (12.4 m/s and 11.4 m/s, respectively). In general ground speed and airspeed was very close, indicating that migrants did not make much use of tailwinds.

6.1.2 Wideumont

3070 targets were tracked during daytime (7h to 19h) and 7657 during the night (19h to 7h). 2495 of the diurnal tracks were identified as birds, whereas 256 could be identified to species or near species level (see table 6.1). In addition to the other sites, frequent fog hampered the identification of the targets. The most common species tracked and identified was the common buzzard (Fig. 6.4).

Table 6.2: Number of species tracked by radar and identified visually by the observer at Wideumont during autumn 2007.

Latin	English	tracks	birds
Phalacrocorax carbo	Cormorant	7	92
Anser sp.	Anser sp.	2	9
Pernis apivorus	Honey Buzzard	1	1
Milvus milvus	Red Kite	3	3
Accipiter gentilis	Goshawk	1	1
Accipiter nisus	Sparrowhawk	54	49
Buteo buteo buteo	Buzzard	70	68
Buteo lagopus	Rough-legged Buzzard	3	3

Circus cyaneus	Hen Harrier	2	1
Circus aeruginosus	Marsh Harrier	4	4
Falco peregrinus	Peregrine Falcon	1	1
Falco columbarius	Merlin	1	1
Falco tinnunculus	Kestrel	21	24
Falco sp.	unident. Falcon	3	2
Grus grus	Crane	2	73
Vanellus vanellus	Lapwing	3	60
Larus sp.	unident. Gull	2	2
Columba palumbus	Wood Pigeon	1	20
Columba/Streptop.sp.	unident. Dove	1	2
Lullula arborea	Woodlark	2	7
Alauda arvensis	Skylark	9	95
Hirundo rustica	Swallow	8	104
Delichon urbica	House Martin	1	40
Hirundinidae sp.	unident. Swallow	6	50
Corvus corax	Raven	2	1
Phoenicurus ochruros	Black Redstart	1	1
Turdus philomelos	Song Thrush	1	34
Anthus pratensis	Meadow Pipit	3	5
Anthus sp.	unident. Pipit	4	15
Motacilla alba	Pied Wagtail	4	3
Sturnus vulgaris	Starling	3	10
Carduelis spinus	Siskin	1	50
Fringilla coelebs	Chaffinch	20	140
Fringilla montifringilla	Brambling	5	50

Mean flight directions were towards SW very similar during day and night (225° and 222°, respectively), and well concentrated in both time periods (Fig. 6.5). Mean headings were almost the same (222° and 227°, respectively), indicating a low impact of wind drift. Mean ground speed was clearly higher through the day than the night (15.3 m/s and 12.8 m/s, respectively), and much more scattered than air speed (Fig. 6.6). Mean airspeed was only slightly higher during the day than the night (12.8 m/s and 12.2 m/s, respectively). The considerable difference in ground speed between diurnal and nocturnal must be due to the difference in wind support between day and night, because air speeds did not differ much. In contrast to the other sites (s. above and below) the distribution of air speeds does not seem to be truncated at 5 m/s, which indicates that the proportion of insects was low in this dataset.

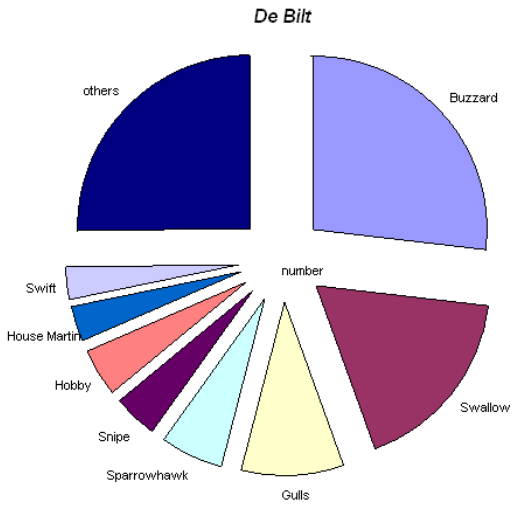

Figure 6.1: Species composition of identified diurnal migration near De Bilt during autumn 2007. There are only tracks included where visual identification was possible (N=513). Shown are only the 8 most abundant species (cf. table 6.1)

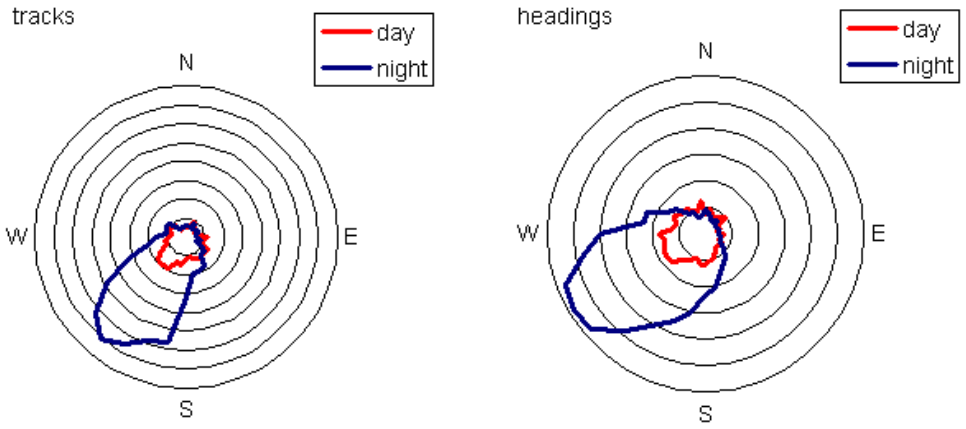

(a) (b)

Figure 6.2: Distribution of track - and heading directions of diurnal and nocturnal migrants near De Bilt during autumn 2007. There are only tracks included where wind data were available within 6h for the calculation of headings (N=4927).

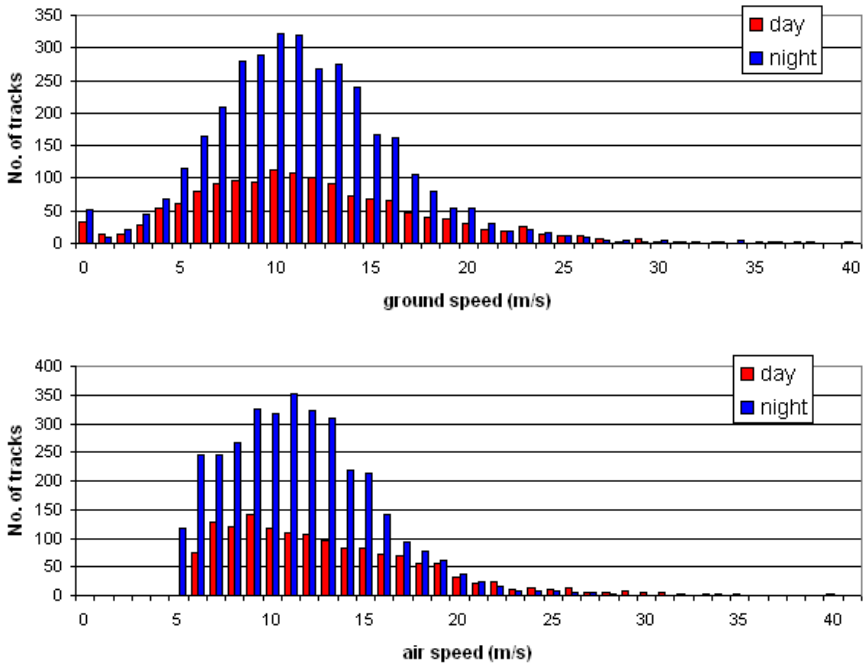

Figure 6.3: Distribution of ground- and air speeds of diurnal and nocturnal migrants near De Bilt during autumn 2007. There are only tracks included where wind data were available within 6h for the calculation of headings (N=4927). Tracks with airspeeds below 5 m/s were considered as non-birds (insects) and excluded.

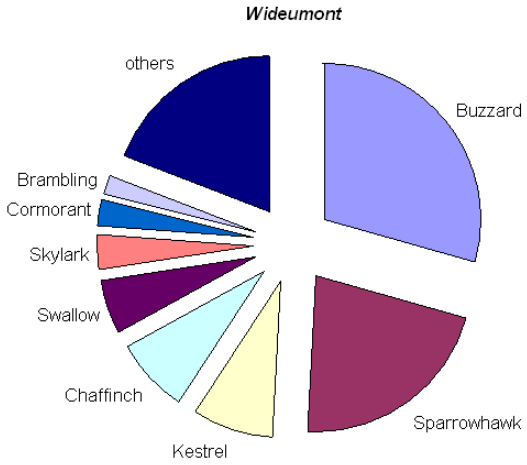

Figure 6.4: Species composition of identified diurnal migration near Wideumont during autumn 2007. There are only tracks included where visual identification was possible (N=252). Shown are only the 8 most abundant species (cf. table 6.2)

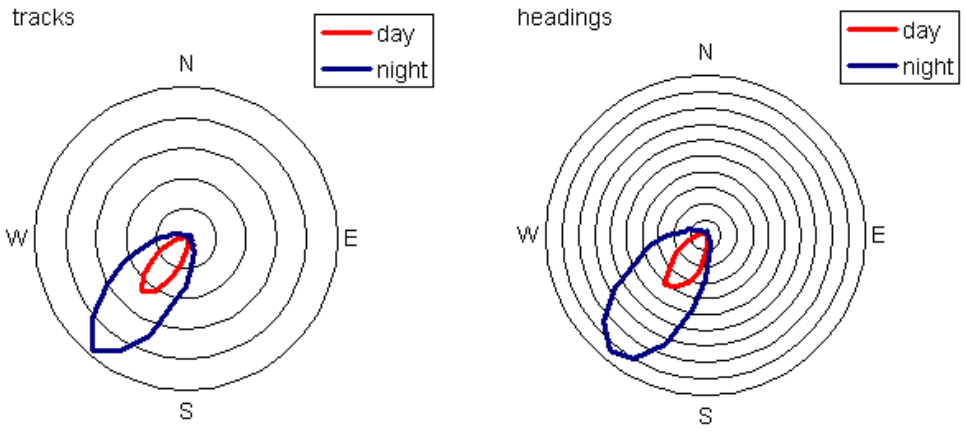

(a) (b)

Figure 6.5: Distribution of track - and heading directions of diurnal and nocturnal migrants near Wideumont during autumn 2007. There are only tracks included where wind data were available within 6h for the calculation of headings (N=9459).

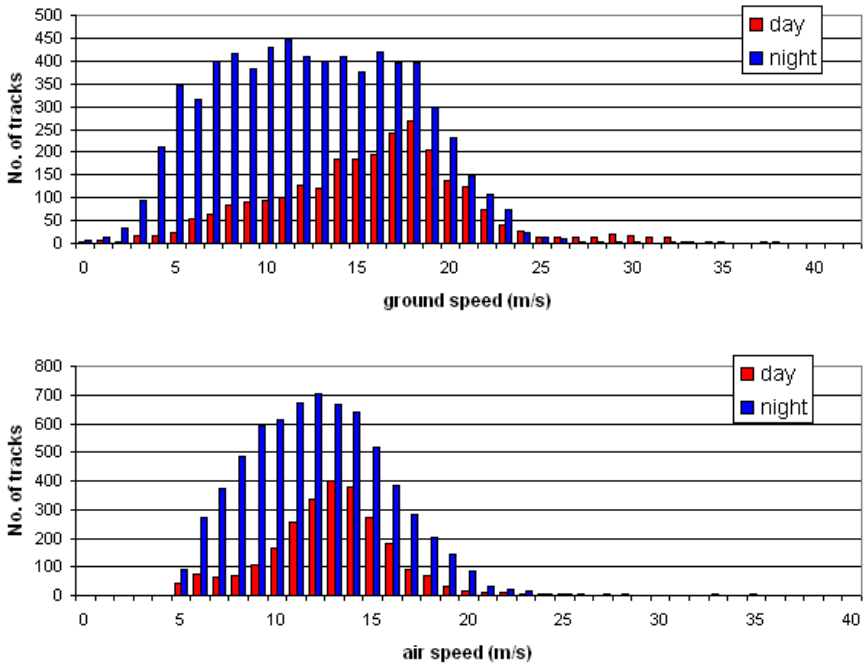

Figure 6.6: Distribution of ground- and air speeds of diurnal and nocturnal migrants near Wideumont during autumn 2007. There are only tracks included where wind data were available within 6h for the calculation of headings (N=9459). Tracks with airspeeds below 5 m/s were considered as non-birds (insects) and excluded.

6.1.3 Trappes

4993 targets were tracked during daytime (7h to 19h) and 7350 during the night (19h to 7h). 4280 of the diurnal tracks were identified as birds, whereas 559 could be identified to species or near species level (see table 6.3). Small passerines like larks, thrushes and finches accounted for the vast majority of tracked birds, but were in most cases to distant for identification. The most common species tracked and identified was the common swift (Fig. 6.7).

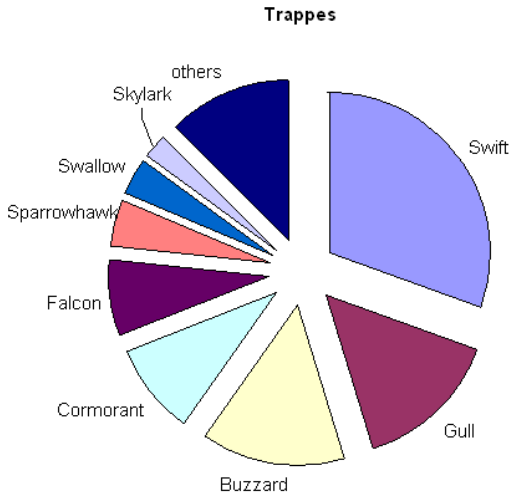

Figure 6.7: Species composition of identified diurnal migration near Trappes during spring 2008. There are only tracks included where visual identification was possible (N=559). Shown are only the 8 most abundant species (cf. table 6.3)

Table 6.3: Number of species tracked by radar and identified visually by the observer at Trappes during spring 2008.

Latin	English	tracks	birds
Phalacrocorax	carbo Cormorant	50	163
Ardea cinerea	Grey Heron	6	8
Ciconia ciconia	White Stork	3	4
Ciconia nigra	Black Stork	1	2
Anas sp.	Anas sp.	1	8
Pernis apivorus	Honey Buzzard	1	1
Milvus migrans	Black Kite	5	5

Accipiter gentilis	Goshawk	10	10
Accipiter nisus	Sparrowhawk	25	25
Buteo buteo buteo	Buzzard	77	89
Buteo lagopus	Rough-legged Buzzard	1	1
Buteo sp.	unident. Buzzard	2	2
Circus cyaneus	Hen Harrier	3	3
Circus pygargus	Montagu's Harrier	1	1
Circus aeruginosus	Marsh Harrier	2	2
Circus sp.	unident. Harrier	7	7
Pandion haliaetus	Osprey	1	1
Falco peregrinus	Peregrine Falcon	2	2
Falco subbuteo	Hobby	5	6
Falco columbarius	Merlin	1	1
Falco tinnunculus	Kestrel	33	38
Falco sp.	unident. Falcon	2	3
Vanellus vanellus	Lapwing	2	7
Gallinago gallinago	Snipe	2	21
Philomachus pugnax	Ruff	2	63
Larus arg./cachinnans	(Yellow-legged) Herring Gull	12	28
Larus argentatus	Herring Gull	1	1
Larus sp.	unident. Gull	53	117
Larus ridibundus	Black-headed Gull	13	54
Larus sp.	unident. Gull	5	5
Columba livia domestica	Feral Pigeon	1	1
Columba palumbus	Wood Pigeon	4	23
Columba/Streptop.sp.	unident. Dove	4	5
Apus apus	Swift	173	290
Dendrocopos major	Great Spotted Woodpecker	1	1
Alauda arvensis	Skylark	13	42
Hirundo rustica	Swallow	12	14
Delichon urbica	House Martin	5	6
Riparia riparia	Sand Martin	1	1
Hirundinidae sp.	unident. Swallow	9	12
Corvus corax	Raven	1	1
Corvus corone	Carrion Crow	1	2
Corvus corone corone	Carrion Crow	2	4
Fringilla coelebs	Chaffinch	3	17

Mean flight directions were towards NE and very similar during day and night (41° and 44°, respectively), but more scattered during the day than the night (Fig. 6.8). Mean headings were more to the North (31° and 37°,

respectively), as winds were most of the time from West. Mean ground speed was slightly lower through the day than the night (15.9 m/s and 16.5 m/s, respectively), and much more scattered than air speed (Fig. 6.9). In contrast mean airspeed was slightly higher during the day than the night (14.5 m/s and 14.1 m/s, respectively), indicating that nocturnal migrants made more profit out of tailwinds. This might be due to the fact that during day also local bird movements were recorded.

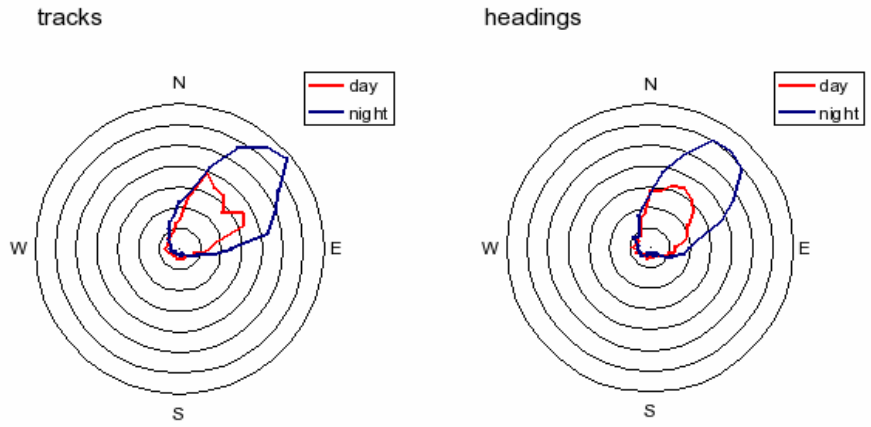

Figure 6.8: Distribution of track - and heading directions of diurnal and nocturnal migrants near Trappes during spring 2008. There are only tracks included where wind data were available within 6h for the calculation of headings (N=10480).

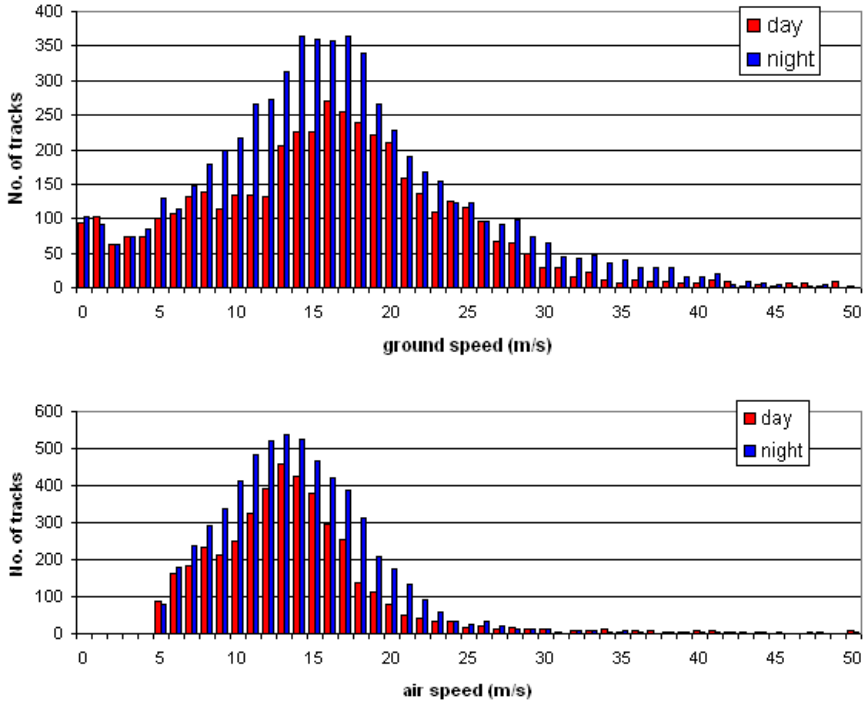

Figure 6.9: Distribution of ground- and air speeds of diurnal and nocturnal migrants near Trappes during spring 2008. There are only tracks included where wind data were available within 6h for the calculation of headings (N=10480). Tracks with airspeeds below 5 m/s were considered as non-birds (insects) and excluded.

6.2 Bird densities and flight altitudes

The seasonal course of bird migration intensity was in accordance with the long term experiences. At all observations sites nocturnal migration exceeded the diurnal movements by a factor of three to five. However, it must be taken into account, that generally diurnal migrants fly in flocks, whereas nocturnal migrants fly singly. Therefore, our estimate of intensity must be taken as the number of birds for nocturnal migration and number of flocks for diurnal migration.

6.2.1 De Bilt

The intensity of bird migration varied considerably during the first half of autumn season with some peak nights towards the end of August (Fig. 6.10). Compared to the other sites (s. below) migration intensity was weak. Towards the end of the observation period (first half of September) only minor migration intensities were recorded. During the night, average migration intensity was about three times higher (MTR = 153 birds $km^{-1}h^{-1}$) than during daytime (MTR = 56 birds $km^{-1}h^{-1}$).

Flight altitudes of diurnal migrants was considerably higher than those of nocturnal migrants (Fig. 6.11). 50% of diurnal migration occurred below 600 m agl, and of nocturnal migration below 300 m agl. The 90% range was at 1800 m agl for diurnal and 950 m agl for nocturnal migration, respectively. The fact that diurnal migration was higher than the nocturnal migration is in contrast to the other results (s. below) and experience from former studies. We assume that due to the generally low intensity a single event, one day with strong high diurnal bird migration (24.8.07) had a strong impact on the diurnal height distribution. Another explanation could be that migrants coming in from the coast during the morning are flying still at high levels after the sea crossing.

6.2.2 Wideumont

The intensity of bird migration increased towards the end of September and decreased slowly towards the end of October (Fig. 6.12). As expected intensity of migration was highest during this observation period. During the night, average migration intensity was about five three times higher (MTR = 1100 birds $km^{-1}h^{-1}$) than during daytime (MTR = 177 birds $km^{-1}h^{-1}$).

Flight altitudes of diurnal migrants was lower than those of nocturnal migrants (Fig. 6.13). 50% of diurnal migration occurred below 250 m agl,

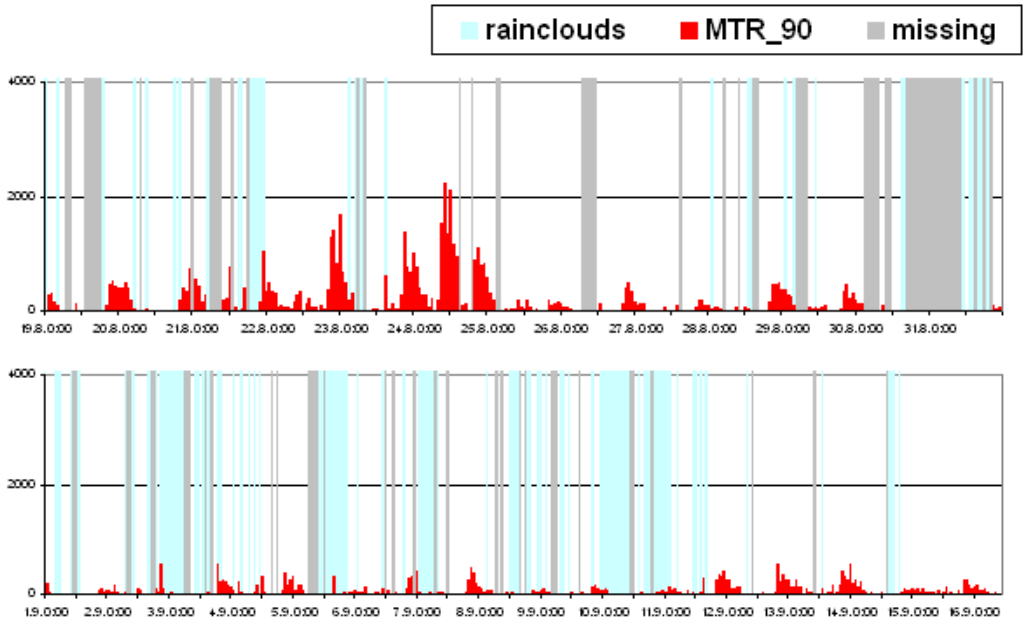

Figure 6.10: Seasonal course of migratory intensity measured near De Bilt during autumn 2007. Migration traffic rate (MTR) is measure for the intensity of migration, it denominates the number of birds crossing a line of one km perpendicular to the migratory direction within one hour. Missing measures due to rain (blue) and technical problems (grey) are indicated.

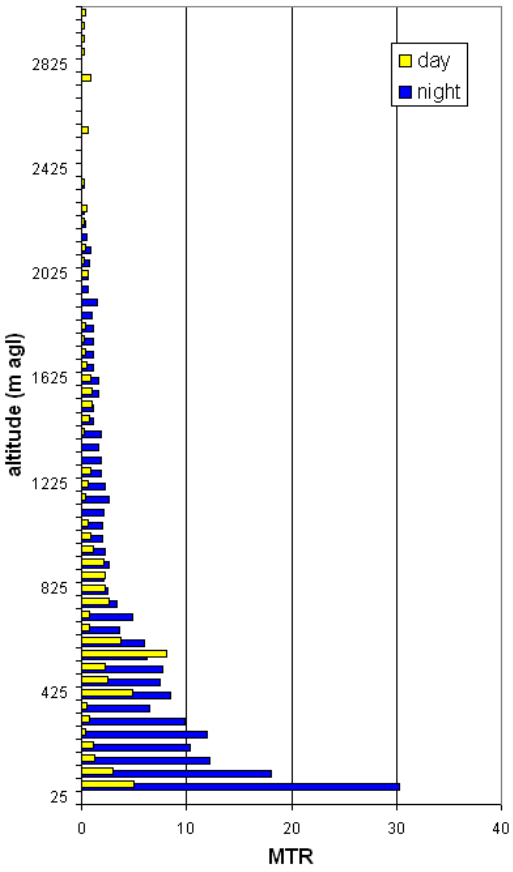

Figure 6.11: Mean seasonal height distributions of diurnal and nocturnal migration near De Bilt as recorded by the bird radar.

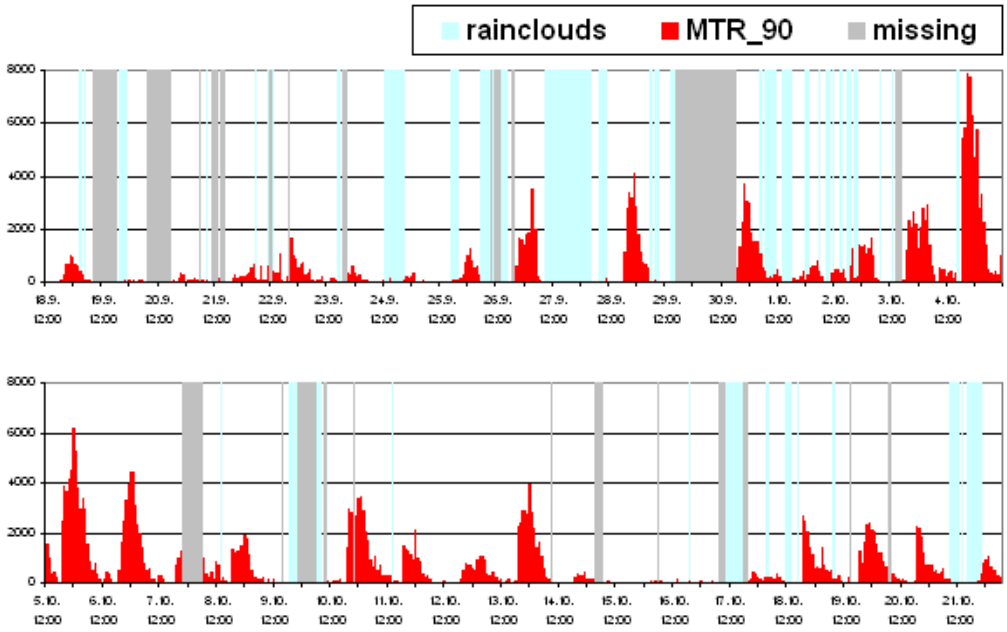

Figure 6.12: Seasonal course of migratory intensity measured near Wideumont during autumn 2007. Migration traffic rate (MTR) is measure for the intensity of migration, it denominates the number of birds crossing a line of one km perpendicular to the migratory direction within one hour. Missing measures due to rain (blue) and technical problems (grey) are indicated.

and of nocturnal migration below 500 m agl. The 90% range was at 800 m agl for diurnal and 1350 m agl for nocturnal migration, respectively.

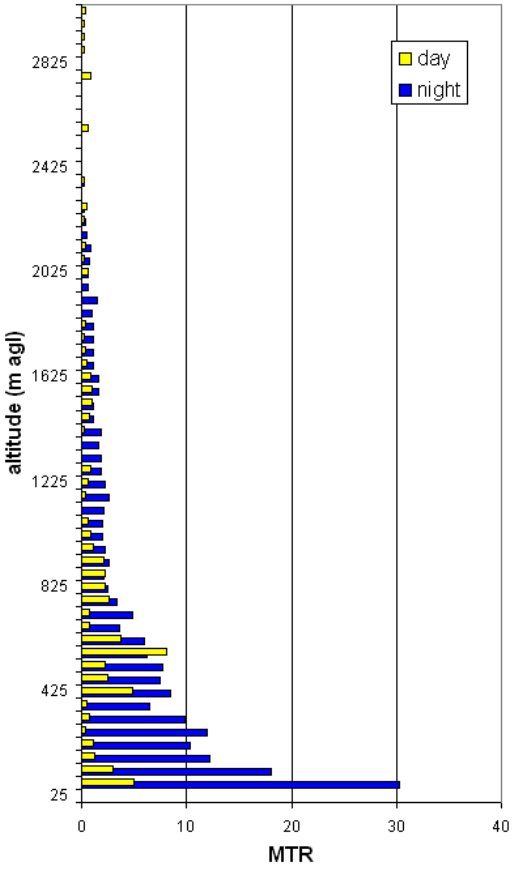

Figure 6.13: Mean seasonal height distributions of diurnal and nocturnal migration near Wideumont as recorded by the bird radar.

6.2.3 Trappes

The intensity of bird migration varied considerably during the spring season with some peak nights in mid March and April (Fig. 6.14). In May only minor migration intensities were recorded. During nighttime, average migration intensity was about four times higher (MTR = 618 birds $km^{-1}h^{-1}$) than during daytime (MTR = 154 birds $km^{-1}h^{-1}$).

Flight altitudes of diurnal migrants was considerably lower than those of nocturnal migrants (Fig. 6.15). 50% of diurnal migration occurred below 350

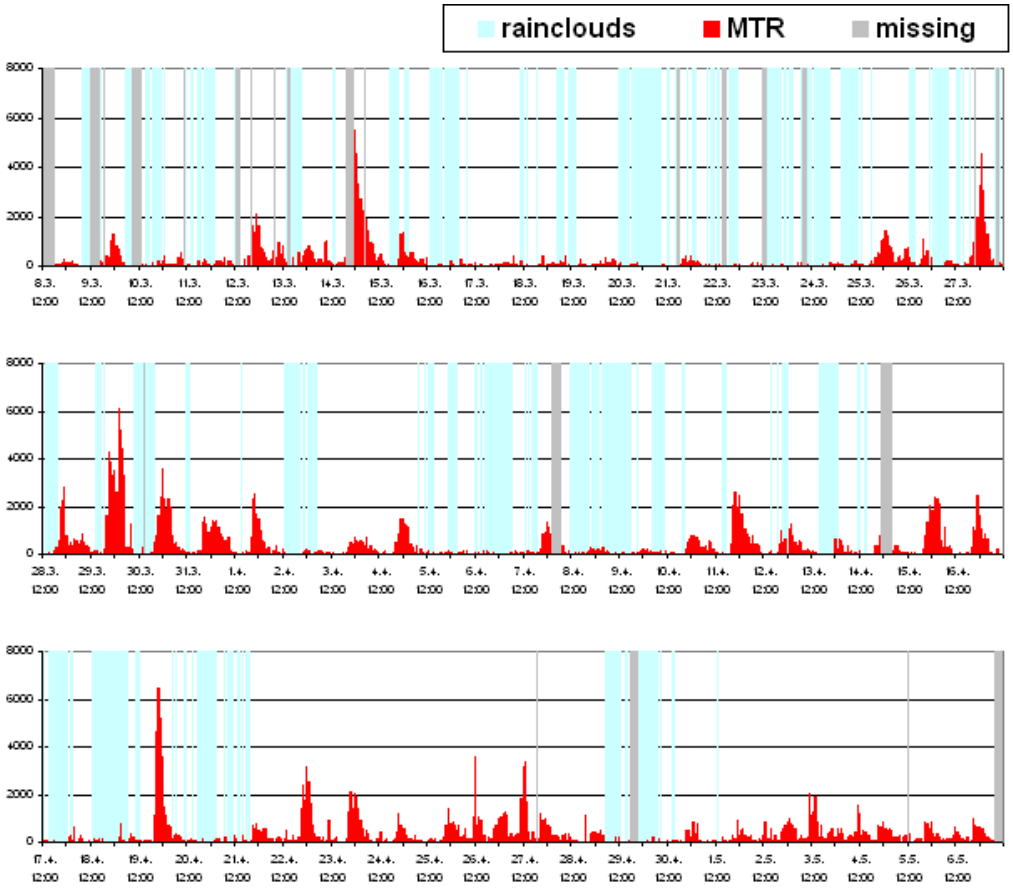

Figure 6.14: Seasonal course of migratory intensity measured near Trappes during spring 2008. Migration traffic rate (MTR) is measure for the intensity of migration, it denominates the number of birds crossing a line of one km perpendicular to the migratory direction within one hour. Missing measures due to rain (blue) and technical problems (grey) are indicated.

m agl, and of nocturnal migration below 750 m agl. The 90% range was at 1300 m agl for diurnal and 2050 m agl for nocturnal migration, respectively. Although average density was higher during the night than during the day, there was a similar absolute density below 100 m agl.

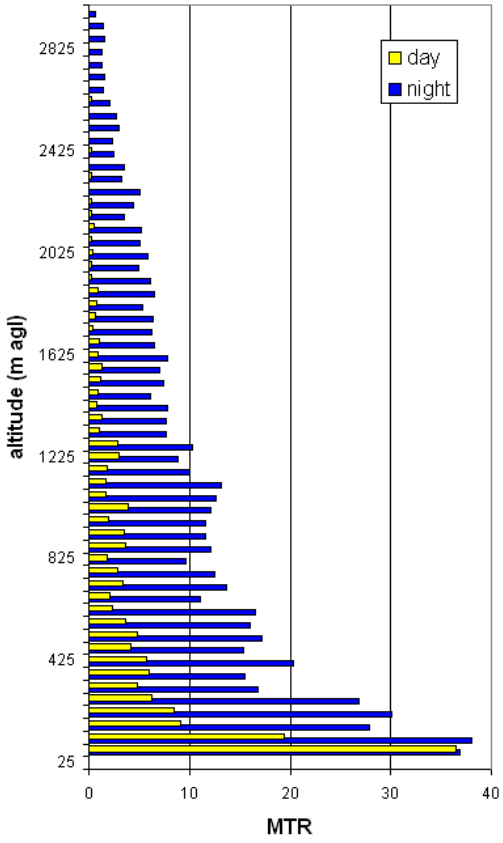

Figure 6.15: Mean seasonal height distributions of diurnal and nocturnal migration near Trappes as recorded by the bird radar.

6.3 Insects and UFO's

According to visual tracking and manual inspection of echoes, we assume that some of the diurnal echoes originating from flocks of small passerines were classified as non-bird echoes, because wing beat pattern of birds flying in flocks can not be detected. Therefore, diurnal migration in late autumn (October) and early spring (March) is underestimated within our data.

6.3.1 De Bilt

Out of 74972 echoes detected with the fixed beam measurements, 90% were automatically classified as non-birds. There were about twice as much non-bird echoes recorded during the day than during the night, with an upper limit (90%) at about 800m agl (day and night). Apart from variable ground clutter and weather phenomena these non-bird echoes consisted to an important proportion of insects (Fig. 6.16). A peak in insect movements was recorded during the 22.08.09 around midday and in the first half of the night.

6.3.2 Wideumont

Out of 104182 echoes detected with the fixed beam measurements, 48% were automatically classified as non-birds. These non-bird echoes were concentrated within the lowest 600m agl, but three times more during the day than the night (see comment above). Although some flocks were probably classified as non-birds, the huge amount of non-bird echoes consists of variable ground clutter and weather or other kind of phenomena. A event with strange echoes is documented in Fig. 6.17. We assume that the layer of diffuse echoes recorded, slowly decreasing in altitude and disappearing within 2.5h, might be due to chaff.

6.3.3 Trappes

Out of 118072 echoes detected with the fixed beam measurements, 51% were automatically classified as non-birds. These non-bird echoes were concentrated within the lowest 200m equally distributed between day and night. They consisted mainly of diffuse weather phenomena (Fig. 6.18). More insect-like echoes were recorded in May.

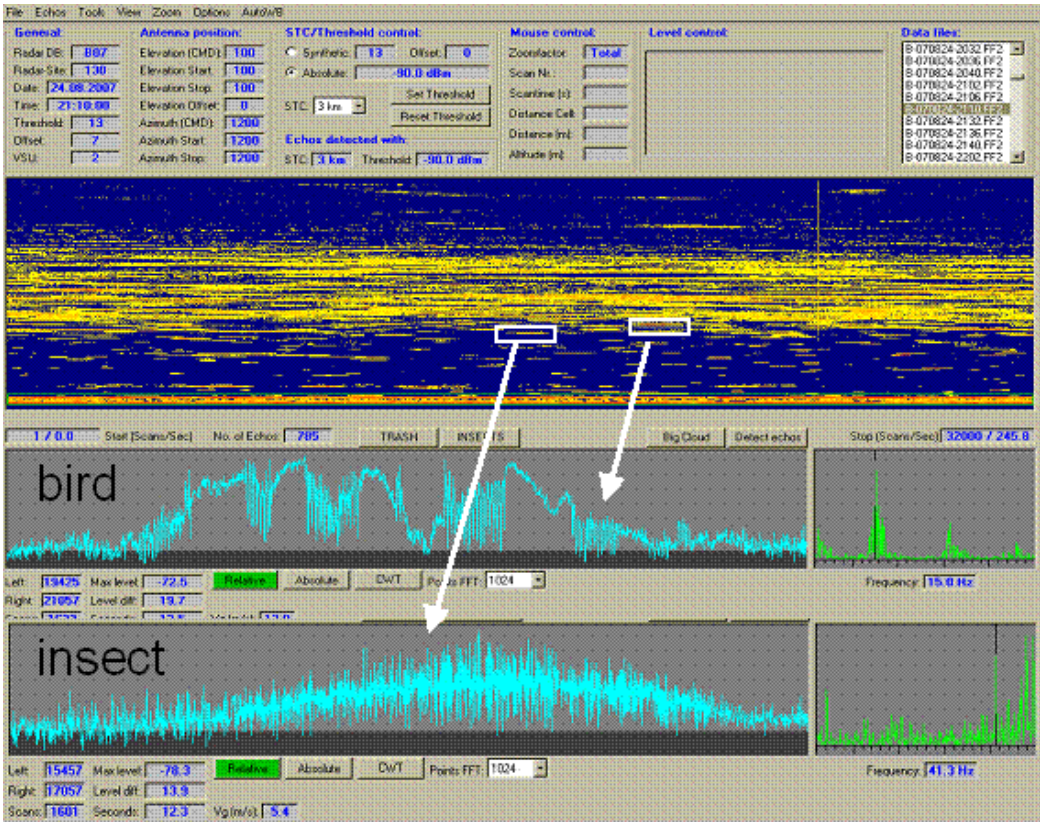

Figure 6.16: Example of non-bird echoes recorded during autumn at De Bilt. The image shows a measurement with strong insect contamination (24.8.09 21;10). Birds and insets can be distinguished due to the echo signature (wing beat pattern). The bird shows a clear pattern of wing beats an pauses with a preferred frequency of 15.0 Hz, typically for a small songbird. The echo signature of the insect shows an irregular, noisy pattern with preferred frequencies above 40 Hz.

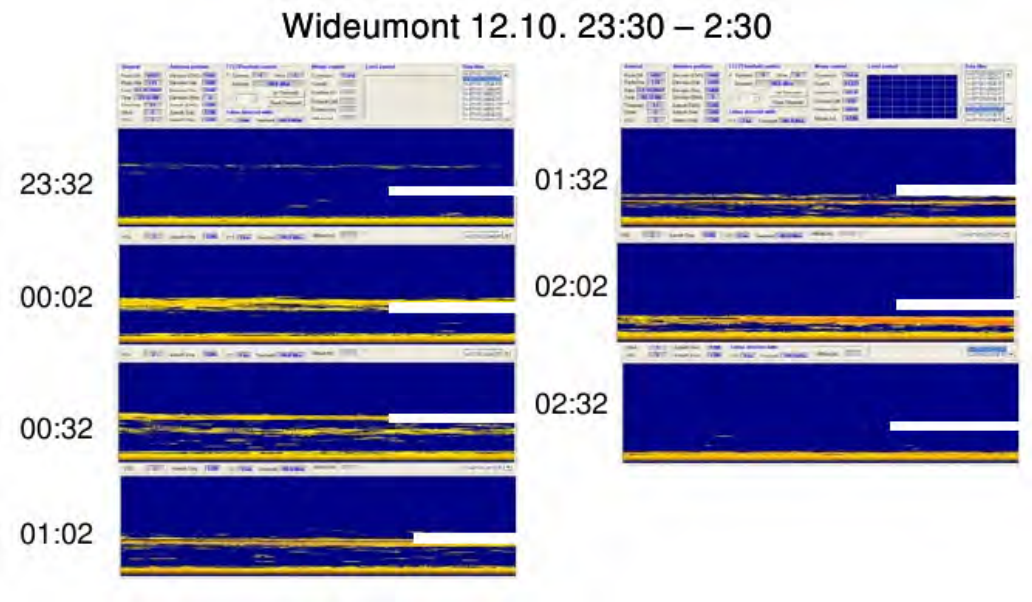

Figure 6.17: Example of non-bird echoes recorded during autumn at Wideumont. The graph shows 7 consecutive vertical fixed-beam measurements. There is a layer of echoes showing up as a fine line on 23:32h, with increased intensity 00:02h and decreasing in altitude slowly through next measurements and disappearing at 02:3h. The white bar on the right of each image indicates 2000m agl.

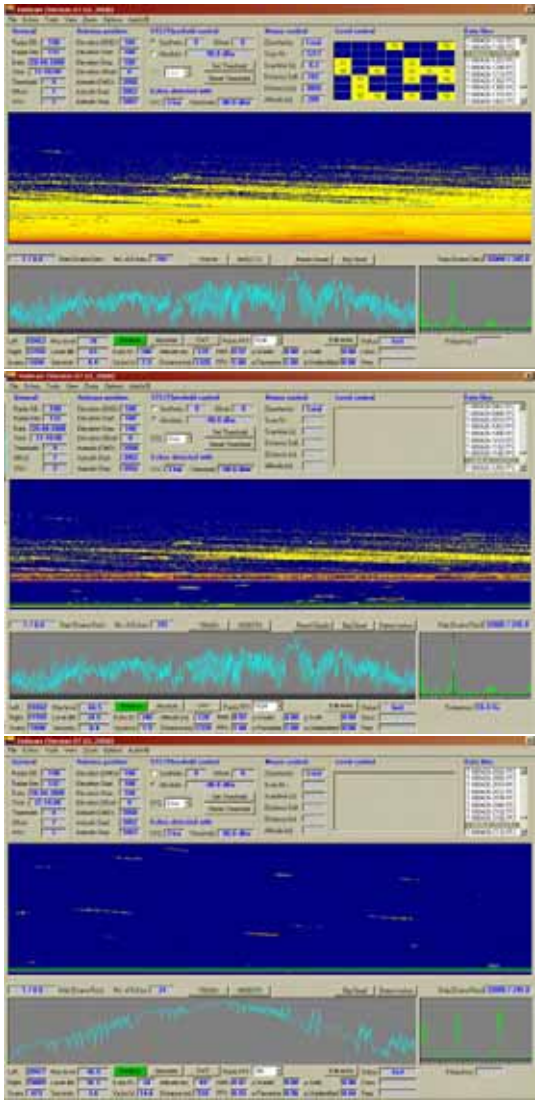

Figure 6.18: Example of non-bird echoes recorded during spring at Trappes. The first two images show the same measurement (26.4.8 12;10 UTC), first as the raw picture and second the image after the application of a 3km STC. Probably the diffuse echoes belong to a weather phenomenon (humidity?). 781 echoes were automatically detected, but only few as birds. The echo signature of the echo marked with a small white rectangle is shown in the subwindow below (with the light blue line). It belongs to a birds with a wing beat frequency of 16.4Hz, most probably a small songbird. The third image shows a measurement ten hours later representing a normal, clear measurement with low intensity of nocturnal migration.

Chapter 7

Bird detection by Doppler weather radar

7.1 Distinguishing birds, insects and hydrometeors

At the heart of a bird migration quantification algorithm lies the ability to automatically distinguish bird-scattered signals from all other echoes detected by weather radar. The list of non-bird echoes is long, including most types of precipitation, dense clouds, insects and echoes related to anomalous propagation.

Radar meteorologists have been aware for long that echoes related to non-meteorological phenomena can 'contaminate' radar images. Such echoes show up most strikingly under stable atmospheric conditions when precipitation echoes are absent, and are therefore commonly referred to as clear-air echoes. While the exact origin of clear-air echoes has been debated for a long time, it is now well established that in C and S-band weather radar these echoes are caused nearly exclusively by flying birds and air-borne insects.

Bird echoes and other clear-air signals tend to be considerably weaker than meteorologically relevant signals from hydrometeors Most radar meteorologist therefore use a reflectivity factor threshold (typically 7 dBZ) to filter out most non-meteorological reflections. At C-band bird-scattered signals are typically found below this reflectivity factor threshold in the low-reflectivity regime of -30 to 10 dBZ[1].

At C-band a reflectivity factor threshold usually successfully selects me-

Responsible Institute: KNMI

[1] At S-band bird reflectivity factors are much higher, easily reaching 50 dBZ (see section 2.3).

teorologically relevant precipitation, but bird scattered signals cannot be selected on the basis of a reflectivity level alone. While most relevant precipitation has a reflectivity factor above 7 dBZ, there are numerous instances where precipitation has a lower reflectivity. Besides precipitation also flying insects give rise to significant scattering. Birds, insects and meteorological scatterers give rise to signals in an overlapping reflectivity regime, and more sources of information need to be considered to distinguish them.

Such additional information is available in Doppler weather radars from the radial velocity of scatterers. Figures 7.1 shows radar images during intense bird migration, during rainfall and during daytime in the absence of birds (when mostly flying insects are present).

Areas of precipitation show a radial velocity that is spatially continuous and locally homogeneous, as is clear from Fig. 7.1(d). The same holds (to a lesser degree) for clear air echoes observed during summer daytime (Fig. 7.1(f)), when convection has uplifted insects and possibly other scatterers into the air. The speed of hydrometeors is fully determined by the wind field and their terminal fall velocity, which are usually spatially smooth variables. Therefore the detected radial velocity field by Doppler radar is spatially smooth as well. The same holds for clear air echoes by insects, which have an active flight speed that is either negligible or non-directional. This causes the average velocity of insect scatterers per range-gate to be equal to the wind field velocity. Directed insect migration has been reported, but again the active flight speeds tend to be low and directed by the wind field.

Bird migration gives rise to a very different spatial structure of the radial velocity scan data, as illustrated in Fig. 7.1(b). A much higher degree of (local) spatial variation in the radial velocities is detected. Additionally, migrating birds give rise to scattered groups of range bins with valid data, causing the radial velocity field to be inhomogeneously filled.

Unlike precipitation a bird performs active flight, which may vary in speed and direction per individual. Bird migration therefore shows a higher variability in the Doppler velocity than precipitation. The lower filling fraction of the radial velocity field during bird migration has a twofold reason. First, a significant fraction of range gates may be simply void of birds (see section 2.5). Second, the Doppler velocity spectrum during bird migration may be highly structured and non-Gaussian, especially when the spread in flight directions high. A low signal quality index may be assigned to range gates with a low spectral brightness of the Doppler signal, causing the gate to be rejected by the signal processor (see section 7.2.1).

In sections 7.3 and 7.4 we discuss how the spatial structure of the radial velocity scan data can be used to filter out precipitation and identify bird-

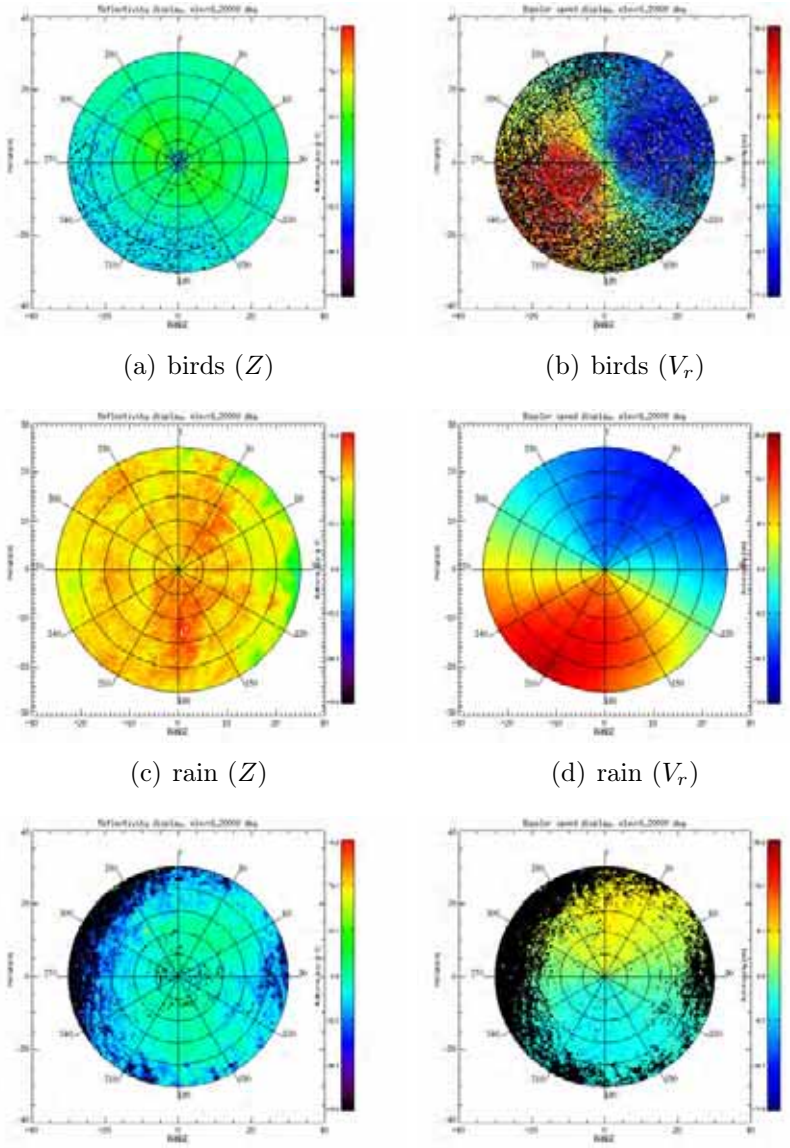

(a) birds (Z) (b) birds (V_r)

(c) rain (Z) (d) rain (V_r)

(e) non birds (Z) (f) non birds (V_r)

Figure 7.1: Reflectivity factor (left) and radial velocity (right) Plan Position Indicators (PPIs) for the Wideumont radar (scan at 1.1° elevation) for a case of intense bird migration (a-b: 05 October 2007, 22:32 UTC), a case of precipitation (c-d: 27 September 2007, 13:32 UTC) and a case showing non bird echoes (as verified by the reference bird radar) observed during daytime (e-f: 23 September 2007, 12:02 UTC). These non bird echoes are probably caused by insects.

scattered signals.

7.2 Clutter filtering

Clutter is an unwanted signal in Doppler radar observations of reflectivity and mean velocity. At low elevations clutter may be caused by backscattering from ground surface or partial beam blockage by high rise buildings in the radar surroundings. Clutter lines along the azimuth are often detected, caused by scattering of the antenna sidelobe power from ground surface. Typically ground clutter is strongest at close range and strongly decreasing with elevation, as illustrated in Fig. 7.2. Temperature inversion in the atmosphere can result in anomalous propagation of the radar beam, refracting the beam down towards the earth's surface. This may lead to strong scattering from the ground also at higher range.

Bird density estimation is based on measuring the intensity of bird echoes in clear air, which tend to be weak. The bird reflectivity estimate is therefore very sensitive to contamination of spurious echoes caused by clutter. Besides reflectivity observations, clutter can also affect the quality of mean radial velocity observations, which is important in the detection of bird presence. Seltmann (2000) has shown that ground clutter superimposed on a hydrometeor signal leads to lower signal quality and a bias towards zero of the mean radial velocity. The following section discusses the clutter filtering strategies used in the developed bird detection algorithm (some radar specific clutter filtering settings were detailed in the previous paragraphs).

7.2.1 pre-processing

Ground clutter interference in the Doppler signal can be suppressed by digital filtering in the time or frequency domain. In the De Bilt, Den Helder and Wideumont weather radars equivalent schemes of digital filtering are employed (no Doppler filtering is employed in the Trappes radar signal processor). Ground clutter gives rise to a narrow peak around zero frequency in the Doppler spectrum. This low frequency component can be removed from the Doppler signal by applying a sharp high-pass filter, resulting in clutter filtered radial velocity and reflectivity fields.

Doppler clutter filtering is less effective during bird migration than in clear sky conditions, as illustrated in Fig. 7.3. For the cases shown, ground clutter is on the order of 0-15 dBZ, while bird echoes are on the order of -2 to 5 dBZ (estimated from the ground clutter free areas (i.e. areas without uncorrected reflectivity during clear sky conditions)). Close to the radar clutter echoes

are of similar or larger magnitude than bird echoes, which implies that the Clutter to Signal Ratio (CSR) should be at least a few dB. Calculating the CSR by dividing the uncorrected reflectivity by the corrected reflectivity however shows that the CSR does not exceed -15 dB (see Fig. 7.3(f) (not considering the regions which have been fully rejected by Doppler filtering, the black area in fig. 7.3(d)). The effectiveness of dynamic Doppler clutter filtering is apparently reduced during bird migration. For bird detection we use a minimum range of 10 km to reduce the mixing in of clutter reflectivity.

Unfortunately the Doppler clutter filtering of the De Bilt and Den Helder radar experienced problems during the autumn of 2007. A software upgrade a few months earlier introduced a problem with the clutter filtering algorithms, which was noticed and resolved only after the field campaigns. Bird density estimates within the lowest 400 m are therefore non-available or unreliable for these radars.

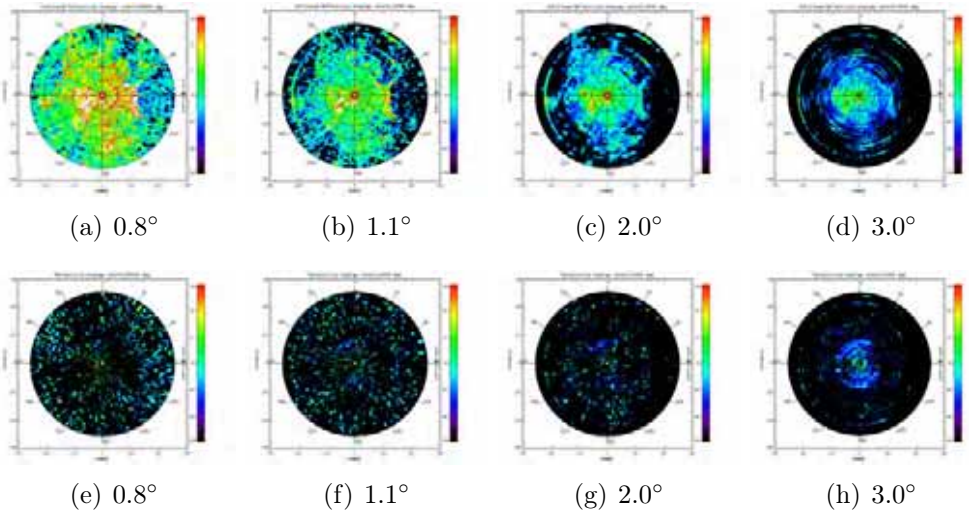

(a) 0.8° (b) 1.1° (c) 2.0° (d) 3.0°

(e) 0.8° (f) 1.1° (g) 2.0° (h) 3.0°

Figure 7.2: PPIs for the measurement window of the de Bilt radar (0-25 km range) showing uncorrected reflectivities (top row) and corrected reflectivities (bottom row) during clear sky conditions (5 January 2009, 12 UTC). The color scale increases from -40 dBZ (black) to 40 dBZ (red).

7.2.2 static clutter map

Static clutter maps were generated by performing an average of the (Doppler filtered) reflectivity for all range gates over several clear-air days without bird migration season (De Bilt / Den Helder: 10 - 19 February 2008. Wideumont:

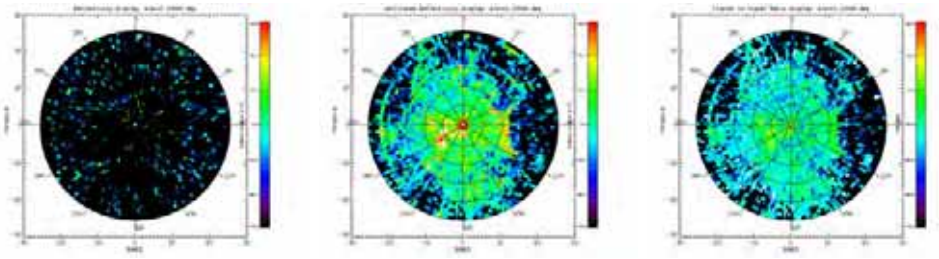

(a) Z filtered (b) Z unfiltered (c) CSR

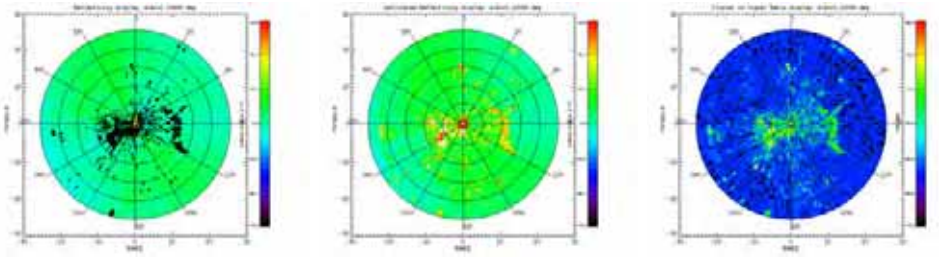

(d) Z filtered (e) Z unfiltered (f) CSR

Figure 7.3: Comparison of the clutter filtering effectiveness during clear sky conditions (top row: 5 January 2009, 12:00 UTC) and during bird migration (bottom row: 29 October 2008, 20:00 UTC). PPIs for the 1.1° scan (0-25 km range) of the de Bilt radar showing uncorrected reflectivity, corrected reflectivity and Clutter to Signal Ratio (CSR) The reflectivity color scale increases from -40 dBZ (black) to 40 dBZ (red) and the CSR color scale from -40 to 20 dB.

10 - 19 February 2008, Trappes March 1 2008 12-17 UTC and March 3 2008 11-17 UTC). All range gates with a reflectivity average above -10 dBZ are rejected permanently.

7.2.3 dynamic clutter map

Since ground clutter gives rise to a narrow peak around zero frequency in the Doppler spectrum, we exclude all range-gates with a Doppler velocity in the interval [-1,1] m s^{-1}. Sea clutter tends to have a non-zero Doppler velocity as it is scattered from a water surface which is in constant motion. Clutter filtering is therefore expected to be worse for a radar positioned close to water, like the Den Helder radar.

7.3 Precipitation filtering

In the context of bird detection precipitation is another source of "clutter" which needs to adequately be accounted for. Hydrometeor scattering tends to be intense compared to scattering from birds. Already small amounts of hydrometeor signal misidentified as birds can cause large overestimation of the bird density and therefore it is crucial to exclude all areas with non-bird echoes.

Meteorologists at KNMI typically use a lower threshold of 7 dBZ for the reflectivity factor to distinguish precipitating hydro-meteor signals from low reflectivity clear-air echoes. At C-band typical bird reflectivity factors indeed tend to be below 7 dBZ, however the same holds for a large variety of meteorologically non-significant hydrometeor signals. Additional information in the Doppler radial velocities is used to distinguish the two.

7.3.1 Reflectivity cell finding

We use a cell finding algorithm analogous to the algorithm described in Gonzales and Woods (1992).

reflectivity threshold criteria

For each elevation scan the reflectivity cell finding algorithm searches for areas that have a reflectivity factor above a certain threshold. This threshold needs to be low in order to include all areas of precipitation, but in doing so unavoidably areas of (intense) bird migration will be selected as well. A second analysis step is required to decide whether a found reflectivity cell is indeed a precipitation cell or not (see next subsection).

We chose the reflectivity threshold to be 0 dBZ, which selects most hydrometeor signal observed during the campaign. Gates with hydrometeor signal below 0 dBZ therefore do not enter the rain clutter maps, which may lead to residual rain contaminations in the bird density estimates. Although in a number of cases precipitation filtering is more effective when choosing a threshold below 0 dBZ, we find that in other cases it may lead to merging of areas of precipitation and bird migration into a single cell, which makes effective rain filtering impossible. Also, the threshold of 0 dBZ is often too low to mask all areas showing insect/non-bird echoes. A global analysis of radial velocities is however very effective in rejecting these echoes afterwards (see section 7.4.2).

filling fraction criteria

For each range gate within a cell we require that it is neighbored by at least 5 other range-gates above the reflectivity threshold. This guarantees that we only select cells which are uniformly filled. A uniform filling is usually observed for areas of precipitation, but often not for areas with bird echoes (see Fig. 7.1 & 7.6 and section 7.1).

7.3.2 Reflectivity cell properties

The radial velocity properties of the reflectivity cells are analyzed to decide whether the cell is a precipitation cell or a region of (intense) bird migration. In the latter case the cell is removed from the precipitation map.

From the radial velocity field a derived texture field is computed that equals the local radial speed standard deviation. For each range gate a block of directly neighboring gates is considered. We compute an additional texture field, which equals the local standard deviation in the radial velocity V_r:

$$\sigma_v(r,\theta) = \sqrt{\langle V_r^2 \rangle_{r,\theta} - \langle V_r \rangle_{r,\theta}^2}, \tag{7.1}$$

where the brackets $\langle \ldots \rangle_{r,\theta}$ denote an average over the 8 direct neighbors of the range gate at range and azimuth (r,θ). Figure 7.4 shows the thus computed

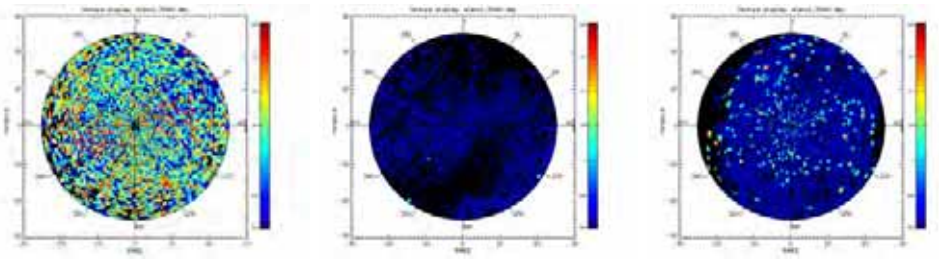

(a) birds (b) rain (c) non birds

Figure 7.4: radial velocity texture field as calculated by Eq. 7.1 for a case of bird migration, precipitation and non-bird echoes (insects). The same scans are shown as in Fig. 7.1. The color scale increases linearly from 0 m s^{-1} (black/blue) to 5 m s^{-1} (red). During bird migration the radial velocity texture is > 1 m s^{-1} for most range gates.

texture field for the same scans are shown as in Fig. 7.1, i.e. during intense bird migration, during rainfall and during mid-day, when mostly insects are detected.

For each reflectivity cell we compute:

1. the average texture $\bar{\sigma_v}$ in [m s^{-1}], excluding gates in the land clutter map (see Sections 7.2.3 and 7.2.2)
2. the log-averaged reflectivity factor $\bar{Z}$ in [dBZ], excluding gates in the land clutter map
3. the cell size in number of range gates $N_{\text{cell},0}$, including gates in the land clutter map
4. the cell size in number of range gates N_{cell}, excluding gates in the land clutter map

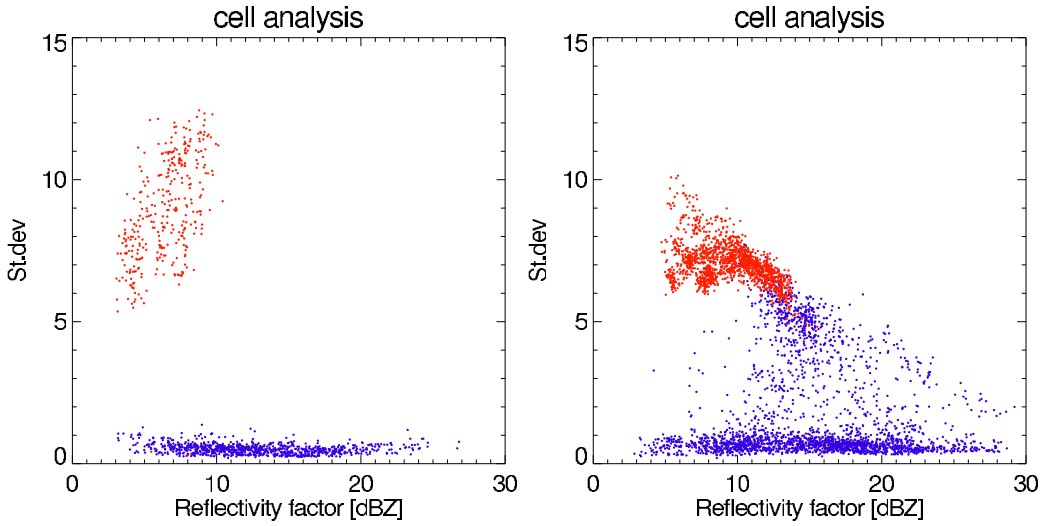

(a) Wideumont (b) De Bilt

Figure 7.5: cell-averaged texture $\bar{\sigma_v}$ versus reflectivity factor $\bar{Z}$ plotted for precipitation cells larger than 800 gates (not including gates in the clutter map) for cases of intense bird migration (red) and cases of convective precipitation (blue).

In Fig. 7.5 the cell-averaged local standard deviation $\bar{\sigma_v}$ and reflectivity factor $\bar{Z}$ are plotted for cells found during intense bird migration and during convective precipitation. By reference measurements of the Superfledermaus bird radar we verified that no birds were present during the precipitation cases (Wideumont: 24 September 9-18 UTC, 26 September 7-18 UTC, 17 October 6-17 UTC and 18 October 9-17 UTC. De Bilt: 2/3 September 12-12

UTC, 8 September 9-18 UTC and 10 September 9-18 UTC). By visual inspection of radar images we verified that no precipitation was present during the bird migration cases (nights only, 17-9 UTC. Wideumont: 4/5, 5/6, 6/7, 7/8 and 13/14 October. De Bilt: 5/6, 6/7, 12/13 and 13/14 October).

From Fig. 7.5 we see that reflectivity cells found during bird migration can be recognized by

- cell-averaged local radial velocity standard deviation $\bar{\sigma_v}$>5 m s^{-1}
- cell-averaged reflectivity $\bar{Z}$<15 dBZ

Reflectivity cells are dropped from the precipitation map if both these criteria are met. An additional criteria is added to keep cells containing a high fraction of land clutter, which mainly applies to the large cell usually found directly surrounding the radar:

- $N_{\text{cell}}/N_{\text{cell},0}$<0.5.

Fig. 7.5 also illustrates that the two types of reflectivity cells are better separated for the Wideumont radar than the De Bilt radar. The higher range resolution used for the Wideumont radar seems to be advantageous. Because of the smaller sample volume more empty range gates are detected, making the filling fraction criteria more adequate during reflectivity cell finding. The larger sample volume in De Bilt also causes the radial velocity to be averaged over more birds, which reduces the texture in the radial velocity standard deviation. Finally, ground clutter is stronger at the De Bilt site, which can cause de-aliasing errors of the radial velocities. Aliasing errors may increase the radial velocity texture for precipitation.

Fig. 7.6 displays the output of the rain masking algorithm for a case of simultaneous bird migration and precipitation. The areas of precipitation are being adequately removed by the algorithm.

7.3.3 Bird density within precipitation areas

Often bird echoes are observed while part of the measurement window is covered in rain. Since precipitation echoes usually screen the much weaker bird echoes completely, no information is available on the presence of birds within areas of precipitation.

There are two simple approaches on dealing with the bird density within precipitation:

1. we assume the bird density to be zero in precipitation

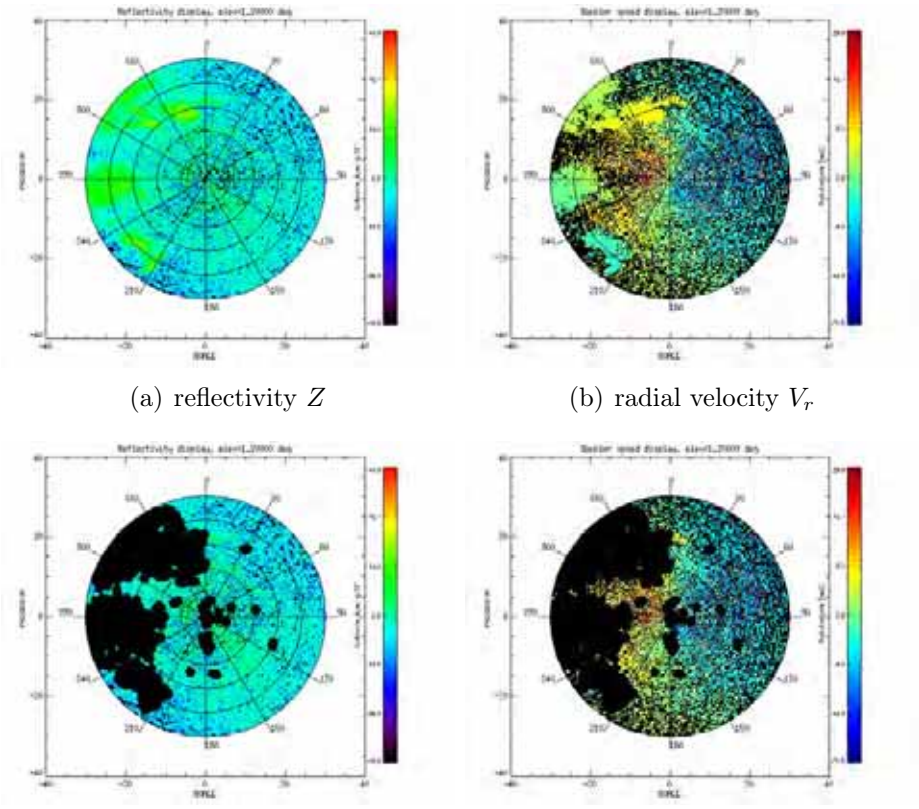

(a) reflectivity Z (b) radial velocity V_r

(c) Z, precipitation filtered (d) V_r, precipitation filtered

Figure 7.6: Reflectivity and radial velocity PPIs (scan at 1.1°) for the Wideumont radar for a case showing bird migration and precipitation simultaneously (01 October 2007, 04:32 UTC). The bottom figures show the same PPIs after removal of the precipitation by the rain masking algorithm.

2. we base the bird density estimate on the areas outside the precipitation areas only (this is equivalent to assuming equal bird densities for the areas inside and outside precipitation).

Although both are non-ideal compromises, we will discuss what is the most favorable choice.

From literature it is known that flying birds are capable of crossing precipitation. Fig. 7.7 shows a radar image of birds migrating southward in a direction different from the residing west north western wind direction. The precipitation cells do not obviously change the distribution and density of the bird echoes on the broad scale. Heavy precipitation on the other hand is usually avoided by birds. Fig. 7.8 shows a case of birds flying into an active thunderstorm. Immediately south of the storm the bird density is reduced.

Convective precipitation often occurs in limited cells over a limited area only. The accidental passage of such a precipitation cell can fill a significant part of our measurement window (the circle indicated in Fig. 7.7 & 7.8 for a limited period of time. Following the first approach, this would cause a strong temporary reduction of the bird density in the measurement window, which is not representative for the situation on the larger scale.

We conclude that the most representative bird density estimate is obtained by basing the bird density calculation on the precipitation free areas only.

7.4 Detection of bird presence

We use a quantitative global analysis of the radial velocity data to assess the possible presence or absence of birds in different height layers of interest. Bird presence or absence is established using the same characteristics of bird echoes discussed previously in Section 7.1, specifically the degree of variance in the measured radial velocities. This variance is quantified by a fitting the radial velocities to a linear wind model. The velocity data analysis is based on a conventional wind profiling technique (Volume Velocity Processing). Earlier work has shown that the spread in radial velocities around a linear wind model can be a skillful indicator of bird migration (van Gasteren et al., 2008; Holleman et al., 2008; Koistinen, 2000).

7.4.1 Volume Velocity Processing (VVP)

A Doppler weather radar measures the radial component of the velocity of scattering hydrometeors or birds. The Doppler weather radar performs a

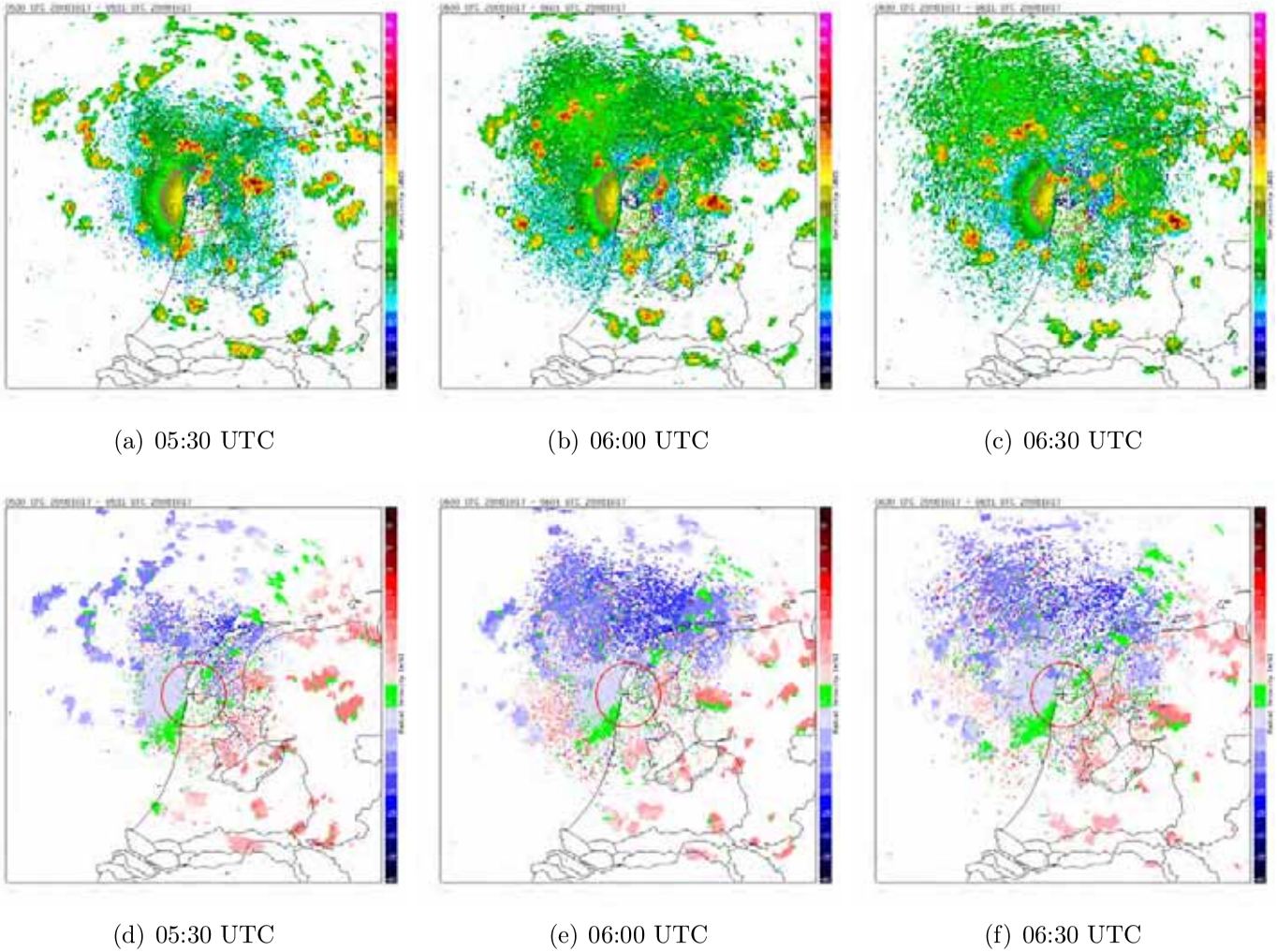

(a) 05:30 UTC (b) 06:00 UTC (c) 06:30 UTC

(d) 05:30 UTC (e) 06:00 UTC (f) 06:30 UTC

Figure 7.7: Dawn ascent of arriving birds from the North Sea (17 October 2008) as observed by the Den Helder radar (PPI of the 0.4° elevation scan). At sunrise birds climb to higher altitudes and come within view of the radar. Active showers move through the areas with flying birds. The echoes directly west of the radar are due to sea clutter. The circle around the radar indicates the measurement window used for bird detection.

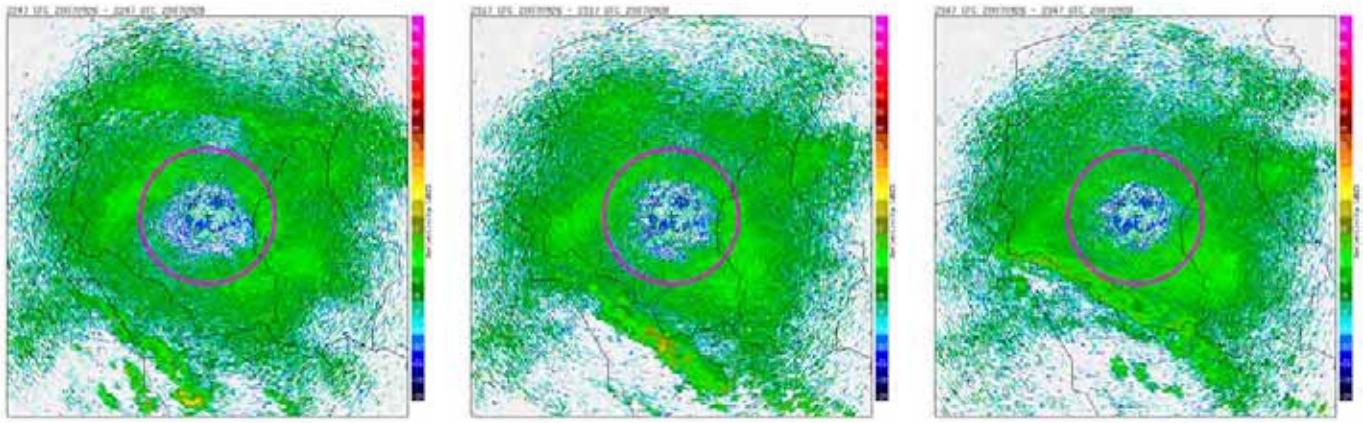

(a) 22:47 UTC (b) 23:17 UTC (c) 23:47 UTC

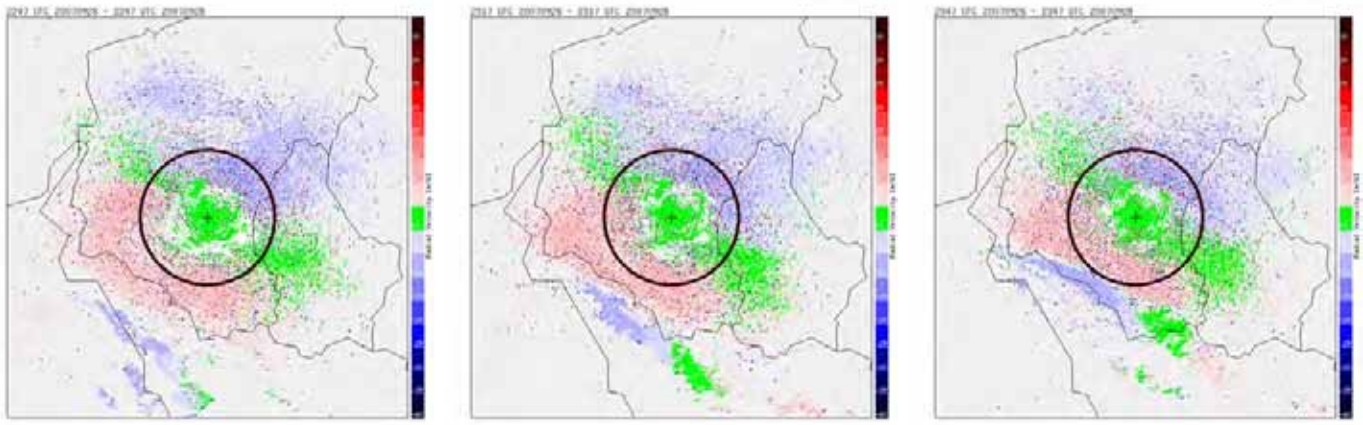

(d) 22:47 UTC (e) 23:17 UTC (f) 23:47 UTC

Figure 7.8: Precipitation approaching from the south during bird migration. The Doppler images reveal a south-western migration heading, while the precipitation has an eastern component. Immediately south of the rain shower the bird density is reduced. The circle indicates the measurement window (25 km range).

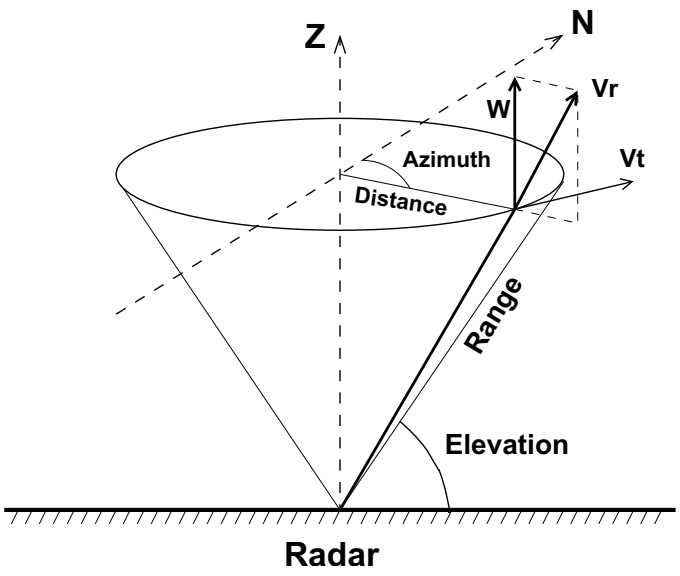

Figure 7.9: Schematic overview of the radar geometry used to measure Doppler wind profiles. The range, azimuth, and elevation, which are the scanning directions of a weather radar, are indicated. In addition, the radial velocity V_r, the tangential velocity V_t, and the vertical velocity w components of the local wind field are shown.

three-dimensional scan and thus provides the mean radial velocity as a function of range, azimuth, and elevation. Information on the local velocity field of scatterers has to be deduced from these radial velocity volume data only. A schematic overview of the typical Doppler radar geometry and the relevant local velocity field vectors is presented in figure 7.9. The figure shows the three scanning directions of a (Doppler) weather radar and the three components of the local velocity field: the radial velocity V_r, the tangential velocity V_t, and the vertical velocity w. Because only one of these components V_r can be observed by the Doppler radar, the other two components can only be estimated using a local velocity field model.

For velocity profiling by single-Doppler radar a linear wind model is often used to approximate the wind field in the vicinity of the radar. This linear wind model is centered horizontally at location of the radar and vertically at the height of interest z_0.

We will assume that the components of the local velocity field in the x-, y-, and z-directions only depend on the height of interest z_0. In locally stratiform situations this will be a good approximation, as well as during directed broad-front bird migration. At the height of interest, the components of the local velocity field in the x-, y-, and z-directions are approximated by constants

u_0, v_0 and w_0.

$$\vec{v}_{\text{model}} = u_0\hat{x} + v_0\hat{y} + w_0\hat{z} \tag{7.2}$$

The radial velocity V_r observed for such a velocity $\vec{v}_{\text{model}}$ at a range gate at position $\vec{r} = r\hat{r}$ equals

$$V_r = \hat{r} \cdot \vec{v}_{\text{model}} \tag{7.3}$$

By expressing the unit position vector $\hat{r}$ in a Cartesian basis ($\hat{r} = \sin\phi\cos\theta\ \hat{x} + \cos\phi\cos\theta\ \hat{y} + \sin\theta\ \hat{z}$) we find

$$V_r(\theta,\phi) = \sin\phi\cos\theta\ u_0 + \cos\phi\cos\theta\ v_0 + \sin\theta\ w_0 \tag{7.4}$$

The available data is analyzed for height layers of 200 m thickness around each height of interest z_0. The scanning strategies listed in Table 3.6 determine the total number of available range gates per height layer, which are listed in Table 7.1. Gates inside the clutter maps are dropped from the analysis.

A minimum range of 10 km is adopted, since at closer range ground clutter contaminations are frequent (see section 7.2). The requested height layer resolution of 200 m puts an upper limit to the range that can be considered, since the beam size is expanding with distance and should remain on the order of the requested height resolution. We find by Eq. 2.20 that the beam diameter has expanded to the 200 m height layer size at 12 km and reaches a 0.4 km diameter at 25 km. A maximum range of 25 km is chosen as a compromise between attaining height resolution and maximizing data availability.

Radial velocity data is fitted to Eq. 7.4, obtaining for each height layer the three cartesian velocity components u_0,v_0 and w_0.

7.4.2 VVP retrieved radial velocity variance: indicator of bird presence

From the fit residuals for each range gate i of the data to Eq. 7.4 we determine the VVP radial velocity standard deviation σ_{r} in a least-squares sense (Press et al., 1992):

$$\sigma_{\text{r}}^2 = \frac{1}{N_{\text{valid}} - M} \sum_{i}^{N_{\text{valid}}} \left[V_{\text{r},i} - V_{\text{r}}(\phi_i,\theta_i)\right]^2 \tag{7.5}$$

where $V_{r,i}$ are the observed radial velocities, N is the number of data points, and M is the number of estimated parameters in the radial velocity model ($M = 3$ in Eq. 7.4).

The weather radar observations have been combined with the bird density data from the bird radar. Fig. 7.10 shows a scatter plot of σ_{r} versus the

Table 7.1: This table shows the number of VADs (scans along the azimuth at constant range and elevation) and the number of range gates available for each height layer (200 m thick). The numbers have been calculated based on the scan strategies listed in Table 3.6. Scans at elevations below 0.6° are not used to reduce clutter contaminations. Only gates in the range interval 5-25 km are considered. The azimuth/range resolution are 1°/1 km, 1°/250 m and 0.5°/240 m. for the De Bilt, Wideumont and Trappes data, respectively.

VVP profile coverage

	De Bilt		Wideumont		Trappes	
Height [km]	VADs	gates	VADs	gates	VADs	gates
3.9	6	2160	8	2880	5	1800
3.7	7	2520	8	2880	9	3240
3.5	9	3240	8	2880	10	3600
3.3	8	2880	8	2880	14	5040
3.1	9	3240	8	2880	16	5760
2.9	9	3240	8	2880	20	7200
2.7	10	3600	8	2880	24	8640
2.5	11	3960	8	2880	25	9000
2.3	11	3960	13	4680	33	11880
2.1	10	3600	13	4680	34	12240
1.9	14	5040	13	4680	43	15480
1.7	12	4320	13	4680	42	15120
1.5	12	4320	16	5760	46	16560
1.3	14	5040	21	7560	45	16200
1.1	17	6120	22	7920	46	16560
0.9	15	5400	28	10080	46	16560
0.7	14	5040	36	12960	43	15480
0.5	14	5040	46	16560	48	17280
0.3	24	8640	40	14400	68	24480
0.1	16	5760	20	7200	41	26640

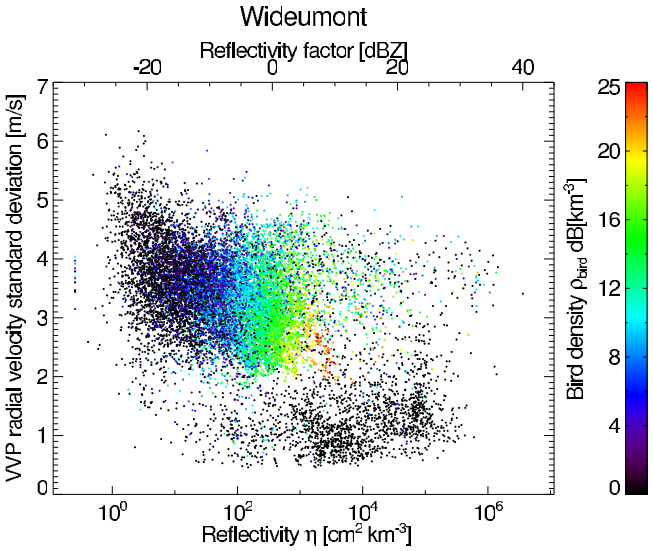

Figure 7.10: Scatter plot of the VVP retrieved radial velocity standard deviation σ_r versus the height layer's average reflectivity η_{full} (including precipitation) for the Wideumont field campaign Wideumont, Belgium (22 September - 21 October 2007). The color coding indicates the simultaneous collocated bird density estimate by the bird radar.

height layer's average reflectivity (i.e. η_{full} including both bird and precipitation echoes, for precise definition see Eq. 7.9 next section) for the complete Wideumont field campaigns. Each scatter point refers to a time-height layer, i.e. a specific height layer measured at a specific time. In color the bird density is indicated as measured simultaneously by the bird radar.

From Fig. 7.10 it is evident that time-height layers with a significant bird density (colored bullets) are found nearly exclusively above the horizontal line of $\sigma_r = 2$ m s^{-1}. Below 2 m s^{-1} we find mostly high reflectivities related to cases of active rainfall.

Also evident from Fig. 7.10 is that time-height layers with higher bird densities also have higher reflectivities. This correlation between bird density and reflectivity is a very important result, demonstrating that reflectivity measurements by weather radar can be used to actually quantify bird densities.

The reflectivity during the most intense bird migration cases (red bullets) never exceeds 15 dBZ. A few height layers in Fig. 7.10 do have a higher reflectivity, but these are height layers that besides birds contain high reflectivity precipitation, as will be shown in section 8.1.

The VVP analysis of radial winds provides an important additional parameter, the radial velocity standard deviation σ_r, which is useful for determining bird presence or absence. Collocated simultaneous measurements by the bird radar reference show that birds are absent in height layers with low σ_r. Detailed data verification is presented in Chapter 8, where we investigate whether this parameter by itself is sufficient to establish bird presence.

7.5 Bird density calculation

This section discussed how we calculate bird densities from reflectivity measurements that have been cleared from precipitation and insect echoes.

7.5.1 range gate classification inventory

The total number of available range gates per height layer N_{total} can be divided into different collections, which we list for later reference:

- collection $\mathbb{N}_{\text{clutter}}$: the N_{clutter} gates present in either the static ground clutter map (see section 7.2.2) or the dynamic ground clutter map ($V_r \approx 0$ and $\eta \neq 0$, see section 7.2.3)
- collection $\mathbb{N}_{\text{precip}}$: the N_{precip} gates in the precipitation map (see section 7.3)
- collection $\mathbb{N}_{\text{fringe}}$: the N_{fringe} gates in the fringes around the areas within the precipitation map.
- collection $\mathbb{N}_{\text{valid}}$: the N_{valid} gates with a nonzero radial velocity and a nonzero reflectivity ($V_r \neq 0$ and $\eta \neq 0$).
- collection $\mathbb{N}_{\text{incomplete}}$: the $N_{\text{incomplete}}$ gates with a nonzero reflectivity ($\eta \neq 0$) but a missing radial velocity. For these gates the radial velocity has been rejected by the signal processor because of a low signal quality index or spectral brightness of the Doppler signal (see section 7.2.1).
- collection $\mathbb{N}_{\text{empty}}$: the N_{empty} empty gates with a reflectivity zero (and no radial velocity).
- collection $\mathbb{N}_{\text{rejected}}$: the N_{rejected} gates for which both the reflectivity and the radial velocity measurements have been rejected by the signal processor because of a low signal quality index or spectral brightness of the Doppler signal. These are typically gates with lots of ground clutter which have not passed digital Doppler filtering (see section 7.2.1).

The total number of gates equals the sum

$$N_{\text{total}} = N_{\text{valid}} + N_{\text{empty}} + N_{\text{incomplete}} + N_{\text{rejected}} + N_{\text{clutter}} + N_{\text{precip}} + N_{\text{fringe}}. \quad (7.6)$$

7.5.2 definition bird reflectivity and density

As motivated in Section 7.3.3 we calculate the average bird reflectivity for each height layer for the precipitation free areas only, according to

$$\bar{\eta}_{\text{bird}} = \overline{\rho_{\text{bird}}\sigma_{\text{bird}}} = \sum_{i \in \mathbb{N}_{\text{valid}}} \eta_i / (N_{\text{valid}} + N_{\text{empty}}), \quad (7.7)$$

$$\bar{\rho}_{\text{bird}} = \sum_{i \in \mathbb{N}_{\text{valid}}} \frac{\eta_i}{\sigma_{\text{bird}}(R_i)} / (N_{\text{valid}} + N_{\text{empty}}), \quad (7.8)$$

where we have disregarded the $N_{\text{incomplete}}$ gates that lack valid Doppler radial speed data, treating them equivalent to clutter. This is a valid assumption as long as the availability of radial speed data is unrelated to bird density, in which case the N_{valid} gates provide a representative set to determine the bird density.

The reflectivity including precipitation $\bar{\eta}_{\text{full}}$ is defined as:

$$\bar{\eta}_{\text{full}} = \sum_{i \in \mathbb{N}_{\text{valid}} \cup \mathbb{N}_{\text{precip}} \cup \mathbb{N}_{\text{fringe}}} \eta_i / (N_{\text{valid}} + N_{\text{empty}} + N_{\text{precip}} + N_{\text{fringe}}). \quad (7.9)$$

The number of empty gates N_{empty} can be calculated if all other terms in Eq. 7.6 are known. Unfortunately signal processors do not necessarily provide information on the number of rejected gates N_{rejected}, and empty and rejected gates cannot be distinguished. The total number of these zero signal gates equals

$$N_0 = N_{\text{empty}} + N_{\text{rejected}}. \quad (7.10)$$

If N_{rejected} is unknown (as is the case for the Wideumont and Trappes radars) we implement the density estimate according to

$$\bar{\eta}_{\text{bird}} = \sum_{i \in \mathbb{N}_{\text{valid}}} \eta_i / (N_{\text{valid}} + N_0), \quad (7.11)$$

$$\bar{\rho}_{\text{bird}} = \sum_{i \in \mathbb{N}_{\text{valid}}} \frac{\eta_i}{\sigma_{\text{bird}}(R_i)} / (N_{\text{valid}} + N_0), \quad (7.12)$$

Eq. 7.11 only gives accurate results when $N_{\text{rejected}} \ll N_{\text{empty}}$, i.e. when ground clutter is limited. This is the case for the Wideumont radar, which because of its ideal location on a hilltop suffers from very little ground clutter. For the Trappes radar at close range and low elevation ground clutter can be

severe, and we may have $N_{\text{rejected}} \gg N_{\text{empty}}$. In such cases the bird density estimate may be underestimated for the two lowest height layers (0-400 m a.g.), or even unavailable as a result of a too low number of data points.

To compare the magnitude of the scattered signal with meteorological signals it is often useful to express the bird reflectivity into a bird reflectivity factor, according to Eq. 2.14. Using the index of refraction of water ($|K_m|^2$=0.93 Doviak and Zrnić (1993)) and the radar wavelength at C-band ($\lambda = 5.3$ cm) we find

$$Z_{\text{bird}} = 10 \log_{10} (\eta_{\text{bird}}/360.7) \tag{7.13}$$

with the reflectivity factor Z in [dB] expressed in units of mm^6/m^3 and η_{bird} in units of cm^2/km^3.

7.6 Bird cross section range dependence

Reflectivity is the combined product of bird density and cross section (Eq. 2.11):

$$\eta_{\text{bird}} = \overline{\rho_{\text{bird}} \sigma_{\text{bird}}}$$

During the field campaigns the bird density ρ_{bird} has been independently determined by the bird radar. Combining these bird density measurements with the weather radar reflectivity measurements, we can calculate the net average bird radar cross section σ_{bird} by Eq. 2.12. We use the Wideumont campaign for determining the bird cross sections, as this campaign contains both cases of intense and weak bird migration, and is expected to be the least contaminated by insect echoes. For each time-height layer a cross sections were determined by dividing the bird reflectivity (Eq. 7.7) by the bird density determined by the bird radar reference. The cross section distribution is shown in Fig. 7.11. The distribution in black is based on all time height layers of the campaign, the distribution in grey is based on time height layers in the high reflectivity regime ($Z_{\text{bird}} > 5$ dBZ) only. The cross section distribution shows a spread that reflects both the imperfect correlation between weather and bird radar observations and a true variability in bird cross section. We find means of 14 and 11 cm^2 for the full distribution and high reflectivity distribution, respectively (17 and 14 cm^2 when including the lowest 200 meter).

We checked for range dependencies in the weather radar bird signal. Time-height layer reflectivities were computed by considering gates within 2 km range intervals, where the central range was varied by steps of 2 km

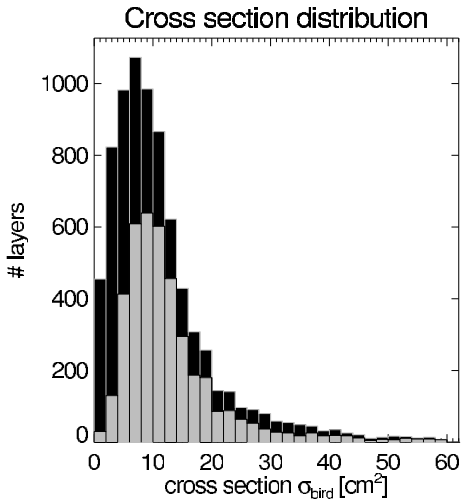

Figure 7.11: Distribution of bird weather radar cross sections based on collocated measurements with the bird radar during the Wideumont campaign. The distribution in grey is based on time height layers in the high reflectivity regime ($Z_{\text{bird}} > 5$ dBZ) only.

from 4-30 km. From these range-specific reflectivities we determined cross sections by dividing out the corresponding bird radar bird densities. The cross section means as a function of range are shown in Fig. 7.12. The bird cross section clearly decreases with range.

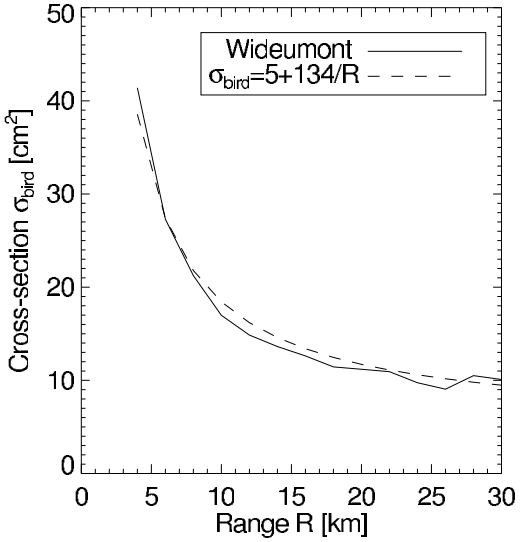

Figure 7.12: Mean bird cross section $\bar{\sigma}_{\text{bird}}(R)$ as a function of range. The cross section decreases approximately proportional to range

In section 7.2.1 we showed that at close range ground clutter is not completely eliminated by the Doppler filtering during bird migration. This explains the cross section increase at close range in Fig. 7.12: at close range additional reflectivity is detected originating from mixed in ground clutter. It is not very likely that the decrease in radar cross section is caused by detection losses at larger range, since typical bird radar cross sections at low bird densities give rise to reflectivity factors that are well above the weather radar noise level at the maximum range used of 25 km (e.g. a bird cross section of 10 cm^2 at 1 bird/km^3 amounts to -16 dBZ by Eq. 2.15, while the noise level at 25 km range is below -25 dBZ).

For bird density quantification we discard gates at a range closer than 10 km, to suppress the effects of clutter contamination. Over the range interval 10-25 km a mild decrease in cross section remains. In our bird migration quantification algorithm this range dependence will lead to a mild height dependence in the bird radar cross sections, since e.g. height layers at high altitude contain more gates at larger range.

A cross section correction may be desirable for the lowest height layer, where mixing in of ground clutter signal leads to overestimation of the bird density, as illustrated in Fig. 7.13. In this figure we compare the bird density height profiles extracted by bird radar and weather radar. At 200 m height bird densities are overestimated by 40 %.

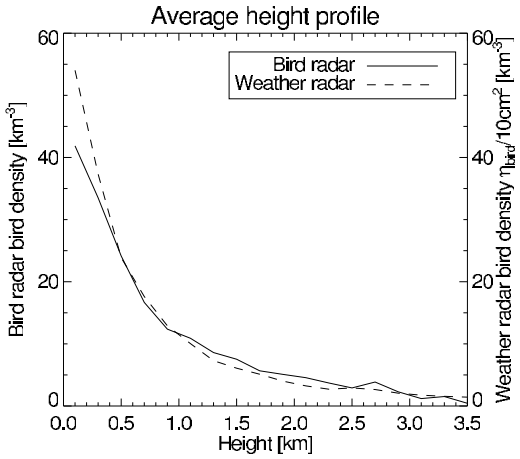

Figure 7.13: Average bird density height profile during the full Wideumont campaign. Bird reflectivity was converted into bird density by using a constant cross section of 10 cm^2 (dashed line)

An azimuthal dependence of the cross section is also commonly observed, as illustrated in Fig. 7.14. At azimuths perpendicular to the line of flight the

reflectivity is enhanced. This is related to the orientation of the bird's body relative to the radar beam, scattering more in side view than in front view. An azimuthal correction for the conversion of reflectivity to bird density has not been implemented.

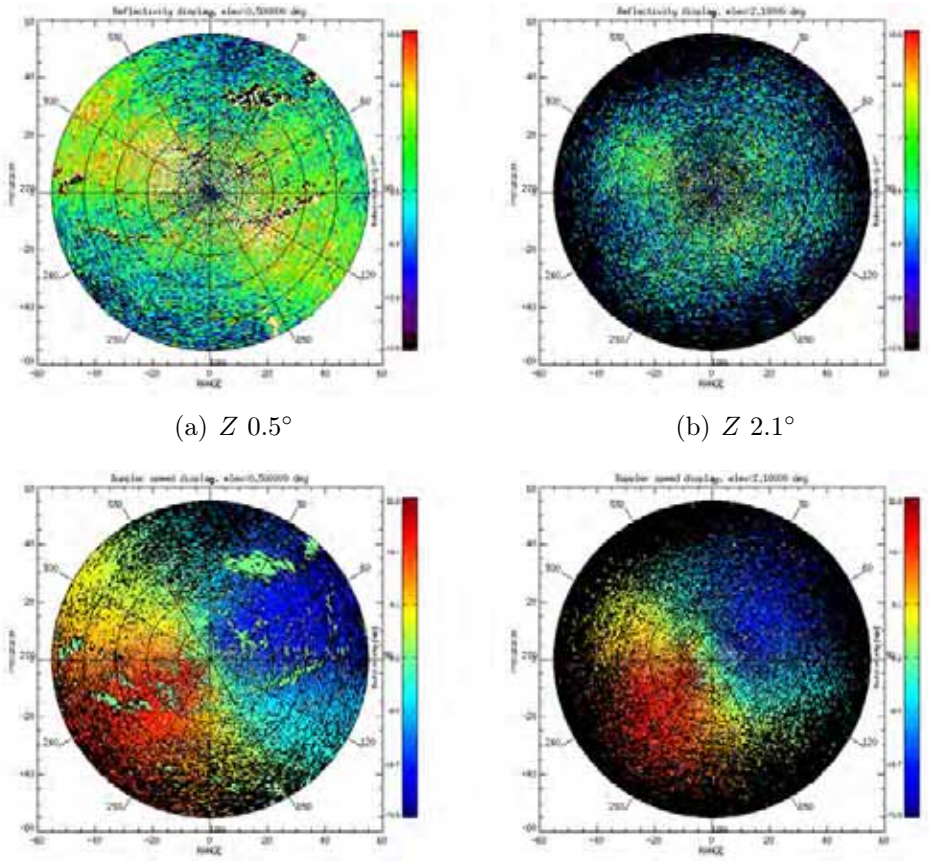

(a) Z 0.5° (b) Z 2.1°

(c) V_r 0.5° (d) V_r 2.1°

Figure 7.14: Reflectivity PPI (0-25 km range) in Wideumont during intense bird migration (6 October 2007, 5:32 UTC). The reflectivity is colored over a more limited range (-15 to 10 dBZ) to highlight the azimuthal variance. Especially at low elevation view, the reflection on side view is more intense than in head/tail view. From the reflectivity pattern we can derive that the body axis was oriented at 210°. From the radial velocity measurement we find an average heading of 230°. This heading results from the sum of the airspeed (headed at 210°) and the wind speed (4 m/s from ENE heading 65°).

7.7 Bird cross section seasonal patterns

Seasonal trends in bird radar cross section are shown in Fig. 7.15 for all field campaigns. For each time step we calculated an average radar cross section by dividing the height-integrated reflectivity for weather radar by the height-integrated bird density for bird radar (0.2-4 km). These cross sections were subsequently averaged to nightly means.

In late autumn (Wideumont) bird radar cross sections were observed to increase, while in spring (Trappes) cross sections decreased. These trends are directly related to the seasonal trends in the species composition of migratory birds. Migration of larger species (non-passerines and Thrushes) takes place in late autumn and early spring, while in early autumn and late spring migration is dominated by small passerines only.

A high number of days in De Bilt (early autumn) showed large bird radar cross sections. During the De Bilt campaign ground clutter Doppler filtering was not functioning properly. Ground clutter contamination may therefore have increased bird radar cross sections. Also insects were fairly numerous as determined with the bird radar (See Sec. 6.3.1), which may have biased the cross sections to larger values as well. The large scatter in cross section in De Bilt is also partly explained from the very low migration intensity during this campaign. The bird radar measurements are less accurate at very low bird densities.

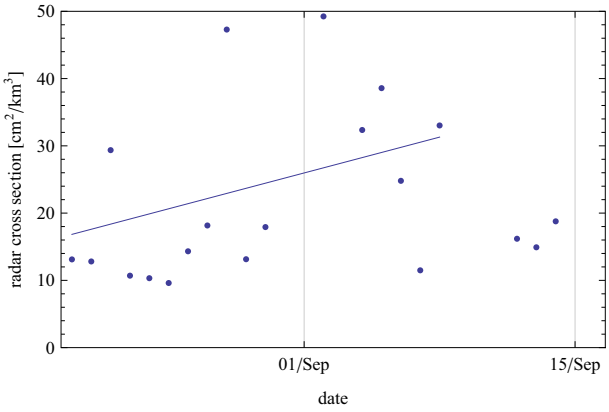

(a) De Bilt

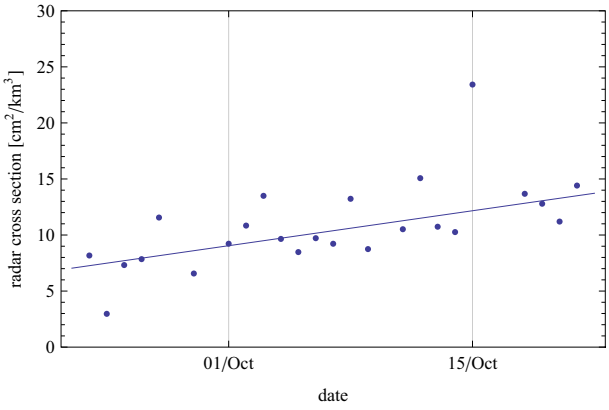

(b) Wideumont

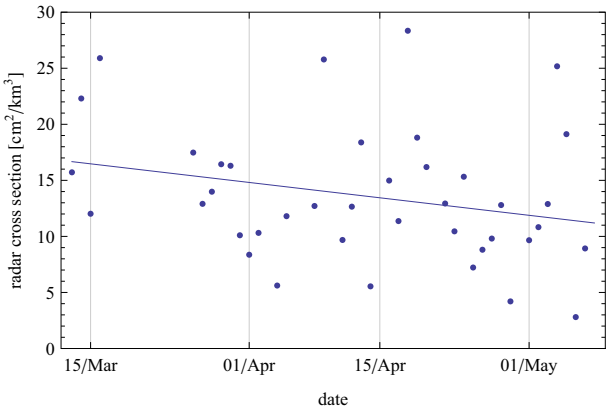

(c) Trappes

Figure 7.15: Seasonal trend in nightly mean bird radar cross section.

7.8 Assessing bird speed and direction

By fitting the radial velocity data to Eq. 7.4 we also find the average ground speed and heading of the observed scatterers.

The ground speed v is calculated by

$$v = \sqrt{u_0^2 + v_0^2} \tag{7.14}$$

and the heading α (clockwise with respect to N) by

$$\alpha = \arctan u_0/v_0 \tag{7.15}$$

where the arc tangent is defined such that it takes into account the quadrant in which the point (u_0,v_0) lies.

The current VVP algorithm may experience problems in quantifying speed and heading of fast flying birds. This only applies to scans with a relatively low unambiguous velocity (see Table 3.6), like the 5 lowest elevation scans of the De Bilt and Den Helder radar. Especially in situation of favorable tail winds the bird ground speed can exceed the unambiguous velocity. As a result the radial speeds may get unfolded in the wrong Nyquist interval. An example of such a case is shown in Fig. 7.16.

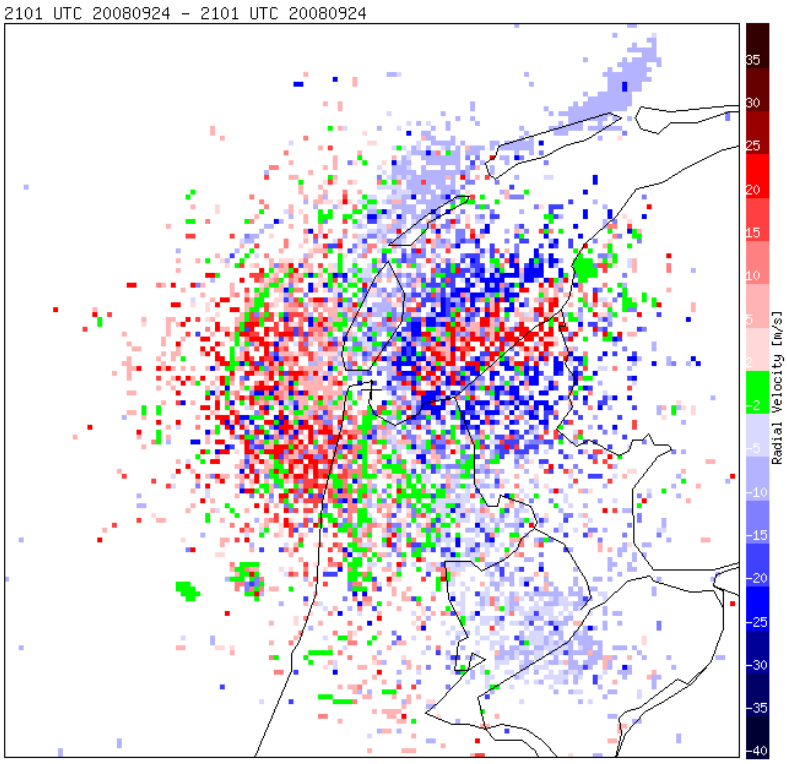

Figure 7.16: PPI of the radial velocity for the Den Helder radar, 24 September 2008, 21:00 UTC. Fast flying birds above the Waddenzee (possibly Waders) cause the radial speeds to be unfolded in the wrong Nyquist interval. This gives an apparent speed of $\approx$ 15 m/s *away from* the radar. The true speed is found by subtracting twice the unambiguous velocity according to 15-2v_m = 15-2$\times$23.9 $\approx$ -33 m/s *towards* the radar.

Chapter 8

Validation and verification

In the previous chapter we outlined a method to identify and reject weather radar echoes from non-bird targets. A reflectivity quantity η_{bird} was formulated (Eq. 7.7) designed to be related to bird echoes only. The quality and validity of η_{bird} for the purpose of bird density estimation is assessed in this section by verification with independent bird density observations of the bird radar reference.

8.1 Wideumont campaign

The campaign in Wideumont, Belgium, took place from 22 September to 21 October 2007, coinciding with the peak period of autumn bird migration. The collected data contain several nights with strong bird migration. For two of such nights (4 and 6 October 2007), the bird densities detected by bird radar and weather radar (as determined by the algorithm described in the previous chapter) are displayed in Fig. 8.1 & 8.2.

These figures show a remarkable correspondence in the detected bird densities by the two sensors. Migration is observed to start around sunset, and during the entire night the height profiles closely match. Both sensors observe a qualitatively different altitude profile for the nights of 3/4 and 5/6 October. On the night of 3/4 October birds are detected only up to 1.5 km height, while on 5/6 October migration extends up to 4 km. Even in detailed features we find a qualitative match between the weather radar and bird radar observations (e.g. the bird density increase around 23 UTC on 5 October 2007 around 800 m height).

We also find differences in the weather radar and bird radar observations. Most notably, a pronounced dusk ascent is observed on 6 October between 5

Responsible Institute: KNMI

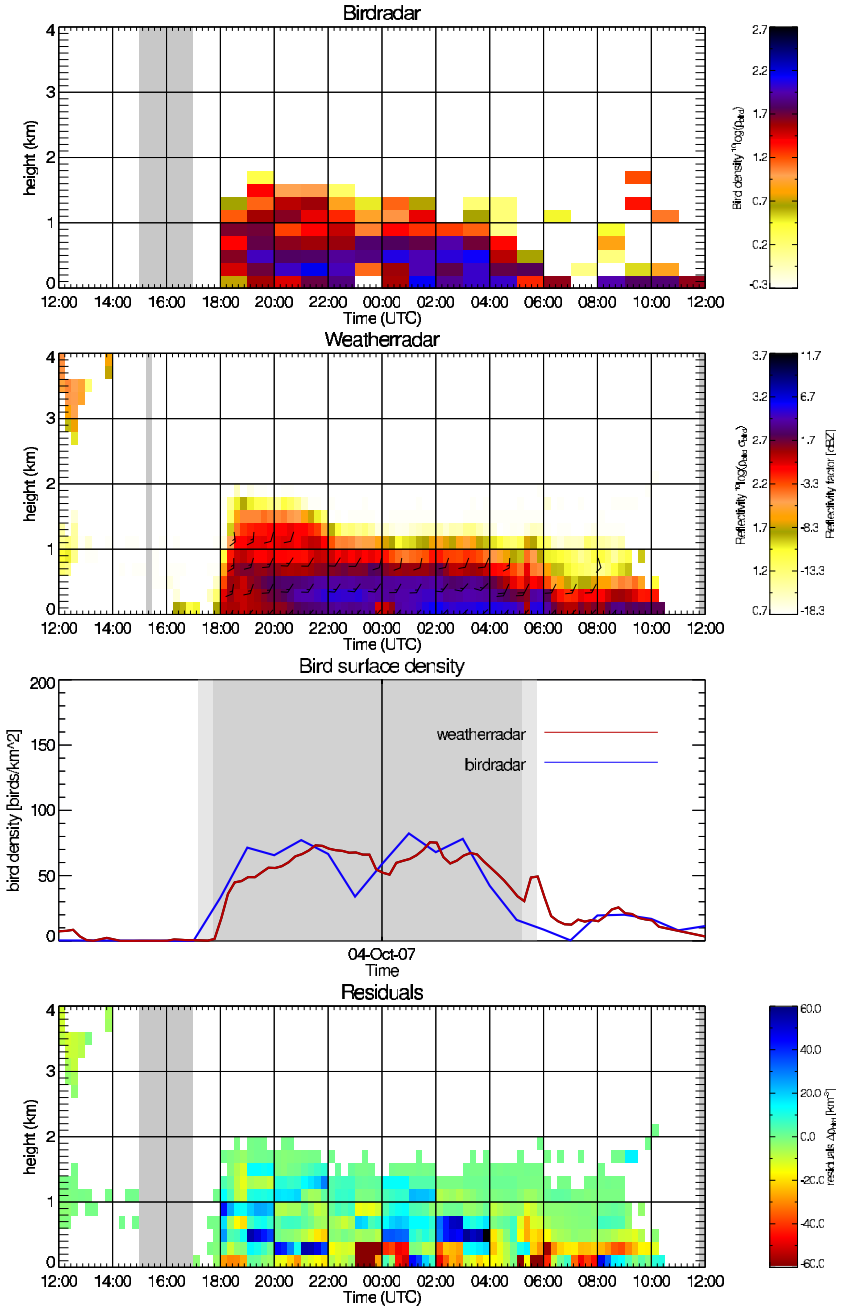

Figure 8.1: Retrieved time-height profiles by bird radar (top) and weather radar (upper middle) in Wideumont for the night of 4 October 2007. The vertically integrated bird densities and weather radar - bird radar density difference are shown as well (lower middle and bottom).

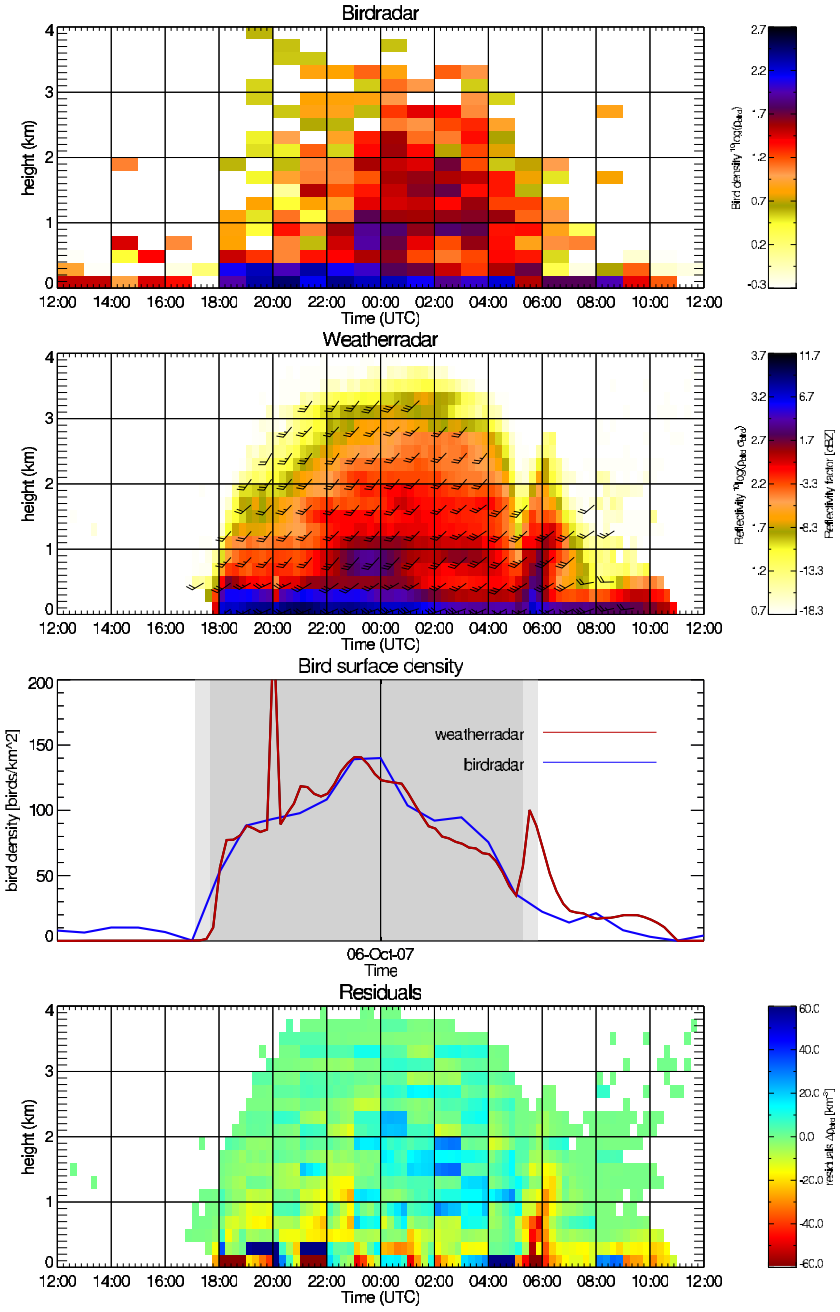

Figure 8.2: Retrieved time-height profiles by bird radar (top) and weather radar (upper middle) in Wideumont for the night of 6 October 2007. The vertically integrated bird densities and weather radar - bird radar density difference are shown as well (lower middle and bottom).

and 6 UTC, which coincides with sunrise and the start of migration of diurnal migrant birds. This ascent is not observed by the bird radar. A close look at the raw data revealed that this mismatch is caused by a measurement artifact of the bird radar. During daytime birds tend to flock, and a single bird echo usually consists of several birds. An echo of a bird flock does not show a clear wing beating pattern, and is therefore rejected as a non-bird by the bird radar detection algorithm. This causes a strong underestimation of the bird density during daytime. The flocking effect makes day-time observations of the bird radar unreliable, and we therefore limit the further analysis to nocturnal migration (for the Wideumont campaign 18.00 - 6.00 UTC).

The rest of this chapter is devoted to a quantitative assessment of the quality of the weather radar bird observations and extensive verification of the weather radar observations against the bird radar reference measurements.

8.1.1 bird detectability

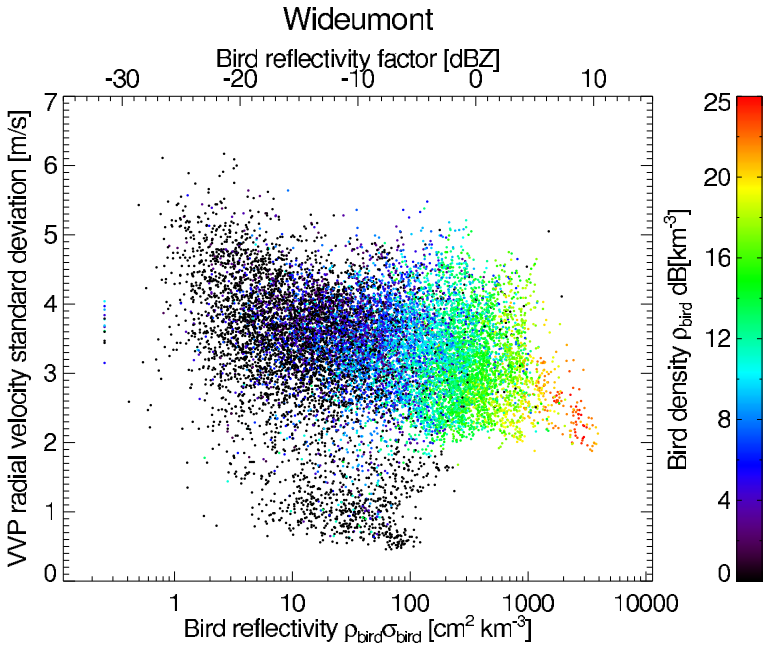

Figure 8.3: Scatter plot of the VVP retrieved radial velocity standard deviation σ_r versus the height layer's average bird reflectivity η_{bird} for the Wideumont field campaign Wideumont, Belgium (22 September - 21 October 2007). The color coding indicates the simultaneous collocated bird density estimate by the bird radar.

The earlier depicted scatter plot of radial velocity standard deviation

versus reflectivity (Fig. 7.10) is replotted using the new reflectivity quantity η_{bird} in Fig. 8.3. The figure shows a clear improvement in the correlation between the reflectivity determined by weather radar and the bird density determined by the bird radar reference. Most notably, Fig. 7.10 showed time-height layers having a high radial velocity standard deviation and a high reflectivity, but lacking a corresponding high bird density. Such time-height layers no longer occur in Fig. 8.3. The previously high reflectivity for these time-height layers resulted from additional hydrometeor scattering in precipitation, which is correctly excluded in the new reflectivity quantity η_{bird}.

The scatter plot in Figure 8.3 can be analyzed quantitatively using so-called performance matrices or contingency tables. Two contingency tables are presented in Table 8.1.1. The contingency table relates bird observations by weather radar (columns) and bird radar (rows). A σ_r threshold of 2 m s^{-1} is used to classify the weather radar time-height layers into "birds" and "no birds". For the bird density data from the bird radar a threshold of 1 km^{-3} is used to determine the presence or absence of birds. WR and BR refers to Weather Radar and Bird Radar, respectively. The four symbols in the left table, H, M, F, and R, refer to the number of Hits, Misses, False alarms, and correct Rejections, respectively. The right contingency table lists the actual numbers for the 14742 weather radar time-height layer observations for the field campaign in Wideumont.

WR Birds	WR No Birds
H	M
F	R

	WR Birds	WR No Birds
BR Birds	8780	159
BR No Birds	4141	1662

Table 8.1: Contingency table for the quality controlled weather radar bird observations against the bird radar observations. "BR" refers to Bird Radar and "WR" refers to Weather Radar. A standard deviation threshold of $\sigma_r = 2.0$ m s^{-1} and a bird density threshold of 1.0 km^{-3} have been applied.

Various statistical scores can be derived from a contingency table (Wilks, 1995). The Probability Of Detection (POD), False Alarm Ratio (FAR), and Fraction Correct (FC), are calculated as follows :

$$\text{POD} \equiv \frac{H}{H+M} = 0.98 \tag{8.1}$$

$$\text{FAR} \equiv \frac{F}{H+F} = 0.32 \tag{8.2}$$

$$\text{FC} \equiv \frac{H+R}{H+F+M+R} = 0.83 \tag{8.3}$$

using the symbols and numbers in Table 8.1.1.

Using a radial velocity standard deviation threshold of $\sigma_r = 2.0$ m s^{-1}, 83 % of the weather radar bird observations are classified correctly (FC). POD reflects the fraction of bird observations that are accepted correctly and FAR reflects the fraction of false positive bird detections. While the detection probability is close to 100 %, the number of false positive detections is relatively high at 32 %. For the current bird detection system, reducing the number of incorrect bird observation is therefore much more crucial than improving the detection sensitivity. To what extent the false positive detections are problematic also strongly depends on what regime of bird densities is sensitive to false detection. As will be discussed below, in fact most false alarms occur in the regime of low bird density, which is of little interest to most users.

Naturally the standard deviation threshold in σ_r can be changed and contingency tables can be compiled for each threshold value. Figure 8.4(a) shows the derived statistical scores as a function of the radial velocity standard deviation threshold. It is evident that the number of false alarms is reduced when the threshold is changed from 0 m s^{-1} upward, which is due to an increasingly better rejection of low σ_r non-bird echoes. If the standard deviation threshold in σ_r is increased above 2 m s^{-1} the detection probability starts to decrease steeply, as an increasing number of bird observations gets rejected as well. A default threshold of 2 m s^{-1} is proposed in Figure 8.4(a) by the vertical dashed line, which minimizes the false positive detections while attaining a high detection probability of 98 %.

The absence of birds at low σ_r is further illustrated in Fig. 8.5(a). This figure shows the distribution in radial velocity standard deviation for all time-height layers (black) and the subset of these layers for which there are simultaneous bird observations by the bird-radar (grey). The first distribution shows two peaks, one around $\sigma_\mathrm{r} = 1$ m s^{-1} and one around $\sigma_\mathrm{r} = 3.5$ m s^{-1}. The low standard deviation peak results from non-bird echoes moving with the wind field (both precipitation and clear-air/insects) as for most of these height layers a simultaneous bird observation by the bird radar is lacking. Nearly all bird radar observations are for layers that make up the high standard deviation peak.

Fig. 8.5(a) also shows that a significant fraction of height layers with a high radial velocity standard deviation ($\sigma_\mathrm{r} > 2$ m s^{-1}), does not have a corresponding bird observation by the bird radar. This causes the high False Alarm Ratio of 32% in Eq. 8.1. The mismatch between bird radar and weather radar is caused either by false detections of the weather radar, or by missed detections by the bird radar reference. Significant misdetections by the bird radar can only occur in the regime of very low bird densities,

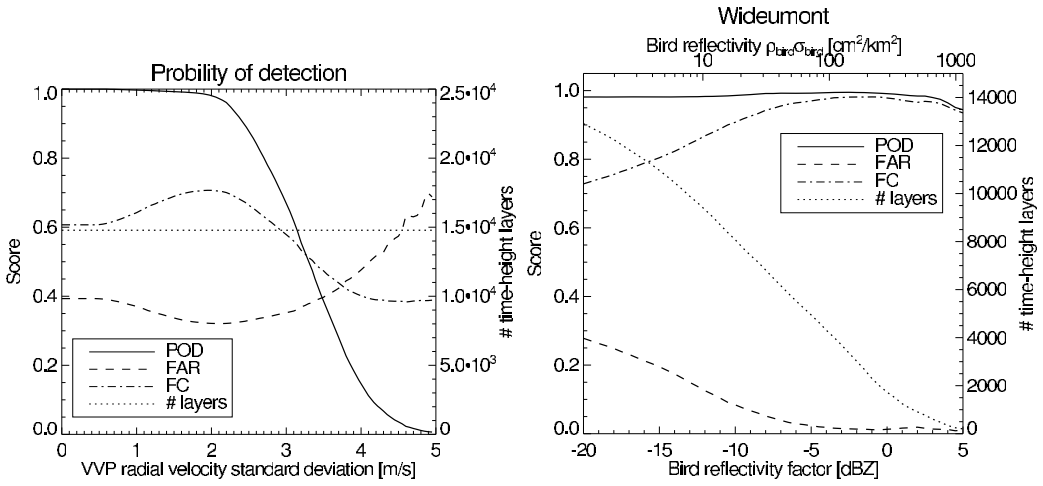

(a) (b)

Figure 8.4: Left (a): Probability of detection (POD, solid) and False Alarm Rate (FAR, dash) as a function of VVP radial velocity standard deviation threshold. Right (b): Probability of detection (POD, solid), False Alarm Rate (FAR, dash) and Fraction Correct (FC, dash-dot) as a function of reflectivity threshold. Data taken by the Wideumont radar, Belgium from 18 September - 22 October 2007.

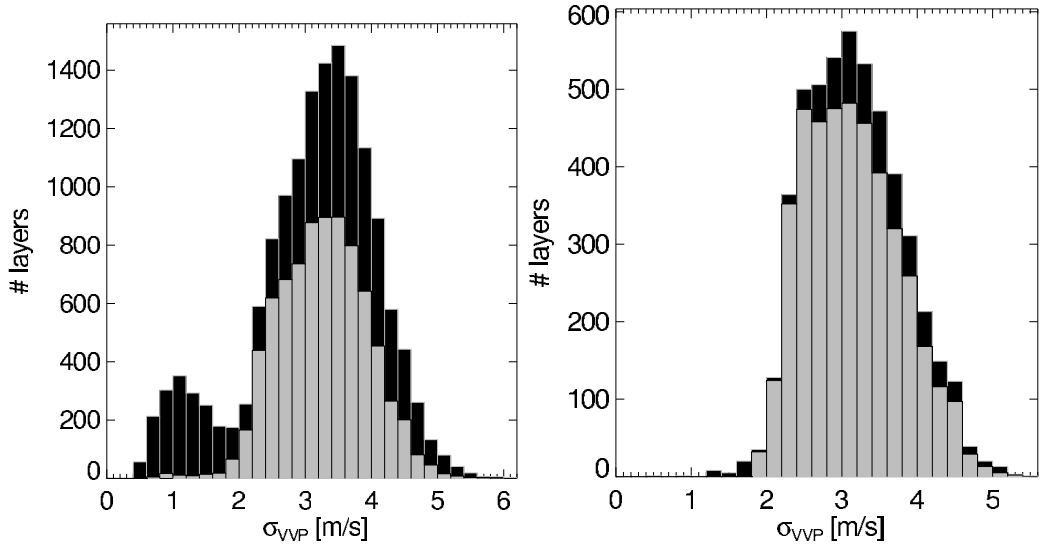

(a) all layers (b) $Z_{\mathrm{bird}} > -5$ dBZ only

Figure 8.5: Distribution of VVP retrieved radial velocities in Wideumont. In grey the subset of height-layers is shown for which birds were detected simultaneously by the bird radar reference.

when it suffers from statistical noise due to low bird count. Because of the wider coverage by weather radar, the probability of detection in the low bird density regime might be higher for weather radar.

Since for both radars bird detection is expected to improves at higher bird densities, we investigate how the detectability depends on the observed bird reflectivity. Contingency tables are compiled for a series of data subsets, each containing only those time-height layers for which the bird reflectivity is higher than the threshold $\tilde{\eta}_{bird}$. The scores of Eq. 8.1 are plotted in Fig. 8.4(b) as a function of this reflectivity threshold, where we have fixed the radial velocity standard deviation threshold to $\sigma_{\mathrm{r}} = 2$ m s^{-1}. Also the size of the data subset in number of time-height layers is shown. The figure shows that by limiting the analysis to observations with higher bird reflectivity, the False Alarm Ratio drops spectacularly from 32 % to 2 % only for $\tilde{\eta}_{bird} > -5$ dBZ. False positive bird observations by weather radar nearly all occur in the low bird reflectivity regime. We may redraw Fig. 8.5(a) for the data subset of $\tilde{\eta}_{bird} > -5$ dBZ in Fig. 8.5(b), showing that at higher bird reflectivities nearly all height layers with high radial velocity standard deviation also contain bird observations by the bird radar.

So far we have limited our analysis to assessing the detectability of birds

by weather radar. In the next paragraph we investigate the correlation between bird reflectivity and bird density as determined by the bird radar reference. The degree of correlation is important for the accuracy by which we can produce bird density estimates by weather radar.

8.1.2 Accuracy weather radar bird densities

Fig. 8.3 already showed qualitatively that the (bird) reflectivity measured by weather radar is correlated to bird density. This important result demonstrates that weather radar can deliver height-specific information on bird densities using reflectivity measurements. In this section we quantify the correlation between bird reflectivity and bird density and compare with the theoretically predicted correlation (Eq. 2.11).

Fig. 8.6 correlates the weather radar bird reflectivity to the bird density determined by bird radar, both on a basis of height layers (a) and vertically integrated profiles (b). For comparison theoretical correlation curves have been plotted assuming average bird cross sections of 5,10 and 20 cm^2 (see Eq. 2.11). Fitting the data to Eq. 2.11 with σ_{bird} as the only fit parameter gives us σ_{bird} =12±14 cm^2 (median and median deviation 8.8±4.1 cm^2) and correlation coefficient of 0.74. The corresponding cross section distribution is shown in Fig. 7.11

The correlation is relatively worse in the low bird reflectivity regime ($Z_{\text{bird}} > -5$ dBZ) than in the high bird reflectivity regime. Although the standard deviation $\mu_{\rho_{\text{bird}}}$ in bird densities increases with η_{bird} roughly from 20 to 50 birds/km^3 (see Fig. 8.25), the coefficient of variation ($\rho_{\text{bird}}/\mu_{\rho_{\text{bird}}}$ drops from 1 to 0.3.

We choose to convert bird reflectivity to bird density by Eq. 2.11, assuming σ_{bird} =10 cm^2 (i.e. the median of the cross section distribution for the high bird reflectivity regime ($Z_{\text{bird}} > 5$ dBZ)). Limiting to the high bird reflectivity regime we find that the weather radar bird density estimate is correct within a factor 1.5 for 52% of the time-height layers, within a factor of 2 for 74% and within a factor of 3 for 87% of the time-height layers ("correct within a factor i" we define as the weather radar bird density equals the bird radar bird density by a multiplicative factor of $i^{\pm 1}$). The residual bird density equals 14 ± 20 birds/km^3. The residual height-integrated bird density equals 11 ± 18 birds/km^2 (based on events where the bird radar height-integrated exceeded 1 bird/km^2 only).

To test for any height dependencies correlation plots are shown in Fig. 8.7, where we have split the height-layer observations into different height categories (0-500 m, 500-1500 m, 1500-2500 m and 2500-4000 m). At higher altitudes we typically find lower reflectivities and bird densities, which is a

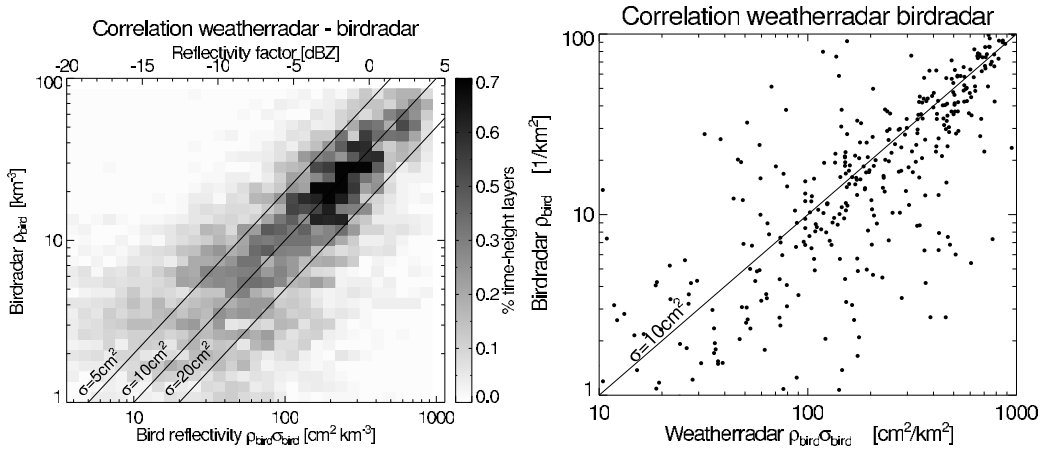

Figure 8.6: Left (a): Correlation between bird densities determined by bird radar and reflectivity measured by weather radar. Right (b): Correlation between the vertically integrated bird surface density determined by bird radar and vertically integrated reflectivity measured by weather radar

simple reflection of the typical height distribution of migrating birds during autumn (see Fig. 7.13). Bird concentrations are typically much higher at low altitudes than at high altitudes. Interestingly we see that at higher altitudes the observed reflectivity shifts to values that are more consistent with lower bird cross sections. Since in ornithological research on passerine migration a clear relation between bird size and flight altitude has never been found, the cross section change with altitude is most likely a measurement artifact. In Section 7.6 we discussed that we observe a net decrease in bird radar cross section with range. Since higher altitudes are typically measured at longer range, this range dependent cross section is likely responsible.

In Fig. 8.8 and Fig. 7.13 the distribution in height layers is shown. The weather radar detects birds in a higher number of layers than the bird radar reference, however most of these false positive detections occur in the low bird reflectivity regime. At least part of the false positive detections are explained by missed detections of the bird radar. As an example, in Fig. 8.2 the bird radar sometimes detects no birds (especially at higher altitudes and low bird densities), whereas the weather radar shows a very smooth variation in bird density which seems more realistic. Especially at high altitude and low bird densities the bird radar density estimates are based on a very low number of observed echoes, and the estimate becomes less reliable.

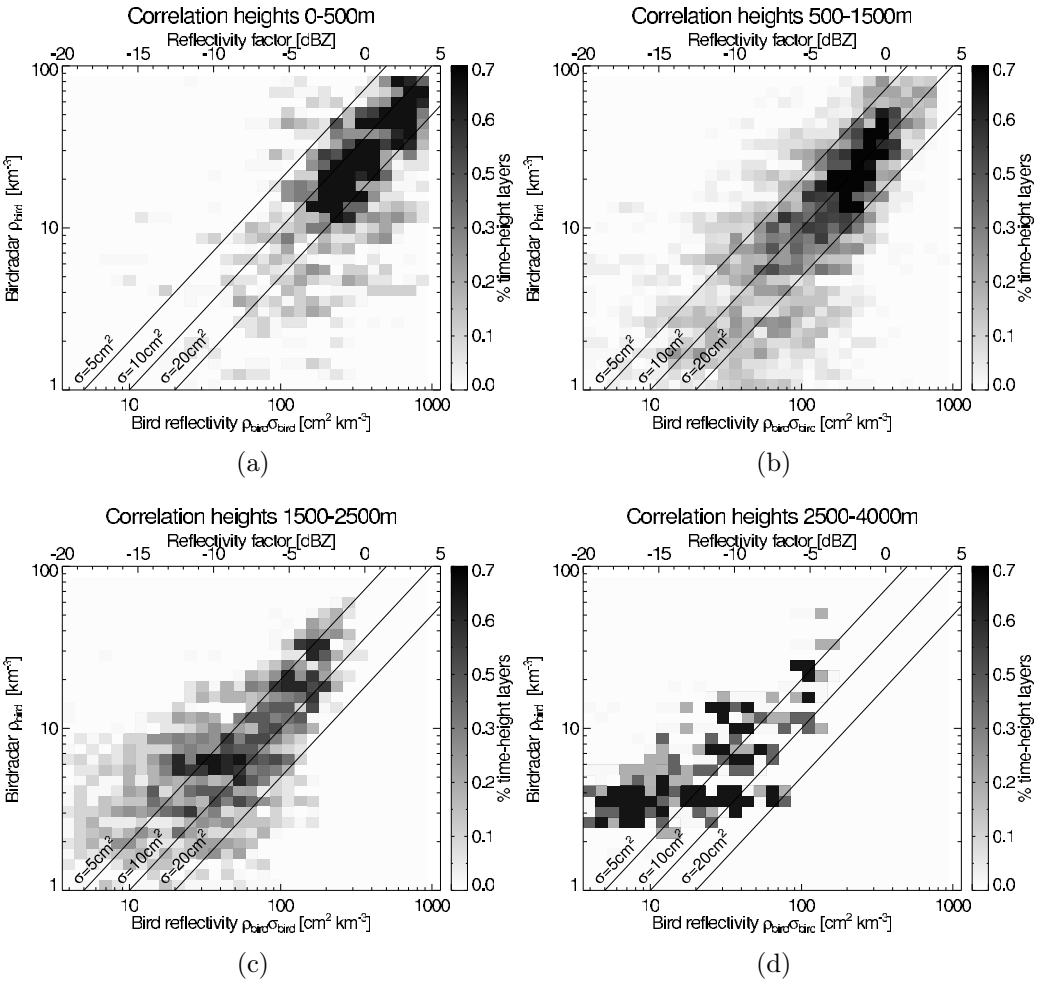

Figure 8.7: Correlation between the bird density determined by bird radar and vertically integrated reflectivity measured by weather radar in Wideumont for height layers between (a) 0-500 m, (b) 500-1500 m, (c) 1500-2500 m and (d) 2500-4000 m.

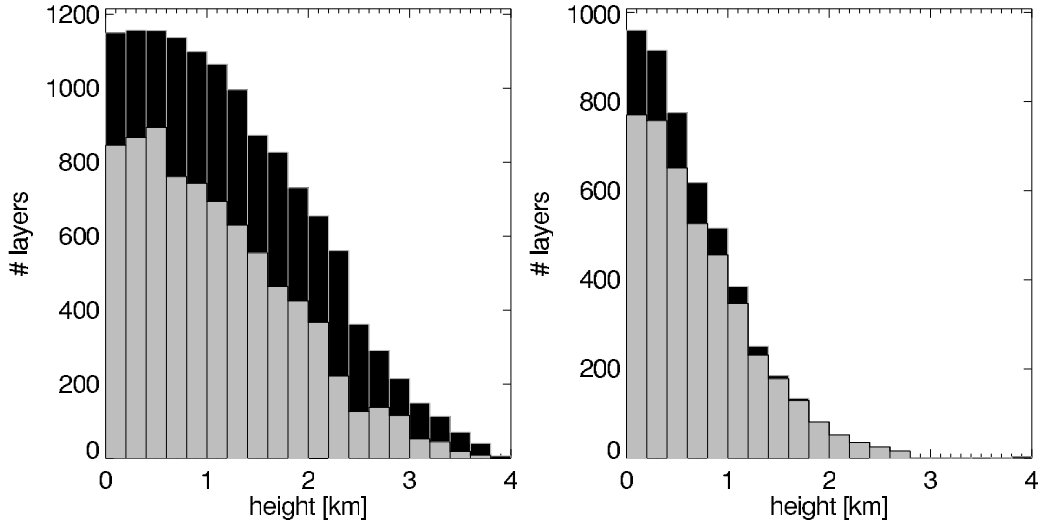

(a) all layers (b) $Z_{\text{bird}} > -5$ dBZ only

Figure 8.8: Number of detected time-height layers per altitude layer for the Wideumont campaign. In grey the subset of height-layers is shown for which birds were detected simultaneously by the bird radar. reference.

8.1.3 Bird ground speed and direction

We use the bird radar tracking data (see Sec. 6.1.2) to validate the VVP-retrieved bird ground speeds for weather radar (see Sec. 7.8). Both track data and weather radar speeds and directions were averaged into six-hourly means (18-00 UTC and 00-06 UTC) for three height categories (0-1000, 1000-2000 and 2000-3000 m).

We find good correspondence between bird radar in weather radar for both bird ground speed and direction (Fig. 8.9). A small bias of -2 to -3 m/s is observed in the weather radar ground speeds, which decreases when the ground speed increases (see Fig. 8.10). Directions for the lowest height category (0-1000 m) are biased by a few degrees towards the south. We find an average speed residual of 2 ± 1 m/s and an average direction residual of $8\pm8°$.

Both air-borne scatterers like insect and clutter contamination can bias extracted ground speeds and directions. Mixing in of clutter will bias the extracted ground speed towards zero, while insect scattering will bias the ground speed vector towards the wind speed (which is directed predominantly to the south-west). Clutter contamination is better excluded by time-domain Doppler clutter filtering (see Sec. 7.2.1) when bird ground speeds are large, since then the Doppler frequency separation between clutter (radial velocity zero) and bird scattering is larger. This may explain a decrease in the velocity bias with bird ground speed. The fact that we observe a slight bias towards southern directions suggests also insect scattering is important, since this points to a bias towards the predominant south-westerly wind direction.

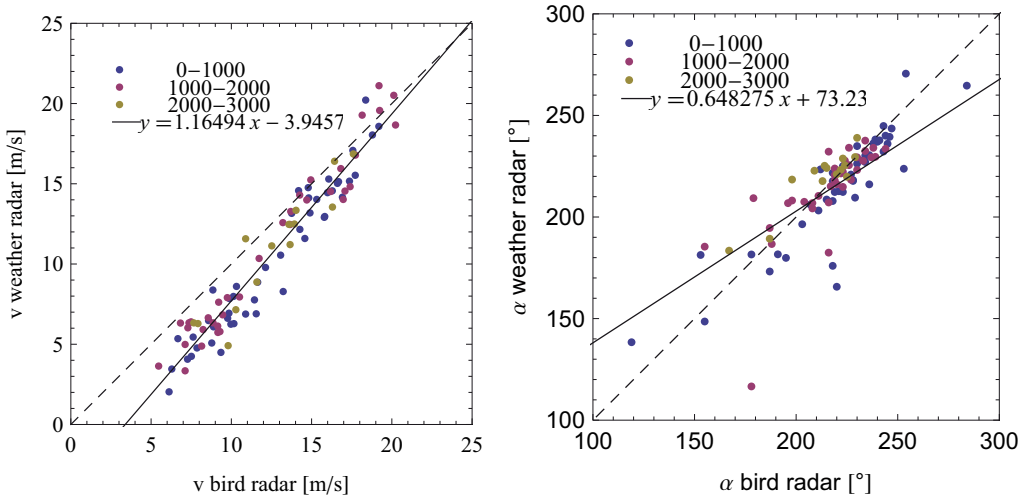

(a) speed (b) direction

Figure 8.9: Correlation bird ground speed and direction as determined by weather radar and bird radar. Data points are colored according different altitude intervals (0-1000,1000-2000 and 2000-3000 m). The dashed line is the curve for full correlation, the solid line a best linear least-squares fit.

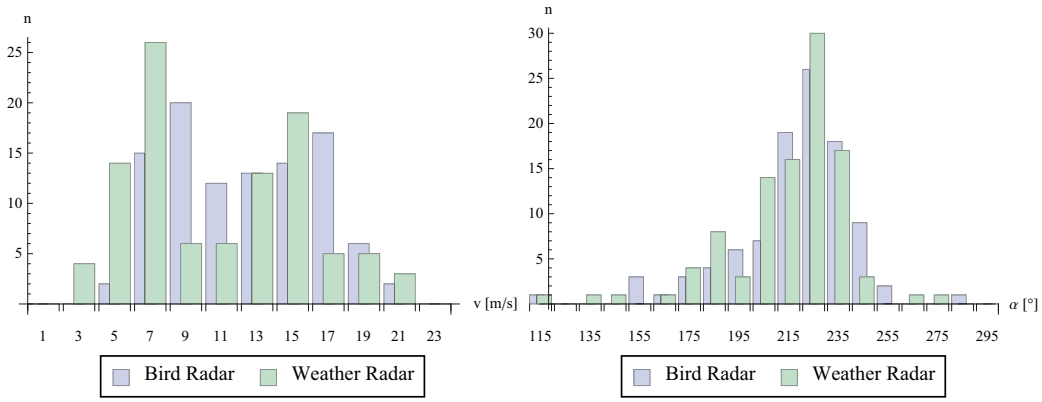

(a) speed (m/s) (b) direction (°)

Figure 8.10: Distribution of bird ground speed and direction as determined by weather radar and bird radar.

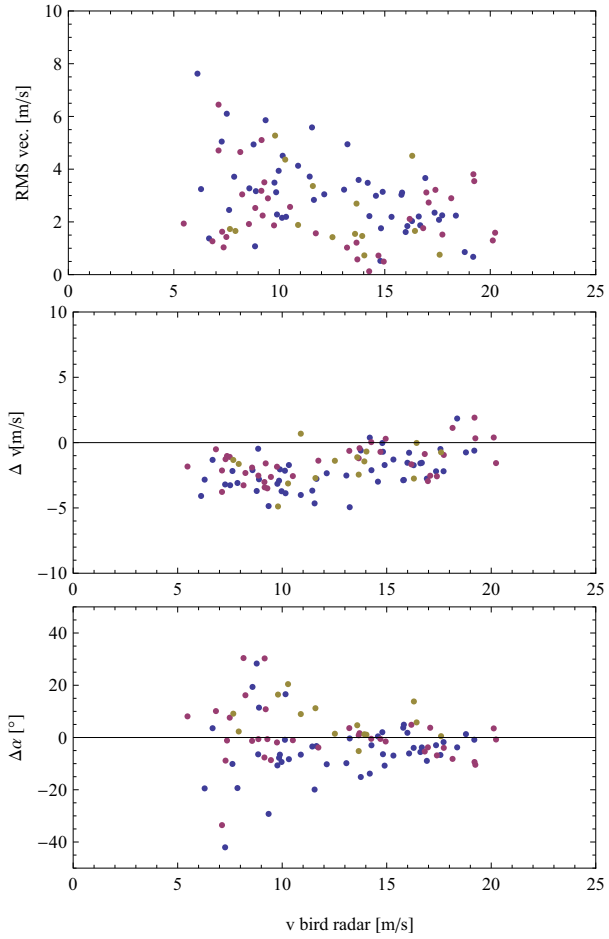

Figure 8.11: Average root-mean-square (RMS) ground speed vector difference (top), ground speed difference (middle) and directional difference (bottom) between bird radar and weather radar as a function of bird ground speed. Data points are colored according different altitude intervals as in Fig. 8.9.

8.2 De Bilt campaign

The campaign in De Bilt, The Netherlands, lasted from 20 August to 16 September 2007. The number of migrant birds in early autumn is considerably lower than in late autumn. Early migrating species are typically smaller passerines, while in late autumn larger species (mostly Thrushes) dominate. Compared to the Wideumont campaign, the De Bilt campaign contains a high fraction of observations in the low bird reflectivity regime, because both the bird densities and cross sections are lower. A further complication in early autumn is a relatively high abundance of insects. The data will be analyzed analogous to the Wideumont data.

Fig. 8.12 shows the extracted bird density height profile for one of the stronger migration nights during the De Bilt campaign. Typically no data is available for the lowest height layer as a result of strong ground clutter. After the campaign a problem with the ground clutter Doppler filtering was identified and resolved. The problem was software related and introduced by a software update a few months earlier. Ground clutter during the De Bilt campaign is therefore higher than normal (which imposes additional challenges for the algorithm), and the semi-operational bird detection currently running at KNMI does have data available for the lowest height layer. Fig. 8.12 shows qualitative correspondence between the extracted bird densities by weather radar and bird radar, however bird densities are overestimated at the lowest height layers. This may be either due to mixed in clutter reflectivity or possibly due to insect echoes, which were frequently detected during the De Bilt campaign.

Another example is shown in Fig. 8.13 for weak migration mid September. Migration is restricted to the lowest 600 m. The high time resolution of the De Bilt radar (5 min.) resolves the end of nocturnal migration around 5 UTC migration and the subsequent start of diurnal migration. Like in Wideumont, diurnal migration is poorly detected by the bird radar because of difficulties detecting bird flocks. For this reason only nighttime migration is studied (for this campaign 19.00 - 5.00 UTC).

8.2.1 bird detectability

Scatter plots of radial velocity standard deviation versus reflectivity (Fig. 7.10) are shown in Fig. 8.14. A derived contingency table is shown in Table 8.2.1 (using thresholds σ_r=2 m s^{-1} and ρ_{bird}=1 km^{-3}). Using these figures we find for the Probability Of Detection POD=0.94, False Alarm Ratio FAR=0.67 and Fraction Correct FC=0.64.

The variation of these scores with the applied radial velocity threshold σ_r

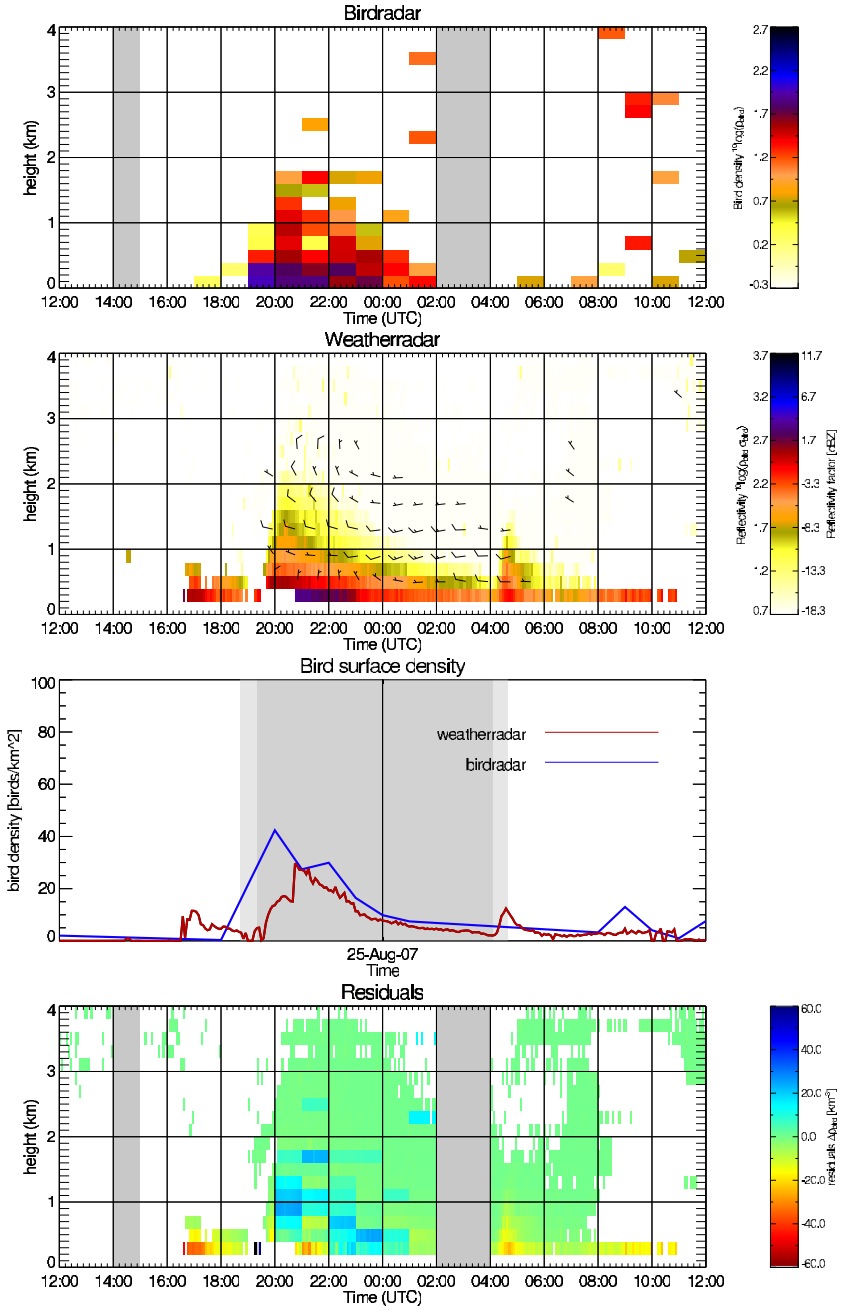

Figure 8.12: Retrieved time-height profiles by bird radar (top) and weather radar (upper middle) in De Bilt for the night of 25 August 2007. The vertically integrated bird densities and weather radar - bird radar difference are shown as well (lower middle and bottom).

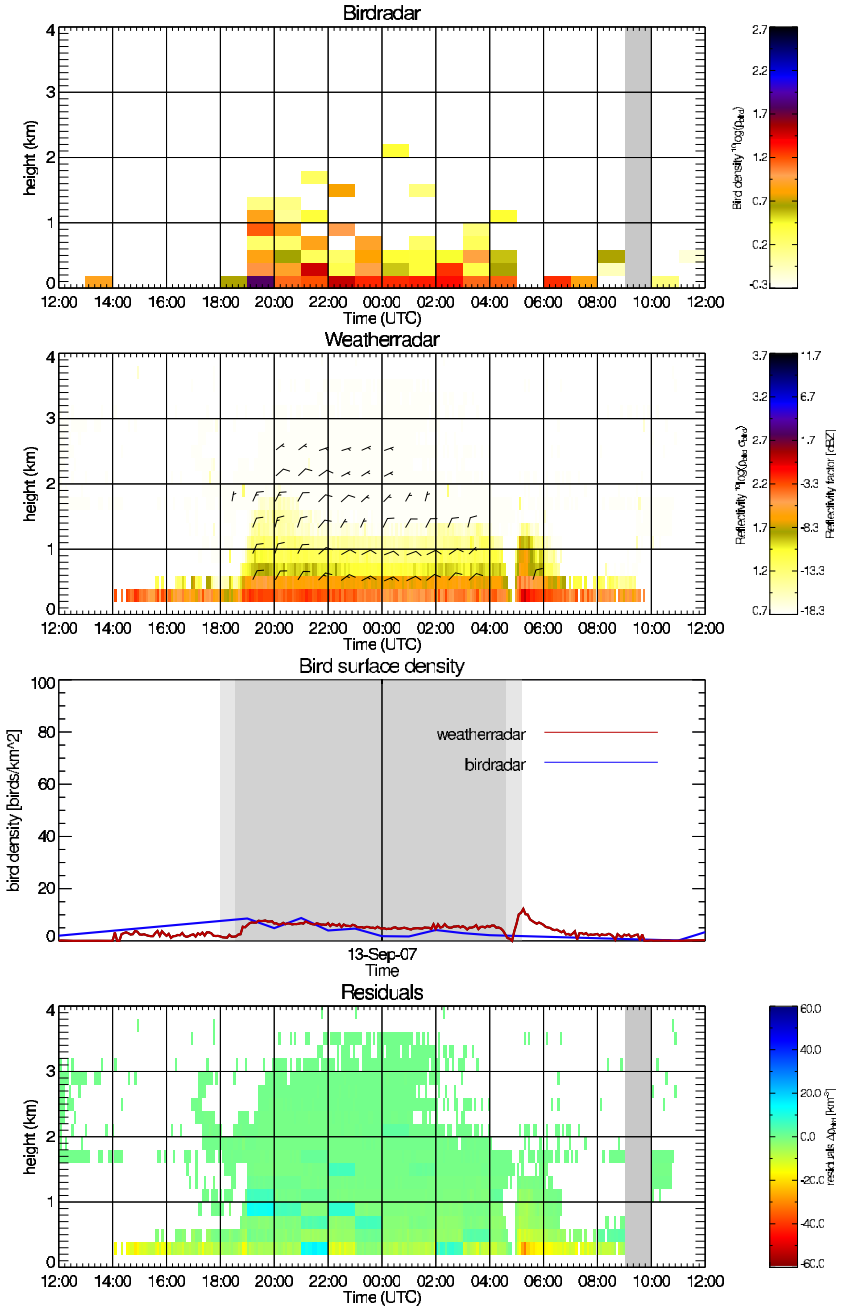

Figure 8.13: Retrieved time-height profiles by bird radar (top) and weather radar (upper middle) in De Bilt for the night of 13 September 2007. The vertically integrated bird densities and weather radar - bird radar difference are shown as well (lower middle and bottom).

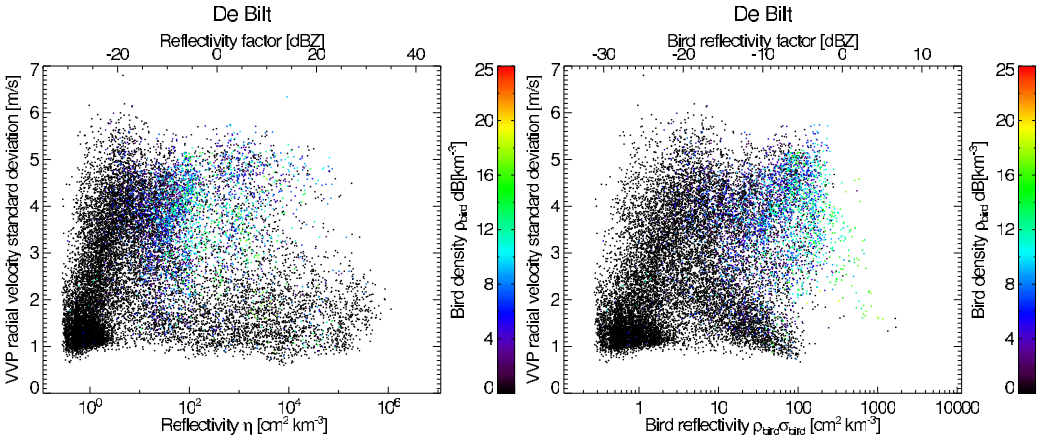

(a) (b)

Figure 8.14: Scatter plots of the VVP retrieved radial velocity standard deviation σ_{r} versus the height layer's average full reflectivity η_{full} (left) and bird reflectivity η_{bird} (right) for the De Bilt campaign. The color coding indicates the simultaneous collocated bird density estimate by the bird radar.

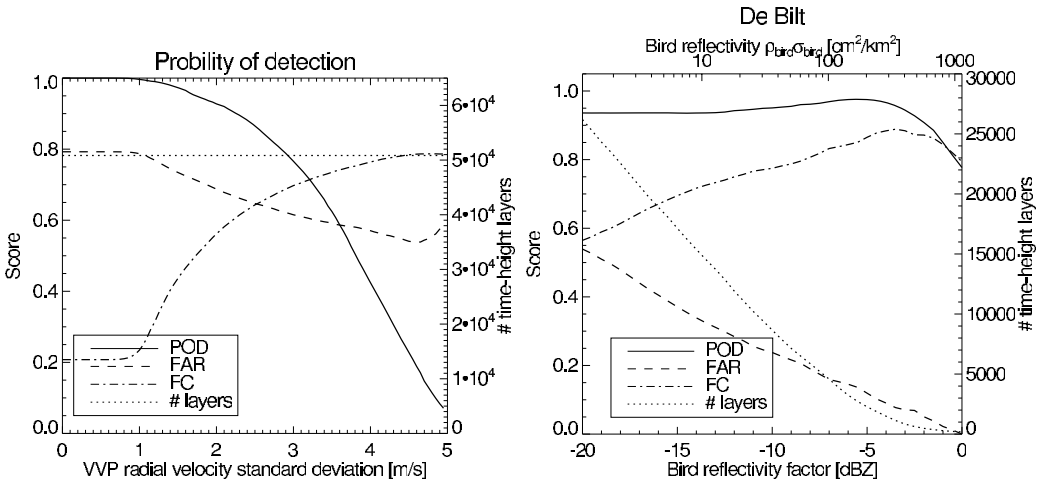

(a) (b)

Figure 8.15: Left (a): Probability of detection (POD, solid) and False Alarm Rate (FAR, dash) as a function of VVP radial velocity standard deviation threshold. Right (b): Probability of detection (POD, solid), False Alarm Rate (FAR, dash) and Fraction Correct (FC, dash-dot) as a function of reflectivity threshold. Data taken by the De Bilt radar, Netherlands from 19 August - 16 September 2007.

is shown in Fig. 8.15(a). Like in Wideumont, a threshold σ_r=2 m s^{-1} is a good compromise between lowering the False Alarm Ratio and attaining a high Probability of Detection. Unfortunately, the Fraction of Correct detections (FC) is only moderately improved by the rejection of low σ_r height layers.

WR Birds	WR No Birds
H	M
F	R

	WR Birds	WR No Birds
BR Birds	10034	650
BR No Birds	20202	27690

Table 8.2: Contingency table for the quality controlled weather radar bird observations against the bird radar observations. "BR" refers to Bird Radar and "WR" refers to Weather Radar. A standard deviation threshold of σ_r = 2.0 m s^{-1} and a bird density threshold of 1.0 km^{-3} have been applied.

As was observed during the Wideumont campaign, height layers with radial velocity standard deviation $\sigma_r < 2$ m s^{-1} have a very low probability of containing birds, as is evident from both Fig 8.14 and the radial velocity distributions shown in 8.16. Unfortunately, the number of height layers with $\sigma_r > 2$ m s^{-1} *not* containing birds is higher than during the Wideumont campaign, the False Alarm Ratio reaching 67 %.

Again most false positive detections occur in the regime of low bird reflectivity, as illustrated in Fig 8.15(b). For the selection of height layers with a bird reflectivity > -5 dBZ, the FAR drops to 8 % and the fraction of correct detections increases to 90 %.

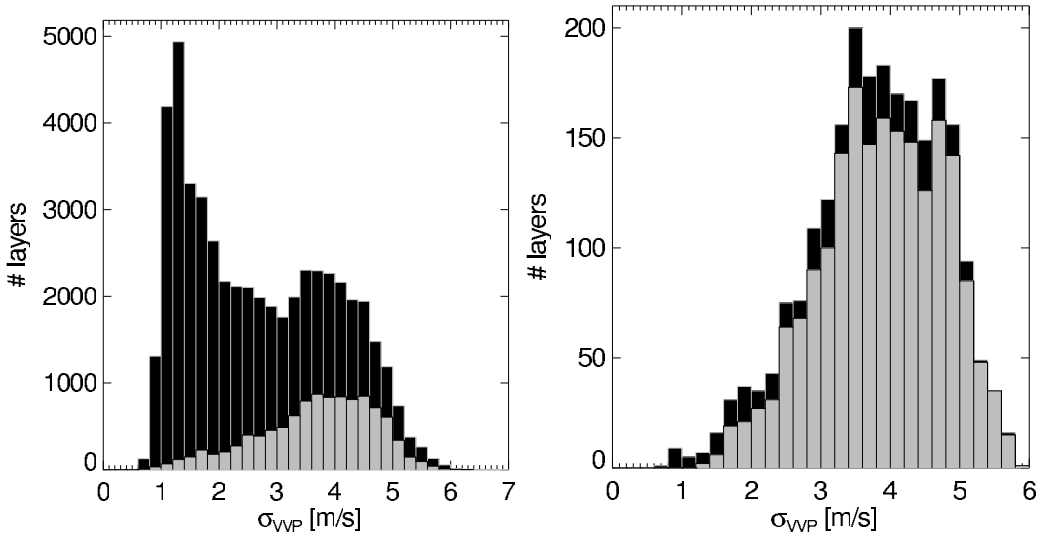

(a) all layers (b) $Z_{\text{bird}} > -5$ dBZ only

Figure 8.16: VVP radial velocity distributions De Bilt. In grey the subset of height-layers is shown for which birds were detected simultaneously by the bird radar reference.

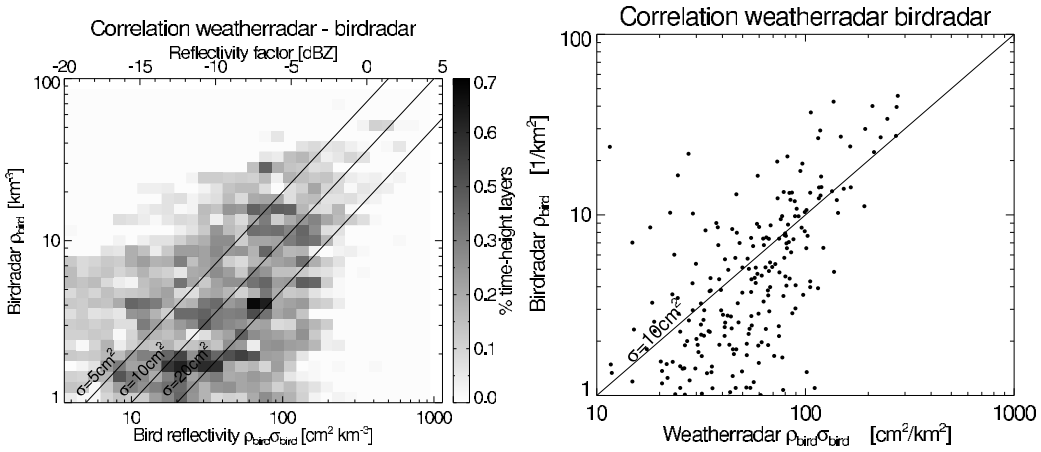

(a) (b)

Figure 8.17: Left (a): Correlation between bird densities determined by bird radar and reflectivity measured by weather radar. Right (b): Correlation between the vertically integrated bird surface density determined by bird radar and vertically integrated reflectivity measured by weather radar. The lowest height layer (0-200m) was excluded from analysis.

8.2.2 Accuracy weather radar bird densities

Fig. 8.17 correlates the weather radar bird reflectivity to the bird density determined by bird radar, both on a basis of height layers (a) and vertically integrated profiles (b). Most points are scattered in the low bird density regime, where the correlation between bird density and reflectivity worse. Fitting the data to Eq. 2.11 with σ_{bird} as the only fit parameter gives us a mean σ_{bird} =15±22 cm^2 (median and median deviation 8±6 cm^2) and a correlation coefficient of 0.38.

The cross section distribution determined for this campaign is shown in Fig. 8.19. Compared to the cross sections determined for the Wideumont campaign (Fig. 7.11) there tend to be more time-height layers with a low radar cross sections. This may be due to the fact that early autumn typically smaller bird species are migrating (however due to the clutter filtering problems and low bird densities in De Bilt quantitative statements on the bird cross sections are difficult). The average bird cross section during the campaign turns out comparable to Wideumont.

We convert bird reflectivity to bird density by Eq. 2.11, assuming σ_{bird} =10 cm^2. Limiting to the high bird reflectivity regime we find that the weather radar bird density estimate is correct within a factor 1.5 for 26% of the time-height layers, within a factor of 2 for 44% and within a factor of 3 for 59% of the time-height layers ("correct within a factor i" we define as the weather radar bird density equals the bird radar bird density by a multiplicative factor of $i^{\pm 1}$). The residual bird density equals 12 ± 15 birds/km^3. The residual height-integrated bird density equals 4 ± 6 birds/km^2 (based on events where the bird radar height-integrated exceeded 1 bird/km^2 only).

Migration during the De Bilt campaign took place primarily at low altitudes. Fig. 8.21 shows the average altitude distribution of birds during the campaign, determined by bird radar and weather radar. Altitude layers with high bird reflectivity ($Z_{\text{bird}} > -5$ dBZ) are nearly exclusively found in the lowest 500 m (see Fig. 8.20). The bird density in De Bilt is mostly overestimated by weather radar at the lowest altitudes (0-500 m). At these heights the bird reflectivity turns out high irrespective of the bird density, as shown in Fig.8.18 (a). At these altitudes clutter contamination often dominates over the bird signal, primarily due to the clutter filtering problem discussed earlier. We cannot exclude that also a high number insect echoes contributes to bird density overestimation in the lowest layers.

Like in Wideumont at high altitudes the reflectivities (cross sections) turn out lower.

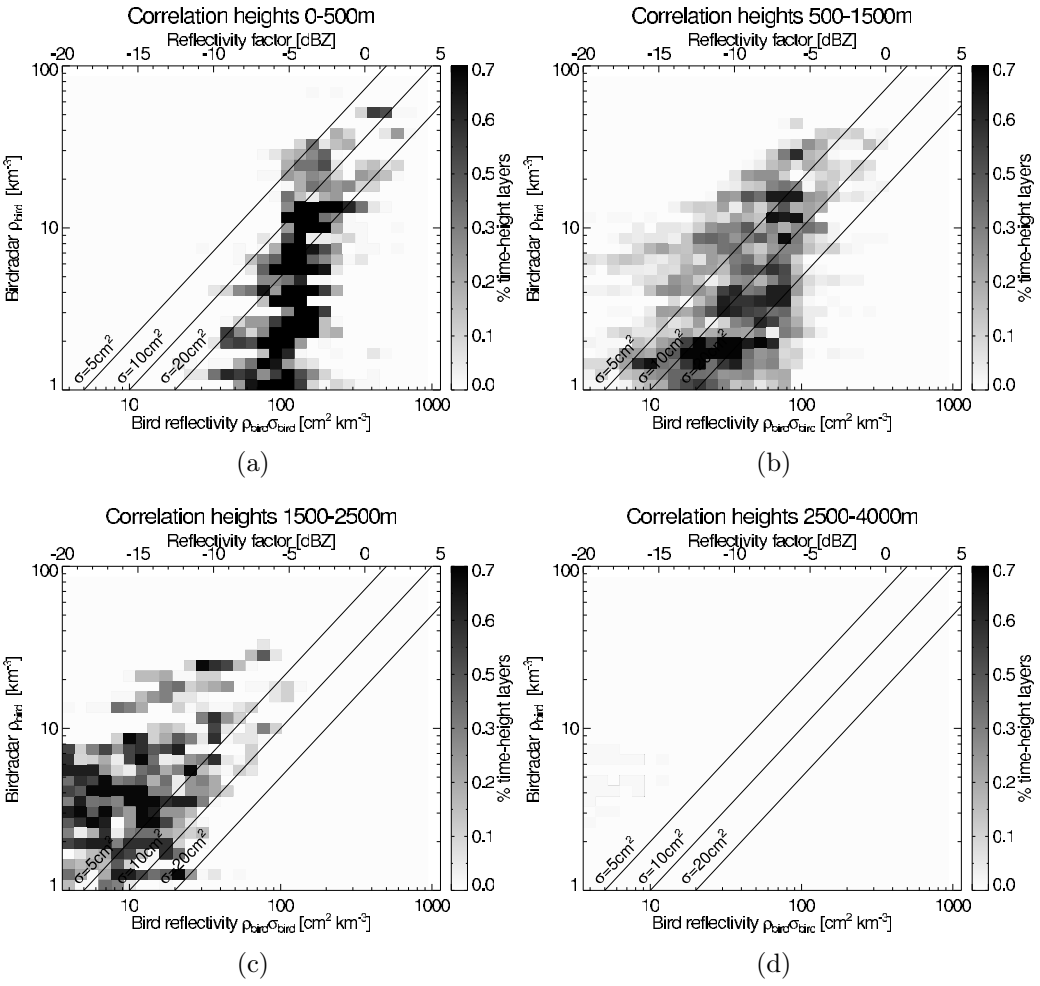

Figure 8.18: Correlation between the bird density determined by bird radar and reflectivity measured by weather radar in De Bilt for height layers between (a) 0-500 m, (b) 500-1500 m, (c) 1500-2500 m and (d) 2500-4000 m. The lowest height layer (0-200m) was excluded.

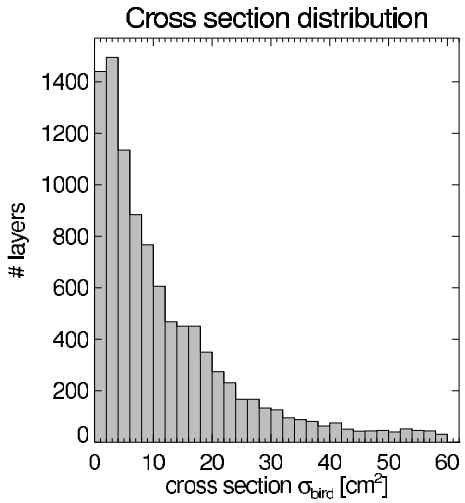

Figure 8.19: Distribution bird cross sections determined for the De Bilt campaign.

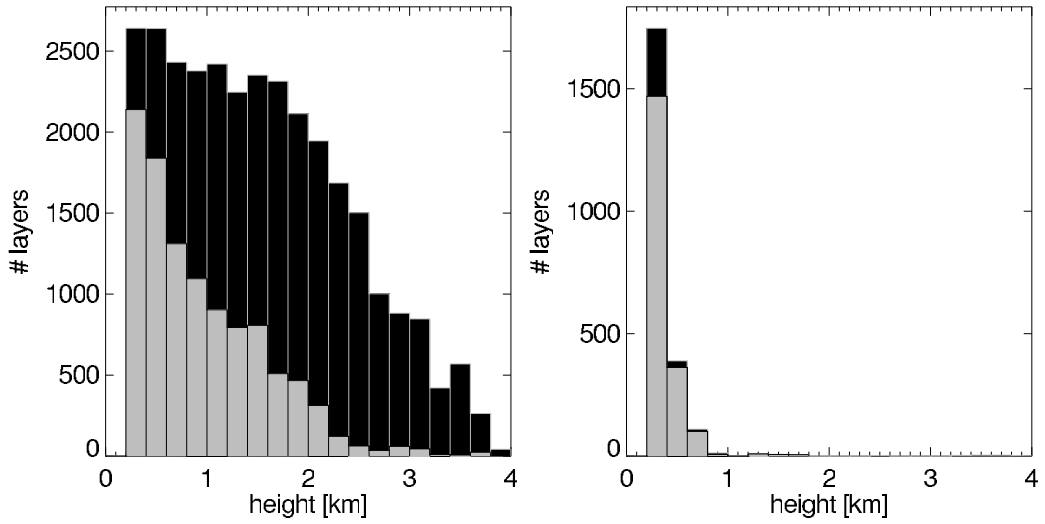

(a) all layers (b) $Z_{\text{bird}} > -5$ dBZ only

Figure 8.20: Number of detected time-height layers per altitude layer for the De Bilt campaign. In grey the subset of height-layers is shown for which birds were detected simultaneously by the bird radar. reference.

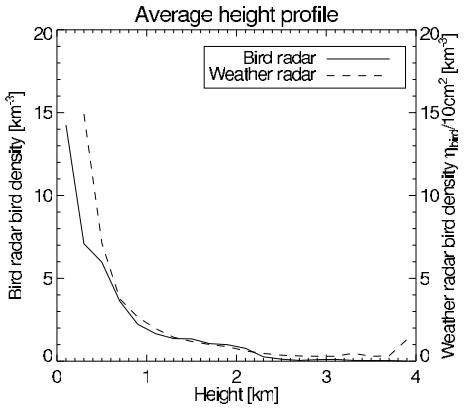

Figure 8.21: Average bird density height profile during the full De Bilt campaign. Bird reflectivity was converted into bird density by assuming a constant cross section of σ_{bird}=10 cm^2.

8.2.3 Bird ground speed and direction

We use the bird radar tracking data (see Sec. 6.1.1) to validate the VVP-retrieved bird ground speeds for weather radar (see Sec. 7.8). Both track data and weather radar speeds and directions were averaged into six-hourly means (18-00 UTC and 00-06 UTC) for three height categories (0-1000, 1000-2000 and 2000-3000 m).

Compared to the Wideumont campaign (see Sec. 8.1.3), correspondence between bird radar in weather radar for both bird ground speed and direction (Fig. 8.9) is worse. We observe a bias of -5 m/s in the weather radar ground speeds. This bias may originate from clutter contamination, insect contamination or a combination of both. Directions are biased quite strongly towards more southerly directions by on average 20°. This points towards a considerable contribution of wind-born scatterers, since westerly winds were frequent during the measurement campaign. A westerly component added to the south-westerly migration direction would result in more southerly weather radar extracted ground speeds. We find an average speed residual of 5±2 m/s and an average direction residual of 25±17°.

Clutter will bias extracted bird speeds towards zero and insect contamination will bias extracted bird speeds towards the wind speed. During the campaign a problem with the ground clutter Doppler filtering was identified in De Bilt, which has caused stronger ground clutter contamination than normal. Also insects were fairly numerous as determined with the bird radar (See Sec. 6.3.1).

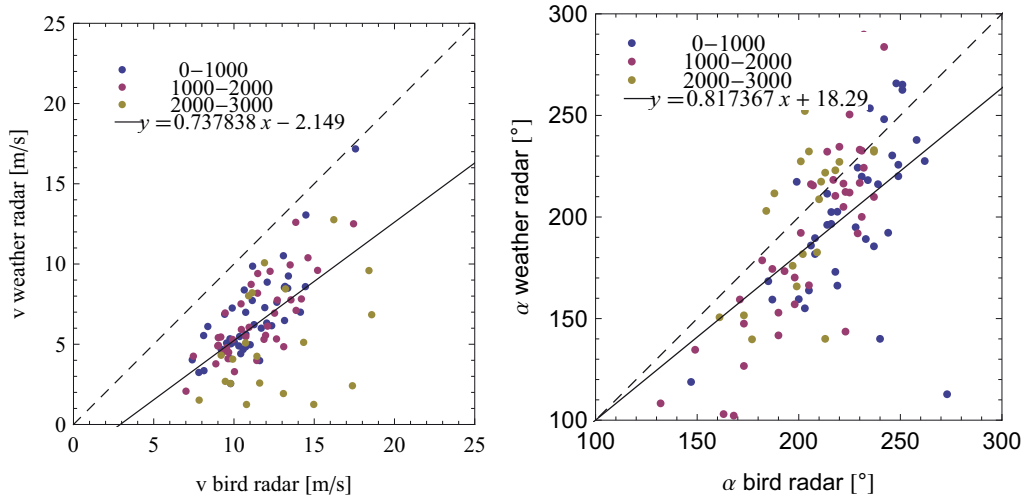

(a) speed (b) direction

Figure 8.22: Correlation bird ground speed and direction as determined by weather radar and bird radar. Data points are colored according different altitude intervals (0-1000,1000-2000 and 2000-3000 m). The dashed line is the curve for full correlation, the solid line a best linear least-squares fit.

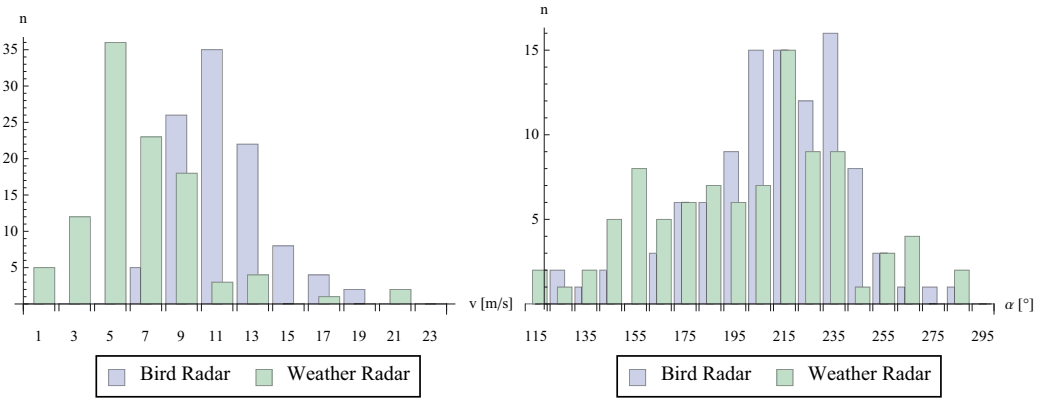

(a) speed (m/s) (b) direction (°)

Figure 8.23: Distribution of bird ground speed and direction as determined by weather radar and bird radar.

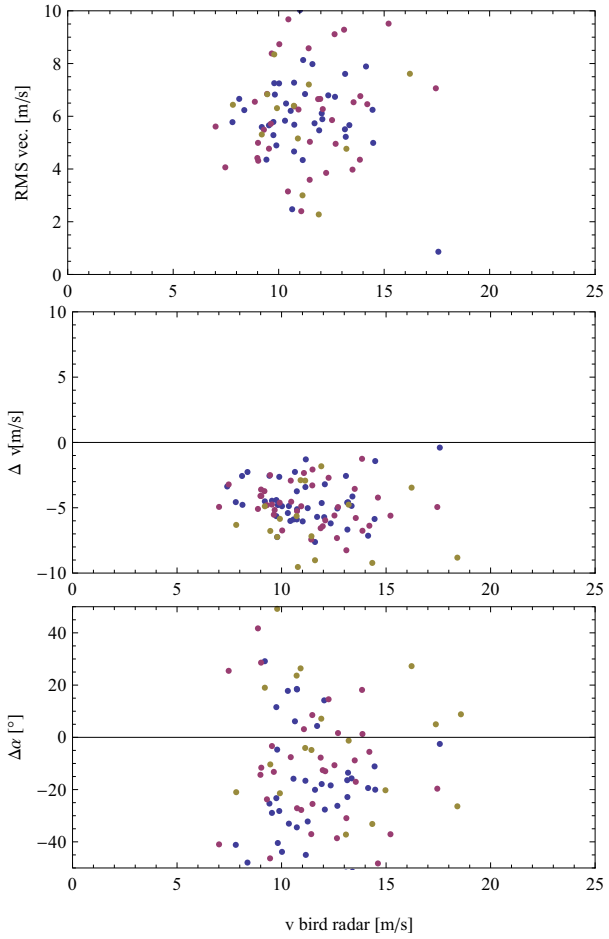

Figure 8.24: Average root-mean-square (RMS) ground speed vector difference (top), ground speed difference (middle) and directional difference (bottom) between bird radar and weather radar as a function of bird ground speed. Data points are colored according different altitude intervals as in Fig. 8.22.

8.3 Summary and comparison of campaigns

The field conditions varied considerably between the De Bilt, Wideumont and Trappes campaigns, affecting the weather radar observations and data quality.

1. The density of migrating birds was considerably higher in Wideumont than in the Bilt due to seasonal differences in migration intensity. In Wideumont weather radar data could be verified over a wide range of bird densities, while in De Bilt verification was limited to low bird densities.

2. The De Bilt radar suffered from clutter filtering problems, which makes the data less reliable for determining absolute bird densities and radar cross sections. Likely clutter contamination has contributed to an overestimation of the bird density observed in the lowest 400 m and a bias towards lower ground speeds, but also insect contaminations may be of influence.

3. The insect densities were considerably higher in De Bilt than in Wideumont. This may have contributed to a systematic overestimation of the bird density in the lowest height layers and to ground speed and direction biases. The size of the insect contribution remains unclear as no quantitative measurements of insect densities are available.

4. The species composition was shifted more towards larger passerines (*Turdidae* thrushes) in Wideumont than in de Bilt. This is probably the cause for a downshifted radar cross section distribution in De Bilt.

detection A radial velocity standard deviation higher than 2 m/s was found to be a skillful indicator of bird presence during both campaigns. The detection probability by the current bird algorithm is very high, even at very low bird densities. Limiting to bird reflectivities $Z_{\text{bird}} > -5$ dBZ (i.e. approximate densities $\rho_{\text{bird}} > 10$ km^{-3}), the number of correct detections is very high (99% Wideumont, 94% De Bilt). Measurements in the low bird reflectivity regime turn out unreliable due to a high number of false positive detections, which are nearly all related to precipitation contaminations.

bird density quantification Limiting to bird reflectivities $Z_{\text{bird}} > -5$ dBZ, 74% of the weather radar bird densities are correct within a factor of 2 and 87% within a factor of 3. Both clutter and insect contamination may contribute to weather radar overestimation of the

bird density (both campaigns lowest 400 m), however these two cannot be distinguished without detailed knowledge on the density of insect targets.

bird ground speed and direction quantification We observe a bias of -2 to -5 m/s in the weather radar ground speeds. In early autumn (De Bilt campaign) directions were biased quite strongly towards more southerly directions (on average 20°), which points towards considerable contamination of wind-born scatterers.

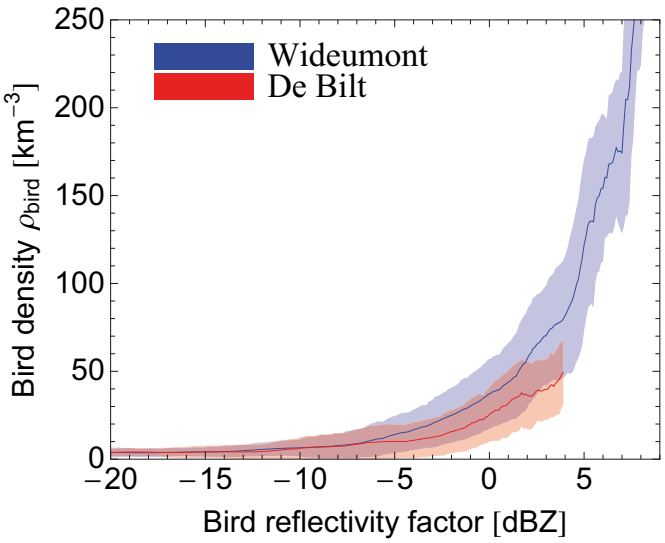

Figure 8.25: Mean bird density (solid lines) as a function of bird reflectivity factor for Wideumont (blue) and De Bilt (red). In color bird densities around the mean within one standard deviation are indicated. Standard deviation and mean were calculated for 2 dBZ reflectivity bins

Chapter 9

Bird migration quantification by polarimetric radar

9.1 Bird migration quantification algorithm for polarimetric radar

Bird detection and quantification follows the method outlined in Chapter 7, except for the precipitation filtering procedure described in Section 7.3. Polarimetric data is now used to identify gates containing precipitation and insects. While precipitation is efficiently identified by a high cross-polar correlation coefficient ρ_{HV} (see Fig. 9.1), insects and birds could not be easily distinguished by polarimetry alone. Both birds and insects give rise to a highly variable values of Z_{DR} (birds 0-3 dB, insects 0-8 dB), Φ_{DP} (birds 0-150°, insects 0-40°) and ρ_{HV} (birds and insects 0.2-0.8). Insect cases could sometimes be identified by a large value of $Z_{\mathrm{DR}} > 3.0$ (Bachmann and Zrnić, 2007), however especially when convective mixing was strong values of Z_{DR} were lower (see Fig. 9.2), and thus similar to values observed for birds. Clear azimuthal patterns in the dual polarization moments are observed for birds but not for insects (see Section 9.4), but polarimetry could not be used to distinguish both types biological scatterers on a single gate basis. Consequently, also for dual-polarization radar we perform a global analysis of the radial velocity data (see Section 7.4) to filter out insect dominated cases.

9.1.1 cell finding

The method described below replaces the precipitation filtering procedure described in Section 7.3 for single polarization radar.

Responsible Institute: KNMI

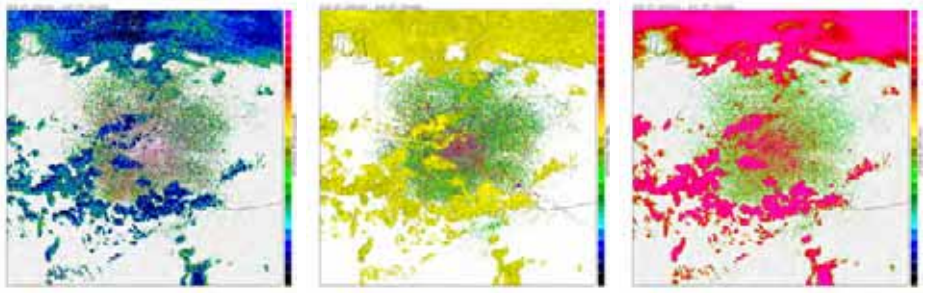

(a) Z_{DR} (b) Φ_{DP} (c) ρ_{HV}

Figure 9.1: Simultaneous observation of bird migration and precipitation on 15 Mar 2008 23:45 UTC. Precipitation is recognized by a high correlation coefficient $\rho_{\mathrm{HV}} > 0.9$, a differential phase around 0°(yellow in the figure), and a low differential reflectivity $Z_{\mathrm{DR}} < 0.5$ dB. Bird migration is recognized highly variable values of Z_{DR} (0-3 dB), Φ_{DP} (0-150°) and ρ_{HV} (0.2-0.8)

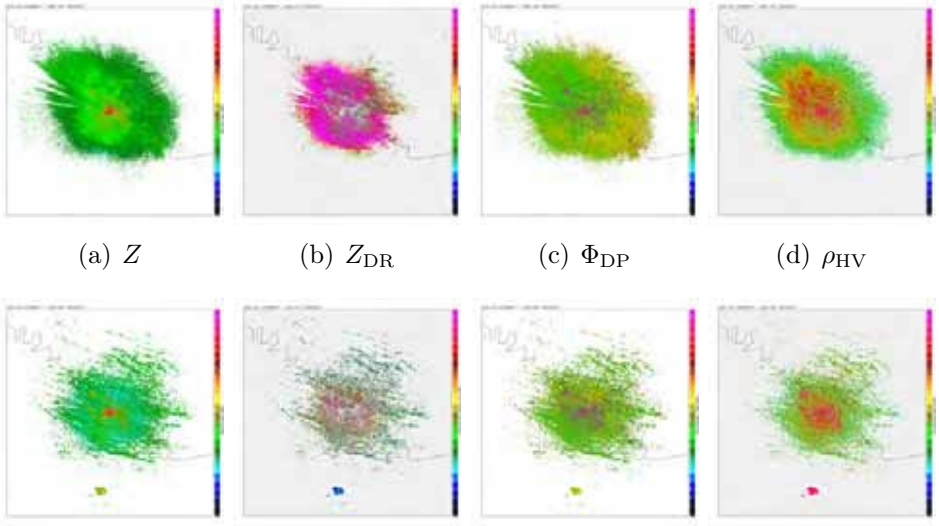

(a) Z (b) Z_{DR} (c) Φ_{DP} (d) ρ_{HV}

(e) Z (f) Z_{DR} (g) Φ_{DP} (h) ρ_{HV}

Figure 9.2: Non-bird scattering (insects) detected on 7 May 2008 at 10:00 UTC (top row, fig. (a)-(d)) and at 14:00 UTC (bottom row, fig. (e)-(h)). The differential reflectivity drops from $Z_{\mathrm{DR}} > 5$ dB at 10:00 UTC to $Z_{\mathrm{DR}} = 0 - 3$ dB at 14:00 UTC, when convective lines have formed along the ESE wind direction.

Each scan at fixed elevation is analyzed by a cell finding algorithm analogous to the algorithm described in Gonzales and Woods (1992). Contiguous areas consisting of gates with a high cross-polar correlation coefficient ρ_{HV} (Eq. 3.3) (indicative of hydrometeors (Bringi and Chandrasekar, 2001)) or high differential reflectivity Z_{DR} (indicative of insects (Bachmann and Zrnić, 2007) or chaff (see Sec. 9.5) are grouped into cells and included in the rain mask.

polarimetric criteria

For each scan at fixed elevation the cell finding algorithm searches for gates that have either $\rho_{\mathrm{HV}} > 0.9$ or $Z_{\mathrm{DR}} > 3.0$. Contiguous areas of gates that match the above polarimetric criteria are grouped into (precipitation) cells.

filling fraction criteria

For each range gate within a cell we require that it is neighbored by at least 5 other range-gates that satisfy the above polarimetric criteria. This guarantees that we only select cells which are uniformly filled. A uniform filling is usually observed for areas of precipitation, but often not for areas with bird echoes.

9.2 Trappes campaign

A campaign with the Superfledermaus bird radar was organized in the vicinity of the polarimetric weather radar in Trappes, France (48.775N/2.009E, 191 m MSL) from 10 Mar 2008 – 9 May 2008. Weather radar bird retrievals are compared to the bird radar bird migration measurements, analogous to the campaigns in De Bilt (see section 8.2) and Wideumont (see section 8.1).

Fig. 9.3 shows the extracted bird density height profile for one of the stronger migration nights during the Trappes campaign. Using the polarimetric version of the bird migration quantification algorithm, we find quantitative correspondence between the extracted bird densities by weather radar and bird radar. Another example is shown in Fig. 9.4, which shows the spectacular dusk ascent of birds to altitudes above 2 km. In this particular case birds avoid lower altitudes because of unfavorable easterly low level winds. The onset of migration is missed by the bird radar because of its much lower temporal resolution. Like in the other field campaigns, diurnal migration is poorly detected by the bird radar because of difficulties detecting bird flocks. For this reason only nighttime migration is studied (for this campaign 18.00 - 6.00 UTC).

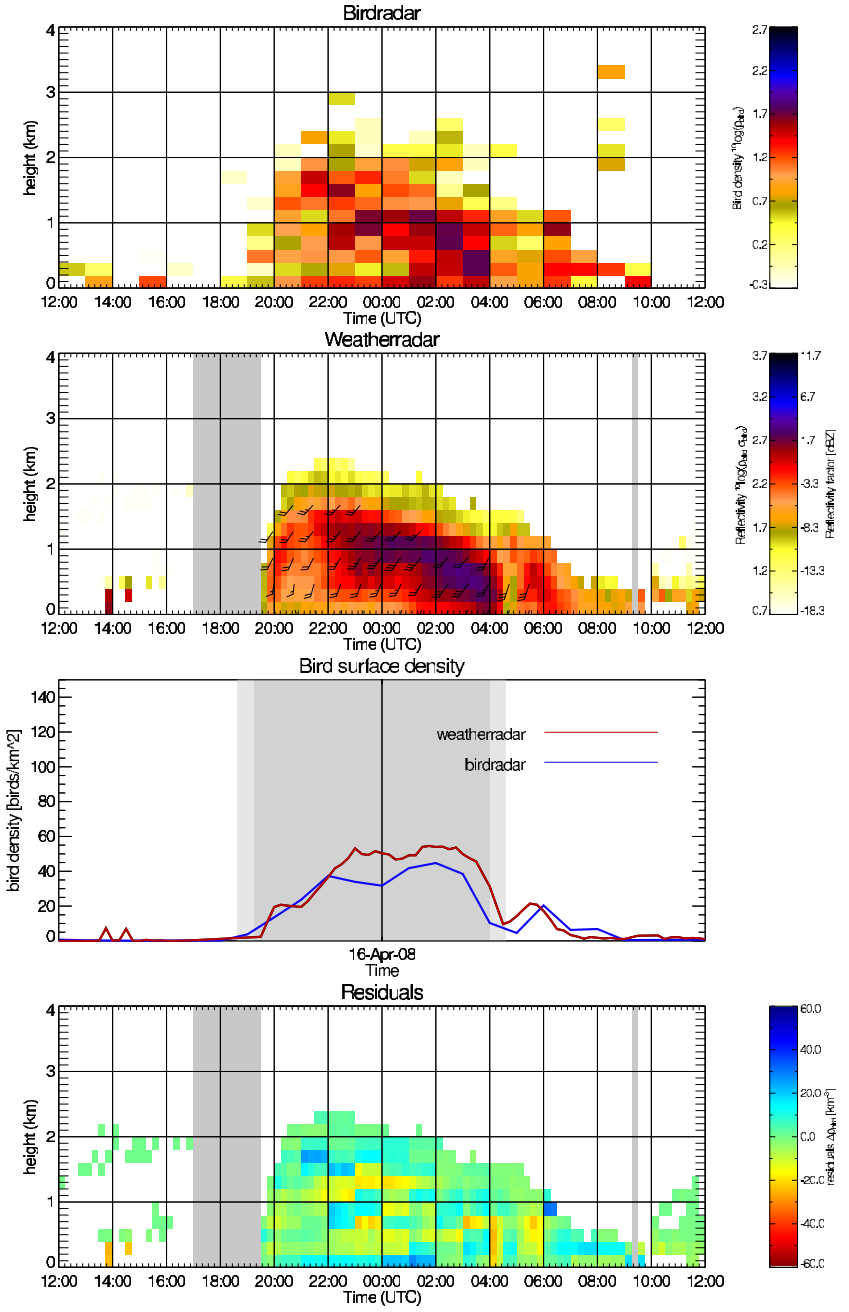

Figure 9.3: Retrieved time-height profiles by bird radar (top) and weather radar (upper middle) in Trappes for the night of 16 April 2008. The vertically integrated bird densities and weather radar - bird radar density difference are shown as well (lower middle and bottom).

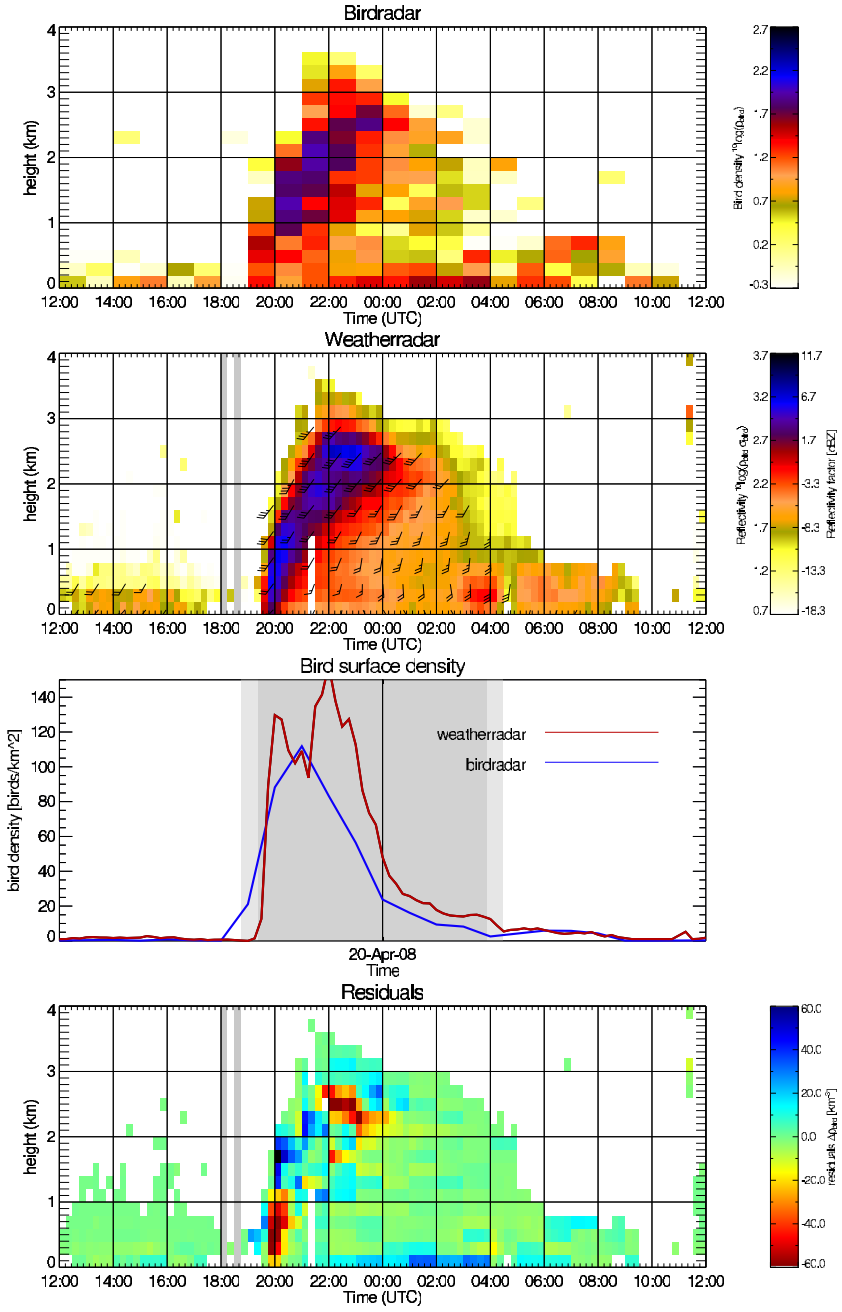

Figure 9.4: Retrieved time-height profiles by bird radar (top) and weather radar (upper middle) in Trappes for the night of 20 April 2008. The vertically integrated bird densities and weather radar - bird radar density difference are shown as well (lower middle and bottom).

9.3 Validation and verification

9.3.1 bird detectability

Scatter plots of radial velocity standard deviation versus reflectivity are shown in Fig. 9.5. As discussed in Section 3.3.2 only 1 by 1 km^2 Cartesian radial velocity data is available. Radial velocity data at close range is therefore very coarse. As a result the VVP analysis of the radial velocities can produce very high radial velocity standard deviations for the lower height layers (which contain mostly gates a close range). The points scattered in the top left corner of Fig. 9.5(b) are a direct result of the poor resolution radial velocity data.

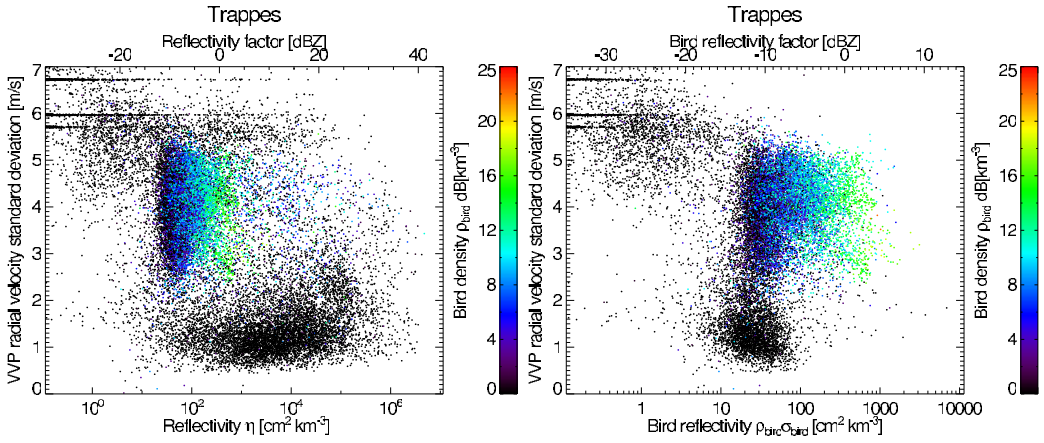

(a) (b)

Figure 9.5: Scatter plots of the VVP retrieved radial velocity standard deviation σ_r versus the height layer's average full reflectivity η_{full} (left) and bird reflectivity η_{bird} (right) for the Trappes campaign. The color coding indicates the simultaneous collocated bird density estimate by the bird radar.

A derived contingency table is shown in Table 9.3.1 (using thresholds σ_r=2 m s^{-1} and ρ_{bird}=1 km^{-3}). Using these figures we find for the Probability Of Detection POD=0.94, False Alarm Ratio FAR=0.41 and Fraction Correct FC=0.69. Not taking into account the layers for which the radial velocity standard deviation is large due to poor resolution radial velocity data (points in the section $V_r > 4$ and $\rho_{bird}\sigma_{bird} < 15$), the scores improve to POD=0.97, FAR=0.28 and FC=0.75.

The variation of the contingency table scores with the applied radial velocity threshold σ_r is shown in Fig. 9.6. Like in Wideumont, a threshold

σ_r=2 m s^{-1} is a good compromise between lowering the False Alarm Ratio and attaining a high Probability of Detection.

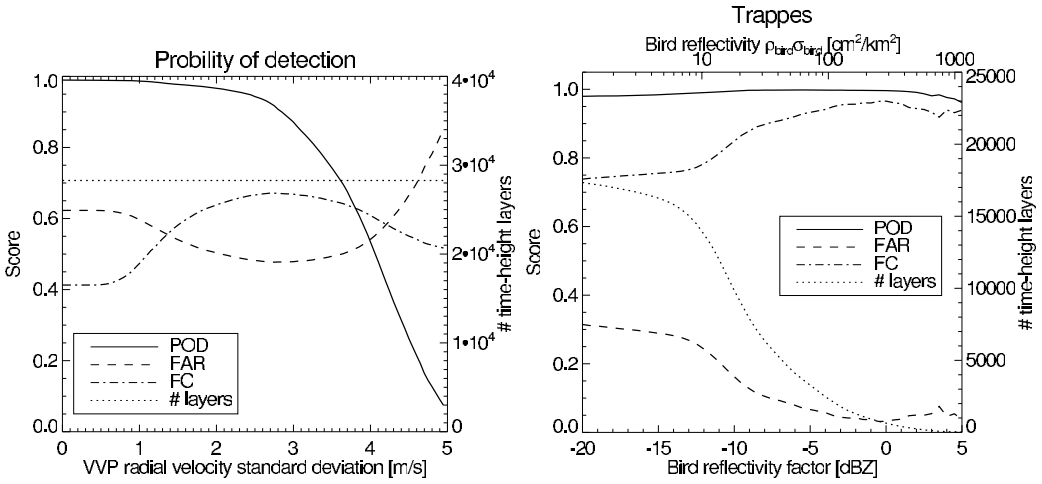

Figure 9.6: Left (a): Probability of detection (POD, solid) and False Alarm Rate (FAR, dash) as a function of VVP radial velocity standard deviation threshold. Right (b): Probability of detection (POD, solid), False Alarm Rate (FAR, dash) and Fraction Correct (FC, dash-dot) as a function of reflectivity threshold. Data taken by the Trappes radar, France from 12 March - 7 May 2008.

As was observed during the De Bilt and Wideumont campaigns, height layers with radial velocity standard deviation $\sigma_r < 2$ m s^{-1} have a very low probability of containing birds, as is evident from both Fig 9.5 and the radial velocity distributions shown in Fig. 9.7. The number of height layers with $\sigma_r > 2$ m s^{-1} *not* containing birds is higher than during the Wideumont campaign, mainly due to the low spatial resolution of the radial velocity data at close range.

Most false positive detections occur in the regime of low bird reflectivity, as illustrated in Fig 9.6. For the selection of height layers with a bird reflectivity > -5 dBZ, the FAR drops to 5 % and the fraction of correct detections increases to 93 %.

Currently detection is in Trappes is not as good as in Wideumont, while better performance is expected for polarimetric radars (because of the additional polarimetric moments that are available for recognizing and filtering precipitation). Bird detection will likely improve when radial velocity data

WR Birds	WR No Birds
H	M
F	R

	WR Birds	WR No Birds
BR Birds	12548	742
BR No Birds	8736	8316

Table 9.1: Contingency table for the quality controlled weather radar bird observations against the bird radar observations. "BR" refers to Bird Radar and "WR" refers to Weather Radar. A standard deviation threshold of $\sigma_r = 2.0$ m s^{-1} and a bird density threshold of 1.0 km^{-3} have been applied.

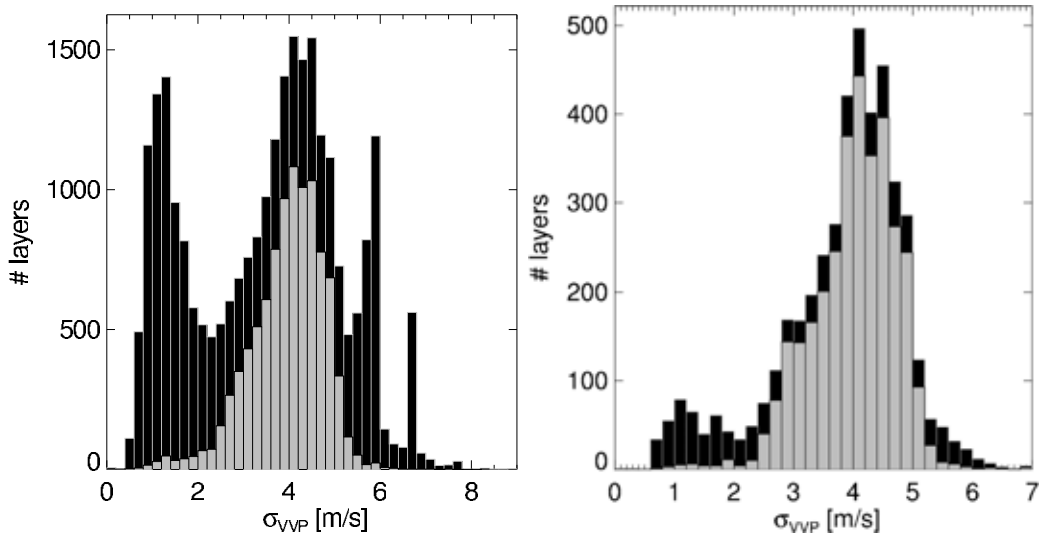

(a) all layers (b) $Z_{\text{bird}} > -5$ dBZ only

Figure 9.7: Distribution of VVP retrieved radial velocities in Trappes. In grey the subset of height-layers is shown for which birds were detected simultaneously by the bird radar reference.

in polar coordinates will be available of comparable quality as in De Bilt and Wideumont. Also in the dual-polarization algorithm filtering of events consisting of air-borne insects still relies on good quality radial velocity (insects are excluded based on a low VVP-retrieved radial velocity standard deviation). Using the current 1 by 1 km Cartesian radial velocity data, in early May some diurnal events of insect scattering were not properly filtered. We expect this will improve using polar data of higher spatial resolution. Several cases of chaff also hindered the bird detection algorithm (5-Mar-2008 20 UTC, 28-Mar-2008 18 UTC, 17-Apr-2008 0 UTC, see Sec. 9.5).

9.3.2 Accuracy weather radar bird densities

Fig. 9.8 correlates the weather radar bird reflectivity to the bird density determined by bird radar, both on a basis of height layers (a) and vertically integrated profiles (b).

Reflectivity factors in the Trappes data were only stored down to a level of -9 dBZ (gates with reflectivities below this threshold are assumed to have a reflectivity of -100 dBZ), which is unfortunate since scattering by birds also occurs at lower reflectivity factors. This is the reason for the absence of very low bird reflectivities in Fig. 9.8(a).

The cross section distribution determined for this campaign is shown in Fig. 9.9. The distribution is similar though slightly shifted to larger values compared to the Wideumont campaign (Fig. 7.11) and the De Bilt campaign (Fig. 8.19). In Trappes no time-domain Doppler clutter filtering is applied (see Sec. 7.2.1). Therefore clutter contamination may be stronger and contribute to a larger net bird radar cross section, however we cannot exclude that also the species composition is shifted towards more larger bird species.

Fitting the data to Eq. 2.11 with σ_{bird} as the only fit parameter gives us σ_{bird} =16±21 cm^2 (median and median deviation 11±6 cm^2) and a correlation coefficient of 0.41.

We convert bird reflectivity into bird density by assuming a constant cross section of σ_{bird}=13 cm^2 (10 cm^2 in De Bilt and Wideumont), such that the seasonal height distribution of bird densities match between bird and weather radar (see Fig. 9.12). Limiting to the high bird reflectivity regime we find that the weather radar bird density estimate is correct within a factor 1.5 for 42% of the time-height layers, within a factor of 2 for 62% and within a factor of 3 for 78% of the time-height layers ("correct within a factor i" we define as the weather radar bird density equals the bird radar bird density by a multiplicative factor of $i^{\pm 1}$). The residual bird density equals 11 ± 19 birds/km^3. . The residual height-integrated bird density equals 10 ± 16 birds/km^2 (based on events where the bird radar height-integrated exceeded

1 bird/km^2 only).

Migration during the Trappes campaign took place more often at high altitudes compared to the two autumn campaigns, since favorable tail winds at higher altitude are much more frequent in spring compared to autumn (in both seasons south-westerly winds are dominant, but the migration directions are reversed). Fig. 9.12 shows the average altitude distribution of birds during the campaign, determined by bird radar and weather radar. Altitude layers with high bird reflectivity ($Z_{\text{bird}} > -5$ dBZ) are found up to 3 km (see Fig. 9.11).

The bird density in Trappes is mostly underestimated by weather radar at the lowest altitudes (0-500 m). At low elevations the French radar signal processor rejects gates contaminated with clutter by putting its retrieved signal to zero. The bird detection algorithm currently cannot recognize these rejected gates and assumes the signal is truly zero, which leads to an underestimation of the bird density. The season averaged height profile of Fig. 9.12 shows that in the lowest altitudes the bird density is underestimated.

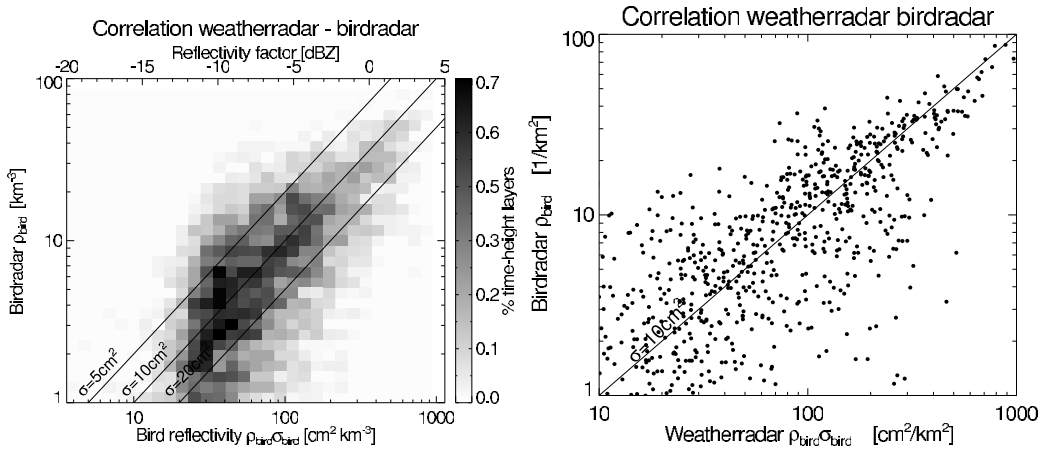

Figure 9.8: Left (a): Correlation between bird densities determined by bird radar and reflectivity measured by weather radar. Right (b): Correlation between the vertically integrated bird surface density determined by bird radar and vertically integrated reflectivity measured by weather radar. The lowest height layer (0-200m) was excluded from analysis.

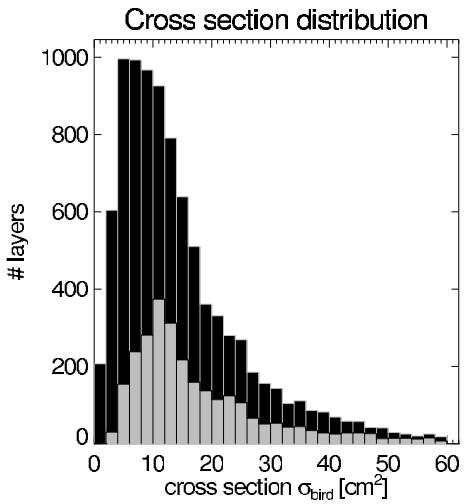

Figure 9.9: Distribution of bird weather radar cross sections based on collocated measurements with the bird radar during the Trappes campaign. The distribution in grey is based on time height layers in the high reflectivity regime ($Z_{\mathrm{bird}} > 5$ dBZ) only.

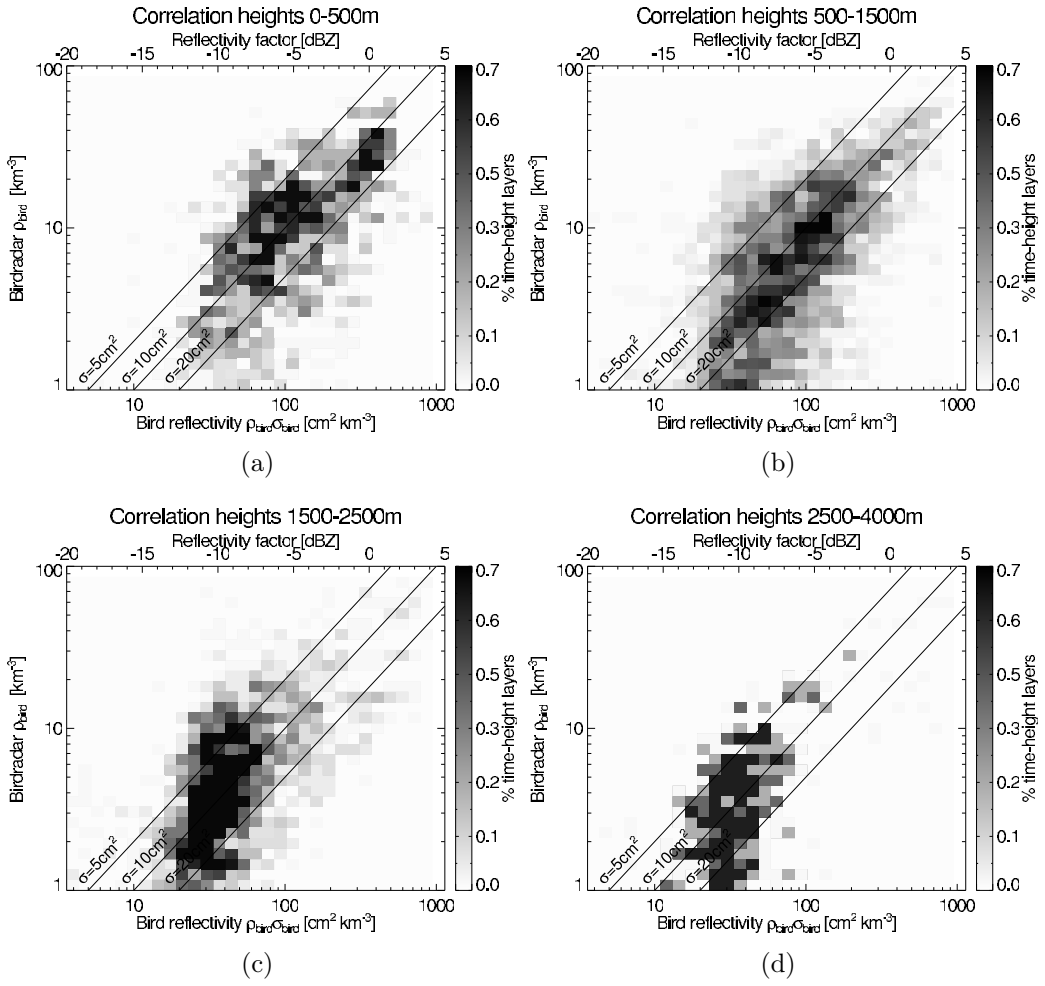

Figure 9.10: Correlation between the bird density determined by bird radar and reflectivity measured by weather radar in Trappes for height layers between (a) 0-500 m, (b) 500-1500 m, (c) 1500-2500 m and (d) 2500-4000 m. The lowest height layer (0-200m) was excluded.

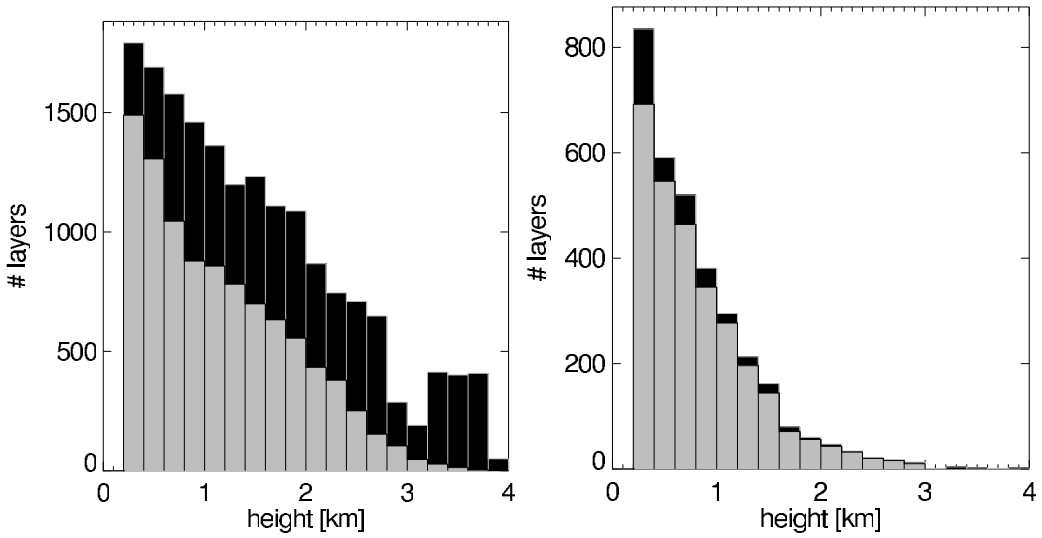

(a) all layers (b) $Z_{\text{bird}} > -5$ dBZ only

Figure 9.11: Number of detected time-height layers per altitude layer for the Trappes campaign. In grey the subset of height-layers is shown for which birds were detected simultaneously by the bird radar reference.

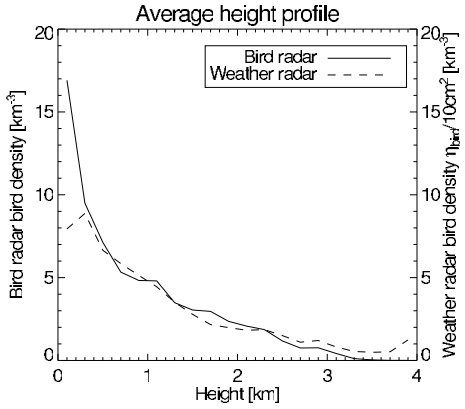

Figure 9.12: Average bird density height profile during the full Trappes campaign. Bird reflectivity was converted into bird density by assuming a constant cross section of σ_{bird}=10 cm^2.

9.3.3 Bird ground speed and direction

We use the bird radar tracking data (see Sec. 6.1.3) to validate the VVP-retrieved bird ground speeds for weather radar (see Sec. 7.8). Both track data and weather radar speeds and directions were averaged into six-hourly means (18-00 UTC and 00-06 UTC) for three height categories (0-1000, 1000-2000 and 2000-3000 m).

The degree of correspondence between bird radar in weather radar (Fig. 9.13) is comparable to the results obtained for single polarization radar. Again a bias around -4 m/s is observed in the weather radar ground speeds. No clear bias is observed in the weather radar directions and no seasonal trends were found for the weather radar - bird radar speed and direction residuals. Increased deviations between weather radar and bird radar speed vectors would indicate contaminations of insect scattering, which is expected to increase in the coarse of spring. Based on the weather radar extracted ground speeds and directions no indications were found that air-borne scatterers like insects introduced any biases during nocturnal spring migration up to half of May.

Speed and direction extraction was less accurate for the lowest altitude category (0-1000 m) due to the very coarse radial velocity data (1 by 1 km cartesian) at close range. Ground speed and direction extraction will likely improve when radial velocity data in polar coordinates will be available of comparable quality as in De Bilt and Wideumont.

We find an average speed residual of 3 ± 3 m/s and an average direction residual of $15\pm17°$.

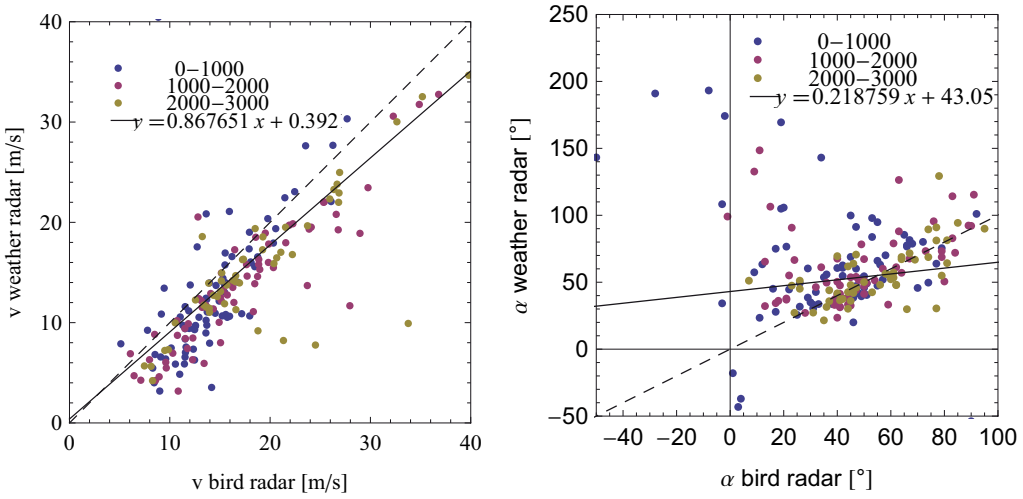

(a) speed (b) direction

Figure 9.13:

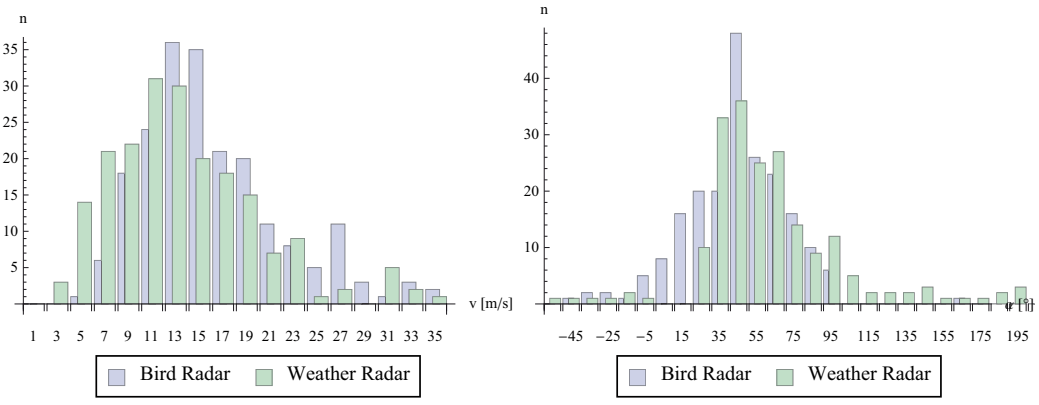

(a) speed (m/s) (b) direction (°)

Figure 9.14:

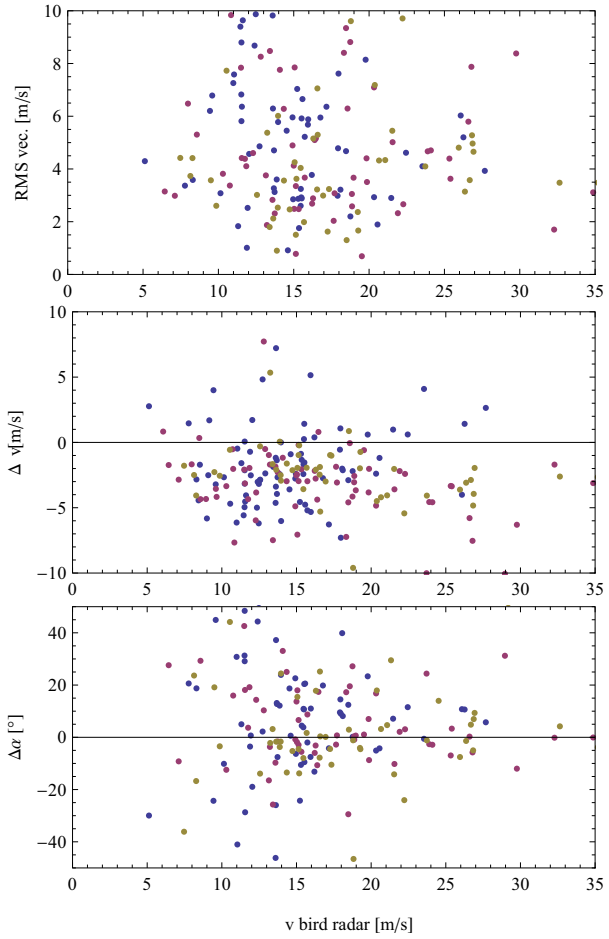

Figure 9.15:

9.4 Azimuthal dependence of polarimetry

During bird migration characteristic azimuthal patterns are observed in the reflectivity and polarimetric observables, which are related to the orientation and geometry of the bird body. Considerable difference in azimuthal patterns are observed for different migration nights, as illustrated by Fig. 9.16 for a night in mid-April and Fig. 9.17 for a night in mid-March. Azimuthal patterns tend to be more pronounced in late spring compared to early spring. In late spring the size distribution of migrating birds is narrower, when predominantly small passerines (6-30 grams) are migrating. In early spring also larger passerines like Thrushes (60-160 grams) and non-passerines are migrating. We may speculate that when migrating birds are of similar geometry, the polarimetric signatures are more pronounced and less blurred out by size-dependent variations of the scattering.

Qualitative description of azimuthal patterns during bird migration

Reflectivity factor Z is much larger in side view than in head or tail view, with a difference in reflectivity factor of up to 6 dBZ. Also in sharp head view the reflectivity factor is sometimes enhanced (e.g. Fig. 9.16(a)), but less so in tail view. The reflectivity pattern can be used to determine the average orientation of the birds body axis and thus their heading (in addition to the average flight direction as derived from the radial velocity). In Fig. 9.17 the flight direction equals approximately 70° while the heading equals approximately 40°. Fig. 7.14 illustrates the same azimuthal variance but then for single-polarization radar during autumn migration.

Differential Reflectivity Z_{DR} is positive at all azimuths, and largest in head and tail view (up to 3 dB). It is smallest at azimuths in between side view and head/tail view (0-1 dB). Sometimes Z_{DR} is large at side view, but these maxima are not visible at all times and peaked sharper along the azimuth than the maxima in head/tail view (see Fig. 9.16(c)). The fact that Z_{DR} is large in head and tail view suggests that the scattering part of the bird body is horizontally elongated, i.e. that likely the wings contribute significantly to the scattering. A bird's body can therefore not be approximated by a prolate spheroid such that wing scattering is neglected, since in the resonant scattering regime we expect $Z_{\mathrm{DR}} = 0$ for scattering along a spheroid's axis of symmetry (that is in head/tail view).

Correlation Coefficient ρ_{HV} is relatively large (0.7) in side view. At az-

imuth angles in between side view and head/tail view the correlation coefficient is low (0.4). Sometimes ρ_{HV} is large in head and tail view as well (see Fig. 9.16(a)).

Differential phase Φ_{DP} is positive and usually follows an azimuthal pattern that is the mirror image of the correlation coefficient ρ_{HV}: the differential phase is large (up to 120°) when ρ_{HV} is small and small (down to 0°) when ρ_{HV} is large.

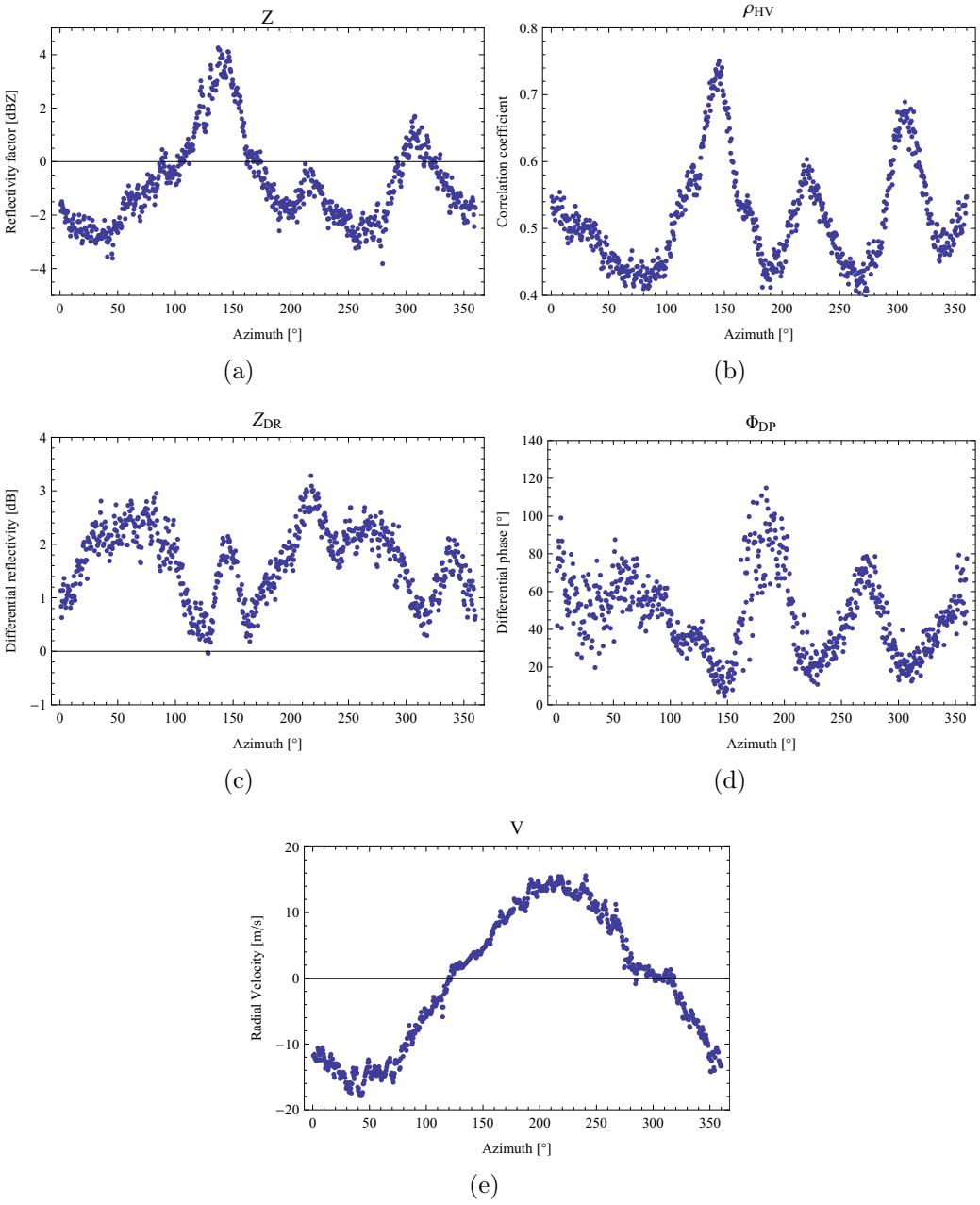

Figure 9.16: Azimuthal dependence on 16 April 2008 02:30 UTC of the Reflectivity, Correlation Coefficient, Differential Reflectivity, Differential Phase and Radial Velocity in Trappes during bird migration for a scan at 1.5° elevation. Each observable was averaged over ranges 10-40 km.

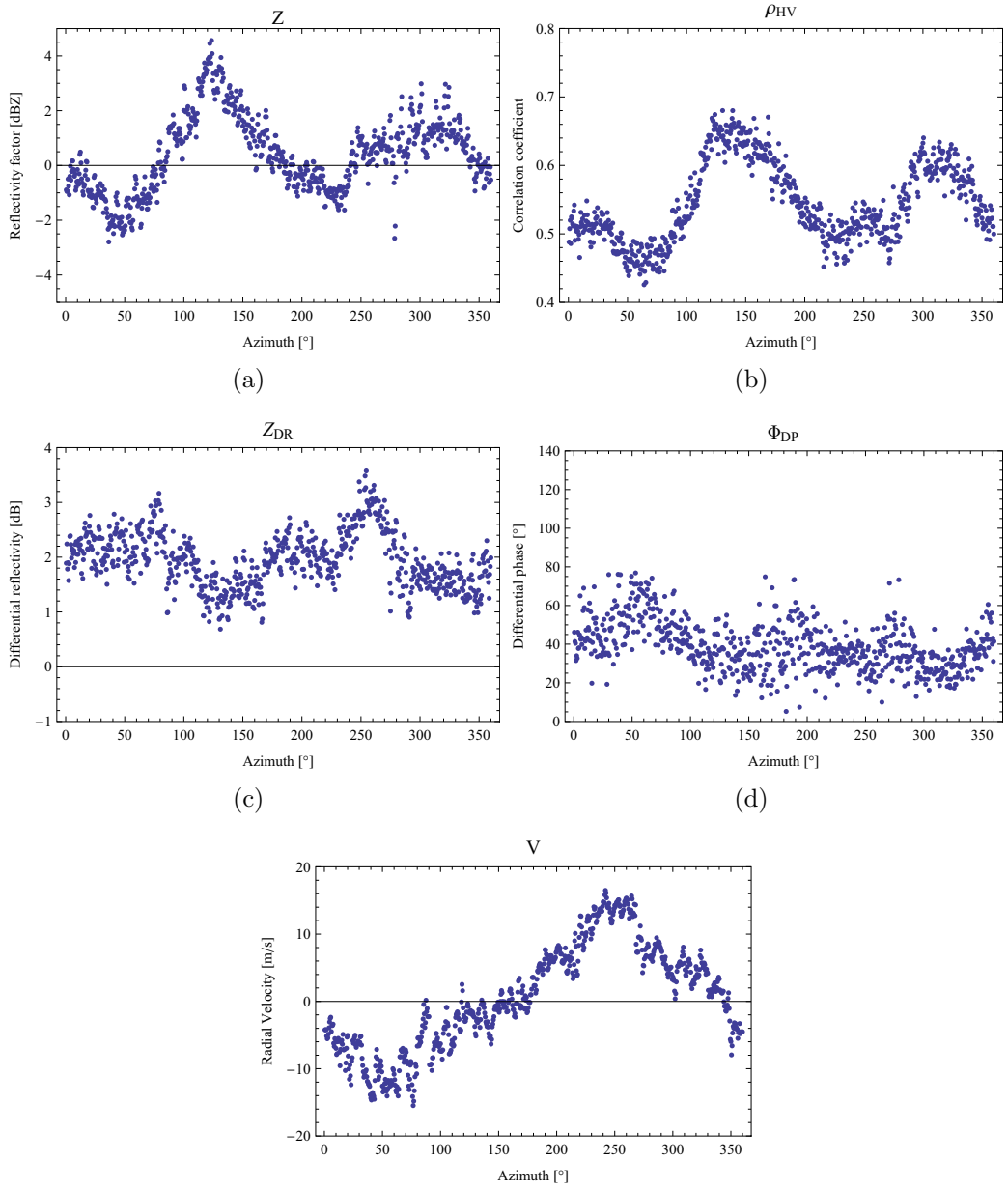

Figure 9.17: Azimuthal dependence on 23 March 2008 23:00 UTC of the Reflectivity, Correlation Coefficient, Differential Reflectivity, Differential Phase and Radial Velocity in Trappes during bird migration for a scan at 1.5° elevation. Each observable was averaged over ranges 10-40 km.

9.5 Chaff contamination

During the spring campaign in Trappes chaff (radar countermeasure used during airforce missions) was observed in several nights, which strongly hindered the bird migration quantification algorithm. In the absence of bird migration chaff echoes were filtered out successfully based on a very high differential reflectivity $Z_{\mathrm{DR}} > 4$ (see Fig. 9.18). When chaff is admixed with migrating birds it no longer shows these characteristic high Z_{DR} values and becomes indistinguishable from bird echoes (see Fig. 9.19). In such cases the bird migration algorithm gives spurious high bird densities.

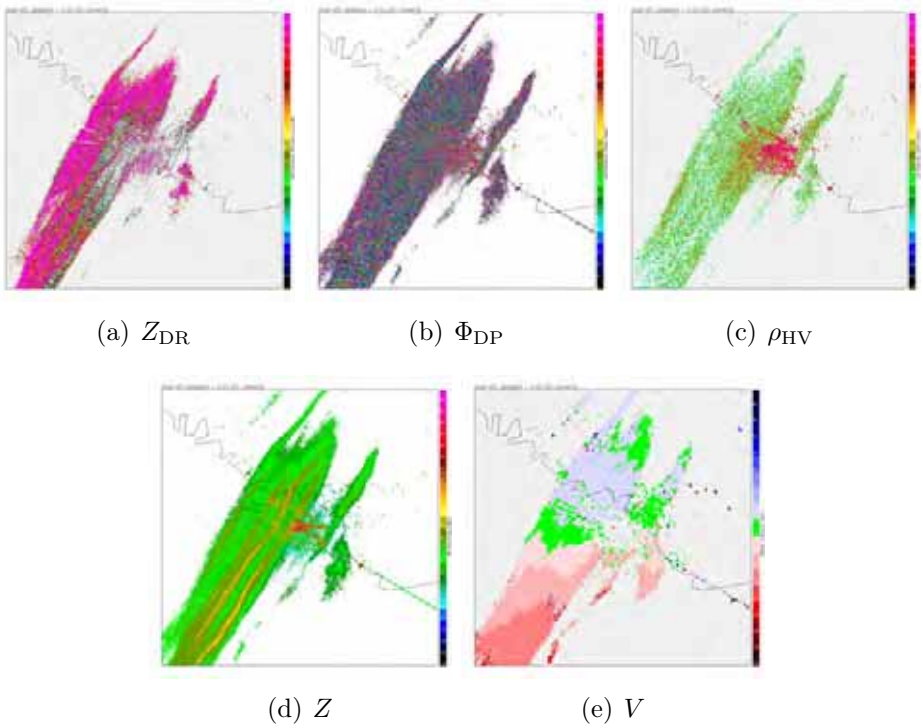

(a) Z_{DR} (b) Φ_{DP} (c) ρ_{HV}

(d) Z (e) V

Figure 9.18: Chaff detected on 05 Mar 2008 20:30 UTC. We find values for the polarimetric observables of $Z_{\mathrm{DR}} > 5$, random Φ_{DP} and low $\rho_{\mathrm{HV}} = 0.2 - 0.5$. Especially a high differential reflectivity is characteristic of chaff.

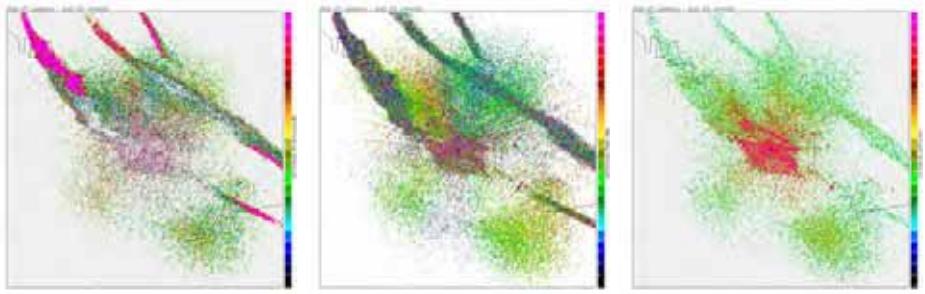

(a) Z_{DR} (b) Φ_{DP} (c) ρ_{HV}

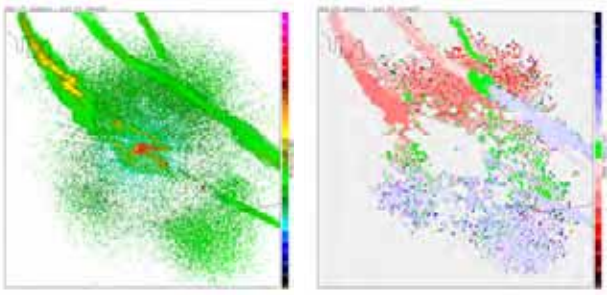

(d) Z (e) V

Figure 9.19: Chaff detected during bird migration on 16 Apr 2008 23:30 UTC. The characteristically high Z_{DR} for chaff is no longer observed as a result of the mixed in scattering by birds. In the bird migration algorithm chaff echoes are no longer properly filtered out, leading to overestimation of bird densities.

Chapter 10

Conclusions and Recommendations

10.1 Conclusions

Operational C-band Doppler weather radar is a reliable sensor for quantification of densities of migrating birds. A bird migration recognition algorithm has been developed, extracting bird density, speed and direction as a function of altitude. Verification against simultaneous and co-located bird density measurements by a high precision bird radar shows that the bird detection systems has the following main characteristics:

1. The detection probability of the bird detection algorithm is very high (up to 99%) and the fraction of false alarms is low (down to 2%), based on the Wideumont campaign. In de Bilt the detection probability reached 94% and the fraction of false alarms was 6%, but due to clutter filtering problems (resolved after the campaign) the data for this campaign are not as reliable.

2. Most false positive detections are caused by precipitation contaminations. To a high degree the quality of the bird density quantification depends of the quality of the algorithms masking areas of precipitation (since at S-band wavelengths bird migration shows up at higher reflectivity more similar to precipitation, application of the algorithm may be more difficult than at C-band wavelengths)

3. Precipitation and insect filtering is performed by a cell finding algorithm. Areas of precipitation and insects are identified based on criteria

Responsible Institute: KNMI and SOI

combining reflectivity, range gate filling factor and variance in Doppler radial velocity. To obtain reliable bird density quantification, contiguous areas of reflectivity down to 0 dBZ consisting of precipitation or insects need to be adequately filtered out.

4. Besides an insect/precipitation filter, a radial velocity standard deviation higher than 2 m/s was used as an indicator of bird presence. During both campaigns time-height layers with a standard deviation lower than 2 m/s contained no significant bird densities.

5. At bird densities higher than 10/km^3 ($Z_{\text{bird}} > -5$ dBZ), 74% of the weather radar bird densities are correct within a factor of 2 and 87% within a factor of 3. The current bird detection algorithm meets the requirements for operational implementation. At the Royal Dutch Airforce (RNLAF), the subsequent levels of Bird Strike Warnings (so-called BIRDTAMs) differ in bird density by factors of 2, which is on the order of accuracy that is obtained by weather radar.

6. Bird speeds determined by weather radar are biased by on average -3 m/s. Bird flight directions determined by weather radar correspond to bird radar tracking measurements on average within 15-20°.

10.2 Recommendations

1. Range gate sampling over 250 m was found to be beneficial over a sampling range of 1 km. In the former case at most bird densities a range gate is occupied by only a single bird or none. A higher variation in radial velocities (due to the variations in speed and heading of individual birds) is detected and a lower range gate filling factor. Both are advantageous to distinguish bird echos from other scatterers

2. Availability of the unfiltered reflectivity images (before (Doppler) clutter filtering by the radar signal processor) is important. The raw reflectivity data can be used to determine which gates should be discarded because of a strong clutter background. Additionally, to suppress ground clutter contamination all gates with radial velocity in the interval [-1,1] m/s should be discarded. The use of a static clutter map is highly recommended, which can be generated from volume data for several clear-air days without bird migration or insect scattering (preferably mid-winter). In the current algorithm all range gates with a reflectivity average above -10 dBZ were rejected.

3. It is recommended to extend the unambiguous velocity to an interval of at least [-50,50] m/s (using dual-PRF techniques) to cover most wind and bird ground velocities. Currently the bird detection algorithm is not robust for radial velocity aliasing.

4. In the current study a constant bird radar cross section of 10 cm^2 has been assumed to convert weather radar reflectivity to bird densities (seasonal variances in radar cross section were observed but not corrected for). Scattering by bird targets occurs in a resonant regime where radar wavelength and scatterer size are comparable. In this regime bird radar cross sections depend in a complex way on the bird geometry and view angle. A better understanding of the resonant scattering process on birds will likely lead to more adequate methods of converting weather radar reflectivity into bird densities, and a better insight in the polarimetric signatures of bird migration.

5. Overestimation of bird density in the lowest 200 m (Wideumont) to 400 m (De Bilt) have been observed. This overestimation may be due to a systematic error related clutter contamination or due to insect contamination. Quantitative information on insect densities are necessary to assess these relative contributions.

6. The current study shows that weather radar has a high potential for providing information on the spatial distribution of birds during migration. This is especially important in areas with prominent topographical features, like the Netherlands where large water bodies and coastal areas structure the spatial distribution of birds. Birds are often seen up to 100 km range by weather radar, suggesting that spatial information covering a large area is possible by weather radar.

7. Further research on the use dual polarization radar for bird detection is highly recommended. This study suggests that the combined use of dual-polarization techniques for precipitation filtering and high quality Doppler techniques for insect filtering would be most adequate for bird detection purposes. Unfortunately the Trappes radial velocity data are of insufficient quality, most likely related to disadvantages of the triple-PRT Doppler scheme in the context of bird detection. A field study using a weather radar that combines these characteristics would be valuable for exploring the full potential of operational weather radar for bird detection.

8. Operational implementation of the current bird detection algorithm is highly recommended.

10.3 Extending migration monitoring to European scale

It is recommended to extend the application of weather radars for bird migration monitoring to the whole of Europe using the Operational Program on Exchange of Radar data (OPERA) running within EUMETNET, which is the network grouping of 26 European National Meteorological Services. OPERA's operational network consists of more than 180 weather radars. An OPERA Data Center is currently being developed and the start of operation is planned for January 2011. More information on OPERA can be found in Appendix A of this report. This data center will collect and process the radar volumetric data, both reflectivity and radial velocity, that are also needed for the bird migration detection algorithm presented here. The algorithm has been successfully applied to radar data from three different countries, but application to data from 30 countries will require further development and calibration. Both the data policy and the procedure for inclusion of new algorithms for the OPERA Data Center still have to be established.

10.3.1 weather radar technical requirements

To be compatable with the currently developed bird migration algorithm, individual radars within the OPERA network need to meet the following requirements:

radar wavelength in C-band The current bird detection algorithm is developed for C-band radar only. Currently 157 out of 191 weather radars in OPERA are C-band.

Doppler capability Radial velocity information is essential for the bird detection algorithm. Non-Doppler radars cannot be used for bird migration quantification. Currently 177 out of 191 weather radars in OPERA are dopplerized, and this proportion is expected to grow with future radar hardware updates in several countries.

spatial resolution The bird detection algorithm has been shown to function at azimuthal/range resolutions smaller or equal than $1^\circ/1$ km. Additional verification and testing is required for radars operating at coarser spatial resolutions and the radial velocity thresholds σ_r (see Sec 7.4.2) and σ_v (see Sec. 7.3.2) may need adjustments.

scanning strategy The radar should provide a full Doppler volume scan consisting of several elevations to be able to constract an altitude profile

at 200 m height resolution (At minimum four elevations in the range of 0-15°, e.g. 0.5°, 3.0°, 6.0°and 12.0°). A volume scanning interval of every 5 minutes is recommended (reveals most detail in the altitudinal dynamics of flight altitudes), however a scanning interval of 15 minutes is sufficient for flight warning applications.

clutter The current bird detection algorithm makes use of a static ground clutter map. These ground clutter maps need to be maintained for all radars.

These technical requirements are currently met by approximately 80% of the weather radars in OPERA.

10.3.2 Future developments and verification

Although the bird migration algorithm can process data from all radars that meet the technical requirements listed in the previous section, additional verification and development is necessary in specific cases:

inclusion S-band radars The algorithm will need to be adjusted for operation on S-band radars, which is a common type of radar in soutern mediterranean Europe. Reflectivity factors during bird migration tend to be a factor 16 stronger at S-band than at C-band (see Sec. 2.3), which makes bird migration echoes more comparable to precipitation at S-band. The precipitation cell filtering procedures (Sec. 7.3.1) will need to be modified for C-band radars and additional bird radar field campaigns are essential to verify algorithm performance. Collocated bird density measurements with a bird radar are required for verification and testing of the new S-band algorithm.

assessment climate effects The current algorithm is reliable during peak migration in the moderate climate of western Europe (45-55°N, 0-10°E), where bird density quantification was shown to be only weakly affected by insect contaminations. The degree of insect contamination should be checked for radars operating in qualitatively different enviromental conditions. We therefore recommend to organize additional bird radar field campaigns for weather radars operating in

- southern/mediterranean Europe
- eastern continental Europe
- northern taiga climate

diurnal migration Quantification of diurnal bird migration still needs to be verified. This verification depends on a reliable estimation by the bird radar used in this study of the size of flocks of birds. Automatic bird flock size estimation is currently not implemented on the bird radar and additional development is necessary to achieve this.

integraton Visualisation, integration and extrapolation of the bird migration information of individuals radars over the european continent need to be developed.

10.3.3 Roadmap

We recommend to start European scale extension of bird migration detection at the national and european level simultaneously. At the national level:

- Radar manufacturers are encouraged to incorporate a bird migration algorithm into their operational radar software package.
- Bird radar field campaigns mentioned in the previous section can be organized at national levels and coordinated within the framework of OPERA.

At the European level developments should be aimed at incorporating the bird migration algorithm into the OPERA Data Center:

- data policy and the procedure for inclusion of new algorithms for the OPERA Data Center need to be established.
- The bird migration algorithm will need to be modified for handling to the new OPERA dataformat.
- development of visualisation, integration and extrapolation tools

Acknowledgements

We would like to thank Laurent Delobbe from RMI and Pierre Tabary from Météo France for their contributions to chapter 3 and their kind assistance in providing the Belgian and French weather radar data. We gratefully acknowledge the field campaign collaborators: Herbert Stark, Claudio Koller, Thomas Luiten, Valère Martin, Pirmin Nietlisbach, Marco Thoma and Andreas Wagner. We thank Ton Vermaas of the Royal Dutch Airforce at Soesterberg Airfield, Serge Sorbi of the Belgian Royal Airforce at Saint-Hubert Air Base and Mr. Bizeul of Lyonnaise des Eaux for their support stationing the bird radar. We thank Hans Beekhuis, Geert De Sadelaer, Christophe Ferauge, Jean-Claude Heinrich and Antoine Kergomard for technical support. We also thank Hans van Gasteren from the Royal Dutch Airforce for useful discussions and for providing MPR data as additional reference. This work was conducted within the framework of the European Space Agency's (ESA) Flysafe project.

References

Bachmann, S. and D. Zrnić: 2007, Spectral Density of Polarimetric Variables Separating Biological Scatterers in the VAD Display. *J. Atmos. Oceanic Technol.*, **24**, 1186–1198.

Bringi, V. N. and V. Chandrasekar: 2001, *Polarimetric Doppler Weather Radar*. Cambridge University Press.

Doviak, R. J. and D. S. Zrnić: 1993, *Doppler Radar and Weather Observations*. Academic Press, second edition, 562 pp.

Gonzales, R. C. and R. E. Woods: 1992, *Digital Image Processing*. Addison-Wesley.

Green, D. R. and R. A. Clark: 1972, Vertically Integrated Liquid Water - A new analysis tool. *Monthly Weather Review*, **100**, 548–552.

Holleman, I. and H. Beekhuis: 2003, Analysis and Correction of Dual-PRF Velocity Data. *J. Atmos. Oceanic Technol.*, **20**, 443–453.

Holleman, I., H. van Gasteren, and W. Bouten: 2008, Quality Assessment of Weather Radar Wind Profiles during Bird Migration. *J. Atmos. Oceanic Technol.*, **25**, 2188–2198.

Koistinen, J.: 2000, Bird Migration Patterns on Weather Radars. *Phys. Chem Earth B*, **25**, 1185–1194.

Marshall, J. S. and W. M. Palmer: 1948, The distribution of raindrops with size. *J. Meteor.*, **5**, 165–166.

Press, W. H., S. A. Teukolsky, W. T. Vetterling, and B. P. Flannery: 1992, *Numerical Recipes in C: the Art of Scientific Computing*. Cambridge University Press, second edition, 994 pp.

Probert-Jones, J. R.: 1962, The radar equation in meteorology. *The Quarterly Journal of the Royal Meteorological Society*, **88**, 485–495.

Seltmann, J. E. E.: 2000, Clutter versus radar winds. *Phys. Chem Earth B*, **25**, 1173–1178.

Sirmans, D., D. Zrnić, and B. Bumgarner: 1976, Extension of Maximum Unambiguous Doppler Velocity by Use of Two Sampling Rates. *17th Conference on Radar Meteorology*, Seattle, WA, AMS, 23–28.

Tabary, P., F. Guibert, L. Perier, and J. P. du Chatelet: 2006, An Operational Triple-PRT Doppler Scheme for the French Radar Network. *J. Atmos. Oceanic Technol.*, **23**, 1645–1656.

van Gasteren, H., I. Holleman, W. Bouten, E. van Loon, and J. Shamoun-Baranes: 2008, Extracting bird migration information from C-band weather radars. *Ibis*, **150**, 674–686, in press.

Wilks, D. S.: 1995, *Statistical Methods in the Atmospheric Sciences*. Academic Press, 467 pp.

Appendices

Appendix A: Information on the OPERA radar network

Since 2007 KNMI is responsible member for the weather radar program of EUMETNET (OPERA). The program focuses on the operational generation and quality control of an European weather radar composite, exchange of reflectivity and velocity volume data, exchange of quality information, and availability of radar data for operations and research. An OPERA Data Center (ODC) has been specified and development has begun mid 2009 and the operation will start early 2011.

Introduction

In 1999 the Operational Program on the Exchange of Weather Radar Information (OPERA) was established within the framework of EUMETNET (the Network of European Meteorological Services, www.eumetnet.eu.org). At that time, the clear objective was "To harmonize and improve the operational exchange of weather radar information between National Meteorological Services". The second phase of OPERA, 2004-2006, has involved a significant renewal of the Program's terms of reference, priorities, activities, and working methods.

Relevant user communities for weather radar data and products are aviation meteorologists, air traffic control, nowcasting, duty forecasters, NWP modelers, public safety authorities, hydrologists, and hydrological modelers. It is with these diverse and important user groups in mind that OPERA established its pilot Data Hub with the goal to demonstrate the full potential in the European Weather Radar Network. The third phase of the OPERA program is a joint effort of 30 European countries, runs from 2007 till 2011, and is managed by KNMI. OPERA-3 is designed to firmly establish the Program as the host of the European Weather Radar Network.

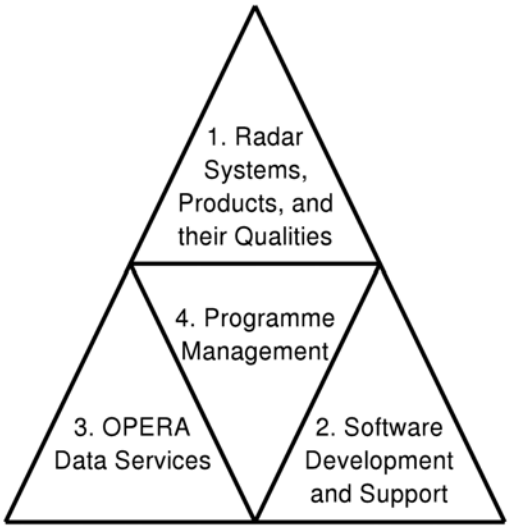

Figure A.1: Overview and interaction of program elements of OPERA-3.

Table A.1: An overview of the 30 European countries that are participating in the third phase of OPERA.

Austria	Belgium	Bulgaria
Croatia	Cyprus	Czech Republic
Denmark	Estonia	Finland
France	Germany	Greece
Hungary	Iceland	Ireland
Italy	Latvia	Luxembourg
Netherlands	Norway	Poland
Portugal	Romania	Serbia
Slovak Republic	Slovenia	Spain
Sweden	Switzerland	United Kingdom

Layout of the Program

Since 1 January 2007 Iwan Holleman (KNMI) is program manager of the third phase of OPERA. An overview of the 30 participating countries is given in Table A.1. Two OPERA meetings are arranged per year by the program manager and they are hosted by different National Meteorological Services (NMSs). Typically around 35 national delegates and project members from

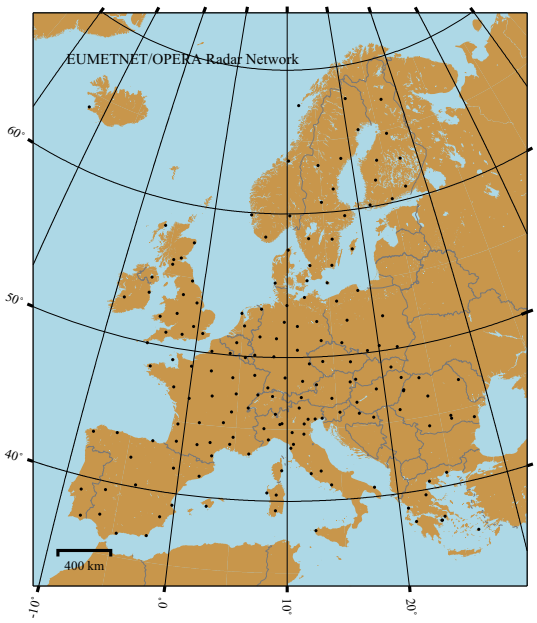

Figure A.2: Map showing the weather radar network of OPERA.

more than 20 countries attend these meetings. The OPERA meetings consist of a plenary session and parallel working group discussions. Two working groups have been established during this phase of OPERA: Working Group 1, chaired by Laurent Delobbe (RMI), is dedicated to "Radar Technology and Algorithms" and Working Group 2, chaired by Anton Zgonc (EARS), is dedicated to "Formats, Software, and Data Hub". The working groups monitor the progress and quality of the OPERA projects. A schematic overview of the program elements of OPERA-3 and their interaction is presented in Figure A.1. Currently OPERA's operational network consists of more than 150 weather radars, of which roughly 100 systems have Doppler processing and about 10 systems have dual-polarization capability. In the coming years the number of dual-polarization systems will increase dramatically, thus offering new opportunities for quantitative precipitation estimation. The European weather radar network of OPERA is displayed in Figure A.2. The OPERA program also interacts with several other EUMETNET programs, like EUCOS (European Composite Observing System), EUMETFREQ (Protection of radiofrequencies), WINPROF (Wind profiles), and SRNWP (Short Range Numerical Weather Prediction).

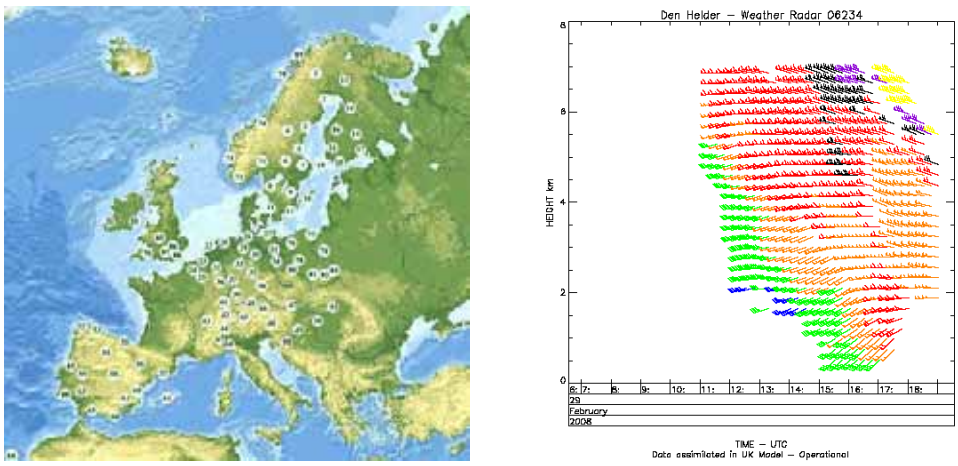

Figure A.3: Map in left frame shows the 91 radar sites that are sending profiles in real-time to CWINDE. The right frame shows an example of the display of WRWP on the CWINDE internet site for the KNMI weather radar in Den Helder.

Operational exchange of radar data

OPERA maintains and develops the agreed-upon mechanisms for exchanging radar data and products in Europe. The number of bilateral links between NMSs where radar data are exchanged operationally using OPERA tools and standards is now around 50. In addition weather radar data from roughly 100 sites are being sent to the pilot data hub. Finally the operational availability of weather radar wind profile (WRWP) products has increased dramatically since 2004 and currently data from 91 sites are exchanged in real-time (see below).

Weather radar wind profiles in CWINDE

The CWINDE data hub is operated as part of the EUMETNET program WINPROF-2 focused on wind profilers and weather radar wind profiles. In this program Austria, Finland, France, Germany, Hungary, Ireland, Netherlands, Switzerland and the United Kingdom are participating. This data hub was developed by the UK Met Office as part of the COST-76 Action on wind profilers and it is now running for more than 10 years. Currently the CWINDE data hub collects wind profiles from 27 wind profilers and 91 weather radars. The profiles are displayed on the internet (see Figure A.3) and monthly statis-

tics are determined.

Projects of OPERA program

Within the framework of the OPERA program a number of projects are conducted in the field of radar technology and algorithms and for development of exchange software and the data hub. Working group 1 is dealing with the following projects:

Weather radars in Europe

This activity is designed for the NMSs to maintain and update their entries to the OPERA radar database, and update the OPERA plenary on the status of their national radar networks.

Application of quality information for radars and radar data

The number of users of weather radar data is increasing and it is becoming increasingly important to incorporate quality information in radar products. In this project, work on quality which has been started in OPERA will be focussed, and recommendations will be formulated on how each NMS can create quality information for their radar data. The goal is to characterize the quality of products which will add value to their application. Close cooperation with the NWP and hydrological modelling communities, along with other data user communities, is required.

Promotion and evaluation of operational radar data use

This is a forum for radar data user communities to be able to meet the radar data providers on a regular basis, in conformance with the WMO recommendations on performing rolling reviews. Examples of such communities are aviation meteorologists, duty forecasters, NWP modellers, hydrologists, and hydrological modellers, and developers of nowcasting models, depending on which of these are nominated from a given country. The emphasis is on operational requirements from these user communities and how data providers can support them in using radar data and products to their greatest potential, as a part of an integrated observing system. Topics include the selection of appropriate radar technology for a given application, radar configuration issues, product definitions, and quality indicators.

Evaluation of new technologies

This is a forum wherein radar experts collect information on and evaluate new and expected radar technology. Examples of such technology are: dual-polarization (started in OPERA-2), multi-parameter systems, rapid-scanning systems, use of phased-array antennas, sensor synergy, physical parameter retrievals, phase-coding algorithms, accuracy of such retrieval algorithms, choice of frequency, gap-filling systems, dual-Doppler, radome issues, sources of error, etc. The results of such evaluations are useful when procuring new radar systems.

Site and frequency protection

This activity serves to collect European expertise on how weather radar is adversely affected by various disturbances such as wind turbines, jamming transmitters, buildings and other structures, and how such disturbances can be constructively minimized, either through pre-emptive administrative management and policy, or through signal/data analysis techniques. OPERA works closely together with EUMETFREQ in this project.

Harmonized production practices

In order to harmonize the application and exchange of weather radar data throughout Europe, either through bilateral agreements or through the data's use at the OPERA Data Hub, an agreed-upon set of guidelines must be available. Such guidelines should address best-practises for radar configuration, and production algorithms for internationally-exchanged data and products. This work is an important part of the efforts of increasing the quality of the radar data and products.
And Working group 2 is dealing with the following projects:

Data exchange software development

Based on the results of OPERA-2, the issue of selecting appropriate technology which will enable and facilitate foreseen needs for the exchange of data and products are carefully analyzed. Once this has been achieved, appropriate tools will be developed, made available, and supported for all OPERA members. Furthermore this project includes a limited development of the OPERA BUFR software.

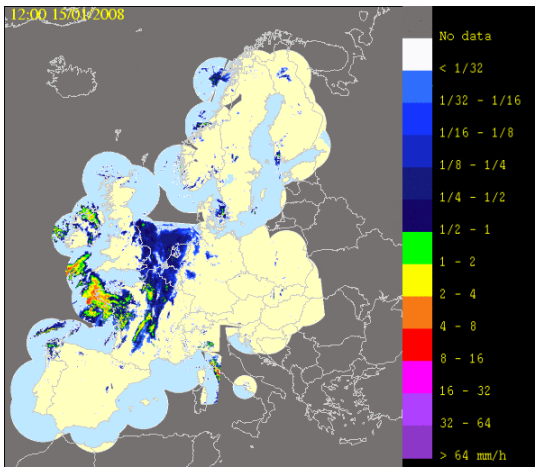

Figure A.4: Example of European radar composite from pilot data hub of 15 January 2008 at 1200 UTC.

BUFR software maintenance

This activity concerns the maintenance of OPERA BUFR software. User support is provided to the OPERA group and other users of the OPERA BUFR software, including commercial radar software suppliers.

BUFR table maintenance

This activity includes defining new descriptors, sequences, and tables for use with OPERA BUFR exchange software, where relevant and applicable, based on results achieved in other projects.

Compositing software support

Within the first OPERA Program, compositing software has been developed that is available to all OPERA members. It is portable software that runs on all commonly available computer platforms. For the continuation, this work package covers the support of the software.

Pilot Data Hub operations

Maintenance and operation of the pilot Data Hub was established during OPERA-2. The pilot hub is expected to run for an initial two years (2007-2008) and also in 2009 during the development of the operational hub. The pilot hub gives data services for quality control purposes and non-commercial

use within NMSs only. A recent example of a European radar composite produced by the pilot data hub is shown in Figure A.4.

Development of OPERA Data Center (ODC)

A project team within OPERA is currently collecting the user requirements for the OPERA Data Center (ODC) and drafting its functional specifications. For this, the project team has evaluated the pilot data hub and other operational radar data hubs, e.g. CWINDE, NORDRAD, and US National Radar Mosaic. In addition four priority user groups have been selected and the user requirements for these groups have been drafted:

- Core services forecasting and nowcasting
- NWP (Assimilation and verification)
- Hydrology
- Civil and military aviation

Since June 2007 visits to Eurocontrol and ECMWF have been paid and valuable feedback on the draft user requirements has been collected. In addition the project team has discussed the user requirements within their institutes. Contacts with COST 731, SRNWP, and JRC Ispra (Flood forecasting) have been established and feedback was received. In April 2008 the project team has finalized the user requirements and the functional specifications. The document was approved by EUMETNET's Program Board for Observations in June 2008. In October 2008 the functional specifications for the operational data were approved by the Council of EUMETNET and subsequently a call tro become Responsible Member for the development and operation of the ODC was issued. At the May 2009 Council meeting Météo France and UK Met Office were selected as Responsible Members and the ODC developement phase has now begun. Start of operation of the ODC is planned for early 2011.

Summary and outlook

The new OPERA program will focus on the operational generation and quality control of a European weather radar composite, exchange of 3D radar reflectivity and wind data, exchange of quality information, and availability of radar data for official duties of NMSs and research. An operational

Figure A.5: Snapshot of the internet site of OPERA.

weather radar Data Center will be specified, developed, and operated during this phase of OPERA. This OPERA Data Center is crucial for reaching the main objective of OPERA-3, i.e., establishing the weather radar networking as a solid element of the European infrastructure. In this paper, the OPERA program and its objectives have been discussed, and opportunities for use of European weather radar data in hydrological research and applications have been highlighted. More information on the OPERA program and the projects can be found on the internet site (www.knmi.nl/opera) and deliverables of the current and previous programs, both software and project documents, can be downloaded (see Figure A.5).

Acknowledgments

All national delegates and project members of OPERA are gratefully acknowledged for their efforts and the pleasant collaboration. Especially the contribution of the other authors of the OPERA-3 proposal (on which a part of this paper is based), i.e., Asko Huuskonen (FMI), Jean-Luc Chèze (Météo France), Stuart Matthews (UK Met Office), and Daniel Michelson (SMHI), is recognized.

Appendix B: Algorithm product sheet and syntax

Algorithm product sheet

Table B.1 summarizes the most important technical characteristics of the developed bird detection system for weather radar.

Table B.1: Bird algorithm product sheet

altitude resolution	200 m
time resolution	5-15 min
minimum-maximum range used	10-25 km
probability of detection	98%
false alarm rate (due to precipitation contamination)	2%
bird density accuracy	within a factor 2-3
bird radar cross section σ_{bird}	12±14 cm^2
explained variance (R^2) bird density (assuming constant σ_{bird})	0.74
sensitivity	< 1 bird/km^3
bird speed accuracy	2±1 m/s
bird speed bias (at ground speeds below 15 m/s only)	-3 m/s
bird direction accuracy	8±8°

Algorithm output data format specification

The weather radar algorithm for bird detection produces three profiles:

profile1 Bird profile, based on gates outside the precipitation map

profile2 Non-bird profile, based on gates inside the precipitation map

profile3 Combined profile including both bird and non-bird gates. This profile is identical to the KNMI operational wind profile.

Table B.2 lists all datasets produced by the weather radar bird detection algorithm. Refer to section 7.5.1 for definitions of the different types of range gates.

Table B.2: HDF5 data format specification of algorithm profile output

Group	Dataset	Description	units
profile1 (birds)	profile_height	height above ground	km
	profile_bird_reflectivity	bird reflectivity η_{bird}	$\mathrm{cm}^2/\mathrm{km}^3$
	profile_reflectivity	bird reflectivity factor Z_{bird}	dBZ (Z in $\mathrm{mm}^6/\mathrm{m}^3$)
	profile_speed	bird ground speed	m/s
	profile_direction	direction ground speed vector (direction *towards* birds are flying)	clockwise °from N
	profile_radial_stddev_wind	radial velocity standard deviation σ_{r}. Identical to profile_radial_stddev in profile3 group	m/s
	profile_radial_stddev	radial velocity standard deviation calculated for range gates $\mathbb{N}_{\mathrm{valid}}$ only	m/s
	profile_fraction_bird	fraction of gates indentified as birds: $(N_{\mathrm{valid}} + N_{\mathrm{empty}})/N_{\mathrm{total}}$	-
	profile_fraction_clutter	fraction of gates excluded as clutter: $(N_{\mathrm{total}} - N_{\mathrm{valid}} - N_{\mathrm{empty}})/N_{\mathrm{total}}$	-
	profile_fraction_fringe	fraction of fringe gates: $N_{\mathrm{fringe}}/N_{\mathrm{total}}$	-
	profile_fraction_nonbird	fraction of non-bird gates (excluding fringes): $N_{\mathrm{precip}}/N_{\mathrm{total}}$	-
	profile_fraction_cellmap	fraction of non-bird gates in the radial velocity analysis and calculation of σ_{r}: $(N_{\mathrm{precip}}+N_{\mathrm{fringe}})/(N_{\mathrm{precip}}+N_{\mathrm{fringe}}+N_{\mathrm{valid}})$	-
	profile_number	number of gates in radial velocity analysis N_{valid} excluding outliers removed by -vdif flag	-
	profile_dbz_number	number of gates in average (bird) reflectivity calculation $N_{\mathrm{valid}} + N_{\mathrm{empty}}$	-
	profile_u_bird	u component of ground speed (positive towards the east)	m/s
	profile_v_bird	v component of ground speed (positive towards the north)	m/s
	profile_w_bird	vertical velocity component	m/s
profile2 (non-birds)	profile_height	height above ground	km
	profile_reflectivity	non-bird reflectivity factor	dBZ
	profile_speed	non-bird ground speed	m/s
	profile_direction	direction ground speed vector	clockwise °from N

	profile_radial_stddev	radial velocity standard deviation calculated for range gates $\mathbb{N}_{\text{precip}}$ only	m/s
	profile_number	number of gates in radial velocity analysis N_{precip} excluding outliers removed by -vdif flag	-
	profile_dbz_number	number of gates in average reflectivity calculation N_{precip}	-
	profile_u_nonbird	u component of ground speed (positive towards the east)	m/s
	profile_v_nonbird	v component of ground speed (positive towards the north)	m/s
	profile_w_nonbird	vertical velocity component	m/s
profile3 (wind)	profile_height	height above ground	km
	profile_reflectivity	reflectivity factor (bird+non-bird)	dBZ
	profile_speed	ground speed	m/s
	profile_direction	direction ground speed vector (direction *towards* the wind is blowing, i.e. conventional meteorological wind direction $+180°$)	clockwise °from N
	profile_radial_stddev	radial velocity standard deviation calculated for range gates $\mathbb{N}_{\text{valid}} \cup \mathbb{N}_{\text{precip}}$	m/s
	profile_number	number of gates in radial velocity analysis $N_{\text{precip}} + N_{\text{valid}}$ excluding outliers removed by -vdif flag	-
	profile_dbz_number	number of gates in average reflectivity calculation $N_{\text{valid}} + N_{\text{empty}} + N_{\text{precip}}$	-
	profile_u_wind	u component of ground speed (positive towards the east)	m/s
	profile_v_wind	v component of ground speed (positive towards the north)	m/s
	profile_w_wind	vertical velocity component	m/s

Algorithm syntax

```
usage: vol2birdprof_h5 <h5-volume> <h5-profile> [options]

   Common user options, with defaults in []:
      -h --help               show this message
      -verbose                Print rain/clutter cell properties to stdout [no]
      -printformat<1/2/3>     Select print output level of detail: medium (1), long (2)
                              or short(3) [1]
      -vad<1/2>/-vvp<1/2/3>   Select profile analysis scheme [vvp1]
      -rmin<range>            Minimum range used in km [10.0]
      -rmax<range>            Maximum range used in km [25.0]
      -amin<azimuth>          Minimum azimuth used in height layer reflectivity
                              average in deg [0.0]
      -amax<azimuth>          Maximum azimuth used in height layer reflectivity
                              average in deg [360.0]
      -rms<scan>              Exclude scan <scan> [no]
      -rscan<scan>min<range>  Set minimum range for scan <scan> [rmin]
      -rscan<scan>max<range>  Set maximum range for scan <scan> [rmax]
      -img                    Output rainmask and texture fields into <h5-profile> [no]

   Rain/clutter masking user options, with defaults in []:
      -cm <h5-cluttermap>  Assign static clutter map in KNMI hdf5 format [no]
      -dbzclutter<x>       Reflectivity threshold in static cluttermap for excluding
                           pixels as clutter in dBZ [-10.0]
```

```
   -vmin<x>            Minimum absolute value of velocity of pixels that are
                       excluded as clutter in m/s [1.0]
   -dbzx<x>            Maximum pixel reflectivity to include in height layer
                       averaged reflectivity in dBZ [20.0]
   -dbzrain<x>         Lower reflectivity threshold in dBZ for considering pixels
                       for inclusion in clutter/rain map [0.0]
   -dbzcell<x>         Lower threshold of cell-averaged reflectivity
                       for valid raincells [15.0]. Cell-averaged reflectivity
                       calculated for clutter free areas (ref. -vmin and -cm flags)
                       only.
   -stdevcell<x>       Upper threshold of cell-averaged radial velocity standard
                       deviation for valid raincells [5.0]. Cell-averaged radial
                       velocity calculated for clutter free areas (ref. -vmin and
                       -cm flags) only
   -clutcell<x>        Always keep raincells in the cluttermap that have a higher
                       fraction of clutter than this threshold. [0.5] Guarantees
                       that the central clutter area around the radar is never
                       dropped from cluttermap by -dbzcell/-stdevcell criteria
   -emask<x>           Width of fringe by which to enlarge the identified cells
                       in the rainmask in km [3.0]
   -cellarea<x>        Drop cells from cluttermap that have a smaller area than this
                       threshold in no of pixels [4]. False detections of small
                       raincells often occur within areas of birds. Dropping these
                       cells prevents that a disproportionately large area would be
                       masked as rainclutter after fringing these cells according to
                       -emask criterium
   -rcellmax<x>        Maximum range over which to compute rainmask in km [rmax+5]
   -tex<1/2>           Compute texture as the radial velocity standard deviation
                       sigma_v (tex1) or as a coefficient of variation
                       10log10(Z/sigma_v) (tex2) [tex1]
   -cv                 Coefficient of variation threshold for raincell finding [0.0].
                       Only applies when -tex2 flag is set.
   -ntexbinazim<x>     Dimension in pixels in azimuthal direction of area over which
                       to calculate texture field [3]
   -ntexbinrang<x>     Dimension in pixels in range of area over which to calculate
                       texture field [3]
   -ntexmin<x>         Minimum number of valid pixels for allowing texture field
                       calculation [4]

Radial velocity profiling user options, with defaults in []:
   -stdevbird    Radial velocity standard deviation threshold to decide on bird
                 presence [2.0]
   -vdif<x>      Maximum allowed deviation from first fit in m/s
                 (to drop outliers) [10.0]
   -ngapmin<x>   Minimum required number of data points per 45.0 deg azimuth
                 segment [5]
   -vsignflip    Flip the radial velocity sign [no]

Dual polarization user options, with defaults in []:
   -dualpol     Use dual-pol fields for rain masking [no]
   -rhomin      Correlation coefficient threshold for inclusion in rainmap [0.9]
   -zdrmin      Differential reflectivity threshold for inclusion in rainmap
                (to mask insect echoes) [3.0]
```

Appendix C: Bird density height profiles

Table C.1: Description height profile color scales. The bird density color scale is logarithmic and spans a range of bird densities of 0.5-500 birds/km^3. The color scale of weather radar reflectivities matches the bird density scale for σ_{bird}=13 cm^2.

color	$^{10}\log \rho_{\text{bird}}$	ρ_{bird} [km^{-3}]	Z_{bird} [dBZ]	η_{bird} [cm^2 km^{-3}]
Yellow	-0.3 – 0.7	0.5 – 5	-18 – -8	5 – 50
Orange	0.7 – 1.2	5 – 15	-8 – -3	50 – 150
Red	1.2 – 1.7	15 – 50	-3 – 2	150 – 500
Purple	1.7 – 2	50 – 100	2 – 5	500 – 1000
Blue	2 – 2.4	100 – 250	5 – 9	1000 – 2500
Blackish	>2.4	>250	>9	>2500

Bird speed and direction are plotted as wind barbs. Each half flag represents 5 knots, each full flag 10 knots, each pennant (filled triangle) 50 knots (1 knot = 1.9 km/hour).

Wideumont campaign

The Wideumont weather weather radar is located (49.915N, 5.505E) at 585 m asl. The bird radar reference was stationed at Saint Hubert airbase (N 50° 1.8' / E 5° 26.4' , 577m asl). The depicted heights are heights above mean sea level. Additionally the vertically integrated bird density is shown for the South-East measurement windows of the Medium Power Radar (MPR) in Glons, as determined by the ROBIN-4 system.

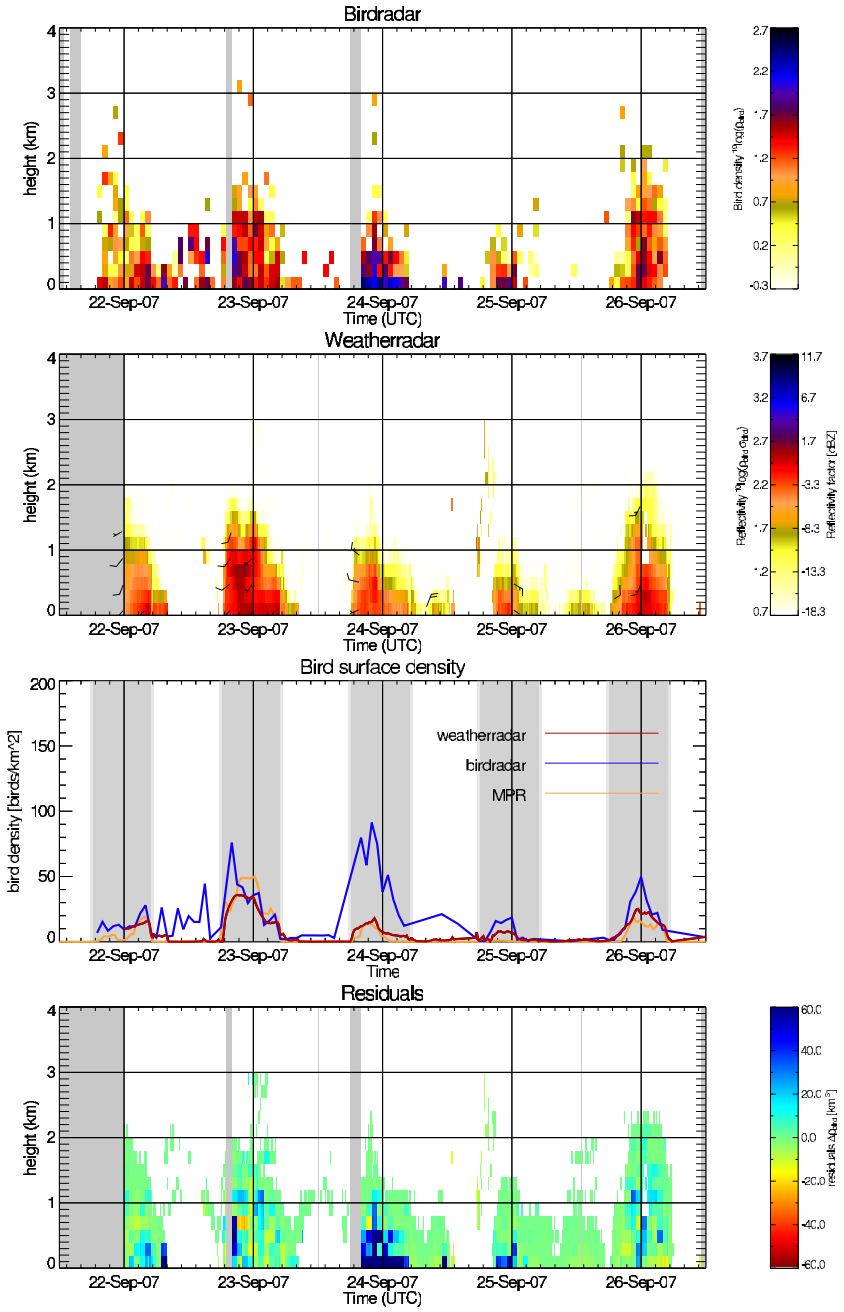

Figure C.1: Retrieved time-height profiles by birdradar (top) and weatherradar (upper middle). The vertically integrated bird densities and weather radar - bird radar density difference are shown in the lower middle and bottom panel, resp.

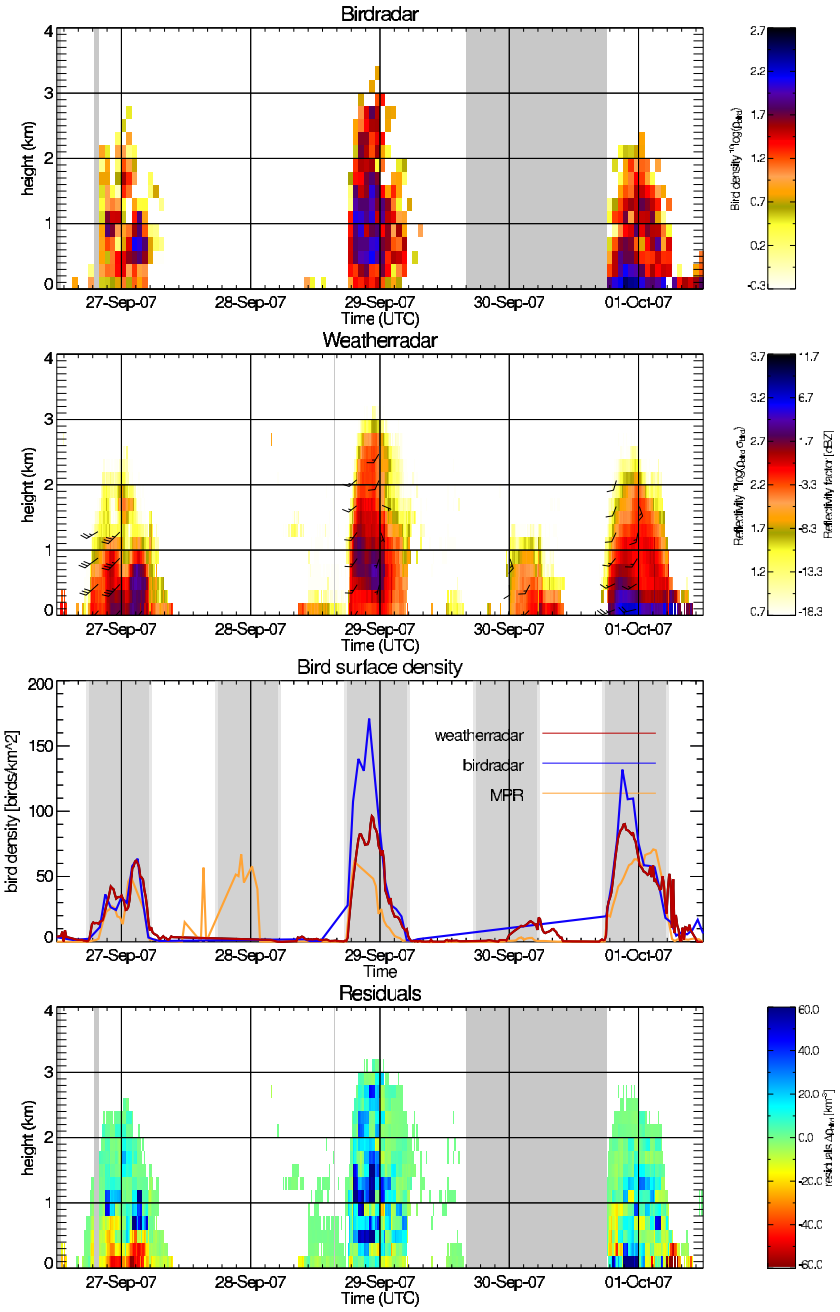

Figure C.2: Retrieved time-height profiles by birdradar (top) and weatherradar (upper middle). The vertically integrated bird densities and weather radar - bird radar density difference are shown in the lower middle and bottom panel, resp.

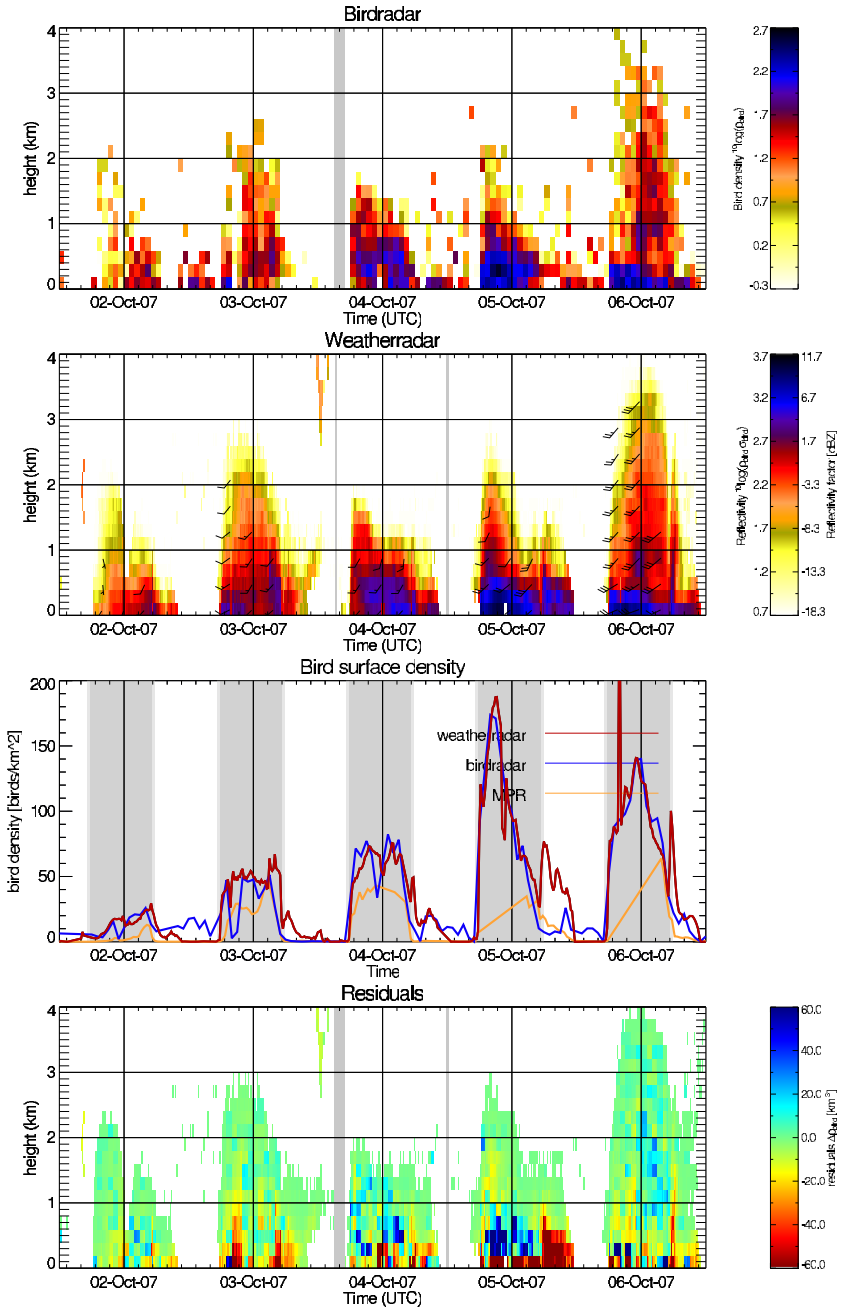

Figure C.3: Retrieved time-height profiles by birdradar (top) and weatherradar (upper middle). The vertically integrated bird densities and weather radar - bird radar density difference are shown in the lower middle and bottom panel, resp.

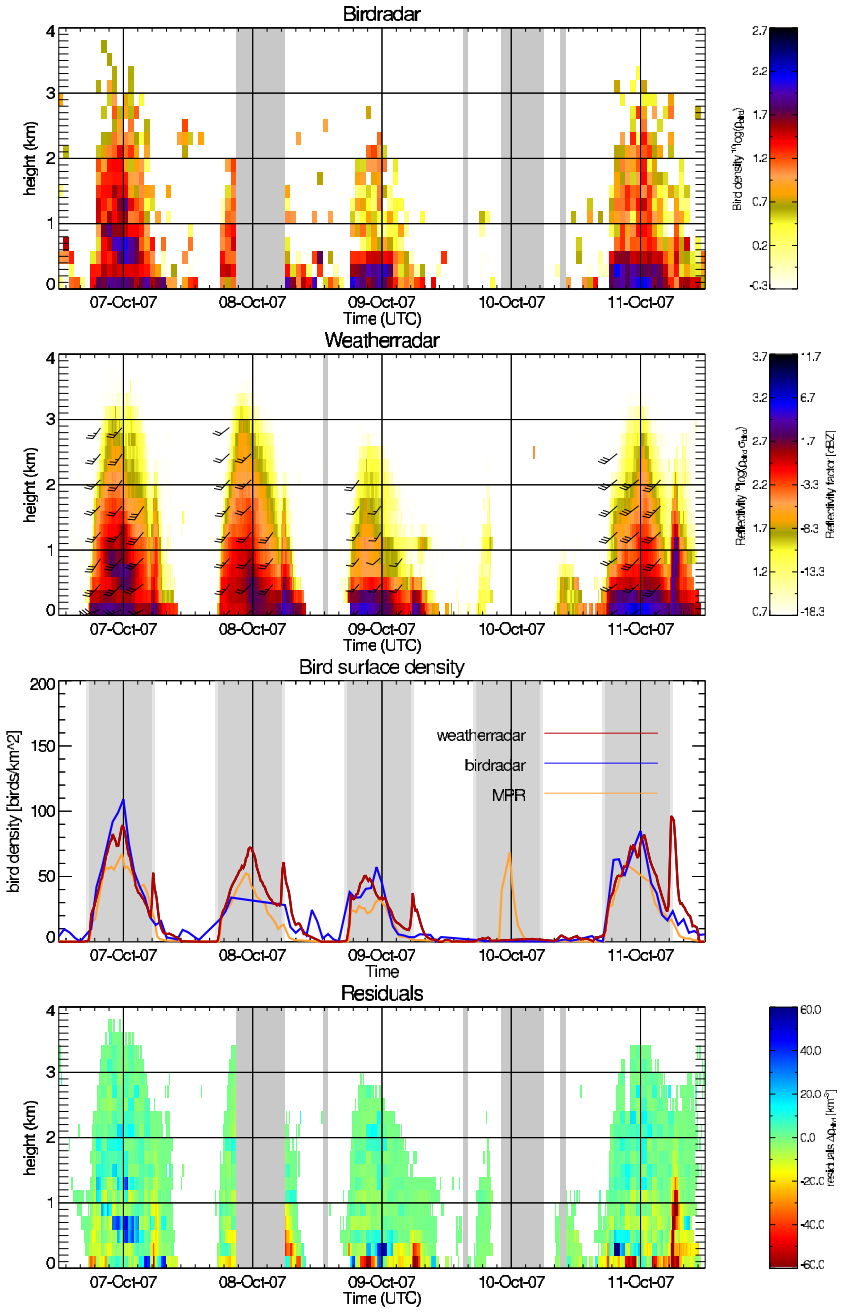

Figure C.4: Retrieved time-height profiles by birdradar (top) and weatherradar (upper middle). The vertically integrated bird densities and weather radar - bird radar density difference are shown in the lower middle and bottom panel, resp.

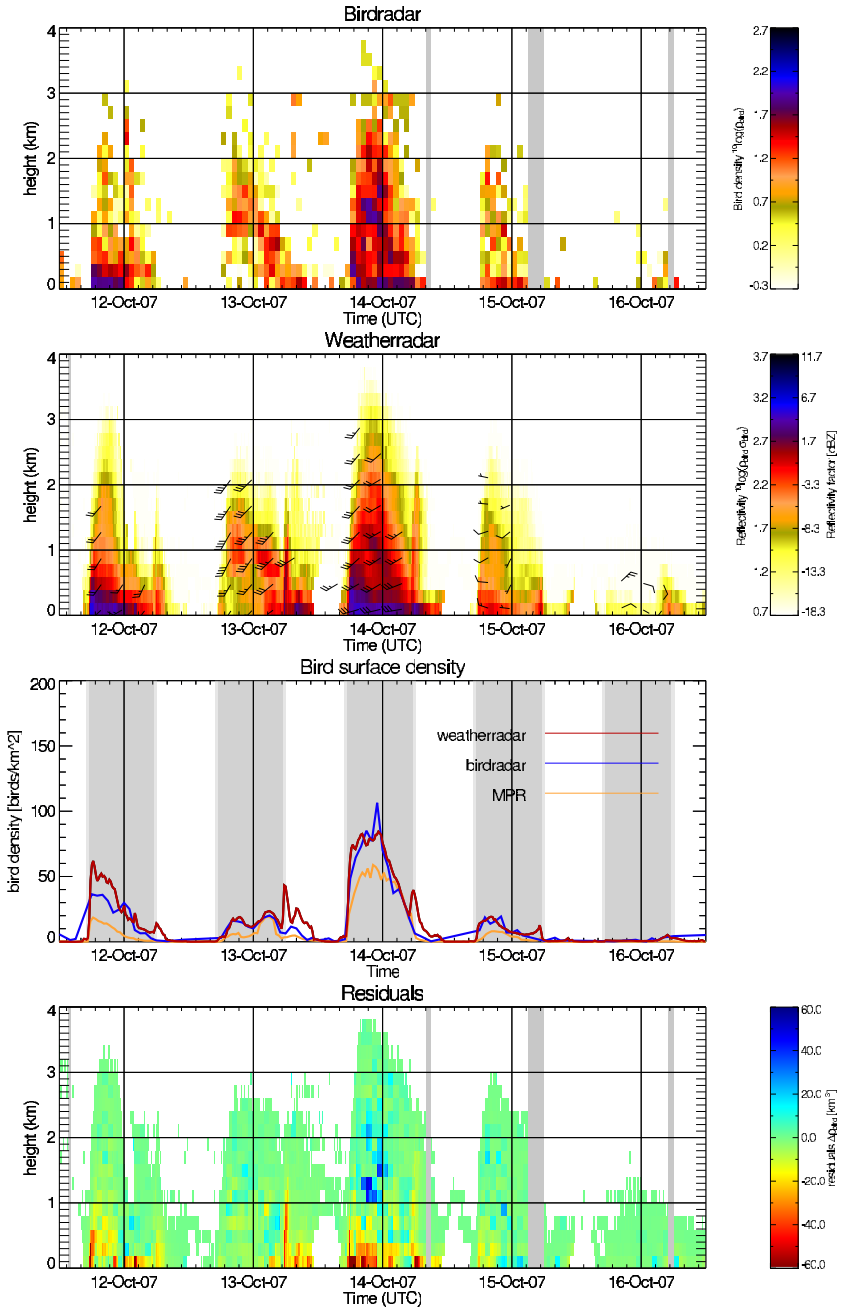

Figure C.5: Retrieved time-height profiles by birdradar (top) and weatherradar (upper middle). The vertically integrated bird densities and weather radar - bird radar density difference are shown in the lower middle and bottom panel, resp.

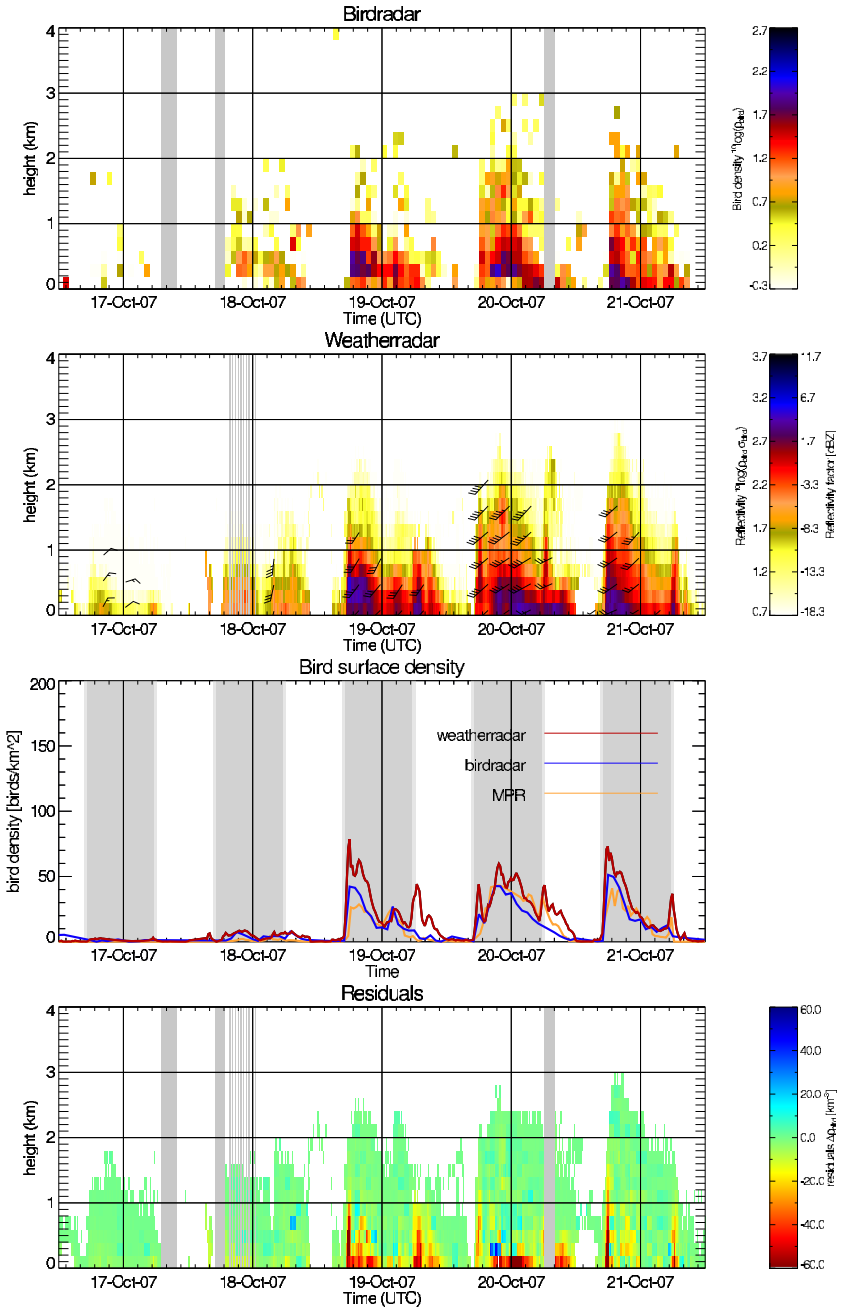

Figure C.6: Retrieved time-height profiles by birdradar (top) and weatherradar (upper middle). The vertically integrated bird densities and weather radar - bird radar density difference are shown in the lower middle and bottom panel, resp.

De Bilt campaign

The De Bilt weather weather radar is located (52.103N, 5.179E). The bird radar reference was stationed at Soesterberg airbase (N 52° 7.8' / E 5° 16.8' , 10m asl). Additionally the vertically integrated bird density is shown for the South-East measurement windows of the Medium Power Radar (MPR) in Wier, as determined by the ROBIN-4 system.

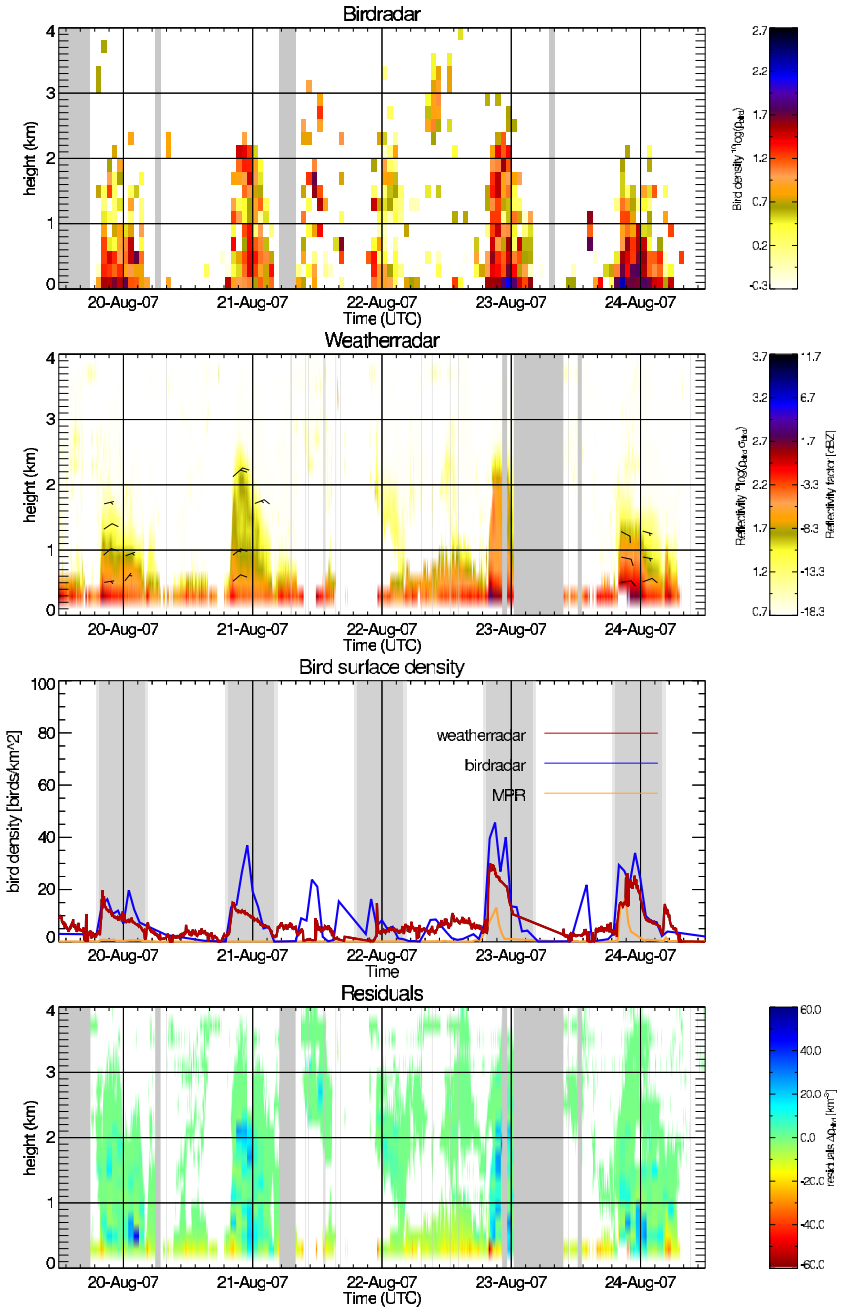

Figure C.7: Retrieved time-height profiles by birdradar (top) and weatherradar (upper middle). The vertically integrated bird densities (lowest 200 m excluded) and weather radar - bird radar density difference are shown in the lower middle and bottom panel, resp.

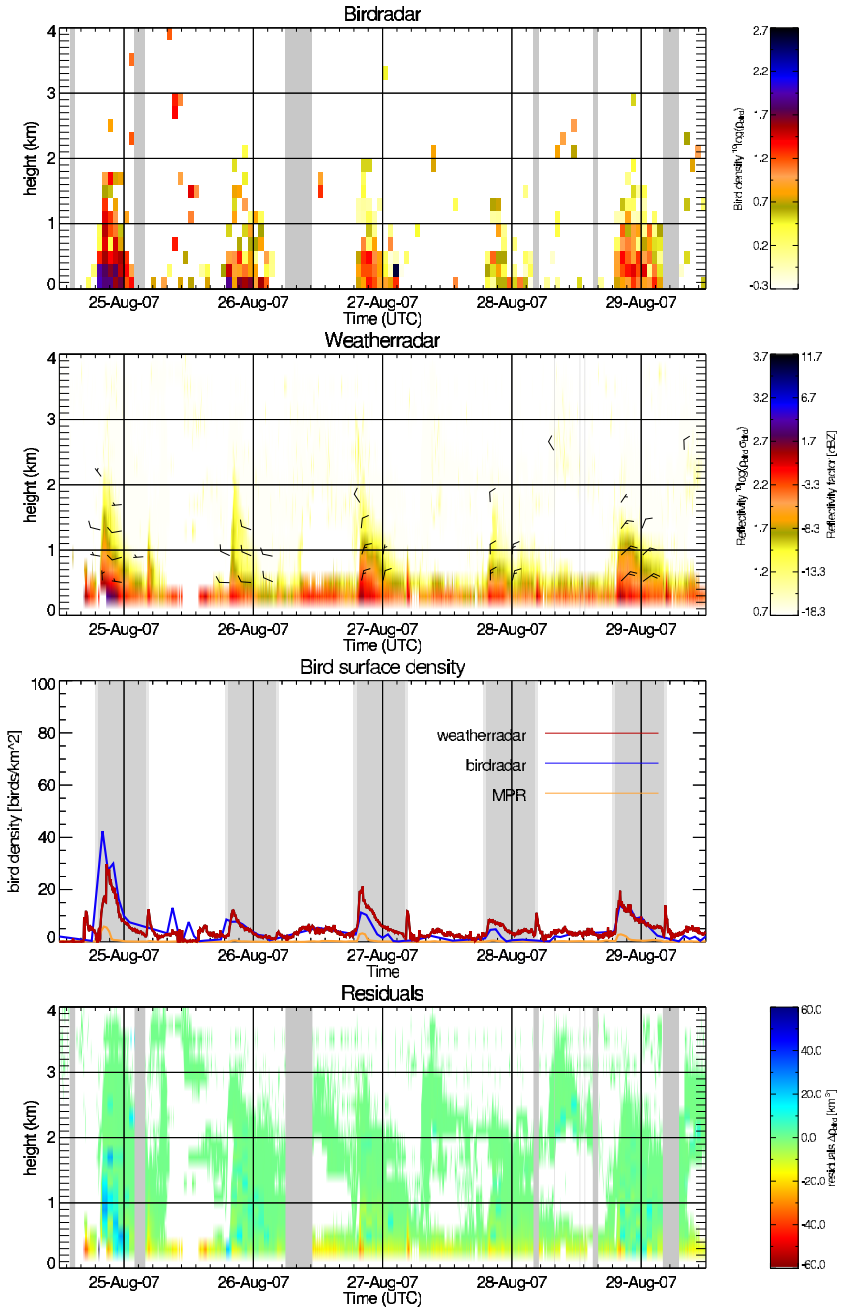

Figure C.8: Retrieved time-height profiles by birdradar (top) and weatherradar (upper middle). The vertically integrated bird densities (lowest 200 m excluded) and weather radar - bird radar density difference are shown in the lower middle and bottom panel, resp.

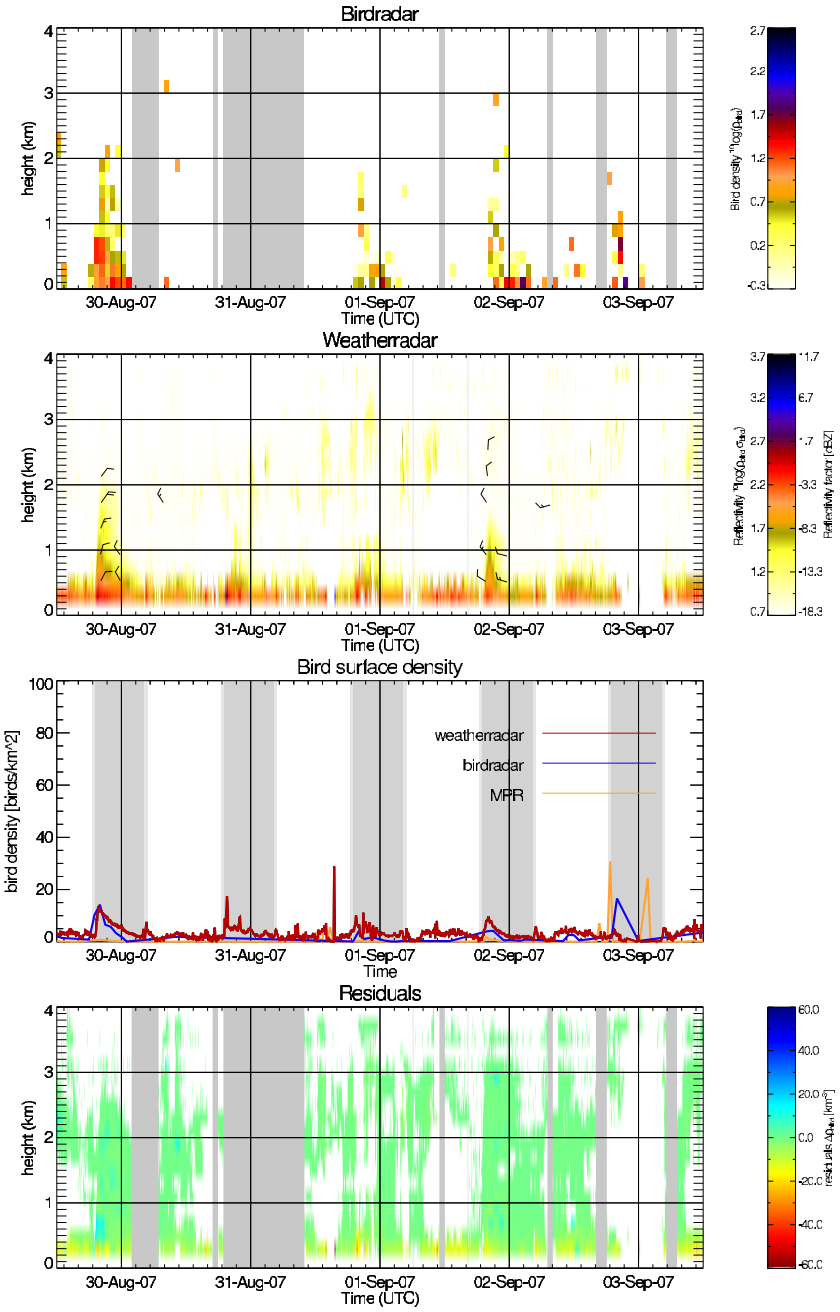

Figure C.9: Retrieved time-height profiles by birdradar (top) and weatherradar (upper middle). The vertically integrated bird densities (lowest 200 m excluded) and weather radar - bird radar density difference are shown in the lower middle and bottom panel, resp.

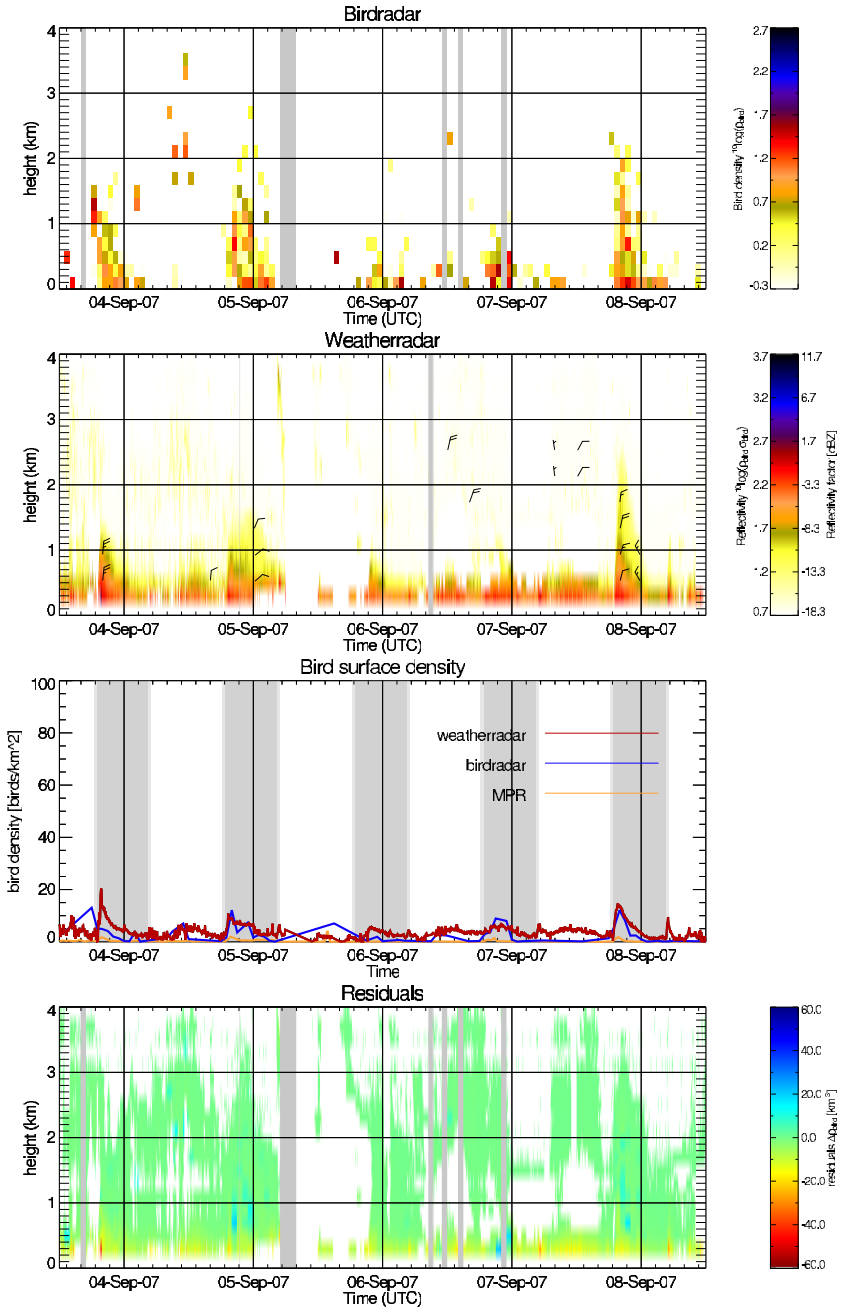

Figure C.10: Retrieved time-height profiles by birdradar (top) and weather-radar (upper middle). The vertically integrated bird densities (lowest 200 m excluded) and weather radar - bird radar density difference are shown in the lower middle and bottom panel, resp.

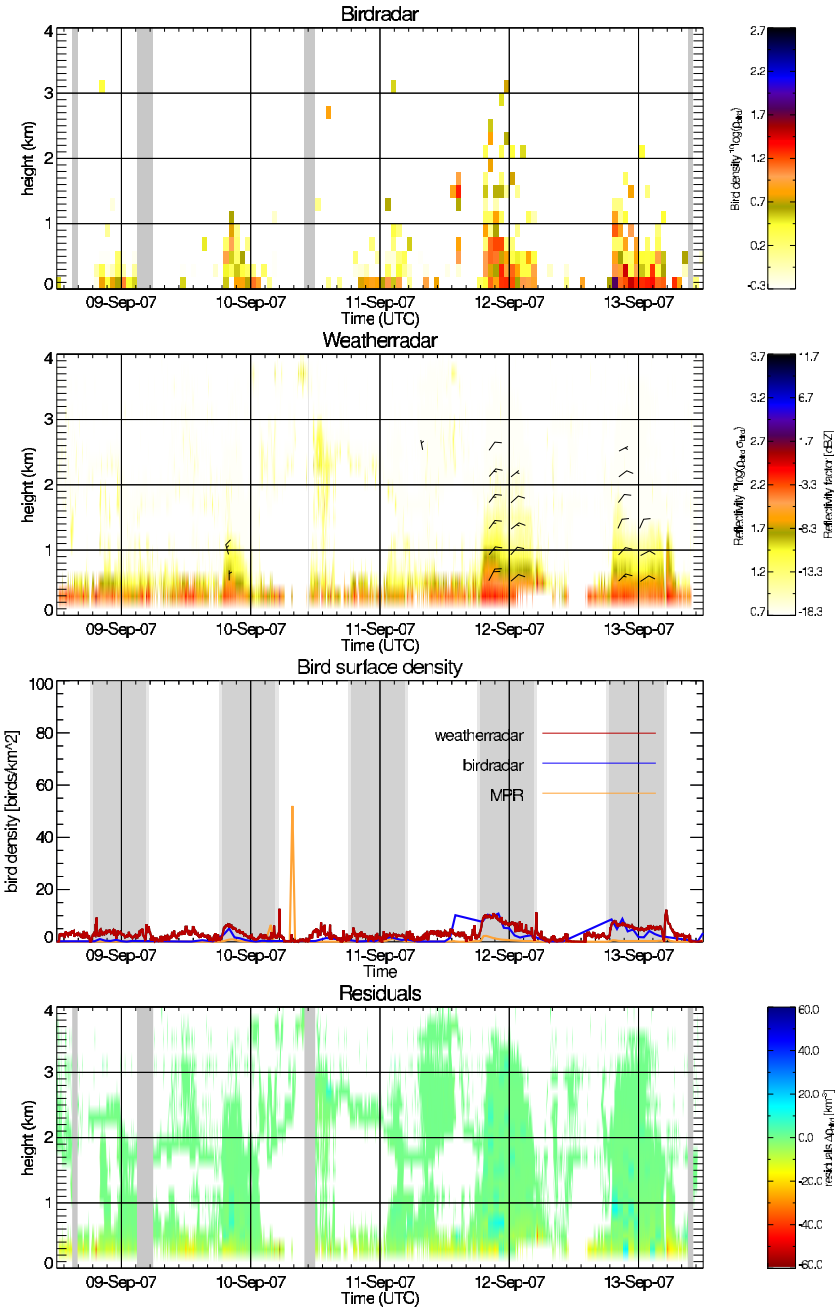

Figure C.11: Retrieved time-height profiles by birdradar (top) and weather-radar (upper middle). The vertically integrated bird densities (lowest 200 m excluded) and weather radar - bird radar density difference are shown in the lower middle and bottom panel, resp.

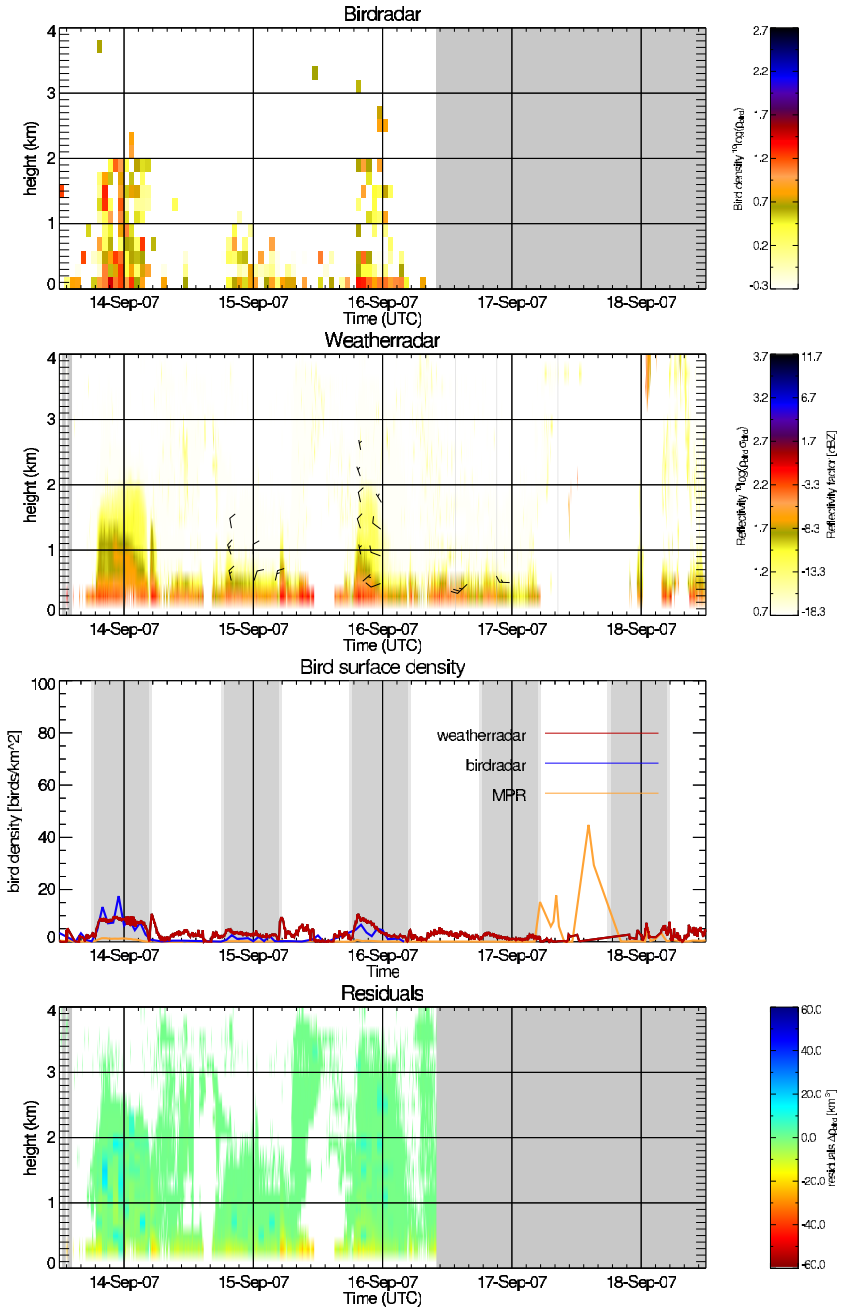

Figure C.12: Retrieved time-height profiles by birdradar (top) and weather-radar (upper middle). The vertically integrated bird densities (lowest 200 m excluded) and weather radar - bird radar density difference are shown in the lower middle and bottom panel, resp.

Trappes campaign

The Trappes weather weather radar is located (48.775N, 2.009E). The bird radar reference was stationed at near Flins sur Seine (N 48° 34.8' / E 1° 31.2', 577m asl)

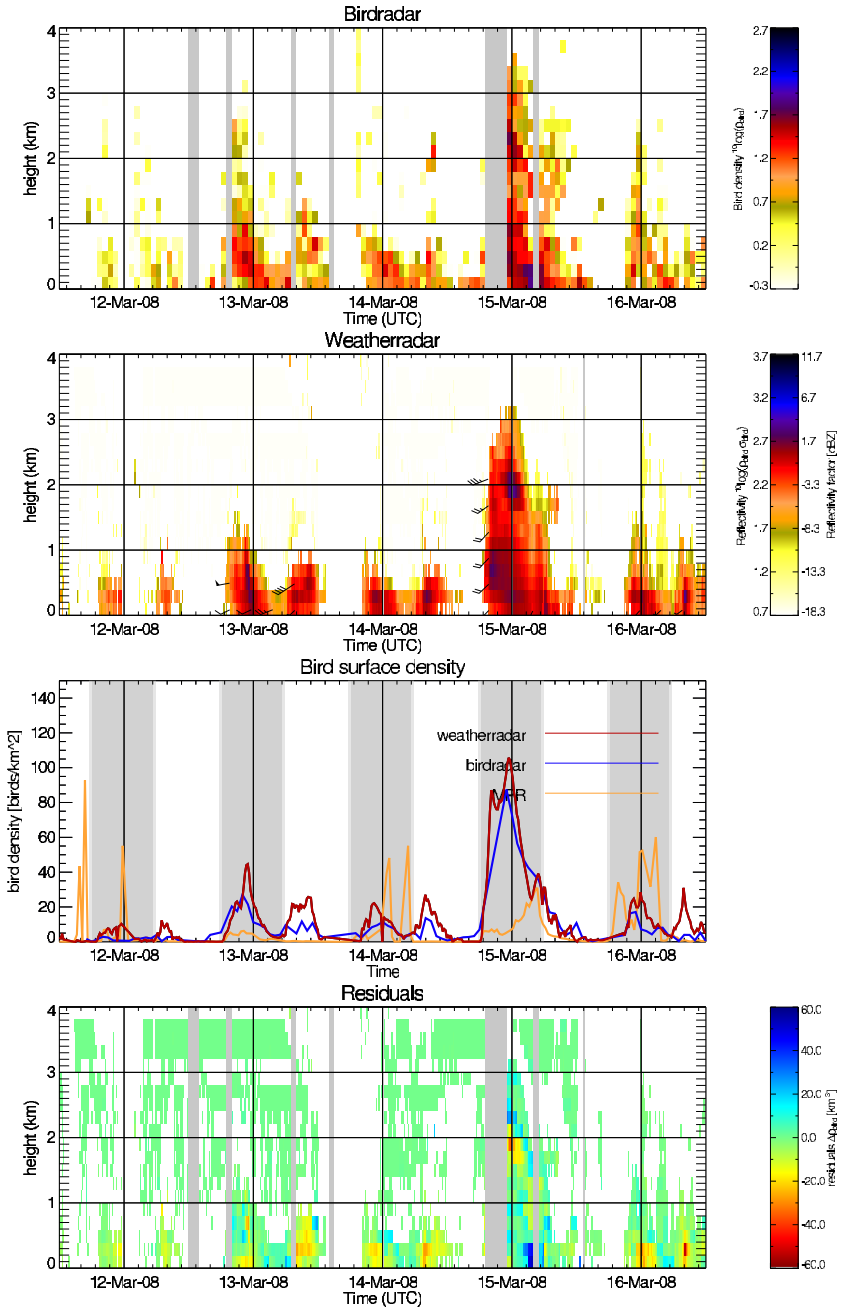

Figure C.13: Retrieved time-height profiles by birdradar (top) and weather-radar (upper middle). The vertically integrated bird densities (lowest 200 m excluded) and weather radar - bird radar density difference are shown in the lower middle and bottom panel, resp.

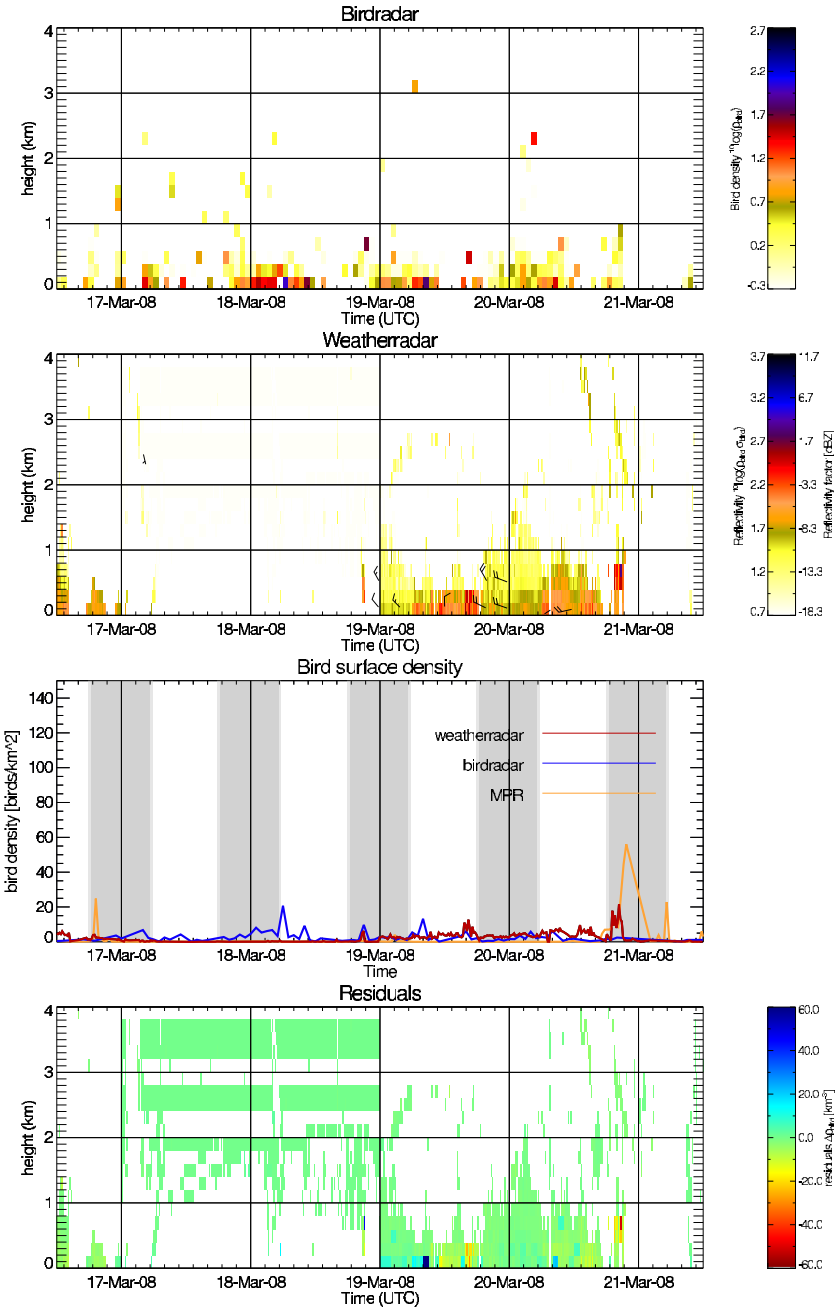

Figure C.14: Retrieved time-height profiles by birdradar (top) and weather-radar (upper middle). The vertically integrated bird densities (lowest 200 m excluded) and weather radar - bird radar density difference are shown in the lower middle and bottom panel, resp.

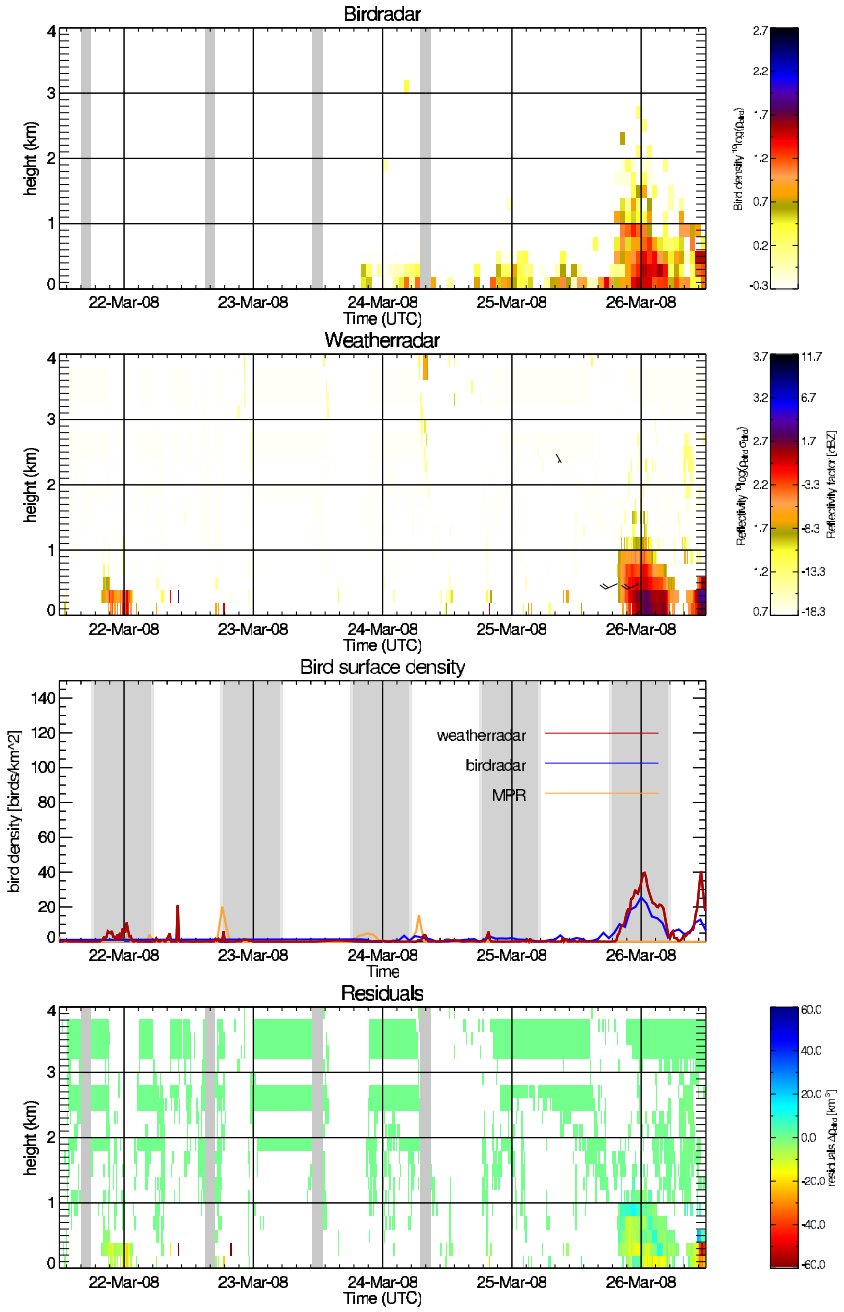

Figure C.15: Retrieved time-height profiles by birdradar (top) and weather-radar (upper middle). The vertically integrated bird densities (lowest 200 m excluded) and weather radar - bird radar density difference are shown in the lower middle and bottom panel, resp.

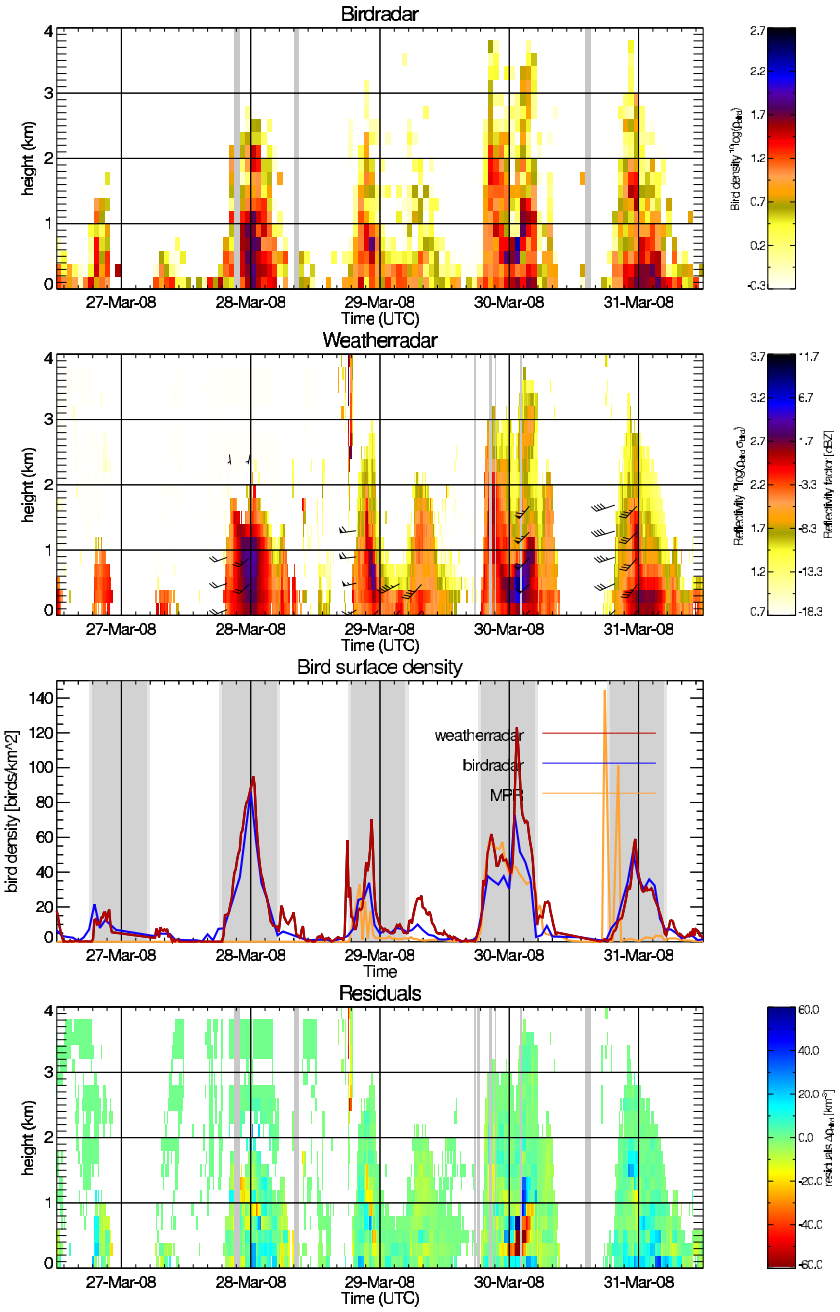

Figure C.16: Retrieved time-height profiles by birdradar (top) and weatherradar (upper middle). The vertically integrated bird densities (lowest 200 m excluded) and weather radar - bird radar density difference are shown in the lower middle and bottom panel, resp.

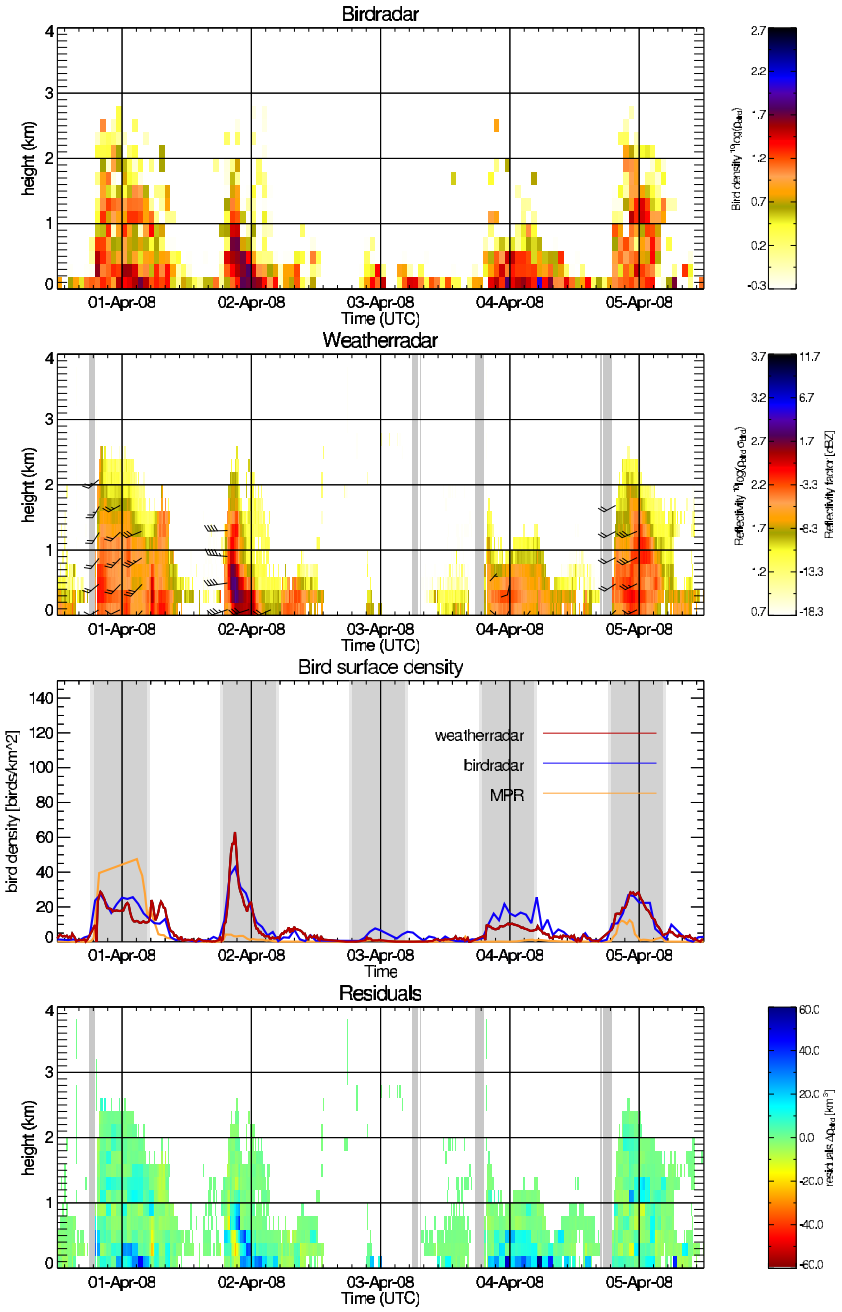

Figure C.17: Retrieved time-height profiles by birdradar (top) and weather-radar (upper middle). The vertically integrated bird densities (lowest 200 m excluded) and weather radar - bird radar density difference are shown in the lower middle and bottom panel, resp.

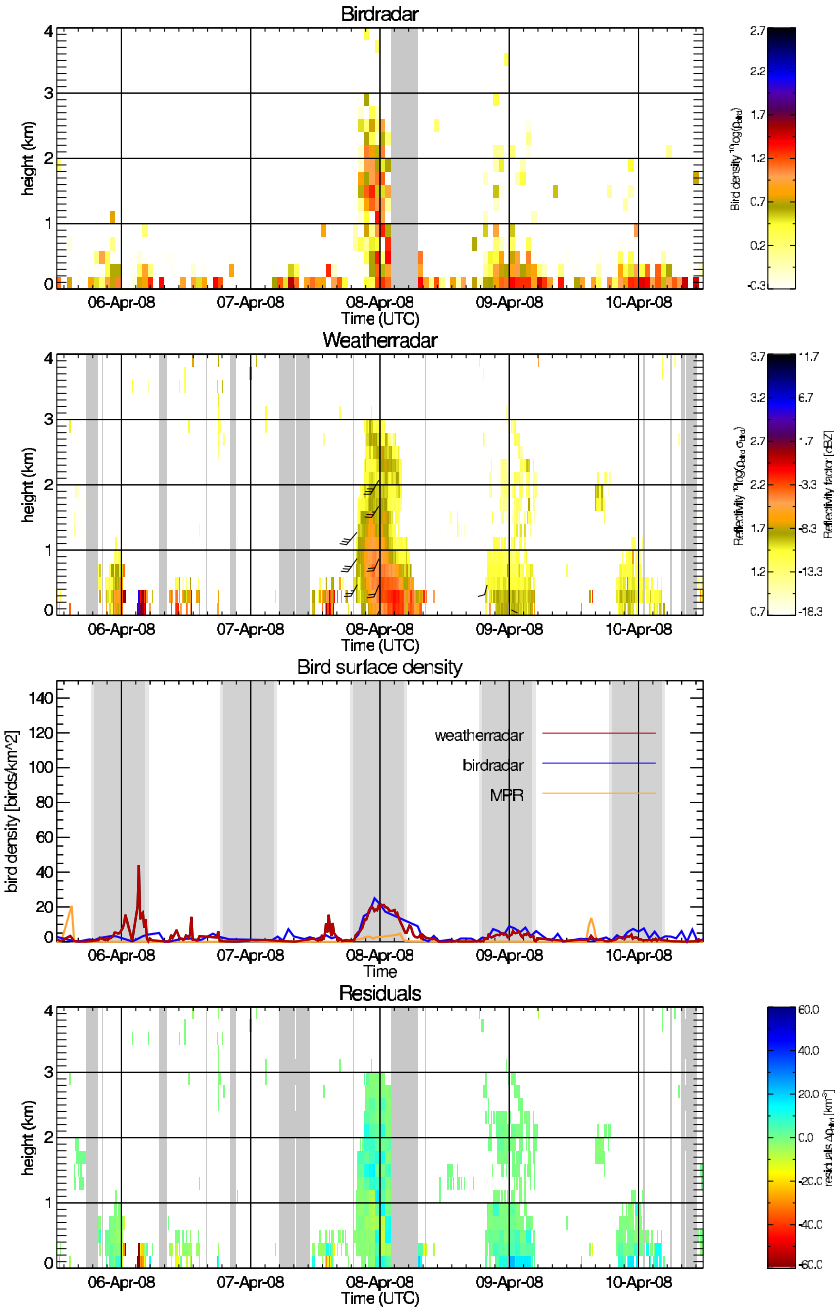

Figure C.18: Retrieved time-height profiles by birdradar (top) and weatherradar (upper middle). The vertically integrated bird densities (lowest 200 m excluded) and weather radar - bird radar density difference are shown in the lower middle and bottom panel, resp.

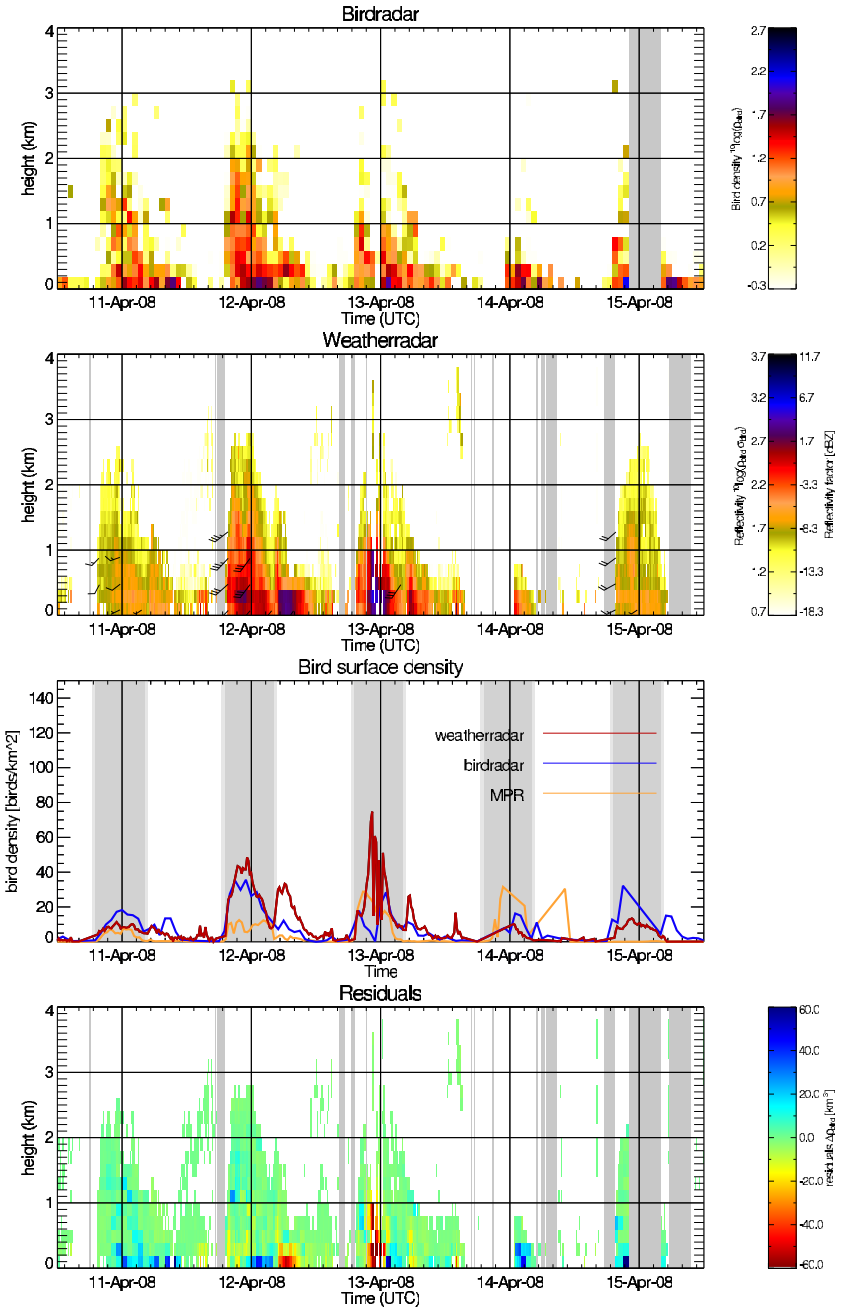

Figure C.19: Retrieved time-height profiles by birdradar (top) and weatherradar (upper middle). The vertically integrated bird densities (lowest 200 m excluded) and weather radar - bird radar density difference are shown in the lower middle and bottom panel, resp.

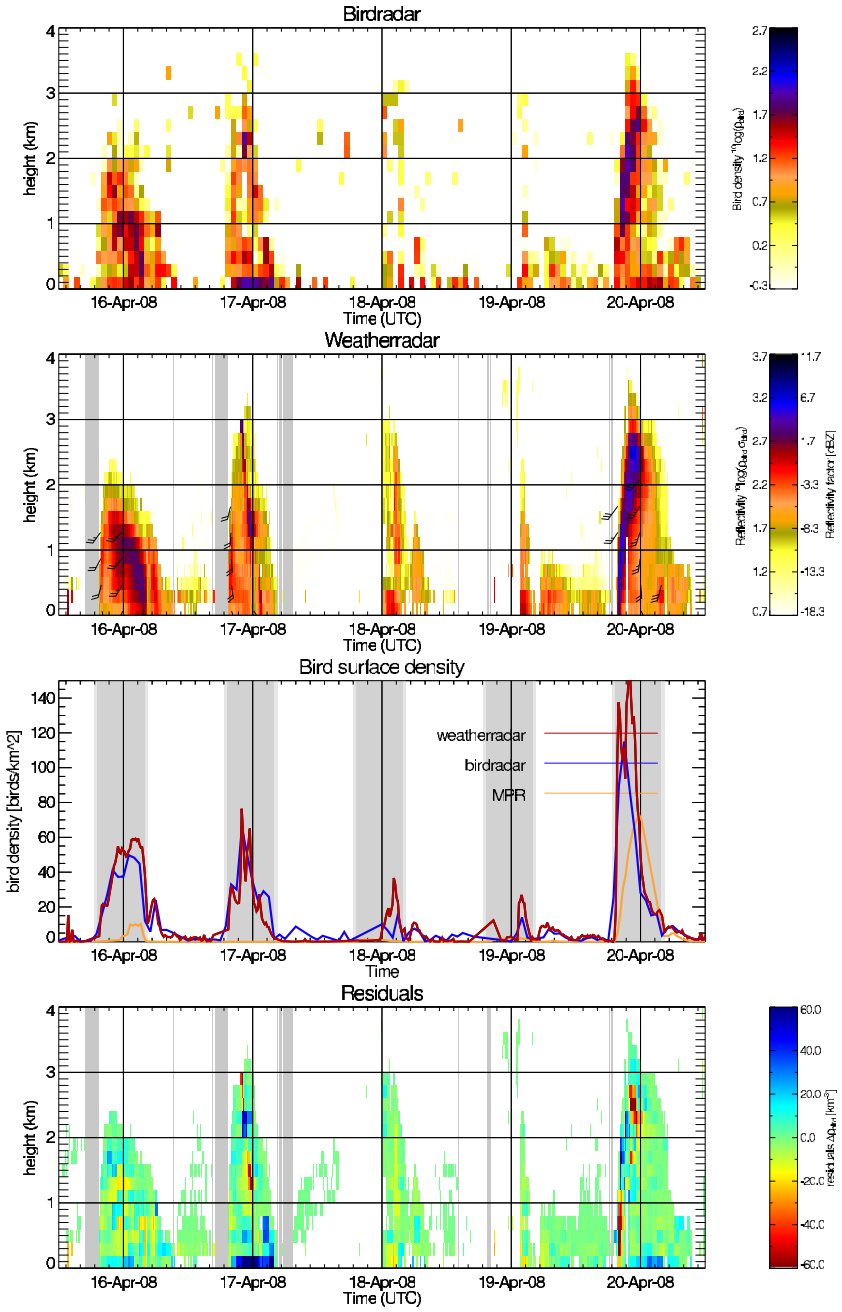

Figure C.20: Retrieved time-height profiles by birdradar (top) and weatherradar (upper middle). The vertically integrated bird densities (lowest 200 m excluded) and weather radar - bird radar density difference are shown in the lower middle and bottom panel, resp.

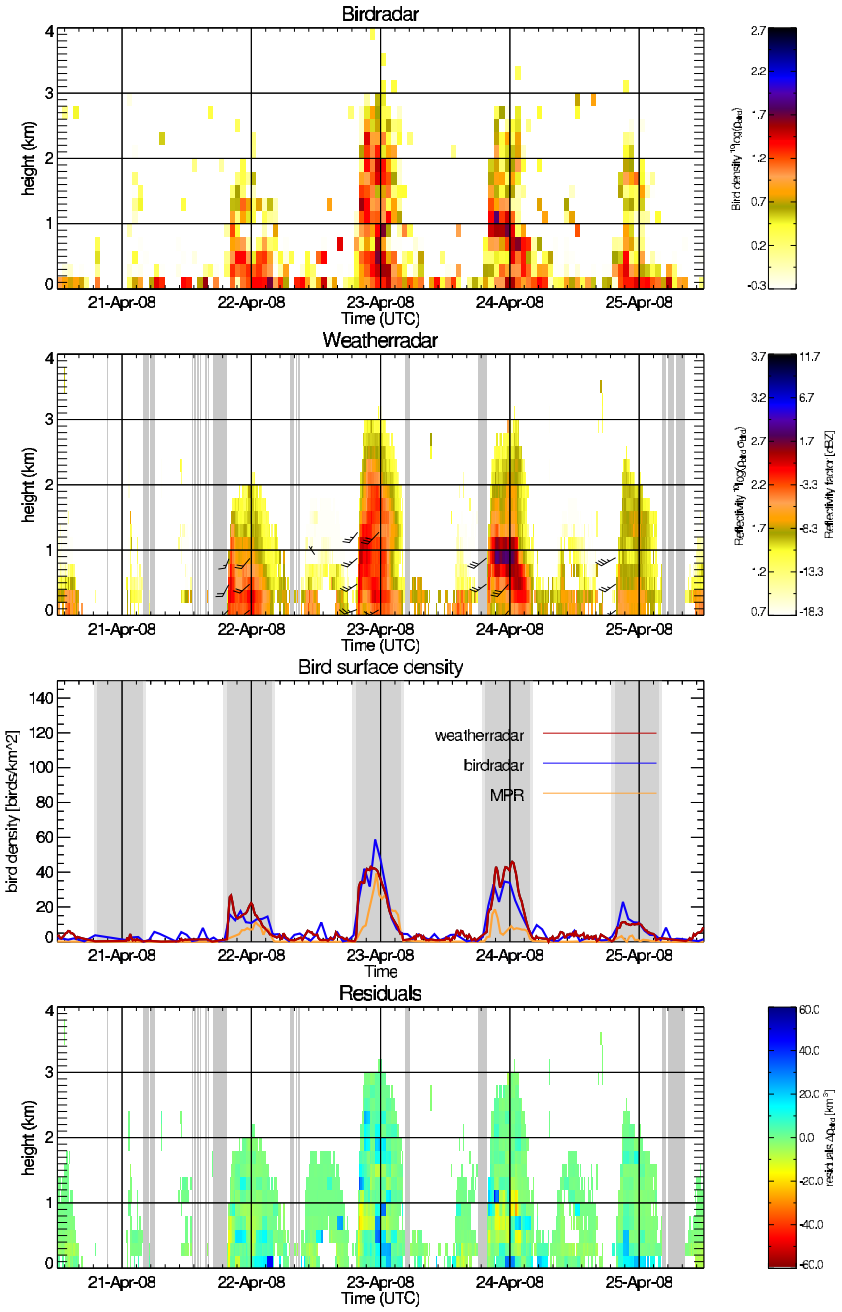

Figure C.21: Retrieved time-height profiles by birdradar (top) and weather-radar (upper middle). The vertically integrated bird densities (lowest 200 m excluded) and weather radar - bird radar density difference are shown in the lower middle and bottom panel, resp.

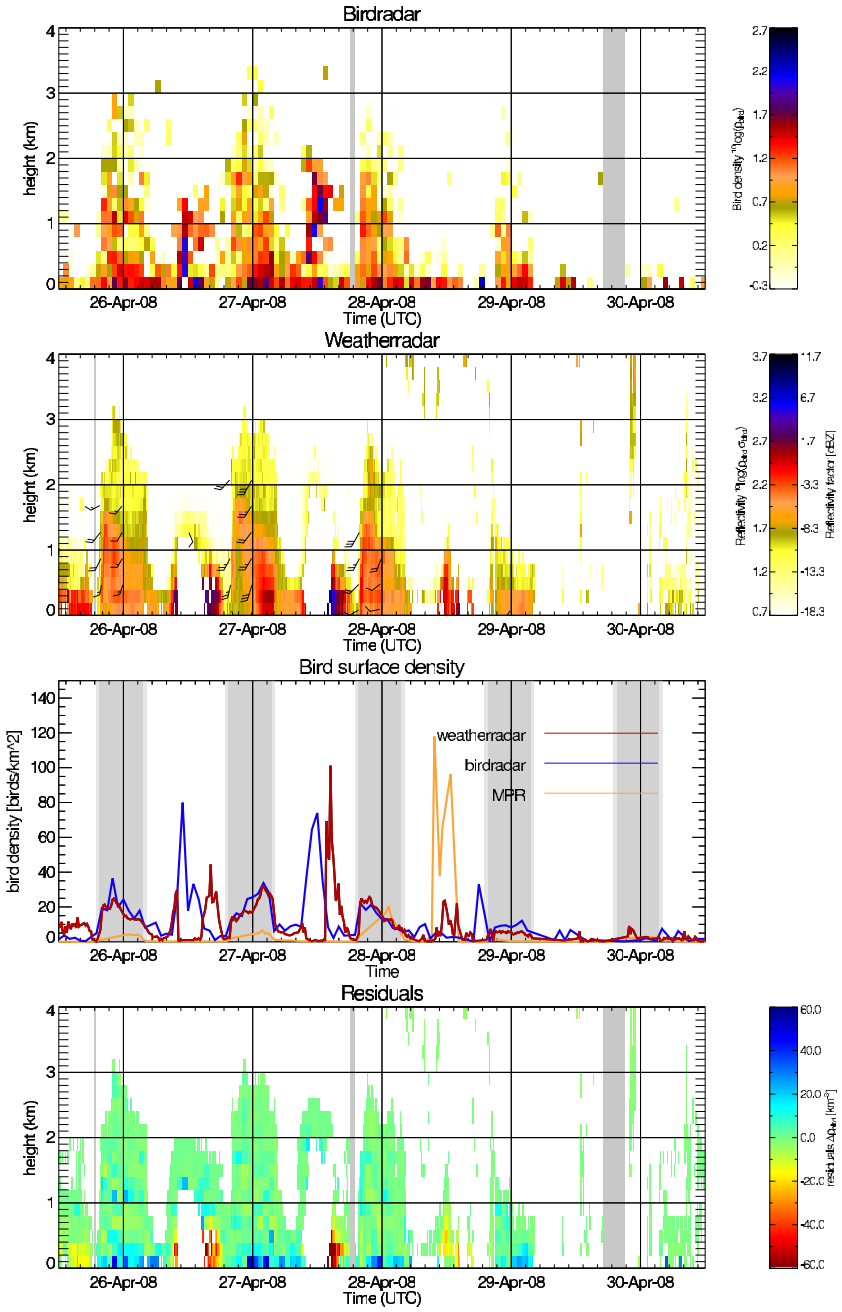

Figure C.22: Retrieved time-height profiles by birdradar (top) and weather-radar (upper middle). The vertically integrated bird densities (lowest 200 m excluded) and weather radar - bird radar density difference are shown in the lower middle and bottom panel, resp.

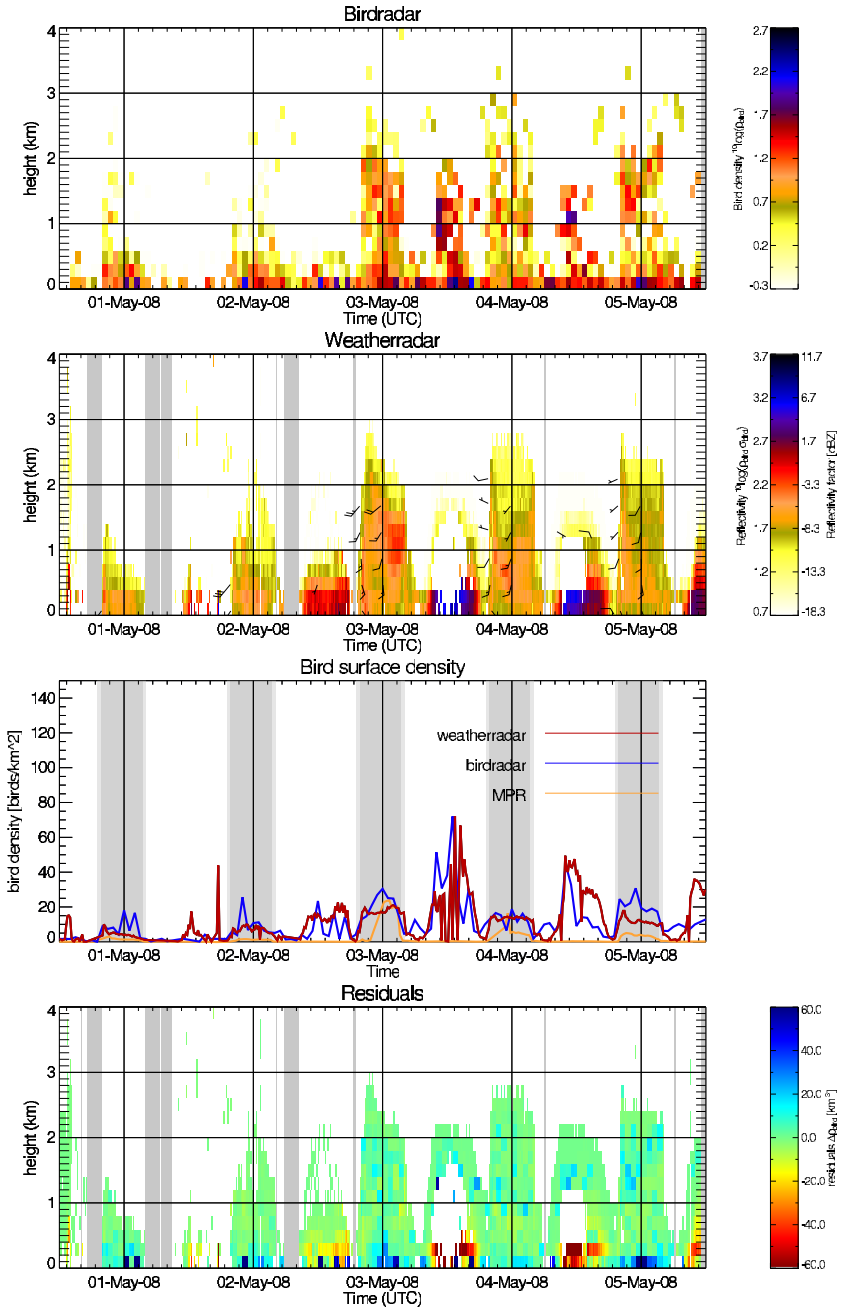

Figure C.23: Retrieved time-height profiles by birdradar (top) and weatherradar (upper middle). The vertically integrated bird densities (lowest 200 m excluded) and weather radar - bird radar density difference are shown in the lower middle and bottom panel, resp.

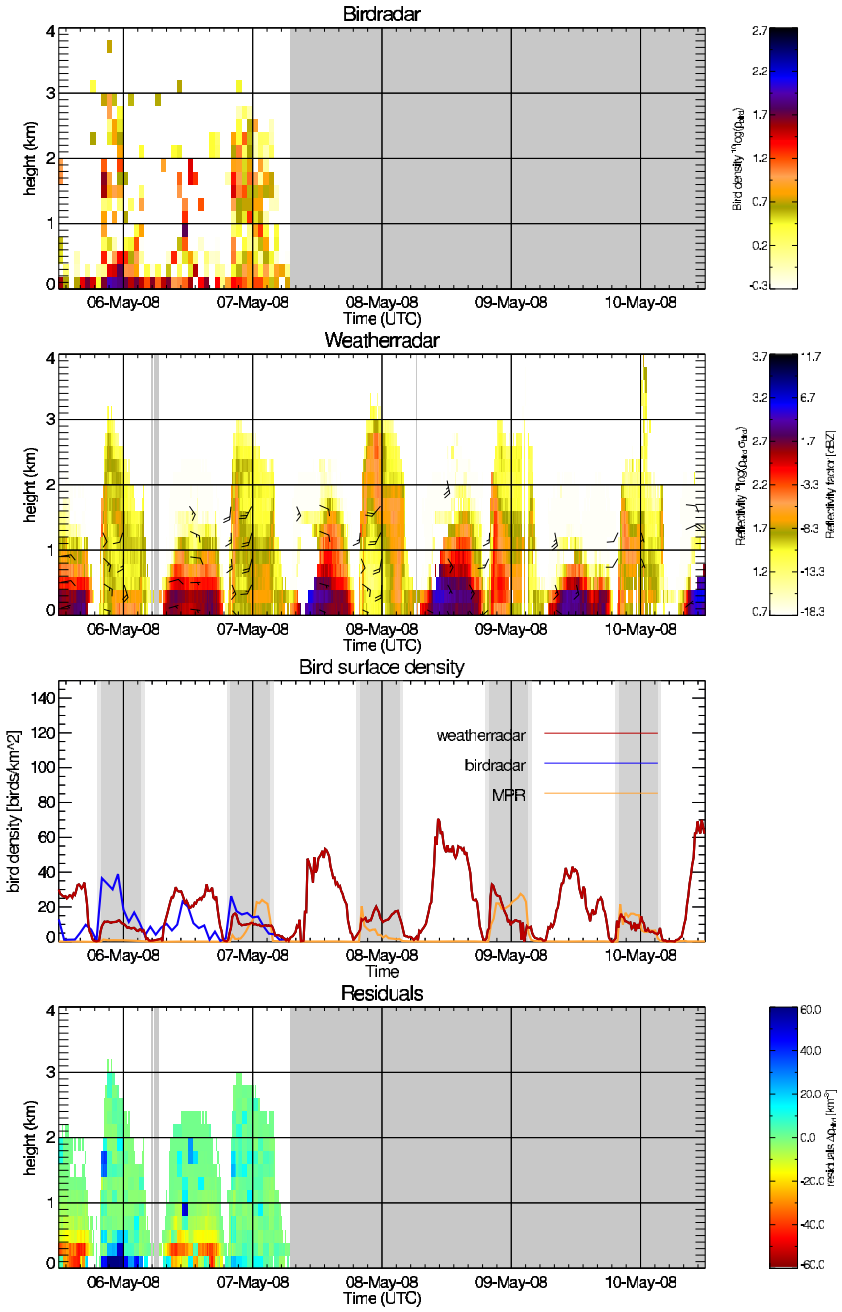

Figure C.24: Retrieved time-height profiles by birdradar (top) and weather-radar (upper middle). The vertically integrated bird densities (lowest 200 m excluded) and weather radar - bird radar density difference are shown in the lower middle and bottom panel, resp.

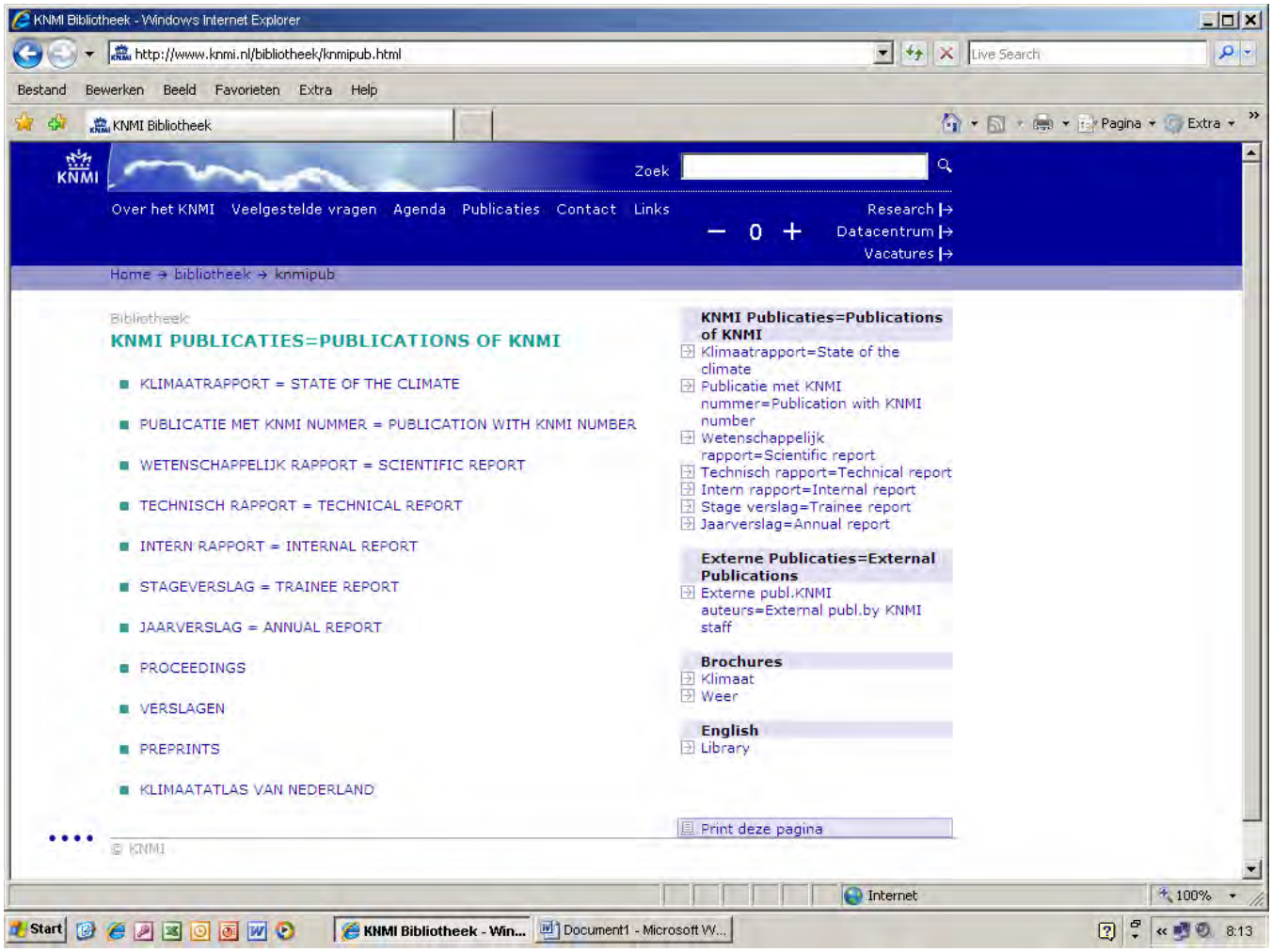

All titles of KNMI-publications (and a full text PDF for the most recent ones) can be found on

http://www.knmi.nl/bibliotheek/knmipub.html

If you have any questions, please contact us: bibliotheek@knmi.nl